Chiral Mesogen-Free Liquid Crystalline Polyethers with Sulfonylated Side Chains and Patchy Brush Nanoparticles

A Dissertation Presented for the

Doctor of Philosophy

Degree

The University of Tennessee, Knoxville

Caleb A. Bohannon

May 2022

Acknowledgements

A sincere thank you to Professor Bin Zhao for the time, effort, and support you have extended to me since we began working together. You have made me a better person from the lessons I have learned with you, and I will not forget them.

To my collaborators Professor Lei Zhu and Dr. Patrick Kwok of Case Western Reserve University, I thank you for your guidance and mentorship during my time here. Without your additional insight, my research on liquid crystalline polymers would not have been possible.

Additionally, I would like to thank my committee members: Professor Mark Dadmun, Professor Ampofo Darko, and Professor Manolis Doxastakis. I have appreciated your advice and the opportunity to be instructed in a way that will prepare me for the future.

I thank the United States Department of Energy (DOE) and the National Science Foundation (NSF) for providing the funding necessary to perform the work detailed in this dissertation.

Thank you to all current and past group members: Dr. Daniel Hen, Dr.Wenxin Fu, Dr. Bryan Seymour, Dr. Ethan Kent, Dr. Evan Lewoczko, Dr. Bo Liu, Dr. Yang Wu, Andrew Chancellor, and Michael Kelly. I will always look back fondly on the professional connections and friendships I made at this stage in my life. A special thanks to Dr. Ethan Kent for his instruction and friendship.

Thank you to my family, my mother and father Mike and Lynn Bohannon, you are the reason I have come this far; your support, kind encouragement, advice, and love has guided me through more than this, and it will continue to guide me through the next chapters in my life. Thank you to my brother, Joshua Bohannon, for helping me with my “experiments” and adventures in our younger days, I’m positive there will be more adventures for us to have in the coming years.

To my wife, Abigail, thank you for your patience, love, and support through the highs and lows during this period of time. I love you and thank you for this.

Abstract

Ferroelectric liquid crystalline polymers (LCPs) hold promise for various applications driven by low electric fields, e.g., electrocaloric materials, because of the higher molecular motion in the liquid crystalline (LC) state. However, traditional chiral smectic C (SmC*) LCPs exhibit small spontaneous polarizations due to the bulky aromatic mesogens and weak polar groups. This dissertation research is focused on the design of mesogen-free sulfonylated LCPs with a goal of seeking the ferroelectric SmC* phase. Such LCPs are expected to exhibit high polarizations owing to the sulfonyl's large dipole moment. A series of poly(oxypropylene)s (POPs), with chirality being introduced into either the backbone or sulfonylated side chains or both, were synthesized, and their self-assembly behavior was investigated.

Chirality was first introduced into the backbone of POPs with linear mono- and di-sulfonylated side chains. Although smectic E and A (SmA) phases were observed, no SmC* was found in these polymers. The backbone chirality had an insignificant influence on the LC self-assembly behavior. Two additional strategies were then explored: decreasing the grafting density of sulfonylated side chains and introducing a methyl branch into the short side chains of POPs. SmA and hexagonal columnar structures were observed for isotactic POPs with various degrees of *n*-dodecylsulfonyl substitution. When a chiral methyl branch was introduced into the short side chains of an isotactic POP, a crystalline phase with titled side chains was discovered. The alkyl tail was then increased and a -$CH_2CH_2CH_2O$- spacer was incorporated, producing a SmC*-like phase for the single chirality POPs. However, no ferroelectric switching was achieved, likely due to the strong dipole-dipole interactions. These studies provide valuable information for future design of mesogen-free ferroelectric SmC* LCPs.

The last part of this dissertation concerned the morphology of binary mixed homopolymer

brush-grafted, 20.4 nm silica nanoparticles (NPs). Transmission electron microscopy showed that the brush NPs phase separated into patchy NPs with 6 to 10 nanodomains (valency) upon solution casting. A linear relationship between valency and core size was observed; the NPs can form physical “bonds” with each other and exhibit an ability to change the valency. This work provides a new approach toward multivalent patchy NPs.

Table of Contents

Chapter 1: Introduction 1

1.1. Introduction 2

1.1.1. Introduction to Electrocaloric Materials 2

1.1.2. Liquid Crystals and Liquid Crystalline Polymers 5

1.1.3. Binary Mixed Homopolymer Brushes on Small Nanoparticles 8

1.2. Characterization Techniques Used in this Dissertation Research 10

1.3 Dissertation Overview 16

References 19

Chapter 2: Effects of Tacticity and Chiral Center-to-Dipole Distance on Mesogen-Free Liquid Crystalline Self-Assembly of Sulfonyl-Containing Comb-Like Polymers 25

Abstract 26

2.1. Introduction 28

2.2. Experimental section 30

2.2.1. Materials 30

2.2.2. Characterization and Instrumentation 32

2.2.3. Synthesis of Atactic Polyethers with *n*-Alkylsulfonylpentylthioether Pendant Groups (aPOP-$SC_5SO_2C_8$ and aPOP-$SC_5SO_2C_{12}$) 34

2.2.4. Synthesis of Isotactic Polyethers with *n*-Alkylsulfonylpentylthioether Pendant Groups (iPOP-$SC_5SO_2C_8$ and iPOP-$SC_5SO_2C_{12}$ 36

2.2.5. Synthesis of Atactic and Isotactic Polyethers with Disulfonyl Pendant Groups 37

2.3. Results and Discussion 38

2.3.1. Synthesis of Isotactic and Atactic Polyethers with Mono- and Disulfonyl Pendant Groups 38

2.3.2. Self-Assembly of Atactic and Isotactic POP-$SC_5SO_2C_{12}$ and POP-$SO_2C_5SO_2C_{12}$ ... 44

2.3.3. Effect of *n*-Alkyl Tail Length on Self-Assembly of Atactic and Isotactic POP-$SC_5SO_2C_8$ and POP-$SO_2C_5SO_2C_8$ 57

2.4. Conclusions 60

References 64

Appendix A 70

Chapter 3: Synthesis of Isotactic Polyethers with Various Degrees of *n*-Dodecylsulfonyl Substitution and Polyethers with Short Sulfonylated Methyl-Branched Side Chains 96

Abstract 97

3.1. Introduction 98

3.2. Experimental section 100

3.2.1. Materials 100

3.2.2. General Characterization 100

3.2.3. Synthesis of Isotactic Polyethers with Various Degrees of *n*-Dodecylsulfonyl Substitution 101

3.2.4. Synthesis of (*S*)-S-(2-Methylbutyl) Ethanethioate 104

3.2.5. Synthesis of iPOP-SO_2bC_{5s}, aPOP-SO_2bC_{5s}, and iPOP-SO_2bC_5 106

3.3. Results and Discussion 110

3.3.1. Synthesis of Isotactic Poly(oxypropylene) Polyethers with Various Degrees of *n*-Dodecylsulfonyl Substitution 110

3.3.2. Mesophase Self-Assembly Behavior of Isotactic Polyethers with Various Degrees of *n*-Dodecylsulfonyl Substitution 115

3.3.3. Synthesis and Self-Assembly of Isotactic and Atactic Polyethers with Chiral or Racemic Methyl-Branched Sulfonylated C5 Side Chains 115

3.4. Conclusions 120

References 121

Appendix B 122

Chapter 4: SmC*-like Self-Assembly in Mesogen-Free Liquid Crystalline Polyethers with Sulfonylated Branched Alkyl Side Chains 141

Abstract 142

4.1. Introduction 143

4.2 Experimental Section 144

4.2.1. Materials 144

4.2.2. Synthesis of Isotactic and Atactic Polyethers with Branched and Linear Thioether Pendant Groups. 146

4.2.3. Synthesis of Atactic and Isotactic Polyethers with Branched and Linear Sulfonylated Pendant Groups 149

4.2.4. Fiber-Drawing Process 151

4.2.5. Instrumentation and Characterization 151

4.3. Results and Discussion 153

4.3.1. Synthesis of Isotactic and Atactic Polyethers with Branched and Linear Sulfonylated Pendant Groups 153

4.3.2. Thermal Behavior of Various Sulfonylated Polyethers 160

4.3.3. Self-assembly of Various Sulfonylated Polyethers Studied by XRD and PLM 163

4.3.4. Dielectric Property Study 171

4.4. Conclusions 173

References 174

Appendix C 178

Chapter 5: Adaptable Multivalent Hairy Inorganic Nanoparticles 210

Abstract 211

5.1. Introduction 212

5.2. Experimental Section 213

5.2.1. Synthesis of Mixed Poly(*tert*-butyl acrylate) (P*t*BA)/polystyrene (PS) Brush-Grafted 20.4 nm Silica NPs 213

5.2.2. Transmission Electron Microscopy (TEM) Study of Polymer Brush-Grafted Silica NPs 213

5.3. Results and Discussion 214

5.4. Conclusions 225

References 226

Chapter 6: Conclusions and Future Work 232

References 237

Vita 238

List of Tables

Table 2.1. Characterization Data for Atactic and Isotactic Polyethers with Mono- and Di-sulfonyl Pendant Groups 42

Table 2.2. Peak Phase Transition Temperatures (above the arrow) and Heats of Transition (kJ/mol, below the arrow) [a] for atactic and isotactic POP-$SC_5SO_2C_{12}$ and POP-$SO_2C_5SO_2C_{12}$ 47

Table 2.3. Peak Phase Transition Temperatures (above the arrow) and Heats of Transition (kJ/mol, below the arrow) [a] for atactic and isotactic POP-$SC_5SO_2C_8$ and POP-$SO_2C_5SO_2C_8$ 61

Table 3.1. Summary of Characterization Data for iCoP-SO_2C_{12}-*x* and iPOP-SO_2C_{12} as well as Corresponding iPOP with Thioether Pendant Groups 114

Table 4.1. SEC and Polarimetry Data for Isotactic and Atactic Polyethers with Branched and Linear Pendant Groups 157

Table 5.1. Characterization of Mixed P*t*BA/PS Brush-Grafted Silica NPs 216

List of Figures

Figure 1.1. Nanostructures of binary mixed homopolymer brushes on nanospheres of a diameter comparable to the polymer sizes with an island number from 2 to 8 at $\sigma_B/\sigma_A = 2$. σ_A and σ_B are the grafting densities of polymer A and polymer B, respectively, R is the nanosphere radius, N_A and N_B are chain lengths of polymer A and polymer B, respectively. (a) (R, σ_{total}, N_A/N_B) = (0.5, 1.0, 20/20); (b) (R, σ_{total}, N_A/N_B) = (1.0, 0.8, 20/20); (c) (R, σ_{total}, N_A/N_B) = (2.0, 1.0, 30/30); (d) (R, σ_{total}, N_A/N_B) = (2.0, 0.7, 20/20); (e) (R, σ_{total}, N_A/N_B) = (2.0, 0.8, 20/20); (f) (R, σ_{total}, N_A/N_B) = (3.0, 0.6, 20/20), and (g) (R, σ_{total}, N_A/N_B) = (4.0, 0.6, 25/30). The first and second rows show only A and B blocks, respectively, and the bottom row is isosurface morphologies of mixed polymer brush. Polymer A and B are represented by green color and blue color, respectively, with a red sphere inside. 9

Figure 1.2. Example DSC thermograms of a liquid crystal polymer, forming both smectic and nematic phases sequentially. (Reproduced from Ref. 37 with permission from the Polish Academy of Sciences)..... 11

Figure 2.1. ^{1}H NMR spectra of (A) aPOP-$SC_5SO_2C_{12}$, (B) iPOP-$SC_5SO_2C_{12}$, (C) aPOP-$SO_2C_5SO_2C_{12}$, and (D) iPOP-$SO_2C_5SO_2C_{12}$ in $CDCl_3$. Peaks labeled with * are from impurities. 39

Figure 2.2. ^{13}C NMR spectra of (A) aPOP-$SC_5SO_2C_{12}$ and (B) iPOP-$SC_5SO_2C_{12}$ in $CDCl_3$. ... 41

Figure 2.3. (A) Second heating DSC curves for atactic and isotactic POP-$SC_5SO_2C_{12}$ and POP-$SO_2C_5SO_2C_{12}$. (B) Second cooling DSC curves for atactic and isotactic POP-$SC_5SO_2C_{12}$ and POP-$SO_2C_5SO_2C_{12}$. The dotted lines in (A) show the T_g values during the first heating cycle. The heating and cooling rates are 20 °C/min. 45

Figure 2.4. PLM images of (A) aPO-PS$C_5SO_2C_{12}$ and (B) iPOP-$SC_5SO_2C_{12}$ during the heating and cooling cycle. The scale bars are 20 μm. 48

Figure 2.5. PLM images of (A) aPOP-$SO_2C_5SO_2C_{12}$ and (B) iPOP-$SO_2C_5SO_2C_{12}$ during the heating and cooling cycles. The scale bars are 20 μm. 49

Figure 2.6. (A) 2D XRD pattern for the aPOP-$SC_5SO_2C_{12}$ fiber at room temperature. The fiber direction is vertical. (B) 1D XRD profiles for the aPOP-$SC_5SO_2C_{12}$ fiber at room temperature and the powder at 95 and 110 °C. The inset shows the schematic double layer structure. The bottom panel shows the 1D XRD profiles for the aPOP-$SC_5SO_2C_{12}$ powder during (C) heating and (D) cooling processes. Peaks labeled with * in B were from the Kapton window, and they are not labeled in C and D. 50

Figure 2.7. (A) 2D XRD pattern for the aPOP-$SC_5SO_2C_{12}$ fiber at room temperature (r.t.) obtained using a Xenocs Xeuss 3.0 SAXS instrument at the University of Tennessee Knoxville. The fiber direction is vertical. (B) and (C) Correspond to SAXS (B) and WAXS (C) 1D XRD profiles for the aPOP-$SC_5SO_2C_{12}$ fiber obtained by the integration of the 2D pattern (A).. 52

Figure 2.8. (A) 2D XRD pattern for the iPOP-$SC_5SO_2C_{12}$ fiber. The fiber direction is vertical. (B) 1D XRD profiles for the iPOP-$SC_5SO_2C_{12}$ fiber at room temperature and the powder at 100 and 115 °C. The inset shows the schematic double layer structure. The bottom panel shows the 1D XRD profiles for the iPOP-$SC_5SO_2C_{12}$ powder during (C) heating and (D) cooling processes. Peaks labeled with * in B were from the Kapton window, and they are not labeled in C and D. 54

Figure 2.9. (A) 2D XRD pattern for the aPOP-$SO_2C_5SO_2C_{12}$ powder at room temperature. (B) and (C) show 1D XRD profiles for the powder sample during the heating and cooling cycle, respectively. The inset shows the schematic double layer structure. 56

Figure 2.10. (A) 2D XRD pattern for the iPOP-$SO_2C_5SO_2C_{12}$ powder at room temperature. (B) and (C) show 1D XRD profiles for the iPOP-$SO_2C_5SO_2C_{12}$ powder during the heating and cooling processes, respectively. The inset shows the schematic double layer structure. 58

Figure 2.11. (A) DSC second heating curves for atactic and isotactic POP-$SC_5SO_2C_8$ and POP-$SO_2C_5SO_2C_8$. (B) DSC second cooling curves for atactic and isotactic POP-$SC_5SO_2C_8$ and POP-$SO_2C_5SO_2C_8$. K: crystal, SmE: smectic E, SmA: smectic A, and I: isotropic. T_g values are determined from the first heating (thin dotted lines in the insets). 59

Figure A.1. ^1H NMR spectrum of iPECH in $CDCl_3$. Peaks labeled with * are from impurities. 77

Figure A.2. (A) ^1H and (B) ^{13}C NMR spectra of aPOP-$SC_5SO_2C_8$ in $CDCl_3$. 78

Figure A.3. Size exclusion chromatography curve of aPOP-$SC_5SO_2C_8$ using $CHCl_3$ as eluent. 79

Figure A.4. ^{13}C NMR spectrum of aPOP-$SC_5SO_2C_{12}$ in $CDCl_3$..... 80

Figure A.5. Size exclusion chromatography curve of aPOP-$SC_5SO_2C_{12}$ using $CHCl_3$ as eluent. 81

Figure A.6. (A) ^1H and (B) ^{13}C NMR spectra of iPOP-$SC_5SO_2C_8$ in $CDCl_3$. 82

Figure A.7. Size exclusion chromatography curve of iPOP-$SC_5SO_2C_8$ using $CHCl_3$ as eluent. 83

Figure A.8. ^{13}C NMR spectrum of iPOP-$SC_5SO_2C_{12}$ in $CDCl_3$. 84

Figure A.9. Size exclusion chromatography curve of iPOP-$SC_5SO_2C_{12}$ using $CHCl_3$ as eluent. 85

Figure A.10. ^1H NMR spectra of (A) aPOP-$SO_2C_5SO_2C_8$ and (B) iPOP-$SO_2C_5SO_2C_8$ in $CDCl_3$. 86

Figure A.11. Size exclusion chromatography curves of (a) aPOP-$SO_2C_5SO_2C_8$, (b) iPOP-$SO_2C_5SO_2C_8$, (C) aPOP-$SO_2C_5SO_2C_{12}$, and (D) iPOP-$SO_2C_5SO_2C_{12}$ using $CHCl_3$ as eluent. 87

Figure A.12. Thermogravimetric analysis (TGA) curves of (A) aPOP-$SC_5SO_2C_8$, (B) iPOP-$SC_5SO_2C_8$, (C) aPOP-$SC_5SO_2C_{12}$, and (D) iPOP-$SC_5SO_2C_{12}$. TGA was performed in a dry N_2 atmosphere at a heating rate of 20 °C/min. 88

Figure A.13. Thermogravimetric analysis (TGA) curves of (A) aPOP-$SO_2C_5SO_2C_8$, (B) iPOP-$SO_2C_5SO_2C_8$, (C) aPOP-$SO_2C_5SO_2C_{12}$, and (D) iPOP-$SC_5SO_2C_{12}$. TGA was performed in a dry N_2 atmosphere at a heating rate of 20 °C/min. 89

Figure A.14. PLM micrographs of (A) aPOP-$SC_5SO_2C_8$ and (B) iPOP-$SC_5SO_2C_8$ at different temperatures during the first heating and cooling cycle. The scale bar is 10 μm. 90

Figure A.15. PLM micrographs of (A) aPOP-$SO_2C_5SO_2C_8$ and iPOP-$SO_2C_5SO_2C_8$ at different temperatures during the first heating and cooling cycle. The scale bars is 20 μm in (A) and 10 μm in (B). 91

Figure A.16. (A) 2D XRD pattern for the aPOP-$SC_5SO_2C_8$ fiber at room temperature. (B) 1D XRD profiles for the fiber at room temperature and the powder at 61 °C. The inset shows the schematic double layer structure. The * symbols indicate reflections from the Kapton window. (C) 1D XRD profiles of the aPOP-$SC_5SO_2C_8$ powder sample during heating and cooling processes. 92

Figure A.17. (A) 2D XRD pattern for the iPOP-$SC_5SO_2C_8$ fiber at room temperature. (B) 1D XRD profiles for the fiber at room temperature and the powder at 70 °C. The inset shows the schematic double layer structure. The * symbols indicate reflections from the Kapton window. (C) 1D XRD profiles of the iPOP-$SC_5SO_2C_8$ powder sample during heating and cooling processes. 93

Figure A.18. (A) 2D XRD pattern for the aPOP-$SO_2C_5SO_2C_8$ fiber at room temperature. (B) 1D XRD profiles for the fiber at room temperature and the powder at 150 and 180 °C. The inset

shows the schematic double layer structure. The * symbols indicate reflections from the Kapton window. (C) 1D XRD profiles of the aPOP-$SO_2C_5SO_2C_8$ powder sample during heating and cooling cycles. 94

Figure A.19. (A) 2D XRD pattern for the iPOP-$SO_2C_5SO_2C_8$ fiber at room temperature. (B) 1D XRD profiles for the fiber at room temperature and the powder at 170 °C. The inset shows the schematic double layer structure. (C) 1D XRD profiles of the iPOP-$SO_2C_5SO_2C_8$ powder sample during heating and cooling cycles. 95

Figure 3.1. ^{1}H NMR spectra of iCoP-SC_{12}-88% and iCoP-SO_2C_{12}-88% in $CDCl_3$. 112

Figure 3.2. Size exclusion chromatography (SEC) curve of iCoP-SO_2C_{12}-88% using THF as the mobile phase. 113

Figure 3.3. Summary of various phase transitions in iCoP-SO_2C_{12}-*x* as a function of the grafting density. 116

Figure 3.4. ^{1}H NMR spectra of (a) iPOP-SO_2bC_{5s}, (b) aPOP-SO_2bC_{5s}, and (c) iPOP-SO_2bC_5 in $CDCl_3$. 118

Figure B.1. ^{1}H NMR spectra of (A) iCoP-SC_{12}-50% and (B) iCoP-SO_2C_{12}-50% in $CDCl_3$.... 123

Figure B.2. Size exclusion chromatography (SEC) curve of iCoP-SO_2C_{12}-50% using THF as the mobile phase. 124

Figure B.3. ^{1}H NMR spectra of (A) iCoP-SC_{12}-60% and (B) iCoP-SO_2C_{12}-60% in $CDCl_3$..... 125

Figure B.4. Size exclusion chromatography (SEC) curve of iCoP-SO_2C_{12}-60% using THF as the mobile phase. 126

Figure B.5. ^{1}H NMR spectra of (A) iCoP-SC_{12}-71% and (B) iCoP-SO_2C_{12}-71% in $CDCl_3$.... 127

Figure B.6. Size exclusion chromatography (SEC) curve of iCoP-SO_2C_{12}-71% using THF as the mobile phase. 128

Figure B.7. ^{1}H NMR spectra of (A) iPOP-SC_{12}-73% and (B) iPOP-SO_2C_{12}-73% in $CDCl_3$... 129

Figure B.8. Size exclusion chromatography (SEC) curve of iCoP-SO_2C_{12}-73% using THF as the mobile phase. 130

Figure B.9. ^{1}H NMR spectra of (A) iCoP-SC_{12}-79% and (B) iCoP-SO_2C_{12}-79% in $CDCl_3$..... 131

Figure B.10. Size exclusion chromatography (SEC) curve of iCoP-SO_2C_{12}-79% using THF as the mobile phase. 132

Figure B.11. ^{1}H NMR spectra of (A) iCoP-SC_{12}-92% and (B) iCoP-SO_2C_{12}-92% in $CDCl_3$.. 133

Figure B.12. Size exclusion chromatography (SEC) curve of iCoP-SO_2C_{12}-92% using THF as the mobile phase. 134

Figure B.13. ^{1}H NMR spectra of (A) iPoP-SC_{12} and (B) iPoP-SO_2C_{12} in $CDCl_3$. 135

Figure B.14. Size exclusion chromatography (SEC) curve of iPoP-SO_2C_{12} using THF as the mobile phase. 136

Figure B.15. (A) ^{1}H and (B) ^{13}C NMR spectra of (*S*)-S-(2-methylbutyl) ethanethioate in $CDCl_3$. 137

Figure B.16. ^{1}H NMR spectra of (A) iPOP-SbC_{5s}, (B) aPOP-SbC_{5s}, (C) iPOP-SbC_5 in $CDCl_3$. 138

Figure B.17. ^{13}C NMR spectra of (A) iPOP-SO_2bC_{5s}, (B) aPOP-SO_2bC_{5s}, (C) iPOP-SO_2bC_5 in $CDCl_3$. 139

Figure B.18. Size exclusion chromatography curves of (A) iPOP-SO_2bC_{5s}, (B) aPOP-SO_2bC_{5s}, (C) iPOP-SO_2bC_5 obtained from PL-GPC-20 using THF as the mobile phase. 140

Figure 4.1. ^{1}H NMR spectra of (a) iPOP-SC_3ObC_{8R}, (b) aPOP-SC_3ObC_{8R}, (c) iPOP-$SO_2C_3ObC_{8R}$, and (d) aPOP-$SO_2C_3ObC_{8R}$ in $CDCl_3$. 156

Figure 4.2. ^{13}C NMR spectra in the range of 80–70 ppm of (A) iPOP-SC_3ObC_{8R} and (B) aPOP-SC_3ObC_{8R} in $CDCl_3$. 159

Figure 4.3. (A) First heating, (B) first cooling, and (C) second heating DSC curves of various sulfonylated side-chain polyether fibers. The heating and cooling rates were 10 °C/min. 162

Figure 4.4. Room temperature (A,C,E) 2D and (B,D,F) 1D XRD results for (A,B) iPOP-$SO_2C_3ObC_{8R}$, (C,D) iPOP-$SO_2C_3ObC_{10R}$, and (E,F) iPOP-$SO_2C_3ObC_8$, respectively. The intensity in 2D XRD patterns is in the logarithmic scale. The insets in (B,D,F) show the double-layer crystalline structures with tilted side chains. 164

Figure 4.5. PLM images of (a-f) iPOP-$SO_2C_3ObC_{8R}$, (g-l) iPOP-$SO_2C_3ObC_{10R}$, and (m-r) iPOP-$SO_2C_3ObC_8$ stretched fibers during the first heating and the subsequent cooling processes. Different phases are assigned based on both DSC and XRD results. K: crystal, SmC*-like: smectic C*-like, and Iso: isotropic. The scale bars are 20 μm. 166

Figure 4.6. (A,D,G) 2D and (B,E,H) 1D XRD results, and (C,F,I) the corresponding azimuthal scan curves for (A-C) aPOP-$SO_2C_3ObC_{8R}$ (-10 °C), (D-F) iPOP-$SO_2C_3ObC_{10}$ (-10 °C), and (G-I) iPOP-$SO_2C_3OC_{8L}$ (25 °C) fibers, respectively. The intensity in 2D XRD patterns is in the logarithmic scale. The insets in (B,E,H) show the double-layer SmC*-like/SmA structures of the melt-drawn fibers. 168

Figure 4.7. PLM images of (a-d) aPOP-$SO_2C_3ObC_{8R}$, (e-i) iPOP-$SO_2C_3ObC_{10}$, and (j-n) iPOP-$SO_2C_3OC_{8L}$ fibers during the heating and the subsequent cooling processes. Different phases are assigned based on both DSC and XRD results. K: crystal, SmC*-like: smectic C*-like, and Iso: isotropic. The scale bars are 20 μm. 169

Figure 4.8. 2D (A) and 1D XRD (B and C; B: linear scale and C: logarithmic scale for Y-axis) results for the iPOP-$SO_2C_3OC_{8L}$ fiber at room temperature. 170

Figure 4.9. Bipolar D-E loops for (A) iPOP-$SO_2C_3ObC_8$, (B) aPOP-$SO_2C_3ObC_{8R}$, and (C) iPOP-$SO_2C_3ObC_{10}$ at room temperature. The poling frequency was 100 Hz with a sinusoidal waveform. The AC electronic conduction is subtracted from these D-E loops (see Figure C.25)..... 172

Figure C.1. (A) ^1H and (B) ^{13}C spectra of (*R*)-(2-allyloxy)octane (C1) in $CDCl_3$. 181

Figure C.2. (A) ^1H and (B) ^{13}C NMR spectra of (*R*)-2-(allyloxy)decane (C2) in $CDCl_3$. 183

Figure C.3. (A) ^1H and (B) ^{13}C spectra of 2-(allyloxy)octane (C3) in $CDCl_3$. 184

Figure C.4. (A) ^1H and (B) ^{13}C NMR spectra of 2-(allyloxy)decane (C4) in $CDCl_3$. 185

Figure C.5. (A) ^1H and (B) ^{13}C spectra of 1-(allyloxy)octane (C5) in $CDCl_3$. 186

Figure C.6. (A) ^1H and (B) ^{13}C spectra of (*R*)-*S*-(3-(octan-2-yloxy)propyl) ethanethioate (D1) in $CDCl_3$. 188

Figure C.7. (A) ^1H and (B) ^{13}C spectra of (*R*)-*S*-(3-(decan-2-yloxy)propyl) ethanethioate (D2) in $CDCl_3$. 190

Figure C.8. (A) ^1H and (B) ^{13}C spectra of *S*-(3-(octan-2-yloxy)propyl) ethanethioate (D3) in $CDCl_3$. 191

Figure C.9. (A) ^1H and (B) ^{13}C spectra of *S*-(3-(decan-2-yloxy)propyl) ethanethioate (D4) in $CDCl_3$. 192

Figure C.10. (A) ^1H and (B) ^{13}C spectra of *S*-(3-(octyloxy)propyl) ethanethioate (D5) in $CDCl_3$. 194

Figure C.11. (A) ^{13}C NMR spectrum of iPOP-SC_3ObC_{8R} in $CDCl_3$ and (B) size exclusion chromatography trace of iPOP-SC_3ObC_{8R} using THF as solvent. 195

Figure C.12. (A) ^1H NMR spectrum of iPOP-SC_3ObC_{10R} in $CDCl_3$ and Size exclusion chromatography trace of iPOP-SC_3ObC_{10R} using THF as solvent. 196

Figure C.13. (A) ^{1}H NMR spectrum of iPOP-SC_3ObC_8 in $CDCl_3$ and (B) size exclusion chromatography of iPOP-SC_3ObC_8 with THF as the mobile phase. 197

Figure C.14. (A) ^{1}H NMR spectrum of iPOP-SC_3ObC_{10} in $CDCl_3$ and size exclusion chromatography of iPOP-SC_3ObC_{10} with THF as the mobile phase. 198

Figure C.15. (A) ^{1}H NMR spectrum of iPOP-SC_3OC_{8L} in $CDCl_3$ and (B) size exclusion chromatography of iPOP-SC_3OC_{8L} with THF as the mobile phase. 199

Figure C.16. (A) ^{13}C NMR spectrum of aPOP-SC_3ObC_{8R} in $CDCl_3$ and (B) size exclusion chromatography of aPOP-SC_3ObC_{8R} with THF as the mobile phase. 200

Figure C.17. Size exclusion chromatography trace of iPOP-$SO_2C_3ObC_{8R}$ using THF as the mobile phase. 201

Figure C.18. (A) ^{1}H NMR spectrum of iPOP-$SO_2C_3ObC_{10R}$ in $CDCl_3$ and (B) size exclusion chromatography trace of iPOP-$SO_2C_3ObC_{10R}$ using THF as the mobile phase. 202

Figure C.19. (A) ^{1}H NMR spectrum of iPOP-$SO_2C_3ObC_8$ in $CDCl_3$ and (B) size exclusion chromatography trace of iPOP-$SO_2C_3ObC_8$ in $CDCl_3$. 203

Figure C.20. (A) ^{1}H NMR spectrum of iPOP-$SO_2C_3ObC_{10}$ in $CDCl_3$ and (B) size exclusion chromatography trace of iPOP-$SO_2C_3ObC_{10}$ in $CDCl_3$. 204

Figure C.21. (A) ^{1}H NMR spectrum of iPOP-$SO_2C_3OC_{8L}$ in $CDCl_3$ and (B) size exclusion chromatography trace of iPOP-$SO_2C_3OC_{8L}$ using THF as the mobile phase. 205

Figure C.22. Size exclusion chromatography trace of aPOP-$SO_2C_3ObC_{8R}$ using THF as the eluent. 206

Figure C.23. (A) DSC second heating curves for iPOP-SC_3ObC_{8R} and aPOP-SC_3ObC_{8R}. The heating rate was 5 °C/min for both polymers. DSC second heating curves for (B) aPOP-SC_n

and (C) aPOP-SO_2C_n from ref. 40 in the main text (copyright American Chemical Society 2019). 207

Figure C.24. 1D XRD profiles of (A) iPOP-$SO_2C_3ObC_{8R}$, (B) iPOP-$SO_2C_3ObC_{10R}$, and (C) iPOP-$SO_2C_3ObC_8$ fibers during the heating process. 208

Figure C.25. Raw data bipolar D-E loops for (A) iPOP-$SO_2C_3ObC_8$, (B) aPOP-$SO_2C_3ObC_{8R}$, and (C) iPOP-$SO_2C_3ObC_{10}$ at room temperature. The poling frequency was 100 Hz with a sinusoidal waveform. The dashed line horizontal loops are AC electronic conduction loops. After subtraction of the AC electronic conduction, the treated loops are presented in Figure 4.9 in the main text. 209

Figure 5.1. TEM micrographs of one P*t*BA-grafted silica NP (a), BNP-6.1k (b), -9.7k (c), -10.9k (d), -12.9k (e), -15.2k (f), -20.0k (g), -23.0k (h), -27.6k (i), and -31.5k (j). Scale bar: 50 nm. The mixed brush NPs were stained with RuO_4 for 7 min. (k) Plot of valency vs. core size for BNP-15.2k after stained with RuO_4 for 2 min. Scale bar: 25 nm. (l) Plot of valency versus average core diameter for the corresponding valency with the standard deviation. The star, diamond, and circle indicate mono-, di-, and tetra-valent NPs from extrapolation. 218

Figure 5.2. Plot of valency vs. core size for BNP-15.2k after stained with RuO_4 for 2 min. Scale bar: 25 nm. This figure is the same as Figure 5.1k except that for each multivalent NP, dashed lines with a larger circle are drawn to guide the view of nanodomains. 220

Figure 5.3. TEM micrographs of individual NPs, different-sized assemblies, and NP lattice for BNP-15.2k (a-l). (m) Plot of average NP valency versus NP number in the assembly. 221

Figure 5.4. TEM micrographs of small NP assemblies of BNP-6.1k (a), -9.7k (b), -10.9k (c), -12.9k (d), -15.2k (e), -20.0k (f), -23.0k (g), -27.6k (h), and -31.5k (i). 223

Figure 5.5. TEM micrographs of NP assemblies of BNP-6.1k (a), -9.7k (b), -10.9k (c), -12.9k (d), -15.2k (e), -20.0k (f), -23.0k (g), -27.6k (h), and -31.5k (i). The hairy NPs were drop cast onto carbon-coated TEM grids, annealed with $CHCl_3$ vapor for ≥ 3 h, and stained with RuO_4 for 7 min. 224

List of Schemes

Scheme 1.1. Comparison of Electrocaloric Cooling Cycle with Compression-Based Cooling Cycle Stages. (Reproduced from Ref. 2 with permission from Elsevier.) 4

Scheme 1.2. Alignment of Sulfone Pendant Group Dipoles Under Electrical Field and Potential Chirality Sites (1), (2), and (3) to Induce the SmC* LC Phase..... 7

Scheme 1.3. Schematic Illustration of an X-Ray Diffraction Experiment Setup. 14

Scheme 1.4. Schematic Illustration of an X-Ray Scattering Pattern for a Tilted Liquid Crystalline Phase from a Stretched Fiber Sample of a Liquid Crystalline Polymer. 15

Scheme 2.1. Syntheses of Isotactic and Atactic Polyethers with Thioether-Monosulfonyl and Disulfonyl Pendant Groups..... 31

Scheme A.1. Synthesis of 5-(Octylsulfonyl)pentyl Ethanethioate and 5-(Dodecylsulfonyl)pentyl Ethanethioate..... 71

Scheme 3.1. Polyethers with Sulfonylated Alkyl Side Chains Synthesized in Chapter 3..... 99

Scheme 3.2. Synthesis of Isotactic Polyethers with Various Degrees (x = 50-100%) of *n*-Dodecylsulfonyl Substitution. Note That When x = 100%, the Polymer is iPOP-SO_2C_{12}. 103

Scheme 3.3. Synthesis of (*S*)-S-(2-Methylbutyl) Ethanethioate. 105

Scheme 3.4. Synthesis of iPOP-SO_2bC_{5s}, aPOP-SO_2bC_{5s}, and iPOP-SO_2bC_5..... 107

Scheme 4.1. Synthesis of Isotactic and Atactic Polyethers with Chiral and Racemic Branched Sulfonylated Pendant Groups and an Isotactic Polyether with Linear Alkylsulfonylated Pendant Groups. 145

Scheme C.1. Synthesis of Chiral and Racemic Branched Thioacetate Side Chain Precursors and a Linear Side Chain Precursor. 180

Scheme 5.1. Synthesis of Binary Mixed Homopolymer Brushes on 20.4 nm Silica NPs and Formation of Multivalent NPs with an 8-Valent NP as Example. 215

Chapter 1: Introduction

1.1. Introduction

This dissertation is composed of two parts: chiral mesogen-free liquid crystalline polyethers with sulfonylated side chains, which is the main focus of my graduate research project and comprises Chapter 2, 3, and 4, and a transmission electron microscopy (TEM) study of binary mixed homopolymer brush-grafted silica nanoparticles (NPs), which is presented in Chapter 5. Although no conventional aromatic mesogens are involved, polyethers with aliphatic sulfonylated side chains have been shown to exhibit liquid crystalline phases due to the strong dipole-dipole interactions. It is our expectation that mesogen-free liquid crystalline polyethers with sulfonylated alkyl pendant groups could exhibit chiral smectic C (SmC*) phases when chirality is introduced into either the backbone or side chains or both. Such SmC* liquid crystalline polyethers could display ferroelectric behavior and thus have potential for use as electrocaloric materials, which is the motivation of the first part of this doctoral research. I will first give a general introduction to electrocaloric materials (Section 1.1) and then focus on liquid crystalline polymers (LCPs), including both conventional aromatic mesogen-based and mesogen-free sulfone-containing LCPs (Section 1.2). Section 1.3 introduces binary mixed homopolymer brushes, with an emphasis on the simulation studies of lateral microphase separation of mixed brushes on small NPs. The principles of common characterization techniques used in this dissertation work are briefly reviewed in Section 1.4, including differential scanning calorimetry (DSC), polarized light microscopy (PLM), small-angle X-ray scattering (SAXS), wide-angle X-ray diffraction (WAXD), and TEM. Finally, Section 2 presents an overview of this dissertation research work described in Chapters 2 to 5.

1.1.1. Introduction to Electrocaloric Materials

Electrocaloric (EC) effect refers to a phenomenon in which a polar material exhibits an adiabatic and reversible temperature change upon the application and removal of an electrical field.

This change in temperature is based upon the entropic change of the material, where the randomization of aligned polar groups in the material in response to the removal of an applied electrical field causes an increase in the entropy of the material, resulting in temperature decreasing.[1] When an electrical field is applied, the net dipole moment of the polar constituents in the material increases, due to the alignment of dipoles along the applied electric field, which decreases the entropy of the system and releases heat from the material, with the opposite effect observed when the electrical field is removed from the material. This thermodynamic cycle is comparable to the vapor compression cooling systems that work through the adiabatic compression and expansion of gasses in a Carnot cycle, where the cooling/heating power of a system is based on the action of a mechanical compressor,[2] as schematically illustrated in Scheme 1.1.

The EC effect is most efficient in ferroelectric (FE) materials, in which the polarization does not increase linearly with the applied electric field and spontaneous polarization is observed in the material when the applied electric field is at zero.[3] EC materials are most popularly seen in ferroelectric ceramic and polymeric materials due to their low cost of production, resistance to breakdown under high electrical loads, and relatively large temperature changes observed when these materials are placed under an electrical field.[4-7] The EC effect of these materials can be measured by comparing the change in temperature of the material to the electrical field applied to the material ($\Delta T/\Delta E$). Despite large temperature changes observed in poly(vinylidene fluoride-*co*-trifluoroethylene) [P(VDF-TrFE)] crystalline polymers around or slightly above room temperature, an exceptionally high electric field ($E > 200$ MVm^{-1}) is required to reach saturation polarization, the state at which all dipoles within the material have been properly oriented to the electrical field. This very high electric field is required due to the densely packed crystalline structure of the P(VDF-TrFE) random copolymers.[8,9] On the other hand, ceramics suffer from

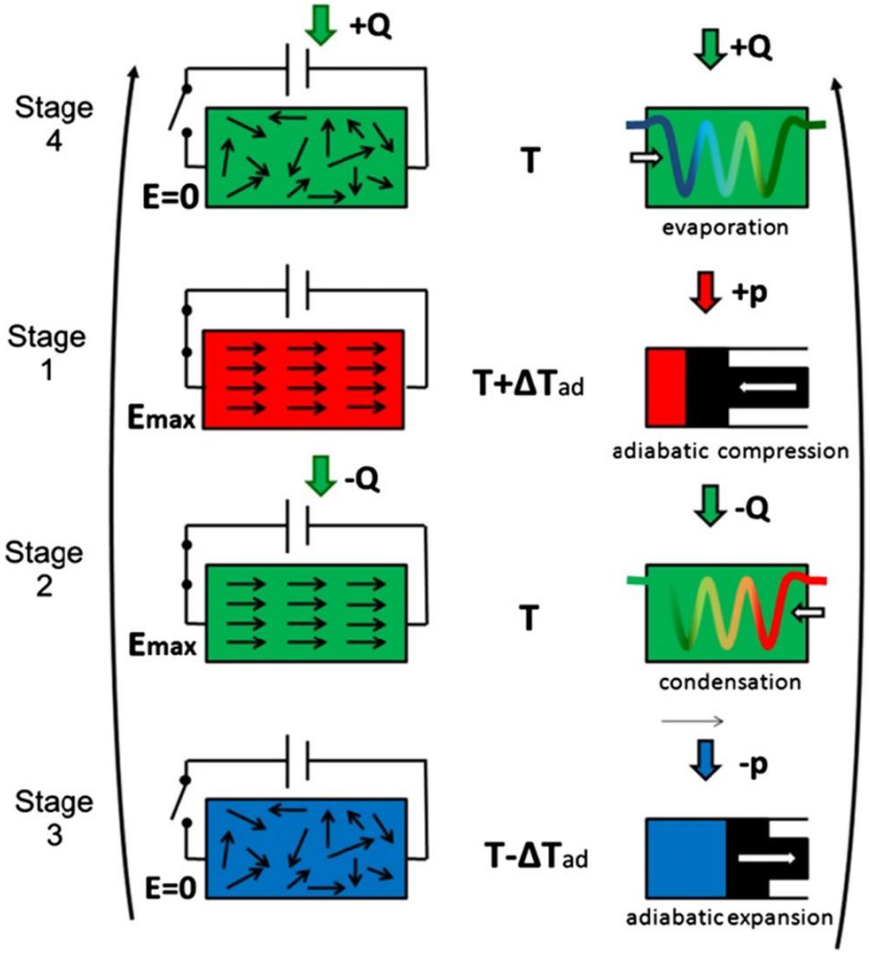

Scheme 1.1. Comparison of Electrocaloric Cooling Cycle with Compression-Based Cooling Cycle Stages. (Reproduced from Ref. 2 with permission from Elsevier.)

high conductivity, and consequently, high electric fields cannot be used on these materials without joule heating.[10,11]

1.1.2. Liquid Crystals and Liquid Crystalline Polymers

The EC effect has also been observed in other polymeric materials, namely, liquid crystalline polymers (LCPs). A liquid crystal (LC), despite the seeming contradictory term, refers to a phase found in certain small molecules and polymers, where a long range orientational order is observed in the bulk, but each molecule or polymer within the bulk retains its ability to flow. This can be considered to be a mesophase, where the LC phase is directly induced from the anisotropic properties of the substance, giving a unique structure to the LC phase. Molecules that exhibit this anisotropy in an LC phase are called mesogens and can be rodlike or discotic. Liquid crystals can be separated into two different classifications, lyotropic and thermotropic LCs. Lyotropic LCs are formed in solution in certain concentration and temperature ranges, while thermotropic LCs are formed purely by the mesogens without any solvent in a given temperature range.[12,13] Thermotropic LCPs can undergo transitions from a crystalline phase to LC mesophases and further into an isotropic melt upon heating. Depending on the constituent mesogens within the LC materials, various LC phases can be observed, differing in polarization and order; nematic LCs are the simplest LC phase, with a long range orientational order but no long-range translational. Smectic phases are more complex, exhibiting a self-assembled layered structure with a weak center of density within each layer. For LCPs, this kind of morphology can be achieved through the addition of mesogenic side chains to a main chain polymer. With the addition of substituents normal to the LC-inducing mesogens, tilted Smectic C phases (SmC) can be induced.

Liquid crystalline self-assembly relies primarily on rigid aromatic mesogens within the softer aliphatic matrix that comprises the “liquid” phase of LCPs. By incorporating aromatic mesogens

into either the main chain or side chains of a given polymer, LC phases can be elicited.[14-17] These polymers with aromatic mesogens have been optimized to elicit a range of phases.[18,19] Incorporation of a chiral center near the aromatic mesogenic unit that forms the SmC phase can break the C_{2h} symmetry and produce the SmC* phase.[20] The resultant spontaneous polarization elicits ferroelectric properties within the material and gives us a strong candidate for the electrocaloric effect. This SmC* phase is the basis for all ferroelectric LCPs and is necessary to elicit the EC effect in these materials.

Besides the use of aromatic mesogens to induce LC self-assembly in polymers, hydrogen bonding and strong dipole-dipole interactions have been shown to induce LC mesophases as well. Shibaev et al. reported LC self-assembly of polymethacrylates with *L*-lysine-containing *n*-alkyl side chains.[21] The incorporation of highly dipolar sulfone moieties into either the main chain[22] or side chain[23] of a polymer can also induce a smectic LC phase. Lee et al. synthesized a series of polyoxypropylene polymers with (*n*-octylsulfonyl)alkylthiomethyl or (*n*-octylsulfonyl)alkylsulfonylmethyl side groups and studied their LC self-assembly behaviors.[24] The strong dipole-dipole interactions of the regularly distributed sulfonyl groups provided a conformational rigidity within the LC matrix, similar to the effect of the aromatic mesogens in conventional LCPs. Smectic A (SmA) phases were observed in these sulfonylated polymers at temperatures above the melting points of the polymers; the inclusion of disulfonyl side chains increased the isotropization temperature. In this dissertation work, we introduced chiral centers into the mesogen-free sulfonylated liquid crystalline polyethers to seek the formation of SmC* phases (Scheme 1.2). The chiral center can be incorporated into the main chain (site 1 in Scheme 1.2) or sulfone-containing side chains (site 2 between the main chain and the sulfonyl group and site 3 in the alkyl tail) or both.

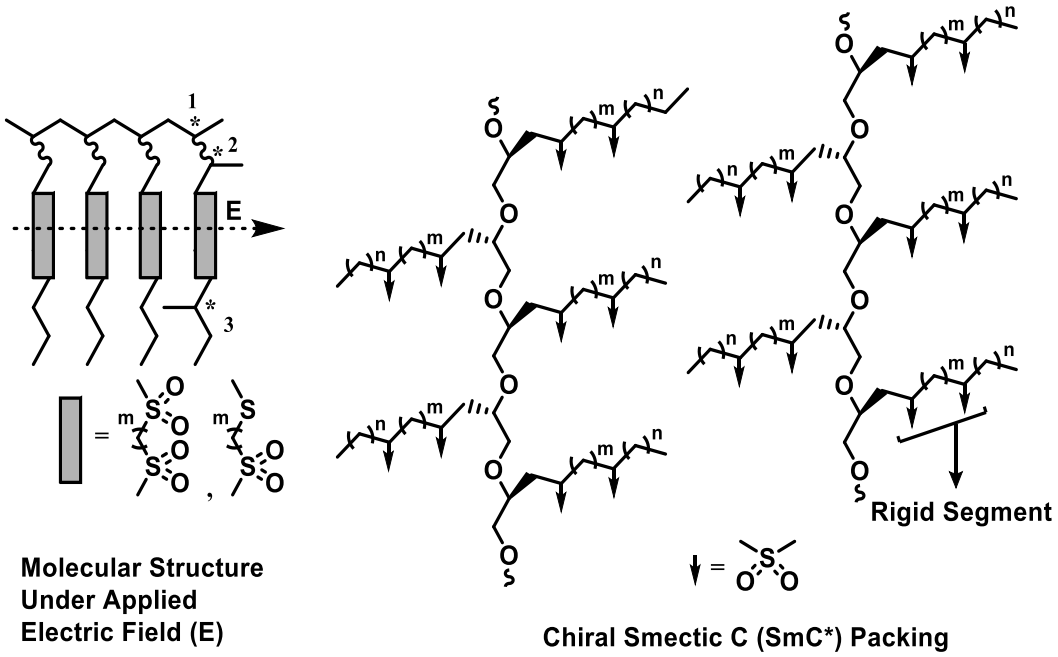

Scheme 1.2. Alignment of Sulfone Pendant Group Dipoles Under Electrical Field and Potential Chirality Sites (1), (2), and (3) to Induce the SmC* LC Phase.

1.1.3. Binary Mixed Homopolymer Brushes on Small Nanoparticles

Polymer brushes are comprised of densely grafted polymer chains to a solid substrate. They have shown promise in a variety of applications, ranging from surface engineering, lubrication, resistance to corrosion and mechanical damages, and lithography.[25-29] Polymer brushes can be prepared via two general approaches, "grafting from", where an initiator is immobilized onto the target surface and polymer chains are subsequently grown from the surface initiator, and "grafting to", where pre-formed, end-functionalized polymer chains are attached to the target surface.[30, 31]

Binary mixed homopolymer brushes, composed of two chemically distinct homopolymers end-tethered to a surface, have received tremendous interest in the past decades due to their intriguing properties associated with the spontaneous reorganization of the two different polymers in the brush layer upon environmental changes.[32] Because of the covalent bonding of the polymer chains to the substrate, macroscopic phase separation is prohibited, and the surface-tethered polymers can only undergo microphase separation in the brush layer. The substrate curvature plays an important role in determining the morphology of mixed homopolymer brushes. Of particular interest here is the binary mixed polymer brushes tethered on spherical nanoparticles with a diameter comparable to the sizes of tethered polymer chains. A number of computer simulation works have been reported in the literature.[33,34] By varying the chain lengths and grafting densities of the two surface-tethered polymers in the brushes and the size of the core nanoparticles, a variety of well-ordered islanded nanostructures with 2-to-12 nanodomains, except 11, have been predicted from microphase separation of mixed brushes on nanospheres (Figure 1.1). On the basis of the simulation study, Roan suggested the use of mixed brushes to fabricate multivalent NPs (i.e., NPs with a small, defined number of nanodomains).[33] In addition, hierarchical self-assemblies of mixed brush NPs have been investigated. However, no experimental study was reported in the literature.

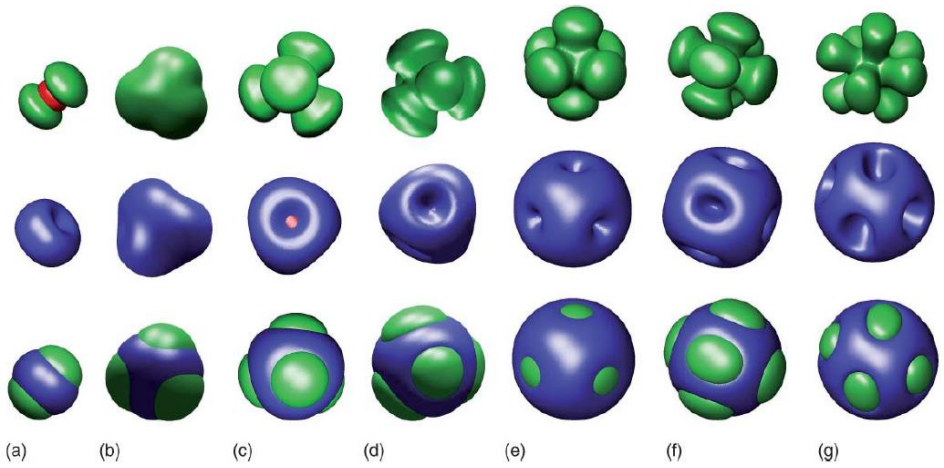

Figure 1.1. Nanostructures of binary mixed homopolymer brushes on nanospheres of a diameter comparable to the polymer sizes with an island number from 2 to 8 at $\sigma_B/\sigma_A = 2$. σ_A and σ_B are the grafting densities of polymer A and polymer B, respectively, R is the nanosphere radius, N_A and N_B are chain lengths of polymer A and polymer B, respectively. (a) (R, σ_{total}, N_A/N_B) = (0.5, 1.0, 20/20); (b) (R, σ_{total}, N_A/N_B) = (1.0, 0.8, 20/20); (c) (R, σ_{total}, N_A/N_B) = (2.0, 1.0, 30/30); (d) (R, σ_{total}, N_A/N_B) = (2.0, 0.7, 20/20); (e) (R, σ_{total}, N_A/N_B) = (2.0, 0.8, 20/20); (f) (R, σ_{total}, N_A/N_B) = (3.0, 0.6, 20/20), and (g) (R, σ_{total}, N_A/N_B) = (4.0, 0.6, 25/30). The first and second rows show only A and B blocks, respectively, and the bottom row is isosurface morphologies of mixed polymer brush. Polymer A and B are represented by green color and blue color, respectively, with a red sphere inside. (Reproduced from Ref. 34 with permission from AIP Publishing.)

1.2. Characterization Techniques Used in this Dissertation Research

1.2.1. Differential Scanning Calorimetry (DSC)

DSC is a key technique used in the identification of LC mesophases in both small molecule compounds and polymeric materials.[35-37] Using this method, the thermal transitions of LCs and LCPs can be observed from the changes in heat capacity and the enthalpy changes in the thermograms. When using DSC, two pans, typically aluminum, are loaded into the instrument chamber. One pan contains the sample of a known mass to be analyzed and the other is empty used as a reference pan. A temperature control system underneath both pans either raises or lowers the temperature at a known rate simultaneously, and sensors measure the temperatures of the sample and reference pans at any moment. By heating the two pans at a constant rate ($\Delta T/\Delta t$), we can measure the heat flow of each pan ($\Delta Q/\Delta t$) and how the heat flow of the sample pan differs from the reference pan. By recording the heat flow into the sample and plotting it against the temperature of the sample at that given time, we can accurately observe thermal transitions for the sample. The heat capacity (C_p) can be determined by dividing the heat flow ($\Delta Q/\Delta t$) of the sample by the heating rate, and the specific heat capacity can be obtained by dividing the C_p by the mass (m) of the sample. The specific heat capacity varies as the sample undergoes thermal transitions upon heating or cooling, such as melting, glass transitions, or changes in LC mesophases (Figure 1.2).[38]

For LCPs, endothermic and exothermic peaks can be observed between different phases of the sample upon heating or cooling. These peaks are caused by the formation of an LC phase from the crystal, a rearrangement from one LC mesophase to another, or the change of the LC phase into an isotropic melt.[36,39] The exact mesophases of a given LCP cannot be determined from DSC alone, but DSC gives crucial information about the temperatures at which these transitions occur and the range in which they persist.

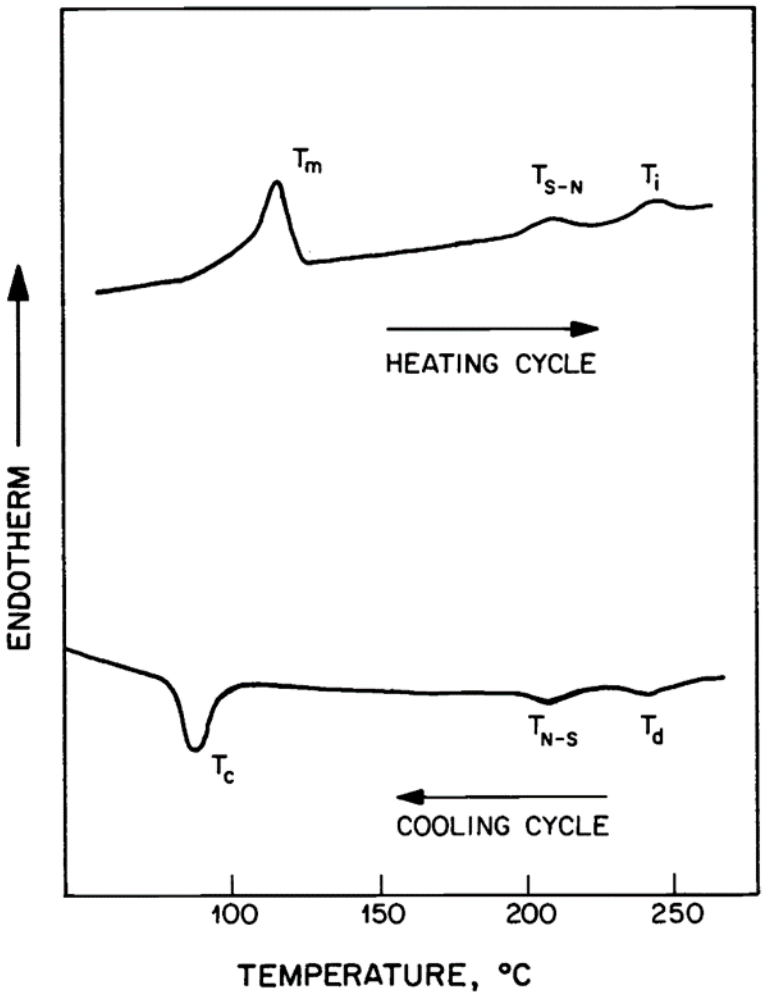

Figure 1.2. Example DSC thermograms of a liquid crystal polymer, forming both smectic and nematic phases sequentially. (Reproduced from Ref. 37 with permission from the Polish Academy of Sciences)

1.2.2. Polarized Light Microscopy

Polarized Light Microscopy (PLM) can be used to qualitatively identify optically anisotropic materials. PLM operates by passing unfiltered light into a polarizer, transmitting it though the sample being analyzed, and passing through another polarizer, called the analyzer, oriented at 90° relative to the polarizer. An optically anisotropic material will exhibit birefringence and separate polarized light emitted from the polarizer into ordinary and extraordinary wave components, each traveling at different velocities and directions through the sample. These components are recombined in the analyzer, where the constructive and destructive interference of the recombined light components give contrast within the material. This instrument has been used to quantitatively study many anisotropic materials, such as semi-crystalline polymers and crystals.[40,41]

LCPs can be identified using PLM due to the optically anisotropic character of their liquid crystalline mesophase.[42] LCs are the only birefringent liquids due to the molecular orientational ordering that occurs in the materials. PLM allows for the identification of an LC phase in the polymer sample in a certain temperature range. In contrast, an amorphous polymer sample is random by nature and is optically isotropic. This would yield no birefringence within the sample and the light would be unable to pass through the analyzer of the microscope, giving no image.

1.2.3. Small-Angle and Wide-Angle X-Ray Scattering

X-Ray diffraction (XRD) has been used to investigate the structure of matter, with beginnings in revealing the size of atoms,[43] determining the length and type of chemical bonds,[44] and confirming the double helix structure of DNA.[45] XRD has expanded our view into the structures of complex compounds and microstructures of matter by relying upon the shorter wavelength of x-rays to observe the small periods that normal light cannot expose. Inundating a sample with a concentrated beam of X-rays causes scattering of the beam from the electrons surrounding the

nucleus of each atom within the sample. In a typical WAXS or SAXS experiment, a flat plate photodetector is placed perpendicular to the X-ray beam and at a known distance from the sample, and the sample is exposed to a narrow beam of x-rays at a known wavelength (λ). The sample will scatter X-rays, and the plate detector will detect the forward scattered X-rays (Scheme 1.3). If there is a periodic structure within the sample, the scattering will occur at given angles relative to the direct beam. Note that the scattering angle is conventionally recorded as 2θ (Scheme 1.3). When considering a basic scattering triangle (Scheme 1.3), a scattered beam can be observed at a distance X from the transmitted beam. From this, the scattering angle can be calculated using simple geometry $\tan(2\theta) = X/L$. Solving for 2θ allows for the calculation of the scattering vector (q) [$q = \left(\frac{4\pi}{\lambda}\right)\sin\theta$] and the periodicity ($d$) via the use of Bragg's law $d = \frac{2\pi}{q}$, where from the latter we can see an inverse relationship between q and d. In a WAXS experiment, the detector plate is placed very close to the sample, thus reducing the distance L and directly influencing the value of 2θ. For SAXS, small q values are obtained, corresponding to large periodicities (d) and as a result, large structures within the sample. The opposite is true of WAXS, where the obtained q values are large and the corresponding periodicities are small, in the range of 1 nm to 1 Å in length scale.

XRD, both small and wide angles, gives valuable structural information of LCPs with different mesophases. Studies of thermotropic LCPs using XRD are useful in their ability to elucidate the orientational order at the nanometer scale. It has proven to be a powerful tool in identifying the type of LC mesophase in LCPs. By measuring the angles of diffraction for the main chains and side chains within an oriented (fiber) sample using both SAXS and WAXS, we can determine the specific LC morphologies in given temperature ranges, namely the tilted SmC*, for our aromatic mesogen-free LCPs. Note that for titled LC phases such as SmC or SmC*, the characteristic scattering appears in the quadrants as illustrated in Scheme 1.4.

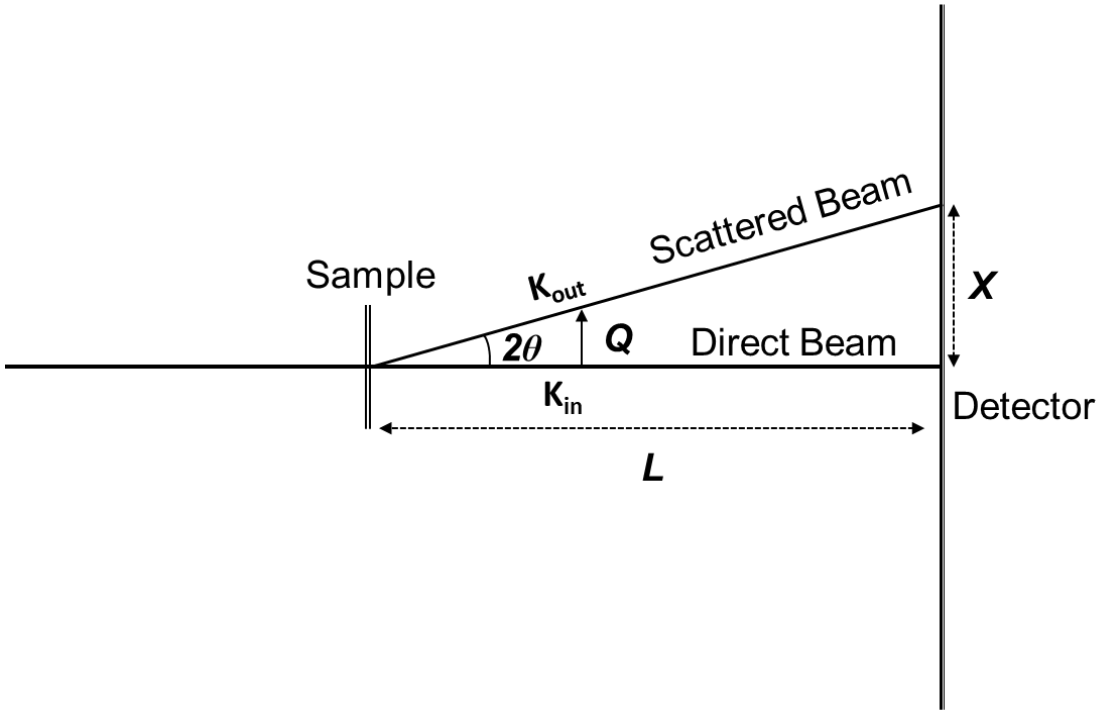

Scheme 1.3. Schematic Illustration of an X-Ray Diffraction Experiment Setup.

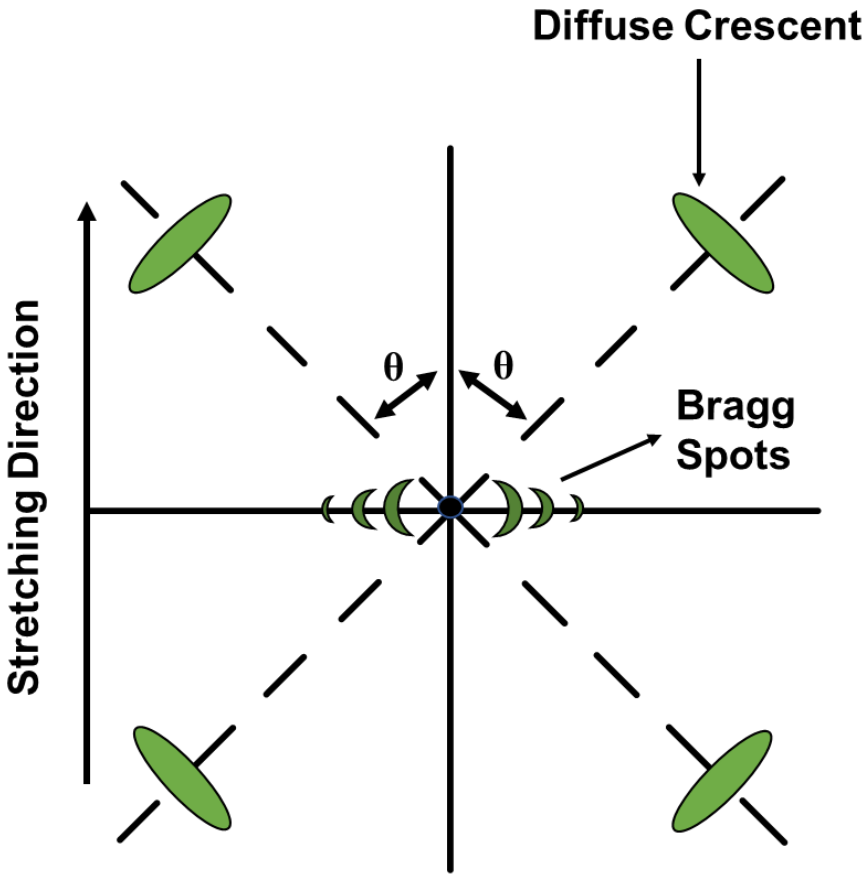

Scheme 1.4. Schematic Illustration of an X-Ray Scattering Pattern for a Tilted Liquid Crystalline Phase from a Stretched Fiber Sample of a Liquid Crystalline Polymer.

1.2.4. Transmission Electron Microscopy

Transmission Electron Microscopy (TEM) is a vital tool in providing structural information at nanometer scale resolutions for the imaging of the morphologies of soft and hybrid materials, including polymer-brush grafted nanoparticles. A high energy beam of electrons is shot from an electron gun and passed through a thin film sample of the bulk material to be analyzed, and the transmitted electrons are captured and imaged using a charge coupled device (CCD) camera. The intensity of the transmitted electrons is inversely proportional to the electron density of the sample being studied, and when it strikes the CCD camera, a contrast within the structures in the sample is observed at a resolution on the nanometer scale. The contrast is typically enhanced through the use of a staining agent such as osmium tetraoxide or ruthenium tetraoxide that reacts selectively with unsaturated bonds, resulting in an increased resolution for the sample's structure. In Chapter 5, TEM is used to characterize the morphology of binary mixed homopolymer brushes grafted on 20 nm silica nanoparticles formed from the lateral microphase separation.

1.3 Dissertation Overview

The focus of this dissertation work is on the design, synthesis, and characterization of aromatic mesogen-free chiral liquid crystalline polyethers with sulfonylated alkyl side chains to seek SmC* phases for electrocaloric applications. Compared with crystalline PVDF-based materials, the use of LCPs in ferroelectric applications could lower the applied electric field to achieve saturated polarization due to the high mobility of the polar groups in the LC phases than in the crystals. Moreover, the replacement of bulky aromatic groups in traditional LCPs with highly dipolar sulfonyl groups could potentially increase the dipole density and thus polarization. Thus, the mesogen-free LCPs with sulfonylated side chains are promising candidates for obtaining large

spontaneous polarization under relatively low electric fields, which could be useful for many potential applications. Through the incorporation of a chiral center into either the main chain or pendant groups or both, a series of chiral polyoxypropylene (POP) polymers, either atactic (aPOP) or isotactic (iPOP), have been successfully prepared, and their LC self-assembly behaviors are investigated by using a combination of DSC, PLM, and XRD experiments.

Chapter 2 presents a study of the effects that the main chain tacticity, the distance between the chiral center and the sulfone dipole, and the number of sulfonyl dipoles per side chain have on the LC self-assembly of POP polyethers with sulfonylated side chains. Isotactic POP polyethers with *n*-alkylsulfonylpentylthioether side chains (iPOP-$SC_5SO_2C_n$, where *n* in the alkyl tail C_n is either 12 or 8) were synthesized by a substitution reaction from isotactic poly[(*R*)-(-)-epichlorohydrin] (iPECH). iPECH was prepared by ring-opening polymerization of (*R*)-(-)-epichlorohydrin using methylaluminoxane as the catalyst, and the isotacticity was previously confirmed. It was found that when the sulfonyl group in the side chain was far away from the chiral center in the main chain, more LC phases were observed and the main chain chirality had an insignificant effect on the LC assembly when compared with the atactic analogs. In addition, when the thioether group in the side chain was oxidized into the sulfonyl moiety (i.e., two sulfonyl groups per side chain in iPOP-$SO_2C_5SO_2C_n$), the phase transitions were shifted to high temperatures. Nevertheless, only SmA phases were observed and no SmC* phase was achieved.

In Chapter 3, the effect of grafting density of *n*-dodecylsulfonyl side chains on the LC self-assembly of iPOP was investigated. A series of isotactic POPs with grafting densities ranging from 50.0% to 100% were prepared by varying the reaction conditions. At a rather high grafting density such as 80–100%, a SmA phase was observed. When the grafting density was lowered to 60–80%, a hexagonal columnar self-assembly was found. In addition, aPOP-SO_2C_5 and iPOP-SO_2C_5

polyethers with methyl-branched side chains were synthesized, and their self-assembly behaviors were investigated. Chapter 4 delves further into the chiral POP polyethers with methyl-branched sulfonylated side chains with a -$CH_2CH_2CH_2O$- spacer incorporated between -SO_2- and the methyl branch in the side chain to seek SmC* phases. Side chain tilting in the smectic layers was observed with the use of a methyl branch in the side chain. A SmC*-like LC phase was obtained when single chirality was introduced into either the main chain or side chains. However, if both the backbone and the side chain contain a chiral center, only crystalline structures appeared upon stretching into fibers. The electric displacement-electric field measurements indicated that the SmC* LCPs exhibited relatively high dielectric constants but no ferroelectric switching, for which the reasons were discussed.

A side project is described in Chapter 5, where the morphologies of binary mixed homopolymer brushes grafted on 20.4 nm silica NPs were studied by TEM. Nine mixed brush silica NP samples with a constant poly(*tert*-butyl acrylate) (P*t*BA) M_n of 19.6 kDa and different polystyrene (PS) M_ns, from 6.1 to 31.5 kDa, were synthesized by Mr. Andrew J. Chancellor, a former graduate student in our research group, and used in this TEM study. Upon casting onto carbon-coated TEM grids from chloroform, a good solvent for both P*t*BA and PS, the mixed brushes microphase separated into patchy brush NPs with a small number of nanodomains, from 6 to 10. The nanodomains from different brush NPs can interact with each other and form bonds.

Chapter 6 provides a brief summary of this dissertation work along with future avenues of investigation and prospects in the areas of aromatic mesogen-free liquid crystalline polymers and patchy brush nanoparticles.

References

1. Kutnjak, Z.; Rožič, B.; Pirc, R. Electrocaloric Effect: Theory, Measurements, and Applications. In *Wiley Encyclopedia of Electrical and Electronics Engineering*, **2015**; pp 1-19.
2. Valant, M. Electrocaloric Materials for Future Solid-State Refrigeration Technologies. *Prog Mater Sci* **2012,** *57* (6), 980-1009.
3. Whatmore, R. Ferroelectric Materials. In *Springer Handbook of Electronic and Photonic Materials*, Kasap, S.; Capper, P., Eds. Springer US: Boston, MA, **2007**; pp 597-623.
4. Malič, B.; Kuščer, D.; Vrabelj, M.; Koruza, J. 5 - Review of Methods for Powder-Based Processing. In *Magnetic, Ferroelectric, and Multiferroic Metal Oxides*, Stojanovic, B. D., Ed. Elsevier: **2018**; pp 95-120.
5. Santucci, S.; Esposito, V. Electrostrictive Ceramics and Their Applications. In *Encyclopedia of Materials: Technical Ceramics and Glasses*, Pomeroy, M., Ed. Elsevier: Oxford, **2021**; pp 369-374.
6. Costa, C. M.; Cardoso, V. F.; Brito-Pereira, R.; Martins, P.; Correia, D. M.; Correia, V.; Ribeiro, C.; Martins, P. M.; Lanceros-Méndez, S. Chapter 1 - Electroactive Poly(vinylidene fluoride)-Based Materials: Recent Progress, Challenges, and Opportunities. In *Fascinating Fluoropolymers and Their Applications*, Ameduri, B.; Fomin, S., Eds. Elsevier: **2020**; pp 1-43.
7. Mischenko, A. S.; Zhang, Q.; Scott, J. F.; Whatmore, R. W.; Mathur, N. D. Giant Electrocaloric Effect in Thin-Film $PbZr_{0.95}Ti_{0.05}O_3$. *Science* **2006,** *311* (5765), 1270-1271.
8. Xin, C.; Xu, H.; Qun-Dong, S. PVDF-Based Ferroelectric Polymers in Modern Flexible Electronics. *Adv Electron Mater* **2017,** *3* (5), 1600460.

9. Lu, S. G.; Rozic, B.; Kutnjiak, Z.; Zhang, Q. M. Electrocaloric Effect in Ferroelectric P(VDF-TrFE) Copolymers. *Integrated Ferroelectrics* **2011,** *125* (1), 176-185.

10. Bradeško, A.; Hedl, A.; Fulanović, L.; Novak, N.; Rojac, T. Self-Heating of Relaxor and Ferroelectric Ceramics during Electrocaloric Field Cycling. *APL Materials* **2019,** *7* (7), 071111.

11. Lu, S.; Li, J.; Cheng, M.; Li, Q.; Li, F.; Lv, Z.; Zhang, Y.; Lu, C.; Li, S. Joule Heating - A Significant Factor in Electrocaloric Effect. *Ceramics International* **2019,** *45* (14), 16992-16998.

12. Mezzenga, R. Physics of Self-Assembly of Lyotropic Liquid Crystals. In *Self-Assembled Supramolecular Architectures*, **2012**; pp 1-20.

13. Williams, G. E. Thermotropic liquid crystal polymers. In *Special Polymers for Electronics and Optoelectronics*, Chilton, J. A.; Goosey, M. T., Eds. Springer Netherlands: Dordrecht, **1995**; pp 256-283.

14. Zhang, L.; Yao, W.; Gao, Y.; Zhang, C.; Yang, H. Polysiloxane-Based Side Chain Liquid Crystal Polymers: From Synthesis to Structure–Phase Transition Behavior Relationships. *Polymers (Basel)* **2018,** *10* (7), 794.

15. Shibaev, V.; Bobrovsky, A.; Boiko, N. Photoactive Liquid Crystalline Polymer Systems with Light-Controllable Structure and Optical Properties. *Progress in Polymer Science* **2003,** *28* (5), 729-836.

16. Shibaev, V. Liquid-Crystalline Polymers: Past, Present, and Future. *Polymer Science Series A* **2009,** *51*, 1131-1193.

17. Donald, A. M.; Windle, A. H.; Hanna, S. *Liquid Crystallie Polymers*. 2 ed.; Cambridge University Press: Cambridge, **2006**.

18. Shibaev, V. 1.10 - Liquid Crystalline Polymers. In *Polymer Science: A Comprehensive Reference*, Matyjaszewski, K.; Möller, M., Eds. Elsevier: Amsterdam, 2012; pp 259-285.

19. Lagerwall, S. T. Ferroelectric and Antiferroelectric Liquid Crystals. *Ferroelectrics* **2004,** *301* (1), 15-45.

20. Dubois, J.-C. Ferroelectric Polymers: Chemistry, Physics, and Applications. *Advanced Materials* **1996,** *8* (6), 542-542.

21. Shibaev, V. P.; Tal'roze, R. V.; Karakhanova, F. I.; Platé, N. A. Thermotropic Liquid Crystalline Polymers. II. Polymers with Amino acid Fragments in the Side Chains. *Journal of Polymer Science: Polymer Chemistry Edition* **1979,** *17* (6), 1671-1684.

22. Zhang, Z.; Zheng, J.; Premasiri, K.; Kwok, M.-H.; Li, Q.; Li, R.; Zhang, S.; Litt, M. H.; Gao, X. P. A.; Zhu, L. High-κ Polymers of Intrinsic Microporosity: a New Class of High Temperature and Low Loss Dielectrics for Printed Electronics. *Materials Horizons* **2020,** *7* (2), 592-597.

23. Lee, J.-C.; Litt, M. H.; Rogers, C. E. Synthesis and Properties of (Alkylthio)methyl-Substituted Poly(oxyalkylene)s and (Alkylsulfonyl)methyl-Substituted Poly(oxyalkylene)s. *Macromolecules* **1997,** *30* (13), 3766-3774.

24. Lee, J.-C.; Han, S.-H.; Cha, S.-H.; Park, S.-Y.; Farmer, B. L. Synthesis and Dipole–Dipole Interaction-Induced Mesomorphic Behavior of Poly(oxyethylene)s Containing (*n*-Octylsulfonyl)alkylthiomethyl or (*n*-Octylsulfonyl)alkylsulfonylmethyl Side Groups. *Polymer* **2003,** *44* (24), 7413-7425.

25. Carbonell, C.; Valles, D.; Wong, A. M.; Carlini, A. S.; Touve, M. A.; Korpanty, J.; Gianneschi, N. C.; Braunschweig, A. B. Polymer Brush Hypersurface Photolithography. *Nature Communications* **2020,** *11* (1), 1244.

26. Wright, R. A. E.; Wang, K. W.; Qu, J.; Zhao, B. Oil-Soluble Polymer Brush-Grafted Nanoparticles as Effective Lubricant Additives for Friction and Wear Reduction. *Angew. Chem. Int. Ed.* **2016**, *55*, 8656-8660.

27. Huang, D.; Valerie, K.; Yang, H. Clickable Biocompatible Brush Polymers as a Versatile Platform toward Development of Multifunctional Drug Delivery Vehicles. *Reactive and Functional Polymers* **2022,** *170*, 105147.

28. Lu, A.-H.; Salabas, E. L.; Schüth, F. Magnetic Nanoparticles: Synthesis, Protection, Functionalization, and Application. *Angewandte Chemie International Edition* **2007,** *46* (8), 1222-1244.

29. Dhingra, S.; Joshi, A.; Singh, N.; Saha, S. Infection Resistant Polymer Brush Coating on the Surface of Biodegradable Polyester. *Materials Science and Engineering: C* **2021,** *118*, 111465.

30. Chancellor, A. J.; Seymour, B. T.; Zhao, B. Characterizing Polymer-Grafted Nanoparticles: From Basic Defining Parameters to Behavior in Solvents and Self-Assembled Structures. *Analytical Chemistry* **2019,** *91* (10), 6391-6402.

31. Zhao, B.; Brittain, W. J. Polymer Brushes: Surface-Immobilized Macromolecules. *Progress in Polymer Science* **2000,** *25* (5), 677-710.

32. Wang, J.; Müller, M., Microphase Separation of Mixed Polymer Brushes: Dependence of the Morphology on Grafting Density, Composition, Chain-Length Asymmetry, Solvent Quality, and Selectivity. *The Journal of Physical Chemistry B* **2009,** *113* (33), 11384-11402.

33. Roan, J.-R. Soft Nanopolyhedra as a Route to Multivalent Nanoparticles. *Phys. Rev. Lett.* **2006,** *96*, 248301.

34. Wang, Y.; Yang, G.; Tang, P.; Qiu, F.; Yang, Y.; Zhu, L. Mixed Homopolymer Brushes Grafted Onto a Nanosphere. *J. Chem. Phys.* **2011,** *134,* 134903.

35. Schick, C. 2.31 - Calorimetry. In *Polymer Science: A Comprehensive Reference*, Matyjaszewski, K.; Möller, M., Eds. Elsevier: Amsterdam, **2012**; pp 793-823.

36. Mourik, P. v.; Norder, B.; Picken, S. J. Transformational Kinetics in Liquid Crystal Polymers and Differential Scanning Calorimetry Calibration. *Liquid Crystals* **2012,** *39* (4), 493-500.

37. Kolek, L.; Massalska-Arodz, M.; Majda, D.; Wantusiak, B.; Zalewski, S.; Kula, P. Studies of Phase Diagram of a Liquid Crystal with 4-[2-(3-Fluorophenyl)ethyl]biphenyl Core of Molecules. *Acta Physica Polonica A* **2012,** *122* (2), 370-374.

38. Lenz, R. W. Characterization of Thermotropic Liquid-Crystalline Polymers. *Pure and Applied Chemistry* **1985,** *57* (7), 977-984.

39. Katerska, B.; Exner, G.; Perez, E.; Krasteva, M. N. Cooling Rate Effect on the Phase Transitions in a Polymer Liquid Crystal: DSC and Real-Time MAXS and WAXD Experiments. *European Polymer Journal* **2010,** *46* (7), 1623-1632.

40. Polowsky, P. J.; Tansman, G. F.; Kindstedt, P. S.; Hughes, J. M. Characterization and Identification of Surface Crystals on Smear-Ripened Cheese by Polarized Light Microscopy. *Journal of Dairy Science* **2018,** *101* (9), 7714-7723.

41. Molnár, J.; Zuba, Z.; Sepsi, Ö.; Ujhelyi, F.; Erdei, G.; Lenk, S.; Menyhárd, A. Structural Investigation of Semicrystalline Polymers. *Polymer Testing* **2021,** *95*, 107098.

42. Jewell, S. Polarized Light in Liquid Crystals and Polymers. *Liquid Crystals Today* **2009,** *18* (2), 59-60.

43. Huxford, T. X-Ray Crystallography. In *Brenner's Encyclopedia of Genetics (Second Edition)*, Maloy, S.; Hughes, K., Eds. Academic Press: San Diego, 2013; pp 366-368.

44. Bragg, W. L. XLII. The Crystalline Structure of Copper. *The London, Edinburgh, and Dublin Philosophical Magazine and Journal of Science* **1914,** *28* (165), 355-360.

45. Watson, J. D.; Crick, F. H. C. Molecular Structure of Nucleic Acids: A Structure for Deoxyribose Nucleic Acid. *Nature* **1953,** *171* (4356), 737-738.

Chapter 2: Effects of Tacticity and Chiral Center-to-Dipole Distance on Mesogen-Free Liquid Crystalline Self-Assembly of Sulfonyl-Containing Comb-Like Polymers

The work presented in this chapter has been published in *Polymer Chemistry* **2020**, *11*, 3018-3031. I synthesized all the polymers, measured their optical activities by polarimetry, conducted thermogravimetric analysis (TGA) and preliminary differential scanning calorimetry (DSC) analysis of all the polymers as well as X-ray diffraction (XRD) studies of some of the polymers at the University of Tennessee Knoxville, and participated in the discussion of DSC and XRD data and the identification of structures. Dr. Man-Hin Kwok performed in-depth DSC and polarized light microscopy (PLM) experiments and prepared fiber samples for the X-ray study. The X-ray data in the publication were collected by Dr. Ruipeng Li at Brookhaven National Laboratory.

Abstract

This chapter presents the synthesis and liquid crystalline self-assembly of mesogen-free comb-like isotactic polyoxypropylenes (iPOPs) bearing mono- or di-sulfonyl groups, which have potential to exhibit high spontaneous polarization for applications in advanced electronic devices. iPOPs with *n*-alkylsulfonylpentylthioether side chains (iPOP-$SC_5SO_2C_n$, where C_n is the alkyl tail with *n* being either 12 or 8) were prepared via a post-polymerization substitution reaction from isotactic poly[(*R*)-(-)-epichlorohydrin]. The effects of main-chain tacticity, chiral center-to-dipole distance, number of sulfonyl dipoles per side chain, and *n*-alkyl tail length on the liquid crystalline self-assembly behavior were investigated by comparing iPOPs with the atactic counterparts. First, when the sulfonyl dipole was placed far away from the chiral center in iPOP-$SC_5SO_2C_n$ compared with the isotactic polyethers containing *n*-alkylsulfonyl side chains (iPOP-SO_2C_n) reported in the literature, the dipole-dipole interactions among the side chains were decreased, which led to more liquid crystalline phases. Smectic E (SmE) and A (SmA) phases were observed after the crystal melting; however, the main-chain chiral center was found to have an insignificant effect on the

liquid crystalline assembly when compared to the atactic samples. Second, the longer C_n tails increased the transition temperatures as a result of stronger van der Waals interactions. Third, after the thioether linkage in the side chain was oxidized into the sulfonyl group, the chiral center-dipole and dipole-dipole interactions in the resultant polymers (i.e., iPOP-$SO_2C_5SO_2C_n$) were enhanced. As a result, the liquid crystalline phase transitions (i.e., crystal→SmE→SmA→I) were pushed to higher temperatures. The knowledge obtained in this study will help us further design and achieve the ferroelectric smectic C* phase in mesogen-free comb-like sulfonylated liquid crystalline polymers.

2.1. Introduction

Ferroelectric liquid crystals and liquid crystalline polymers with high spontaneous polarization (P_s) are attractive functional materials for various electrical and optical applications.[1-9] However, their P_s values are usually below 10 mC/m^2, significantly lower than those of ferroelectric polymers [e.g., ~180 mC/m^2 for the β-form poly(vinylidene fluoride) (PVDF)][10,11] and ceramics (e.g., ~260 mC/m^2 for $BaTiO_3$ single crystals).[12] This can be largely attributed to the weakly dipolar groups in the molecules and bulky aromatic mesogen groups, which decrease the dipole density. The lower P_s values have prevented ferroelectric liquid crystalline polymers from being used for advanced electrical applications.

From the previous study,[13] it is desirable to realize mesogen-free liquid crystalline polymers in order to increase the dipole density. Meanwhile, highly dipolar groups, such as sulfonyl (4.5 Debye or D), cyano (3.7 D), and amide (3.9 D) groups, can be used to further increase the orientational polarization.[14] However, genuine mesogen-free liquid crystalline polymers are rather rare. Note that the rotator phases in *n*-alkanes,[15] the high pressure hexagonal phase in polyethylene [16] and isotactic poly(4-methyl-1-pentene),[17] and the paraelectric (i.e., pseudohexagonal) phase in PVDF (at high pressures)[18] and P(VDF-*co*-trifluoroethylene) [P(VDF-TrFE)][19-21] should not be considered as liquid crystalline self-assembly, because they exhibit obvious supercooling in differential scanning calorimetry (DSC) heating and cooling cycles. Therefore, it is more accurate to define them as mesophases, which are highly defective crystalline phases. One effective way to induce liquid crystalline self-assembly for aliphatic polymers is to introduce hydrogen-bonding or strong dipole-dipole interactions. For example, when *L*-lysine is used to link *n*-alkyl side groups to a polymethacrylate backbone, smectic liquid crystalline phases are induced with high isotropization temperature (T_i).[22,23] Later, main-chain type poly(ester-amide)s with regular

sequences also exhibit liquid crystalline self-assembly above the crystal melting temperature (T_m). [24] Replacing the amide groups with ester groups, liquid crystalline self-assembly disappears. Clearly, hydrogen-bonding plays an important role in achieving liquid crystalline self-assembly in these side-chain and main-chain amide-containing polymers.

Alternatively, sulfonyl groups are also used to induce smectic liquid crystalline phases through the incorporation in either the main chain[25-28] or side chains.[29-37] It is considered that the strong dipole-dipole interactions among the regularly distributed sulfonyl groups provide certain conformation rigidity in the soft aliphatic matrix for the mesophase assembly. For the side chain polymers, disulfonyl side groups exhibited much stronger dipole-dipole interactions than monosulfonyl groups, pushing the isotropization temperature to higher values. Regardless of different chain architectures (main chain vs. side chain) and chemical compositions (aliphatic spacer and tail lengths), only smectic A (SmA) structure was exclusively reported so far for these mesogen-free aliphatic liquid crystalline polymers. For the side-chain polymers grafted with the alkylsulfonyl groups, the regular 2_1 helical conformation is the main reason for the formation of SmA self-assembly.[13]

To achieve the ferroelectric smectic C* (SmC*) phase in mesogen-free aliphatic liquid crystalline polymers, it is necessary to induce the smectic C (SmC) phase with tilted *n*-alkyl side chains and break the C_{2h} symmetry to the C_2 symmetry by introducing chiral centers in either the main chain or the side chains.[2,38] In the first attempt,[13] Kwok and Seymour et al. synthesized a chiral polymer, isotactic polyepichlorohydrin (iPECH), by ring-opening polymerization of (*R*)-(-)-epichlorohydrin, and used it to prepare isotactic poly(propylene oxide) (iPOP) polymers grafted with *n*-alkylsulfonyl pendant groups (iPOP-SO_2C_n, where C_n is the *n*-alkyl tail) via post-polymerization modifications. Although the grafting and oxidation of thioether side chains were

quantitative, again only smectic A phases were obtained for samples with n = 10-12 during cooling from the isotropic melts before crystallization. Upon heating, monotropic phase behavior was observed with only crystal-melting. Therefore, new strategies need to be implemented to achieve the SmC* phase.

In this work, we first increased the distance between the chiral center in the iPOP backbone and the sulfonyl dipole in the side chain to weaken the dipole-dipole interactions and induce smectic phases through the use of *n*-alkylsulfonylpentylthioether pendant groups (Scheme 2.1). Subsequent oxidation of the thioether moieties led to disulfonylated iPOPs with a shorter distance between the chiral center and the inner sulfonyl group, a higher dipole density, and stronger dipole-dipole interactions. Their liquid crystalline self-assembly behaviors were thoroughly investigated by DSC, synchrotron X-ray diffraction (XRD), as well as polarized light microscopy (PLM), to examine if the ferroelectric SmC* phase could be induced via the above strategies. Atactic polyoxypropylene (aPOP) samples with sulfonylated side chains were used to compare with the iPOPs in order to study the tacticity effect on the liquid crystalline self-assembly.

2.2. Experimental section

2.2.1. Materials

1-Octanethiol (97%, Acros), 1-dodecanethiol (99%, Acros), 5-bromo-1-pentanol (90%, TCI), 3-chloroperoxybenzoic acid (*m*-CPBA, 70-75% balance 3-chlorobenzoic acid and water, Acros Organics), methanesulfonyl chloride (98%, Alfa Aesar), thioacetic acid (97% Acros Organics), and *N*,*N*-dimethylacetamide (99.5%, extra dry, Acros Organics) were used as received. Atactic polyepichlorohydrin (aPECH) with a weight-average molecular weight (M_w) of ~700,000 Da (reported by the vendor) was obtained from Sigma-Aldrich. (*R*)-(-)-Epichlorohydrin [(*R*)-(-)-ECH,

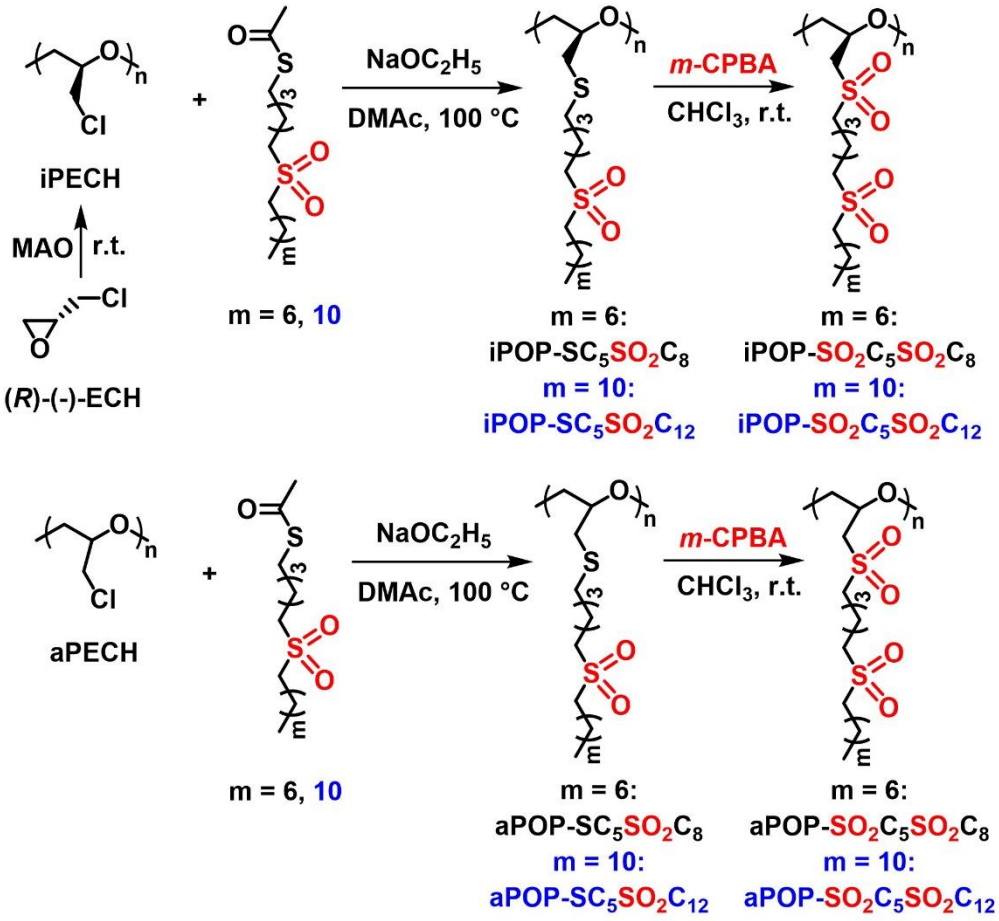

Scheme 2.1. Syntheses of Isotactic and Atactic Polyethers with Thioether-Monosulfonyl and Disulfonyl Pendant Groups

98%, Combi-blocks, Inc.] and diethyl ether (99.8%, certified ACS, Fisher Chemical) were dried with calcium hydride (93%, Acros Organics) and distilled before use. Modified methylaluminoxane (MMAO-12, 7 wt.% aluminum in toluene) was purchased from Sigma-Aldrich and stored in the freezer inside a nitrogen glovebox. iPECH was synthesized by ring-opening polymerization using MMAO-12 as catalyst in a glove box at room temperature as reported previously.[13] Solutions of sodium ethoxide in ethanol with concentrations of 11.3 and 13.1 wt.% were prepared by adding a calculated amount of sodium metal into absolute ethanol under a nitrogen atmosphere and stirring the mixtures until the sodium metal completely reacted. 5-(Octylsulfonyl)pentyl ethanethioate and 5-(dodecylsulfonyl)pentyl ethanethioate (Scheme 2.1) were synthesized according to a method reported in the literature,[34] and their molecular structures were verified by proton (^{1}H) and carbon-13 (^{13}C) NMR, and mass spectroscopy. The detailed synthesis and the characterization data are included in Section I of Appendix A. All other chemicals and solvents were obtained from either Fisher Scientific or Sigma-Aldrich and used as received.

2.2.2. Characterization and Instrumentation

^{1}H and ^{13}C NMR spectra were recorded on either a Varian Mercury 300 NMR, a Varian VNMRS 500 NMR, or a Varian VNMRS 600 spectrometer using the residual solvent proton signal as the internal standard. The high-resolution mass spectrometry (HRMS) experiments were performed using a JEOL Model JMS-T100LC (AccuTOF) orthogonal time-of-flight (TOF) mass spectrometer (Peabody, MA) with an IonSense (Danvers, MA) DART source. Size exclusion chromatography (SEC) of atactic and isotactic polyethers with *n*-alkylsulfonylthioether or disulfonyl pendant groups was performed on a PL-GPC 20 system, an integrated SEC system from Polymer Laboratories, Inc., equipped with a Knauer K-2301 refractive index detector, one PL gel

5 μm guard column (50 × 7.5 mm), and two PLgel 5 μm mixed-C columns (each 300 × 7.5 mm, linear molecular weight range of 200-2,000,000 Da). HPLC-grade chloroform was used as the eluent, and the flow rate was set at 1.0 mL/min. The SEC system was calibrated with narrow dispersity polystyrene (PS) standards (Scientific Polymer Products, Inc.), and the data was processed using the Cirrus SEC software from Polymer Laboratories, Inc.

The optical activities of isotactic polyethers with *n*-alkylsulfonylthioether pendant groups were measured at ambient temperature (~20 °C) using a PerkinElmer 241 polarimeter with a sodium lamp with a wavelength of 589 nm and an integration time of 5 s. The solutions used in the measurements were prepared by dissolving the polymers in $CHCl_3$ at a concentration of ~ 10 mg/mL. For each solution, three measurements were taken, and the average value was used as the optical rotation. The specific rotations of the polymers were calculated by using equation $[\alpha]_{\lambda}^{\mathrm{T}} = \alpha/(cl)$, where [α] is the specific rotation at a certain temperature (T) and wavelength (λ), α is the optical rotation in degrees from the measurements, *c* is the concentration in units of g/mL, and *l* is the path length in dm. The units of specific rotation is $deg \cdot mL/(g \cdot dm)$, which is commonly abbreviated to degrees (°).

Thermogravimetric analysis (TGA) experiments were carried out in a dry nitrogen atmosphere at a heating rate of 20 °C/min from room temperature to 700 °C using TA Instruments Q-50 TGA. DSC experiments were carried out on a TA Discovery DSC 250. Approximately 3 mg samples were used at a scanning rate of 20 °C/min. PLM was carried out on an Olympus BX60, equipped with an Instec HCS402 hot stage (Instec, Inc., Boulder, CO).

Synchrotron XRD was carried out at the 11-BM Complex Materials Scattering (CMS) beamline of National Synchrotron Light Source II (NSLS-II), Brookhaven National Laboratory (BNL). The monochromatized X-ray wavelength was λ = 0.0918 nm. An in-vacuum Pilatus 800K

detector (Dectris, Baden-Dättwil, Switzerland) was used for data collection. The sample-to-detector distance was 373 mm, which was calibrated using silver behenate with the first-order reflection at a scattering vector q = 1.076 nm^{-1} [$q = (4\pi\sin\theta)/\lambda$ with θ being the half-scattering angle]. The data acquisition time was 30 s. A Linkam HFSX350 hot stage was used for temperature control. One-dimensional (1D) XRD curves were obtained by integration of the corresponding two-dimensional (2D) patterns.

Additional XRD experiments were carried out on a Xenocs Xeuss 3.0 SAXS Instrument from Xenocs Inc. (Holyoke, MA), using a Cu K_α source with a wavelength of 1.542 Å operating at 50 kV and 0.6 mA. 2D patterns were collected with an acquisition time of 10 min. A Linkam HFS350X hot stage equipped with a liquid nitrogen cooling accessory was used for temperature control (Linkam Scientific Instruments Ltd., Tadworth, UK). One-dimensional (1D) XRD curves were generated using the SAXS GUI software, by the integration of the corresponding 2D patterns. 1D azimuthal integrations were obtained via integration of the 2D pattern at specific scattering vector (q) values. Fibers of aPOP-$SC_5SO_2C_{12}$ were prepared by heating the sample to 130 °C and subsequently pulling the melt into fibers using a pair of forceps. The fibers were then tabbed to the stage using a Kapton tape for XRD.

2.2.3. Synthesis of Atactic Polyethers with *n*-Alkylsulfonylpentylthioether Pendant Groups (aPOP-$SC_5SO_2C_8$ and aPOP-$SC_5SO_2C_{12}$)

aPOP-$SC_5SO_2C_8$ and aPOP-$SC_5SO_2C_{12}$ were synthesized by reacting aPECH with 5-(octylsulfonyl)pentyl ethanethioate and 5-dodecylsulfonyl)pentyl ethanethioate, respectively (Scheme 2.1). Shown below is the synthesis of aPOP-$SC_5SO_2C_8$. A similar procedure was used for the synthesis of aPOP-$SC_5SO_2C_{12}$. Sodium ethoxide (0.181 g, 2.65 mmol, delivered from a stock solution of sodium ethoxide in ethanol with a concentration of 13.1 wt.%) and 5-

(octylsulfonyl)pentyl ethanethioate (0.822 g, 2.65 mmol) were added into a 50 mL two-necked round bottom flask with a magnetic stir bar. The mixture was stirred at room temperature for 3 h. aPECH (0.144 g, 1.56 mmol) and *N*,*N*-dimethylacetamide (DMAc, extra dry, 10 mL) were weighed into a 20 mL scintillation vial, which was capped, placed on a platform shaker, and shaken overnight. A clear, highly viscous solution was obtained and added into the flask containing the stirring solution of 5-(octylsulfonyl)pentyl ethanethioate and sodium ethoxide. The reaction flask was equipped with a reflux condenser, placed in an oil bath with a preset temperature of 100 ℃, and stirred for 48 h. The solution stayed clear throughout the reaction. After cooling to room temperature, the reaction mixture was precipitated in water, and the solid was collected via vacuum filtration. The polymer was then dissolved in chloroform (5 mL) and precipitated in methanol. This dissolution-precipitation process was repeated one more time, and the collected purified polymer was dried in a vacuum oven, yielding a white fluffy solid (0.521 g, 93% yield). ^{1}H NMR (600 MHz, $CDCl_3$) δ (ppm) = 3.75 – 3.53 (m, -OCH_2CH-, 3H), 2.99 – 2.92 (m, -CH_2CH_2SO_2CH_2CH_2-, 4H), 2.80 – 2.51 (m, -CHCH_2SCH_2CH_2-, 4H), 1.88 – 1.77 (m, -CH_2CH_2SO_2CH_2CH_2-, 4H), 1.68 – 1.51 (m, -CHCH_2SCH_2CH_2CH_2CH_2C$H_2$$SO_2$-, 4H), 1.47 – 1.39 (m, -CH_2(CH_2)$_4$$CH_3$, 2H), 1.39 – 1.23 (-$CH_2$(C$H_2$)$_4$$CH_3$, 8H), 0.88 (t, -C$H_3$, 3H). ^{13}C NMR (151 MHz, $CDCl_3$), δ (ppm) = 79.20, 71.10, 70.90, 70.45, 70.25, 54.34, 52.37, 33.88, 32.65, 31.62, 29.13, 28.99, 28.87, 28.45, 27.61, 22.50, 21.79, 21.40, 13.98. SEC analysis results with chloroform as the eluent: number-average molecular weight ($M_{n,SEC}$) = 129 kDa and dispersity (*Đ*) = 3.0, relative to PS standards.

The yield for the synthesis of aPOP-$SC_5SO_2C_{12}$ was 93%. ^{1}H NMR (600 MHz, $CDCl_3$), δ (ppm) = 3.76 – 3.49 (m, ,-OCH_2CH-, 3H), 3.00 – 2.92 (m, -CH_2CH_2SO_2CH_2CH_2-, 4H), 2.80 – 2.52 (-CHCH_2SCH_2CH_2-, 4H), 1.89 – 1.77 (m, -CH_2CH_2SO_2CH_2CH_2-, 4H), 1.68 – 1.50 (m, -

$SCH_2CH_2CH_2(CH_2)_2SO_2CH_2$-, 4H), 1.47 – 1.20 (m, -$CH_2(CH_2)_9CH_3$, 16H), 0.88 (t, -CH_2CH_3, 3H). ^{13}C NMR (151 MHz, $CDCl_3$), δ (ppm) = 79.33, 71.06, 70.94, 70.43, 70.20, 52.84, 52.39, 33.69, 32.61, 31.81, 29.53, 29.47, 29.27, 29.25, 29.17, 29.14, 29.09, 28.50, 27.62, 22.59, 21.79, 21.39, 14.03. SEC results with chloroform as eluent: $M_{n,SEC}$ = 48.3 kDa and $Đ$ = 2.05, relative to PS standards.

2.2.4. Synthesis of Isotactic Polyethers with *n*-Alkylsulfonylpentylthioether Pendant Groups (iPOP-$SC_5SO_2C_8$ and iPOP-$SC_5SO_2C_{12}$)

iPOP-$SC_5SO_2C_8$ and iPOP-$SC_5SO_2C_{12}$ were prepared from iPECH using corresponding *n*-alkylsulfonylpentyl ethanethioates via a procedure similar to that for aPOP-$SC_5SO_2C_8$ and aPOP-$SC_5SO_2C_{12}$ (Scheme 2.1). The yield for the synthesis of iPOP-$SC_5SO_2C_8$: 86%. ^{1}H NMR (600 MHz, $CDCl_3$), δ (ppm) = 3.74 – 3.53 (m, -OCH_2CH-, 3H), 2.99 – 2.91 (m, -C$H_2SO_2CH_2$-, 4H), 2.77 –2.52 (m, -CH_2SCH_2-, 4H), 1.89 – 1.77 (m, -C$H_2CH_2SO_2CH_2CH_2$-, 4H), 1.67 – 1.52 (m, -$SCH_2(CH_2)_2CH_2$-, 4H), 1.47 – 1.39 (m, -C$H_2(CH_2)_4CH_3$, 2H), 1.36 – 1.22 (m, -$CH_2(CH_2)_4CH_3$-, 8H), 0.88 (t, -CH_3, 3H). ^{13}C NMR (151 MHz, $CDCl_3$), δ (ppm) = 80.04, 72.13, 52.84, 52.39, 33.90, 33.12, 31.63, 29.15, 29.00, 28.89, 28.47, 27.63, 22.51, 21.80, 21.41, 14.00. SEC results with chloroform as eluent: $M_{n,SEC}$ = 92.4 kDa and $Đ$ = 2.66, relative to PS standards.

The yield for the synthesis of iPOP-$SC_5SO_2C_{12}$ was 90%. ^{1}H NMR (600 MHz, $CDCl_3$), δ (ppm) = 3.74 – 3.51 (m, ,-OCH_2CHO-, 3H), 3.01 – 2.91 (m, -$CH_2CH_2SO_2CH_2CH_2$-, 4H), 2.79 – 2.53 (m, -CHCH_2SCH_2CH_2-, 4H), 1.90 – 1.77 (m, ,-C$H_2CH_2SO_2CH_2CH_2$-, 4H), 1.69 – 1.50 (m, -$CHCH_2SCH_2CH_2CH_2$-, 4H), 1.48 – 1.19 (m, -$CH_2(CH_2)_9CH_3$, 18H), 0.88 (t, -CH_3, 3H). ^{13}C NMR (151 MHz, $CDCl_3$), δ (ppm) = 79.36, 71.14, 53.30, 52.41, 38.55, 33.93, 32.69, 31.84, 29.56, 29.50, 29.30, 29.28, 29.17, 29.11, 28.52, 27.65, 22.62, 21.82, 21.42, 14.06. SEC results with chloroform as eluent: $M_{n,SEC}$ = 202 kDa and $Đ$ = 1.83, relative to PS standards.

2.2.5. Synthesis of Atactic and Isotactic Polyethers with Disulfonyl Pendant Groups

All atactic and isotactic polyethers with disulfonyl pendant groups, aPOP-$SO_2C_5SO_2C_8$, aPOP-$SO_2C_5SO_2C_{12}$, iPOP-$SO_2C_5SO_2C_8$, and iPOP-$SO_2C_5SO_2C_{12}$ (Scheme 2.1), were synthesized from the corresponding polyethers with *n*-alkylsulfonylpentylthioether side chains using the same procedure. The following example shows the synthesis of aPOP-$SO_2C_5SO_2C_8$. *m*-CPBA (0.438 g, 1.78 mmol) and aPOP-$SC_5SO_2C_8$ (0.159 g, 0.47 mmol) were dissolved in chloroform (15 mL) in a 50 mL flask and stirred with a magnetic stir bar at room temperature for 3 h. The mixture was poured into a 150 mL separatory funnel and washed with 1 M NaOH (2 × 50 mL). The organic layer was retrieved and dried with anhydrous sodium sulfate. After the removal of sodium sulfate and the solvent, the polymer was dried in a vacuum oven at 65 °C, yielding an opaque, brittle solid (0.156 g, 55% yield). ^{1}H NMR (500 MHz, $CDCl_3$), δ (ppm) = 4.22 – 3.59 (m, -OC*H*$_2$C*H*O-, 3H), 3.49 – 2.80 (m, -CHC*H*$_2$SO$_2$C*H*$_2$-, -C*H*$_2$SO$_2$C*H*$_2$(CH$_2$)$_6$CH$_3$, 8H), 1.96 – 1.73 (m, -CHCH$_2$SO$_2$CH$_2$C*H*$_2$CH$_2$C*H*$_2$CH$_2$SO$_2$ CH$_2$*CH*$_2$(CH$_2$)$_5$CH$_3$, 6H), 1.72 – 1.55 (m, -SO$_2$(CH$_2$)$_2$C*H*$_2$(CH$_2$)$_2$SO$_2$-, 2H), 1.51 – 1.20 (m, -(C*H*$_2$)$_5$CH$_3$, 10H), 0.88 (t, -C*H*$_3$, 3H). SEC results with chloroform as eluent: $M_{n,SEC}$ = 32.8 kDa and *Đ* = 2.05, relative to PS standards.

The yield for the synthesis of aPOP-$SO_2C_5SO_2C_{12}$ was 93%. ^{1}H NMR (600 MHz, $CDCl_3$), δ (ppm) = 4.17 – 3.61 (m, -O*CH*$_2$C*H*- *3H*), 3.47 – 2.85 (m, -CHC*H*$_2$SO$_2$C*H*$_2$-, -C*H*$_2$SO$_2$C*H*$_2$(CH$_2$)$_{10}$CH$_3$, 8H), 1.97 – 1.73 (m, ,-CHCH$_2$SO$_2$CH$_2$C*H*$_2$CH$_2$C*H*$_2$CH$_2$SO$_2$CH$_2$C*H*$_2$-, 6H), 1.70 – 1.56 (m, -SO$_2$(CH$_2$)$_2$C*H*$_2$(CH$_2$)$_2$SO$_2$-, 2H), 1.47 – 1.04 (m, -(C*H*$_2$)$_9$CH$_3$, 18H), 0.88 (t, -C*H*$_3$, 3H). SEC results with chloroform as eluent: $M_{n,SEC}$ = 15.6 kDa and *Đ* = 1.73, relative to PS standards.

The yield for the synthesis of iPOP-$SO_2C_5SO_2C_8$ was 31%. ^{1}H NMR (500 MHz, $CDCl_3$), δ (ppm) = 4.14 – 3.65 (m, -O*CH*$_2$C*H*-, 3H), 3.45 – 2.87 (m, -CHC*H*$_2$SO$_2$C*H*$_2$-, -

C*H*$_2$SO$_2$C*H*$_2$(CH$_2$)$_6$CH$_3$, 8H), 1.94 – 1.75 (m, -SO$_2$CH$_2$C*H*$_2$CH$_2$C*H*$_2$CH$_2$SO$_2$CH$_2$C*H*$_2$-, 6H), 1.68 – 1.59 (m, -SO$_2$(CH$_2$)$_2$C*H*$_2$(CH$_2$)$_2$SO$_2$-, 2H), 1.47 – 1.22 [m, -(C*H*$_2$)$_5$CH$_3$, 10H], 0.89 (t, -C*H*$_3$, 3H). SEC results with chloroform as eluent: $M_{n,SEC}$ = 24.9 kDa and $Đ$ = 2.12, relative to PS standards.

The yield for the synthesis of iPOP-SO$_2$C$_5$SO$_2$C$_{12}$ was 68%. ^{1}H NMR (600 MHz, CDCl$_3$), δ (ppm) = 4.17 – 3.60 (m, -OC*H*$_2$C*H*- 3H), 3.51 – 2.82 (m, -CHC*H*$_2$SO$_2$C*H*$_2$-, -C*H*$_2$SO$_2$C*H*$_2$(CH$_2$)$_{10}$CH$_3$, 8H), 1.92 – 1.74 (m, -CHCH$_2$SO$_2$CH$_2$C*H*$_2$CH$_2$C*H*$_2$CH$_2$SO$_2$CH$_2$C*H*$_2$-, 6H), 1.69 – 1.57 [m, -SO$_2$(CH$_2$)$_2$C*H*$_2$(CH$_2$)$_2$SO$_2$-, 2H], 1.44 – 1.21 [m, -(C*H*$_2$)$_9$CH$_3$, 18H], 0.88 (t, -C*H*$_3$, 3H). SEC results with chloroform as eluent: $M_{n,SEC}$ = 21.3 kDa and $Đ$ = 1.69, relative to PS standards.

2.3. Results and Discussion

2.3.1. Synthesis of Isotactic and Atactic Polyethers with Mono- and Disulfonyl Pendant Groups

Isotactic and atactic POPs with mono-sulfonyl (i.e., *n*-alkylsulfonylpentylthioether) pendant groups were synthesized from aPECH and iPECH, respectively, via a substitution reaction, as illustrated in Scheme 2.1. iPECH was prepared by ring-opening polymerization of (*R*)-(-)-ECH using MMAO as catalyst, and the isotacticity of the obtained iPECH was previously confirmed by ^{13}C NMR spectroscopy.[13] The substitution reactions of aPECH and iPECH with sodium 5-(*n*-octylsulfonyl)pentanethiolate and sodium 5-(*n*-dodecylsulfonyl)pentanethiolate, formed in-situ from 5-(*n*-octylsulfonyl)pentyl ethanethioate and 5-(*n*-dodecylsulfonyl)pentyl ethanethioate in the presence of sodium ethoxide, were carried out in DMAc at 100 °C for 48 h. After the isolation and purification, the obtained polymers were characterized by ^{1}H NMR spectroscopy to determine the degrees of substitution. Figures 2.1A and B show the ^{1}H NMR spectra of aPOP-SC$_5$SO$_2$C$_{12}$ and

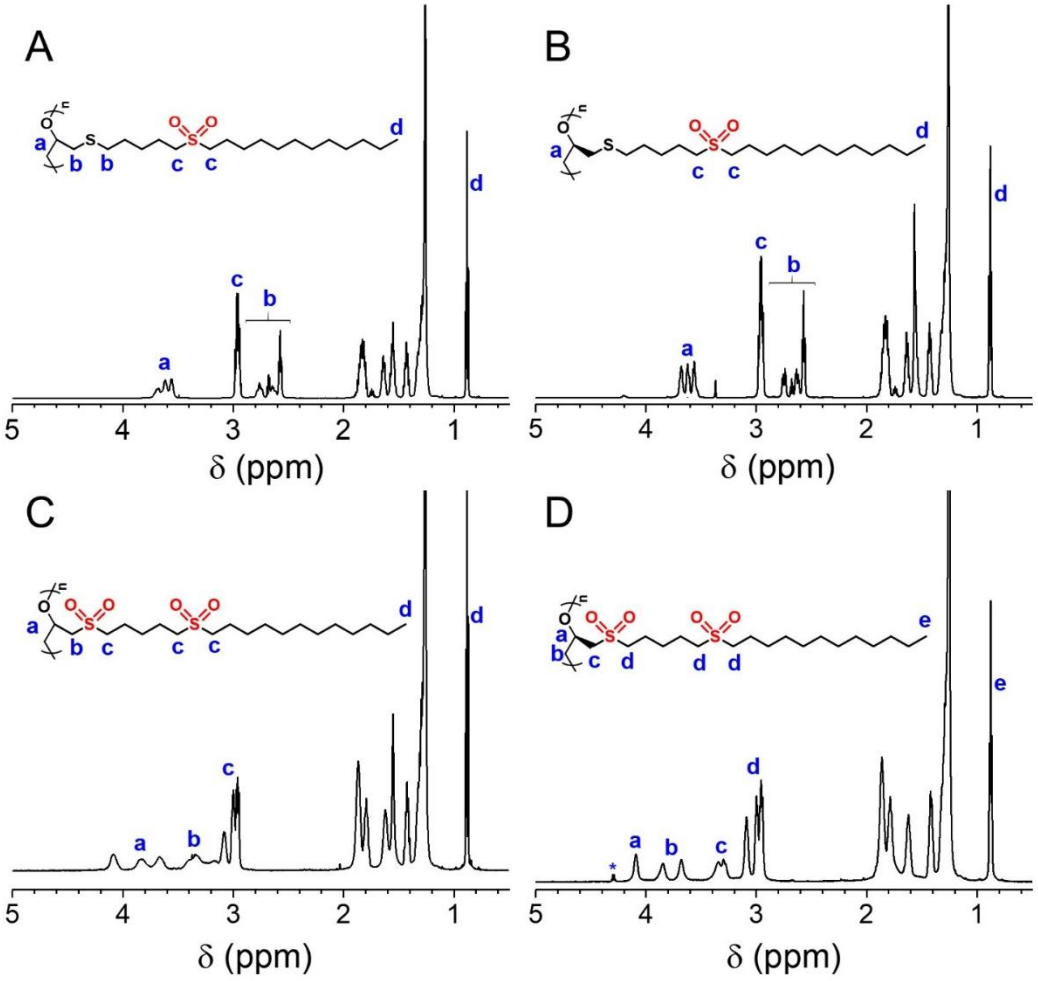

Figure 2.1. ^{1}H NMR spectra of (A) aPOP-$SC_5SO_2C_{12}$, (B) iPOP-$SC_5SO_2C_{12}$, (C) aPOP-$SO_2C_5SO_2C_{12}$, and (D) iPOP-$SO_2C_5SO_2C_{12}$ in $CDCl_3$. Peaks labeled with * are from impurities.

iPOP-$SC_5SO_2C_{12}$ in $CDCl_3$. The ^{1}H NMR spectra of aPOP-$SC_5SO_2C_8$ and iPOP-$SC_5SO_2C_8$ can be found in Figures A.2A and A.6A, respectively, in Appendix A. A comparison of the peak integrals in the range of 3.75 – 3.53 ppm (-OC*H*$_2$C*H*- from the backbone) and 2.99 – 2.92 ppm (-$CH_2CH_2SO_2CH_2CH_2$- from the side chain) or 2.80 –2.51 ppm (-CHC*H*$_2$SC*H*$_2$CH$_2$- from the side chain) indicated that the substitution was essentially complete for all of the polymers.

The polyethers with *n*-alkylsulfonylpentylthioether groups (i.e., POP-$SC_5SO_2C_8$ and POP-$SC_5SO_2C_{12}$) showed a reasonably good solubility in chloroform, allowing us to characterize the tacticity of these polymers by ^{13}C NMR spectroscopy, the optical activities of isotactic polymers by polarimetry, and the molecular weights and dispersities by SEC. Figure 2.2 shows the ^{13}C NMR spectra of aPOP-$SC_5SO_2C_{12}$ and iPOP-$SC_5SO_2C_{12}$ (those of aPOP-$SC_5SO_2C_8$ and iPOP-$SC_5SO_2C_8$ can be found in Figure A.2B and A.6B). While the backbone methylene (-*C*H$_2$-) carbon of the atactic polyethers manifested as multiple peaks in the range of 70 – 72 ppm, there was only a single peak at 71.1 ppm for both isotactic polyethers. These observations are consistent with the previous results,[13] as well as the data reported by Brochu and Ampleman.[39] Similarly, for the backbone methine carbon [-CH$_2$*C*H(CH$_2$S)O-], two peaks were observed at 79.20 and 79.34 for the two atactic polyethers, while the isotactic polymers (i.e., iPOP-$SC_5SO_2C_8$ and iPOP-$SC_5SO_2C_{12}$) exhibited only one peak at 79.33 ppm. Polarimetry measurements showed that atactic polymers did not exhibit an optical activity, with specific rotations of either zero or a negligible value. In contrast, iPOP-$SC_5SO_2C_8$ and iPOP-$SC_5SO_2C_{12}$ showed $[a]_D^{20}$ values of -10.5° and -10.1°, respectively (Table 2.1). Note that the specific rotation of (*R*)-(-)-ECH monomer in methanol was -35.4° (with a concentration of ~10 mg/mL), which is much higher than those of the two isotactic polymers. This could be due to the different heteroatoms (Cl versus S) before and after the substitution and the different molar masses of the repeat units compared with (*R*)-(-)-ECH

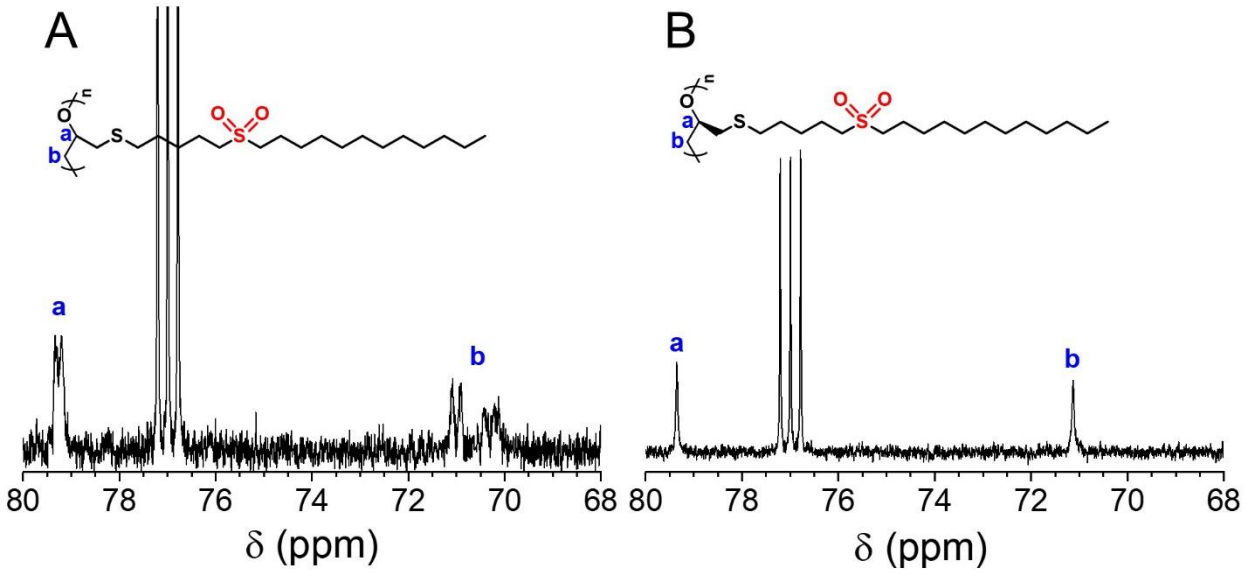

Figure 2.2. ^{13}C NMR spectra of (A) aPOP-$SC_5SO_2C_{12}$ and (B) iPOP-$SC_5SO_2C_{12}$ in $CDCl_3$.

Table 2.1. Characterization Data for Atactic and Isotactic Polyethers with Mono- and Di-sulfonyl Pendant Groups

Sample	$M_{n,SEC}$	$Đ$	$[\alpha]_D^{20}$	$T_{95\%}$
aPOP-$SC_5SO_2C_8$	129 kDa	3.04	-	327 °C
aPOP-$SO_2C_5SO_2C_8$	32.8 kDa	2.05	-	267 °C
iPOP-$SC_5SO_2C_8$	92.4 kDa	2.66	– 10.5°	328 °C
iPOP-$SO_2C_5SO_2C_8$	24.9 kDa	2.12	-	295 °C
aPOP-$SC_5SO_2C_{12}$	48.3 kDa	2.05	-	311 °C
aPOP-$SO_2C_5SO_2C_{12}$	15.6 kDa	1.73	-	333 °C
iPOP-$SC_5SO_2C_{12}$	202 kDa	1.83	– 10.1°	346 °C
iPOP-$SO_2C_5SO_2C_{12}$	21.3 kDa	1.69	-	299 °C

monomer (note that specific rotation [α] is calculated based on the concentration of ~10 mg/mL). If we assume that the contributions of Cl and $SC_5SO_2C_8$ or $SC_5SO_2C_{12}$ to the optical activity are identical, we can normalize the optical activities of iPOP-$SC_5SO_2C_8$ and iPOP-$SC_5SO_2C_{12}$ against the monomer based on the molar masses of the repeat unit. Then, the [α] values were -38.1° and -42.8°, which were comparable to that of (*R*)-(-)-ECH. SEC analysis showed that the $M_{n,SEC}$ values were from 48 to 202 kDa with respect to PS standards and the dispersities were in the range of 1.8 to 3.0 (Figures A.3, A.5, A.7, and A.9). These characterization data are summarized in Table 2.1, along with the specific rotations of iPOP-$SC_5SO_2C_8$ and iPOP-$SC_5SO_2C_{12}$.

The polyethers with *n*-alkylsulfonylpentylthioether pendant groups were then oxidized by *m*-CPBA in chloroform at room temperature for 3 h to produce the polyethers with disulfonyl pendant groups (i.e., POP-$SO_2C_5SO_2C_8$ and POP-$SO_2C_5SO_2C_{12}$). ^{1}H NMR spectroscopy analysis showed that the peaks in the range of 2.50 – 2.80 ppm (-C*H*$_2$SC*H*$_2$-, the thioether linkage) completely disappeared for all four polyethers (Figure 2.1C and D for aPOP-$SO_2C_5SO_2C_{12}$ and iPOP-$SO_2C_5SO_2C_{12}$; Figure A.10 shows the NMR spectra of aPOP-$SO_2C_5SO_2C_8$ and iPOP-$SO_2C_5SO_2C_8$), indicating that the oxidation of the thioether groups was complete. The molecular weights of the disulfonylated polyethers were also characterized by SEC using $CHCl_3$ as eluent (Figure A.11), and the data are summarized in Table 2.1. Compared with the $M_{n,SEC}$ for the thioether precursor polymers, the molecular weights decreased significantly for the disulfonylated polyethers. These results indicated that *m*-CPBA not only oxidized the thioether linkage in the side chains, but also randomly cleaved the polyether main chain. Nevertheless, the $M_{n,SEC}$ values for the resulting disulfonyl polyethers were high enough to be considered as polymers, not oligomers.

The thermal stability of atactic and isotactic polyethers with mono- and di-sulfonyl side chains was studied by TGA in a dry N_2 atmosphere at a heating rate of 20 °C/min, and the results are

shown in Figure A.12. The 5% weight loss temperatures ($T_{95\%}$) for the polyethers with *n*-alkylsulfonylthioether pendant groups are summarized in Table 2.1. The $T_{95\%}$ values for these polyethers were in the range of 310 – 345 °C, with those for the isotactic polymers being slightly higher. For the polyethers with disulfonyl pendant groups, the $T_{95\%}$ values were in the range of 267 – 332 °C, lower than those of the corresponding polyethers with *n*-alkylsulfonylthioether side chains (except for aPOP-$SO_2C_5SO_2C_{12}$). Due to the strong electron-withdrawing ability of the sulfonyl group, alkylsulfonyl compounds have been reported to be prone to β-H elimination, especially under the attack of basic impurities.[40] The different $T_{95\%}$ values of the disulfonyl polyethers may be related to the different amounts of impurities in the samples.

2.3.2. Self-Assembly of Atactic and Isotactic POP-$SC_5SO_2C_{12}$ and POP-$SO_2C_5SO_2C_{12}$

As shown in a study reported in the literature,[13] strong dipole-dipole interactions in comb-like polymers can induce liquid crystalline self-assembly even without any traditional mesogen groups. Here, we investigated the effects of main-chain chirality and chiral center-to-dipole distance on the self-assembly of atactic and isotactic mesogen-free polyethers with one and two sulfonyl groups in the side chains. DSC was first used to study the phase transitions in these strongly interacting comb-like polyethers. Figure 2.3 shows the second heating and second cooling DSC curves of atactic and isotactic POP-$SC_5SO_2C_{12}$ and POP-$SO_2C_5SO_2C_{12}$. During the first heating, T_g was found in the range of 45-50 °C for all of the four polymers. During the second heating cycle, however, the T_g became less obvious. This is likely because the solution-precipitated samples had a lower crystallinity than those crystallized from the melt during DSC cooling, which made it possible for the polymers to exhibit clearer glass transitions. For both aPOP-$SC_5SO_2C_{12}$

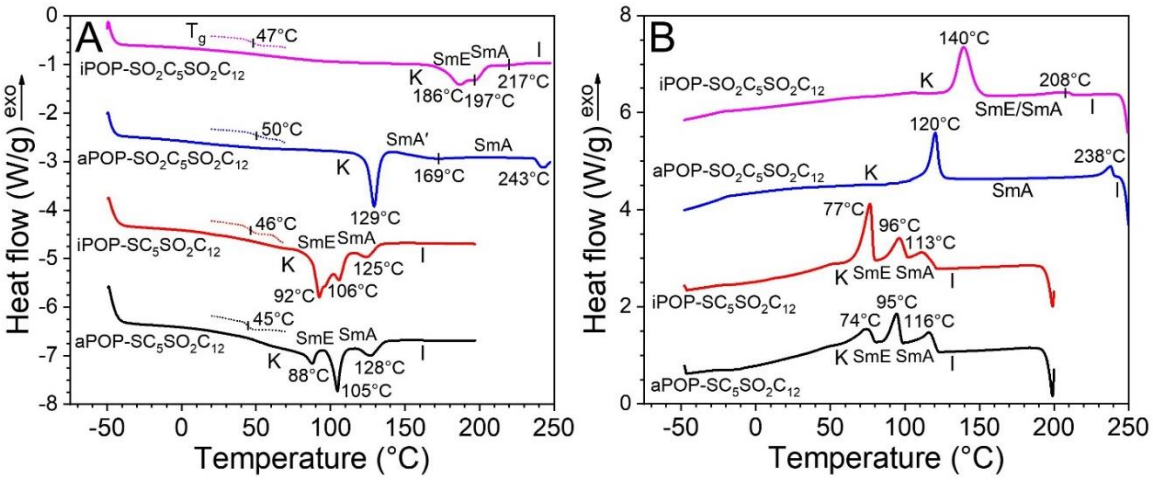

Figure 2.3. (A) Second heating DSC curves for atactic and isotactic POP-$SC_5SO_2C_{12}$ and POP-$SO_2C_5SO_2C_{12}$. (B) Second cooling DSC curves for atactic and isotactic POP-$SC_5SO_2C_{12}$ and POP-$SO_2C_5SO_2C_{12}$. The dotted lines in (A) show the T_g values during the first heating cycle. The heating and cooling rates are 20 °C/min.

and iPOP-$SC_5SO_2C_{12}$, three endothermic peaks were observed in a similar temperature range in the second heating and cooling cycle. The similar thermal behaviors for both atactic and isotactic POP-$SC_5SO_2C_{12}$ samples suggested that the main-chain chiral center had little effect on the self-assembly behavior when the sulfonyl dipole in the side chain was far (i.e., 7-atom) away from the chiral center. After the oxidation of the thioether groups with *m*-CPBA, both aPOP-$SO_2C_5SO_2C_{12}$ and iPOP-$SO_2C_5SO_2C_{12}$ exhibited increased phase transition temperatures. The thermal behavior of the isotactic disulfonyl sample appeared to be quite different from that of the atactic counterpart, indicating that the main-chain chiral center had a significant influence on the self-assembly behavior when a sulfonyl dipole was closer to the chiral center (i.e., separated by one CH_2 group). These phase transition temperatures and heats (summarized in Table 2.2) were used for subsequent PLM and XRD studies.

Figures 2.4 and 2.5 show the PLM images for the POP-$SC_5SO_2C_{12}$ and POP-$SO_2C_5SO_2C_{12}$ samples, respectively. All samples showed obvious fan-shaped textures during the heating and cooling cycle, indicating that they all went through SmA type mesophases. Meanwhile, they exhibited no birefringence at temperatures above their corresponding T_i.

XRD was used to understand the mesophase structures of these samples. Results for aPOP-$SC_5SO_2C_{12}$ are shown in Figure 2.6. The fiber XRD pattern at room temperature in Figure 2.6A is consistent with the layered crystalline (K) structure in the comb-like polymer, as reported before by our group and our collaborators.[13] From the WAXD profiles at 27 °C (Figure 2.6C,D), multiple (hk0) reflections could be discerned for the K phase. In addition, the heats of fusion were also relatively large (see Table 2.2). All the evidence suggested the crystalline structure as the most stable phase. In the fiber, the main chains supposedly are in the drawing (vertical) direction, and the side chains are perpendicular to the main chains. As a result, the side-chain lamellar crystals

Table 2.2. Peak Phase Transition Temperatures (above the arrow) and Heats of Transition (kJ/mol, below the arrow) [a] for atactic and isotactic POP-$SC_5SO_2C_{12}$ and POP-$SO_2C_5SO_2C_{12}$

Sample	Second Heating	Second Cooling
aPOP-$SC_5SO_2C_{12}$	$K \xrightarrow[5.5]{88°C} SmE \xrightarrow[8.6]{105°C} SmA \xrightarrow[4.8]{128°C} I$	$I \xrightarrow[4.2]{116°C} SmA \xrightarrow[4.3]{95°C} SmE \xrightarrow[3.1]{74°C} K$
iPOP-$SC_5SO_2C_{12}$	$K \xrightarrow[12.6]{92°C} SmE \xrightarrow[6.6]{106°C} SmA \xrightarrow[4.1]{125°C} I$	$I \xrightarrow[2.7]{113°C} SmA \xrightarrow[5.5]{96°C} SmE \xrightarrow[10.6]{77°C} K$
aPOP-$SO_2C_5SO_2C_{12}$	$K \xrightarrow[10.0]{129°C} SmA' \xrightarrow[3.7]{169°C} SmA \xrightarrow[2.1]{243°C} I$	$I \xrightarrow[1.6]{238°C} SmA \xrightarrow[9.1]{120°C} K$
iPOP-$SO_2C_5SO_2C_{12}$	$K \xrightarrow[11.5]{186°C} SmE \xrightarrow[1.2]{197°C} SmA \xrightarrow[1.2]{217°C} I$	$I \xrightarrow[1.3]{208°C} SmE/SmA \xrightarrow[13.8]{140°C} K$

[a] Heats of transition are obtained by peak deconvolution using Gaussian function.

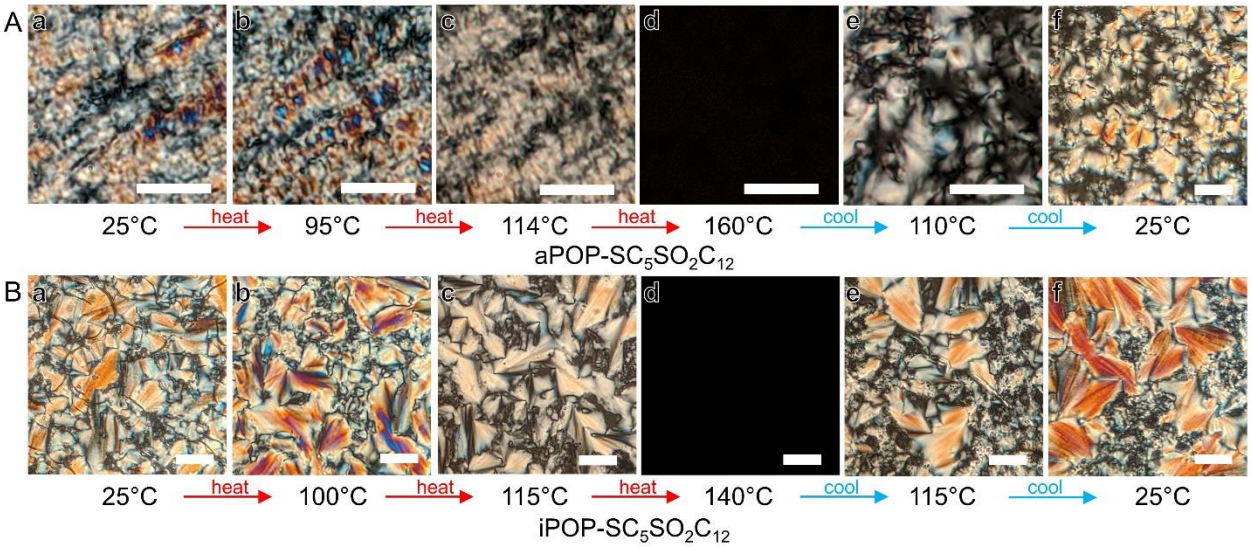

Figure 2.4. PLM images of (A) aPO-PS$C_5SO_2C_{12}$ and (B) iPOP-$SC_5SO_2C_{12}$ during the heating and cooling cycle. The scale bars are 20 μm.

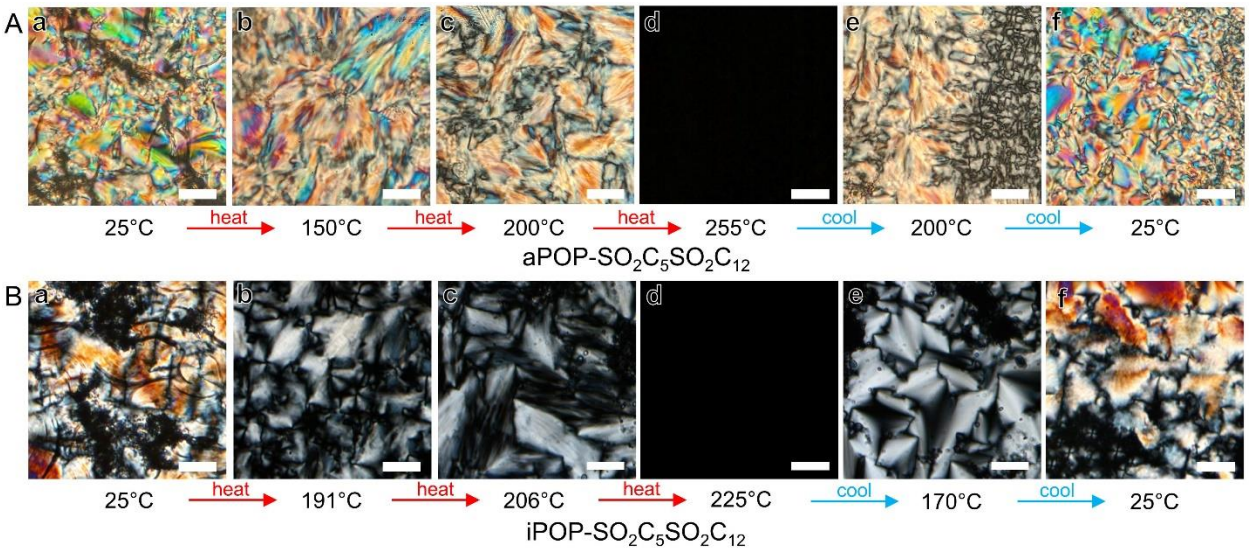

Figure 2.5. PLM images of (A) aPOP-$SO_2C_5SO_2C_{12}$ and (B) iPOP-$SO_2C_5SO_2C_{12}$ during the heating and cooling cycles. The scale bars are 20 μm.

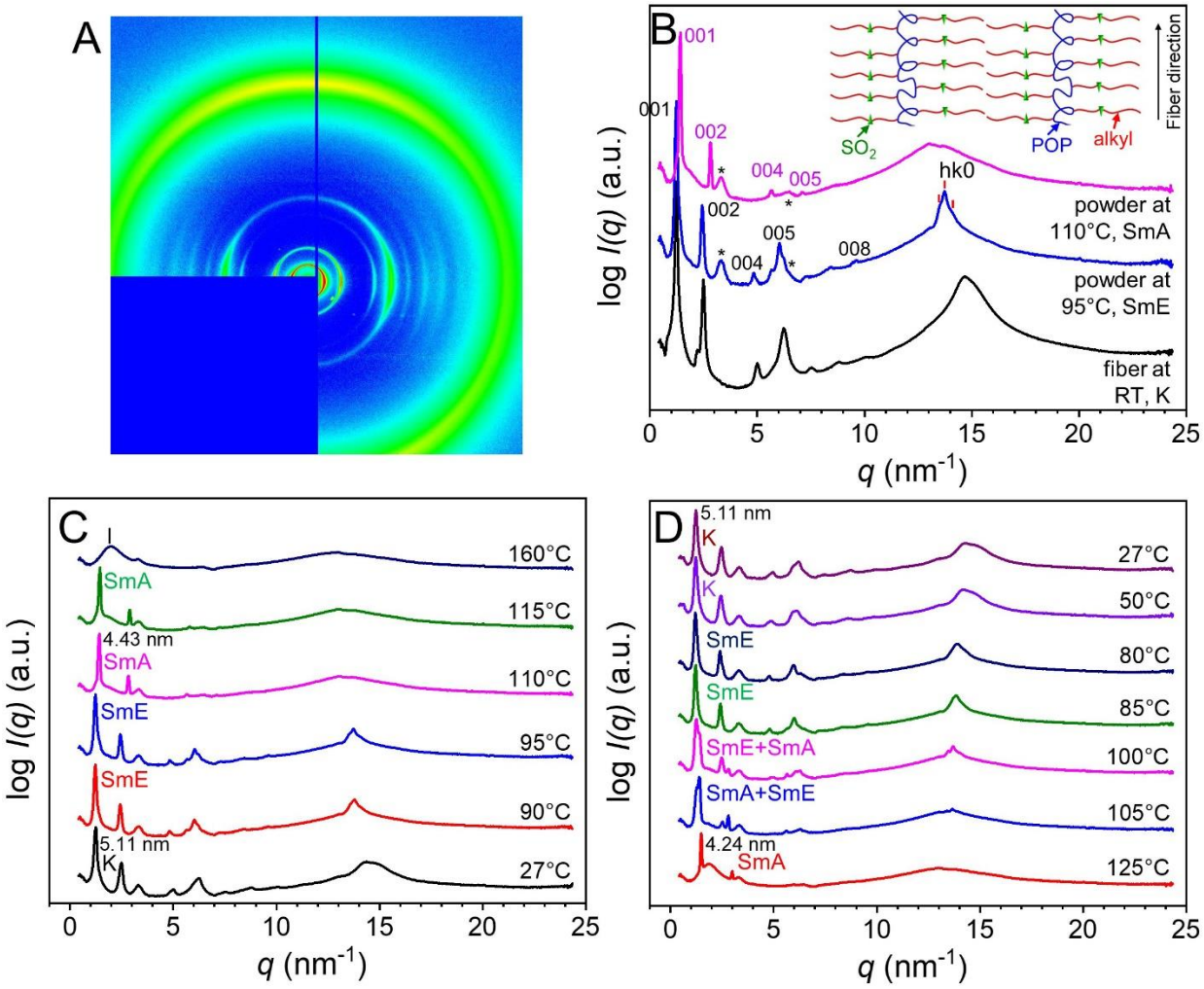

Figure 2.6. (A) 2D XRD pattern for the aPOP-$SC_5SO_2C_{12}$ fiber at room temperature. The fiber direction is vertical. (B) 1D XRD profiles for the aPOP-$SC_5SO_2C_{12}$ fiber at room temperature and the powder at 95 and 110 °C. The inset shows the schematic double layer structure. The bottom panel shows the 1D XRD profiles for the aPOP-$SC_5SO_2C_{12}$ powder during (C) heating and (D) cooling processes. Peaks labeled with * in B were from the Kapton window, and they are not labeled in C and D.

are parallel to the fiber direction. Indeed, well-ordered lamellar scattering [i.e., (00*l*) reflections] was seen in the horizontal direction with the *q* ratios being 1:2:4:5:6:7:8 (note that the 3rd order reflection was either very weak or extinct). The lamellar spacing was 5.11 nm, consistent with the double layer structure of the side chains having an all trans conformation (as reported before for the polyethers with *n*-alkylsulfonyl side chains,[13] the main chain was about 0.836 nm thick, and the length per CH_2/SO_2 was 0.118 nm); see the inset of Figure 2.6B. The (hk0) reflections in the wide-angle region concentrated on the vertical direction (Figure 2.6A). Given too few reflections in the fiber pattern, it is not possible to unambiguously determine the crystalline structure for the sample. Same results were obtained from the XRD experiment of the aPOP-$SC_5SO_2C_{12}$ fiber conducted at room temperature using a Xenocs Xeuss 3.0 SAXS instrument at the Polymer Characterization Laboratory at the University of Tennessee Knoxville (Figure 2.7). Note that the fiber of aPOP-$SC_5SO_2C_{12}$ was drawn at 130 °C. From the 1D curve (Figure 2.7B) integrated from the 2D scattering pattern (Figure 2.7A), the lamellar spacing was calculated to be 5.11 nm, same as that obtained from the synchrotron XRD data. In addition, multiple lamellar scattering peaks can be seen from the 1D WAXD profile (Figure 2.7C).

After heating to 95 °C, which was above the first endothermic peak at 88 °C but below the second endothermic peak at 105 °C (Figure 2.3A), the powder sample kept the double layer structure with the same layer spacing of 5.11 nm (Figure 2.6B, C, and D). This excluded chain-tilted structures. Note that three wide-angle (hk0) reflections became obvious and shifted to lower *q* values (Figure 2.6B). This excluded the hexatic B and smectic B (SmB) structures. Given these features, this structure was assigned as the smectic E (SmE) phase. From the point of view of unit cell structures, the K and the SmE phases have the same symmetry. However, a K phase has a long-range order (at least in one direction) whereas a SmE phase only has a quasi-long range order.

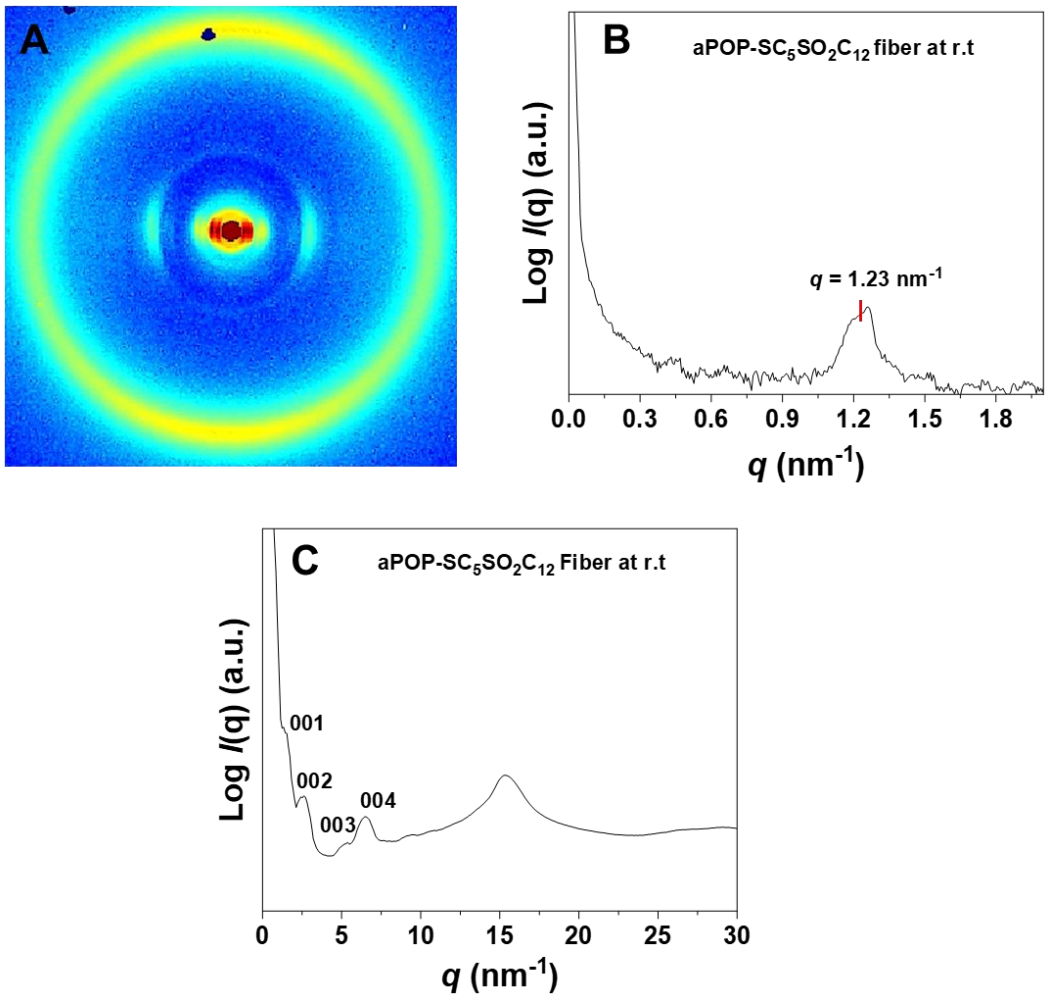

Figure 2.7. (A) 2D XRD pattern for the aPOP-$SC_5SO_2C_{12}$ fiber at room temperature (r.t.) obtained using a Xenocs Xeuss 3.0 SAXS instrument at the University of Tennessee Knoxville. The fiber direction is vertical. (B) and (C) Correspond to SAXS (B) and WAXS (C) 1D XRD profiles for the aPOP-$SC_5SO_2C_{12}$ fiber obtained by the integration of the 2D pattern (A).

This is often reflected from DSC heating and cooling curves. The K phase has a large energy barrier for nucleation and thus shows a large supercooling in DSC heating and cooling curves. However, the SmE phase has a small barrier for nucleation; therefore, no supercooling is often observed. When heating to 110 °C, which was between the second endothermic peak (105 °C) and the third endothermic peak temperature (128 °C), the (001) reflection slightly shifted to a higher *q* value with a smaller double layer spacing of 4.43 nm (Figure 2.6B). The relatively sharp (hk0) reflections in the SmE phase disappeared and the wide-angle scattering became a single broad halo with its center further shifting to lower *q* (*d* = 0.47 nm). Given the lowest heat of fusion (Table 2.2), this phase could be determined as the smectic A (SmA) structure.

Figures 2.6C and D show 1D XRD profiles for the powder sample during heating and cooling processes, respectively. Reversible K↔SmE↔SmA phase transitions were observed, consistent with the DSC study in Figure 2.3. At 160 °C, the isotropic (I) phase with two amorphous halos at 1.98 (3.2 nm) and 13.08 nm^{-1} (0.48 nm) were observed, which originated from the density fluctuation-induced disordered structure[41,42] and the average inter-side chain distance, respectively.

For iPOP-$SC_5SO_2C_{12}$, a similar structure and phase transition behavior was observed. From the fiber XRD pattern in Figure 2.8A, a layered crystalline structure was observed with the *q* ratios being 1:2:4:5:6:7:8:9 (again, the 3rd order reflection is either very weak or distinct). The lamellar spacing was 5.07 nm, again consistent with the double layer structure with all trans side chains (see the inset of Figure 2.8B). The isotactic sample exhibited a SmE phase at 100 °C (lamellar spacing: 5.08 nm) and a SmA [i.e., chiral SmA (SmA*)] phase at 110 and 115 °C (lamellar spacing: 4.53 nm); see Figure 2.8B. Upon heating and cooling, reversible K↔SmE↔SmA phase transitions were observed (Figures 2.8C and D). Comparing the structures and the LC phase transitions, the

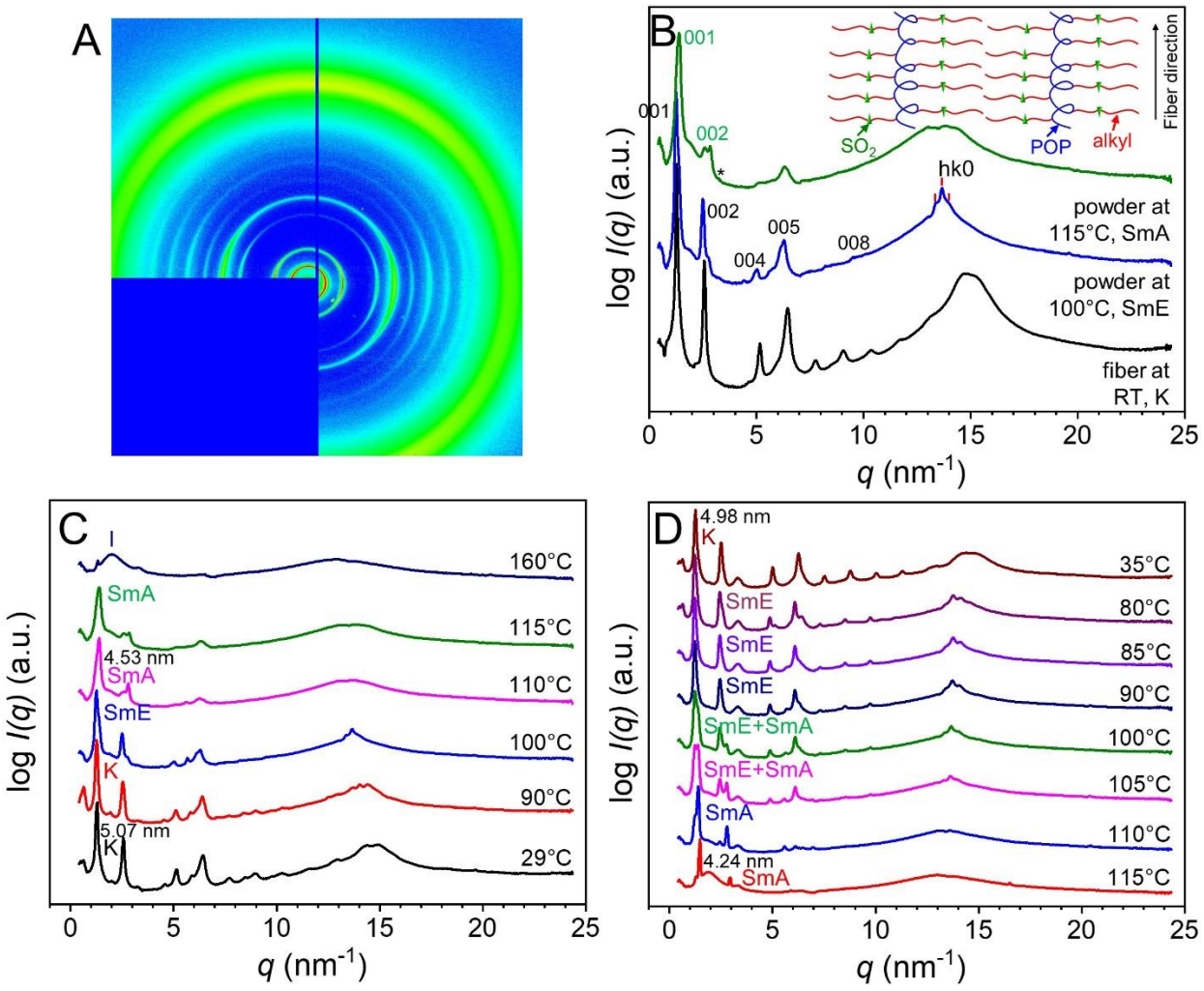

Figure 2.8. (A) 2D XRD pattern for the iPOP-$SC_5SO_2C_{12}$ fiber. The fiber direction is vertical. (B) 1D XRD profiles for the iPOP-$SC_5SO_2C_{12}$ fiber at room temperature and the powder at 100 and 115 °C. The inset shows the schematic double layer structure. The bottom panel shows the 1D XRD profiles for the iPOP-$SC_5SO_2C_{12}$ powder during (C) heating and (D) cooling processes. Peaks labeled with * in B were from the Kapton window, and they are not labeled in C and D.

differences between aPOP-$SC_5SO_2C_{12}$ and iPOP-$SC_5SO_2C_{12}$ are quite small. Therefore, we can conclude that the chiral center on the main chain has little influence on the structure and transitions when the SO_2 dipole is far away from the chiral center. After oxidizing the thioether to the sulfonyl group, the self-assembly behavior changed substantially as a result of additional strong dipole-dipole interactions among the sulfonyl groups adjacent to the main chain. Figure 2.9A shows the 2D XRD powder pattern of aPOP-$SO_2C_5SO_2C_{12}$ at room temperature, revealing a layered crystalline structure. We note here that oriented fibers were very difficult to obtain for these disulfonyl samples, possibly due to the highly crystalline structure. The lamellar spacing was 5.12 nm, again consistent with the double layer structure with the side chains perpendicular to the main chain (see the inset of Figure 2.9C). Upon heating, this K phase was stable up to 129 °C (Figure 2.3A), above which the sharp wide-angle peak around 13.88 nm^{-1} disappeared, and the sample transformed sequentially into two SmA phases with a slightly different layer spacing; 4.44 nm for the SmA′ in the temperature range of 129 to 169 °C (Figure 2.3A) and 3.81 nm in the range of 169 – 243 °C for SmA. A similar SmA' phase with partial interdigitation was also reported before for other atactic samples.[34] Above 243 °C, the sample entered the I phase with two amorphous halos at 1.86 (3.44 nm) and 12.70 nm^{-1} (0.49 nm), respectively (Figure 2.9B), slightly larger than those of aPOP-$SC_5SO_2C_{12}$ in the I phase at 160 °C (3.2 nm and 0.48 nm, respectively, Figure 2.6C). Upon cooling, reverse phase transitions were seen as shown in Figure 2.9C. Compared with aPOP-$SC_5SO_2C_{12}$ having one sulfonyl group far away from the main chain, aPOP-$SO_2C_5SO_2C_{12}$ has much higher T_m and T_i. This can be explained by the additional dipole-dipole interaction and also smaller entropy change during the phase transitions. It is not clear why the SmE phase was not observed for this sample.

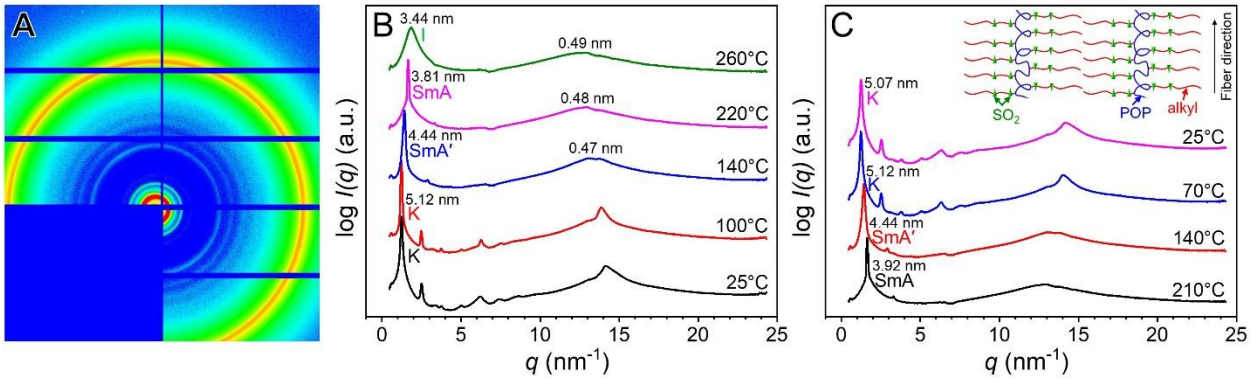

Figure 2.9. (A) 2D XRD pattern for the aPOP-$SO_2C_5SO_2C_{12}$ powder at room temperature. (B) and (C) show 1D XRD profiles for the powder sample during the heating and cooling cycle, respectively. The inset shows the schematic double layer structure.

For iPOP-$SO_2C_5SO_2C_{12}$, the T_m was pushed to even higher temperatures (186 °C) due to the regular packing of the side chains and strong dipole-dipole interactions (see Figure 2.3A). At room temperature, the layered crystalline structure was again observed (Figure 2.10A). The lamellar spacing was 5.10 nm, indicating the double layer structure (see the inset of Figure 2.10C). Upon heating to 175 °C, part of the crystals melted into the SmE phase with multiple (hk0) peaks in the wide-angle region (Figure 2.10B). Further heating to 195-215 °C, a SmA (or SmA*) phase appeared with a layer spacing of 3.69 nm. Finally at 230 °C, the I phase was obtained. Because of high T_m, the T_m to T_i range was quite small for iPOP-$SO_2C_5SO_2C_{12}$. The T_i of iPOP-$SO_2C_5SO_2C_{12}$ was in fact lower than the T_i of aPOP-$SO_2C_5SO_2C_{12}$ by more than 20 °C. For the SmA phase before the I phase, iPOP-$SO_2C_5SO_2C_{12}$ might have a lower entropy compared to aPOP-$SO_2C_5SO_2C_{12}$. If we assume that their I phases had a similar entropy, then a smaller entropy change will be expected for the isotropization of aPOP-$SO_2C_5SO_2C_{12}$. As a result, aPOP-$SO_2C_5SO_2C_{12}$ exhibited a higher T_i than iPOP-$SO_2C_5SO_2C_{12}$. Upon cooling, the reverse I→SmA→SmE→K transitions were observed (Figure 2.10C).

2.3.3. Effect of *n*-Alkyl Tail Length on Self-Assembly of Atactic and Isotactic POP-$SC_5SO_2C_8$ and POP-$SO_2C_5SO_2C_8$

From the above study, we understand that chirality is effective in changing the liquid crystalline self-assembly behavior, when the sulfonyl dipole is close to the chiral center [i.e., stronger chiral center-dipole interaction (or chiral center-induced stronger dipole-dipole interaction)]. How will the *n*-alkyl tail length affect the self-assembly of atactic and isotactic sulfonylated polyethers? To answer this question, we reduced the side-chain alkyl tail length from C_{12} to C_8. Figure 2.11A,B shows the second heating and second cooling DSC curves for atactic and isotactic POP-$SC_5SO_2C_8$ and POP-$SO_2C_5SO_2C_8$, respectively. The T_m and T_i values and the corresponding heats

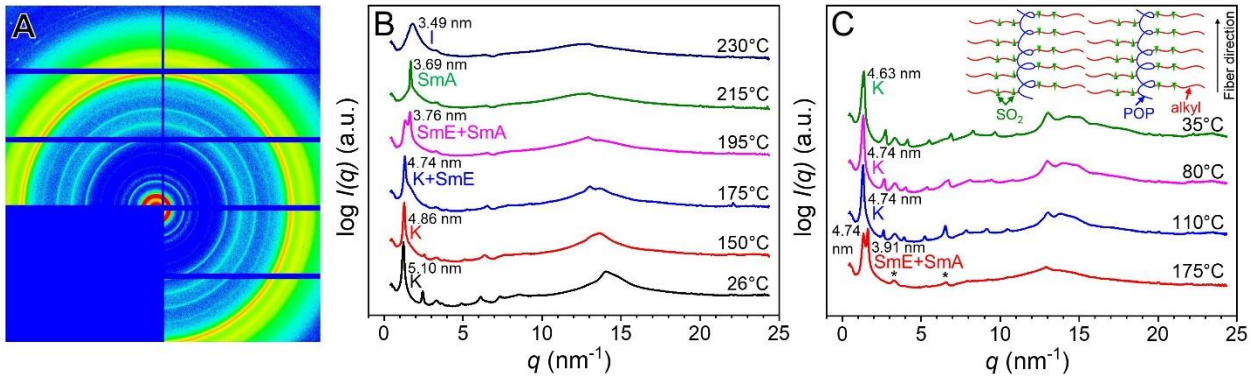

Figure 2.10. (A) 2D XRD pattern for the iPOP-$SO_2C_5SO_2C_{12}$ powder at room temperature. (B) and (C) show 1D XRD profiles for the iPOP-$SO_2C_5SO_2C_{12}$ powder during the heating and cooling processes, respectively. The inset shows the schematic double layer structure.

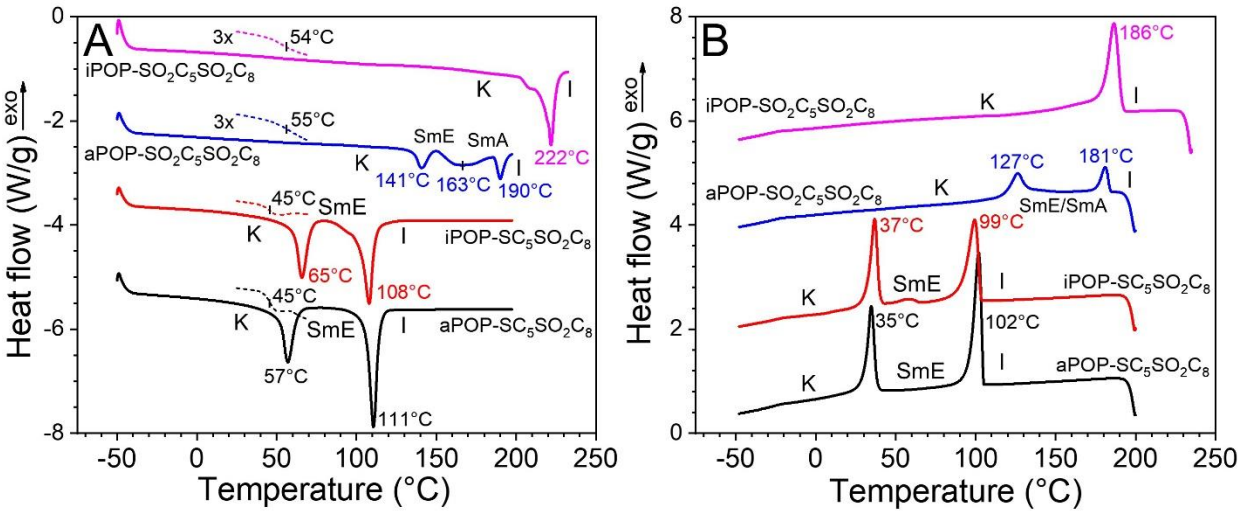

Figure 2.11. (A) DSC second heating curves for atactic and isotactic POP-$SC_5SO_2C_8$ and POP-$SO_2C_5SO_2C_8$. (B) DSC second cooling curves for atactic and isotactic POP-$SC_5SO_2C_8$ and POP-$SO_2C_5SO_2C_8$. K: crystal, SmE: smectic E, SmA: smectic A, and I: isotropic. T_g values are determined from the first heating (thin dotted lines in the insets).

of fusion are summarized in Table 2.3. From the PLM and XRD studies (see Section III in Appendix A), different mesophases were identified. For example, atactic and isotactic POP-$SC_5SO_2C_8$ exhibited K, SmE, and I phases with increasing temperature. The difference in structure and phase transitions between these two samples were small, corroborating our observations from aPOP-$SC_5SO_2C_{12}$ and iPOP-$SC_5SO_2C_{12}$ that the chiral center in the main chain had little effect on the liquid crystalline self-assembly when the sulfonyl dipole was far away. Compared with POP-$SC_5SO_2C_{12}$ samples, a notable difference is the absence of the SmA phase, which is likely because the shorter *n*-alkyl tail could not stabilize the SmA phase. In addition, the T_m and T_i values of atactic and isotactic POP-$SC_5SO_2C_8$ were lower than those of atactic and isotactic POP-$SC_5SO_2C_{12}$. These results suggested that the van der Waals interaction among the relatively long alkyl tails should also play an important role in the self-assembly. A similar phenomenon was previously reported from our group and our collaborators for atactic and isotactic POP-SO_2C_n, namely, T_m and T_i increased upon increasing the *n*-alkyl tail length.[13]

For aPOP-$SO_2C_5SO_2C_8$, the K→SmE→SmA→I phase transitions were observed upon heating (see structure identification in Section III in Appendix A). The T_m was higher whereas the T_i was lower than those for aPOP-$SO_2C_5SO_2C_{12}$. For iPOP-$SO_2C_5SO_2C_8$, only a high T_m around 222 °C was observed. From these results, it is likely that the strong dipole-dipole interaction among the disulfonyl groups overwhelmed the van der Waals interactions among the alkyl tails.

2.4. Conclusions

In this work, the effects of main-chain chirality (i.e., isotactic vs. atactic), chiral center-to-dipole distance, number of sulfonyl dipoles per side chain, and *n*-alkyl tail length on liquid crystalline

Table 2.3. Peak Phase Transition Temperatures (above the arrow) and Heats of Transition (kJ/mol, below the arrow) [a] for atactic and isotactic POP-$SC_5SO_2C_8$ and POP-$SO_2C_5SO_2C_8$

Sample	Second Heating	Second Cooling
aPOP-$SC_5SO_2C_8$	$K \xrightarrow[9.1]{57^\circ C} SmE \xrightarrow[14.5]{111^\circ C} I$	$I \xrightarrow[15.0]{102^\circ C} SmE \xrightarrow[9.6]{35^\circ C} K$
iPOP-$SC_5SO_2C_8$	$K \xrightarrow[9.6]{65^\circ C} SmE \xrightarrow[14.0]{108^\circ C} I$	$I \xrightarrow[12.5]{99^\circ C} SmE \xrightarrow[9.7]{37^\circ C} K$
aPOP-$SO_2C_5SO_2C_8$	$K \xrightarrow[2.9]{141^\circ C} SmE \xrightarrow[7.7]{163^\circ C} SmA \xrightarrow[2.7]{190^\circ C} I$	$I \xrightarrow[2.8]{181^\circ C} SmE/SmA \xrightarrow[6.9]{127^\circ C} K$
iPOP-$SO_2C_5SO_2C_8$	$K \xrightarrow[16.0]{222^\circ C} I$	$I \xrightarrow[14.4]{186^\circ C} K$

[a] Heats of transition are obtained in units of kJ/mol by peak deconvolution using Gaussian function.

self-assembly behavior of sulfonylated polyethers were investigated in our effort to seek for SmC* phases in mesogen-free comb-like polymers. The main findings are summarized below.[44]

(i) The main-chain chirality had little effect on the self-assembly of POP-$SC_5SO_2C_{12}$ and POP-$SC_5SO_2C_8$, because the sulfonyl dipole was far away from the chiral center (i.e., weak chiral center-dipole interaction). As a result, both atactic and isotactic polyethers exhibited the same phase transitions (K→SmE→SmA→I for POP-$SC_5SO_2C_{12}$ and K→SmE→I for POP-$SC_5SO_2C_8$) with similar transition temperatures.

(ii) The alkyl tail length played an important role in the self-assembly of POP-$SC_5SO_2C_{12}$ and POP-$SC_5SO_2C_8$ due to the van der Waals interactions. Namely, the longer the alkyl tails, the higher the phase transition temperatures. In addition, the longer *n*-alkyl tail (C_{12}) stabilized the SmA phase and no such mesophases were found in the POP-$SC_5SO_2C_8$ between the SmE and I phases.

(iii) After the oxidation of the thioether to the second sulfonyl group, the adjacent chiral center in iPOP-$SO_2C_5SO_2C_{12}$ significantly changed the self-assembly behavior as compared to aPOP-$SO_2C_5SO_2C_{12}$, i.e., the crystal T_m and liquid crystalline transition temperatures were shifted to much higher temperatures. Meanwhile, the dipole-dipole interactions among the disulfonyl side chains were much stronger, overwhelming the van der Waals interactions among the alkyl tails. As a result, the alkyl tail length played a less significant role in the self-assembly of disulfonylated polyethers. For iPOP-$SC_5SO_2C_8$, the changes in self-assembly after the oxidation were even more dramatic, with no liquid crystalline phases observed but the direct melting of the K to the I phase, while aPOP-$SO_2C_5SO_2C_8$ exhibited reversible K→SmE→SmA→I phase transitions.

Although strongly interacting mono- or di-sulfonyl groups could induce liquid crystalline self-assembly (SmE and SmA) in these mesogen-free polyethers, the targeted SmC* phase was not realized in the polyethers with chiral centers in the main chain, regardless of whether there were

one or two sulfonyl groups in each side chain. Note that the SmA phase in the isotactic polyethers should be chiral SmA, which has been reported to have a giant electroclinic property.[43] To achieve the SmC* phase, most studies choose to implement the chiral center in the side chains, in either the aliphatic spacer between the main chain and the dipole or the tail.[2] Meanwhile, it is important to keep the dipole close to the chiral center. Currently, we are implementing the chiral center in the side chains to induce the SmC* phase. The findings reported in this work not only enhance our understanding of the liquid crystalline self-assembly behavior of polyethers with sulfonyl side chains, but also provide a valuable guide in the design of new mesogen-free chiral liquid crystalline polymers with ferroelectric behavior.

References

1. Pirkl S.; Glogarova, M. Ferroelectric Liquid Crystals with High Spontaneous Polarization. in *Ferroelectrics - Physical Effects,* M. Lallart, Ed., InTech, 2011, Chapter 17, pp. 407-428.
2. Scherowsky, G. Ferroelectric Liquid Crystal (FLC) Polymers. in *Ferroelectric Polymers: Chemistry, Physics, and Applications,* H. S. Nalwa, Ed., Marcel Dekker, Inc., New York, 1995, Chapter 10, pp. 435-537.
3. Zentel R.; Brehmer, M. Ferroelectric Liquid-Crystalline Elastomers. *Adv. Mater.* **1994**, *6*, 598-599.
4. Brehmer, M.; Zentel, R.; Wagenblast G.; Siemensmeyer, K. Ferroelectric Liquid-Crystalline Elastomers. *Macromol. Chem. Phys.* **1994**, *195*, 1891-1904.
5. Shilov, S.; Gebhard, E.; Skupin, H.; Zentel R.; Kremer, F. Electric-Field-Induced Segmental Reorientation in Ferroelectric Liquid Crystalline Polymers and Elastomers. *Macromolecules* **1999**, *32*, 1570-1575.
6. Kremer, F.; Lehmann, W.; Skupin, H.; Tolksdorf, C.; Gebhard, E.; Zentel, R.; Kruger P.; Losche, M. Giant Lateral Electrostriction in Ferroelectric Liquid-Crystalline Elastomers. *Nature* **2001**, *410*, 447-450.
7. Yu, Y.; Maeda, T.; Mamiya J.; Ikeda, T. Photomechanical Effects of Ferroelectric Liquid-Crystalline Elastomers Containing Azobenzene Chromophores. *Angew. Chem. Int. Ed.*, **2007**, *46*, 881-883.
8. Ohm, C.; Brehmer, M.; Zentel, R. Liquid Crystalline Elastomers as Actuators and Sensors. *Adv. Mater.* **2010**, *22*, 3366-3387.

9. Luo, H.; Ma, C.; Zhou, X.; Chen, S.; Zhang, D. Interfacial Design in Dielectric Nanocomposite Using Liquid-Crystalline Polymers. *Macromolecules*, **2017**, *50*, 5132-5137.

10. Nakhmanson, S. M.; Nardelli, M. B.; Bernholc, J. Ab Initio Studies of Polarization and Piezoelectricity in Vinylidene Fluoride and BN-Based Polymers. *Phys. Rev. Lett.* **2004**, *92*(*11*), 115504.

11. Nakhmanson, S. M.; Nardelli, M. B.; Bernholc, J. Collective Polarization Effects in Beta-Polyvinylidene Fluoride and its Copolymers with Tri- and Tetrafluoroethylene. *Phys. Rev. B* **2005**, *72*(*11*), 115210.

12. Shu, Y. C.; Bhattacharya, K. Domain Patterns and Macroscopic Behaviour of Ferroelectric Materials. *Philos. Mag. B.* **2001**, *81*(*12*), 2021-2054.

13. Kwok, M.; Seymour, B.; Li, R.; Litt, M.; Zhao, B.; Zhu, L. Tacticity Effect on Mesogen-Free Liquid Crystalline Self-assembly Induced by Strong Dipole-Dipole Interactions. *Macromolecules* **2019**, *52* (10), 3601-3611.

14. Zhu, L. Exploring Strategies for High Dielectric Constant and Low Loss Polymer Dielectrics. *J. Phys. Chem. Lett.* **2014**, *5*(*21*), 3677-3687.

15. Mukherjee, P. K. Phase Transitions Among the Rotator Phases of the Normal Alkanes: A Review. *Phys. Rep.* **2015**, *588*, 1-54.

16. Bassett, D. C. Principles of Polymer Morphology. Cambridge University Press: Cambridge Eng. ; New York, 1981; p ix, 251 p.

17. Rastogi, S.; Newman, M.; Keller, A. Pressure-Induced Amorphization and Disordering on Cooling in a Crystalline Polymer. *Nature* **1991**, *353* (6339), 55-57.

18. Hattori, T.; Hikosaka, M.; Ohigashi, H. The Crystallization Behaviour and Phase Diagram of Extended-Chain Crystals of Poly(vinylidene fluoride) under High Pressure. *Polymer* **1996**, *37*(*1*), 85-91.

19. Hattori, T.; Watanabe, T.; Akama, S.; Hikosaka, M.; Ohigashi, H. The High-Pressure Crystallization Behaviours and Piezoelectricity of Extended Chain Lamellar Crystals of Vinylidene Fluoride Trifluoroethylene Copolymers with High Molar Content of Vinylidene Fluoride. *Polymer* **1997**, *38*(*14*), 3505-3511.

20. Furukawa, T. Structure and Functional Properties of Ferroelectric Polymers. *Adv. Colloid Interface Sci.* **1997**, *71-2*, 183-208.

21. Tashiro, K.; Tanaka, R. Structural Correlation between Crystal Lattice and Lamellar Morphology in the Ferroelectric Phase Transition of Vinylidene Fluoride-Trifluoroethylene Copolymers as Revealed by the Simultaneous Measurements of Wide-Angle and Small-Angle X-Ray Scatterings. *Polymer* **2006**, *47*(*15*), 5433-5444.

22. Shibaev, V. P.; Talroze, R. V.; Karakhanova, F. I.; Plate, N. A. Thermotropic Liquid-Crystalline Polymers. 2. Polymers with Amino-Acid Fragments in the Side-Chains. *J. Polym. Sci. Polym. Chem.* **1979**, *17*(*6*), 1671-1684.

23. Plate, N. A.; Shibaev, V. P. *Comb-Shaped Polymers and Liquid Crystals*. Springer, Boston, 1987.

24. Aharoni, S. M. Hydrogen-Bonded Highly Regular Strictly Alternating Aliphatic Aromatic Liquid-Crystalline Poly(Ester Amides). *Macromolecules* **1988**, *21* (7), 1941-1961.

25. Zhang, T. H.; Litt, M. H.; Rogers, C. E. Synthesis and Dielectric Analysis of Aliphatic Poly(carbonate-sulfone)s Based on 1,4-Bis(3-hydroxypropylsulfonyl)butane. *J. Polym. Sci. Polym. Chem.* **1994**, *32*(*15*), 2809-2816.

26. Zhang, T. H.; Litt, M. H.; Rogers, C. E. Dipole-Dipole Interaction Directed Liquid-Crystalline Polymers. 1. Aliphatic Poly(carbonate-sulfone)s Based on 1,3-bis(3-hydroxypropylsulfonyl)propane. *J. Polym. Sci. Polym. Chem.* **1994**, *32*(*12*), 2291-2300.

27. Zhang, T. H.; Litt, M. H.; Rogers, C. E., Synthesis and Characterization of Poly(ester-sulfone)s. *J. Polym. Sci. Polym. Chem.* **1994**, *32*(*7*), 1351-1360.

28. Zhang, T. H.; Litt, M. H.; Rogers, C. E. Synthesis and Characterization of Poly(urethane-sulfone)s. *J. Polym. Sci. Polym. Chem.* **1994**, *32* (8), 1531-1537.

29. Lee, J. C.; Litt, M. H. Crystallization Behavior of Poly(oxyethylene)s with (Alkylsulfonyl)methyl Side Groups. *J. Ind. Eng. Chem.* **1999**, *5*(2), 155-159.

30. Lee, J. C.; Litt, M. H.; Rogers, C. E. Synthesis and Properties of (Alkylthio)methyl-Substituted Poly(oxyalkylene)s and (Alkylsulfonyl)methyl-Substituted Poly(oxyalkylene)s. *Macromolecules* **1997**, *30*(*13*), 3766-3774.

31. Lee, J. C.; Litt, M. H.; Rogers, C. E. Synthesis and Properties of Liquid Crystalline Polymers Containing an Oxyethylene Backbone and *n*-Octylsulfonylmethyl Side Groups. *Macromolecules* **1998**, *31*(*8*), 2440-2446.

32. Lee, J. C.; Oh, K.; Lee, H. B.; Kim, Y. G.; Jho, J. Y.; Kwak, S. Y.; Park, S. Y.; Farmer, B. L. Synthesis and Mesomorphic Properties of Poly(oxyethylene) with [(6-Heptylsulfonyl)hexylthio]methyl Side Groups. *Macromol. Rapid Commun.* **2001**, *22*(*11*), 815-819.

33. Park, S. Y.; Farmer, B. L.; Lee, J. C. The Structures of Poly(oxyethylene)s Having Sulfone Groups in the Side Chains. *Polymer* **2002**, *43*(*1*), 177-183.

34. Lee, J. C.; Han, S. H.; Cha, S. H.; Park, S. Y.; Farmer, B. L. Synthesis and Dipole-Dipole Interaction-Induced Mesomorphic Behavior of Poly(oxyethylene)s Containing (*n*-

Octylsulfonyl)alkylthiomethyl or (*n*-Octylsulfonyl)alkylsulfonylmethyl Side Groups. *Polymer* **2003**, *44*(*24*), 7413-7425.

35. Kim, J. U.; Lee, J. C. Synthesis and Liquid Crystalline Properties of Poly(ethylene oxide) Brushes with Amphiphilic Side Groups. *Macromol. Chem. Phys.* **2005**, *206*(*9*), 951-960.

36. Kim, B. G.; Moon, J. K.; Sohn, E. H.; Lee, J. C.; Yeo, J. K. Polysiloxanes Containing Alkyl Side Groups: Synthesis and Mesomorphic Behavior. *Macromol. Res.* **2008**, *16*(*1*), 36-44.

37. Kim, B. G.; Chung, J. S.; Sohn, E. H.; Kwak, S. Y.; Lee, J. C. Comb-Like Fluorinated Polystyrenes Having Different Side Chain Interconnecting Groups. *Macromolecules* **2009**, *42*(*9*), 3333-3339.

38. Lagerwall, S. T. Ferroelectric and Antiferroelectric Liquid Crystals. Wiley-VCH: Weinheim ; New York, 1999; p xviii, 427 p.

39. Brochu, S.; Ampleman, G. Synthesis and Characterization of Glycidyl Azide Polymers Using Isotactic and Chiral Poly(epichlorohydrin)s. *Macromolecules* **1996**, *29*(*17*), 5539-5545.

40. Zhao, Y. L.; Jones, W. H.; Monnat, F.; Wudl, F.; Houk, K. N. Mechanisms of Thermal Decompositions of Polysulfones: A DFT and CBS-QB3 Study. *Macromolecules* **2005**, *38*(*24*), 10279-10285.

41. Sakamoto, N.; Hashimoto, T. Order-Disorder Transition of Low-Molecular-Weight Polystyrene-*block*-Polyisoprene. 1. SAXS Analysis of 2 Characteristic Temperatures. *Macromolecules* **1995**, *28*(*20*), 6825-6834.

42. Sakamoto, N.; Hashimoto, T. Ordering Dynamics of a Symmetric Polystyrene-*block*-Polyisoprene. 2. Real-space analysis on the formation of lamellar microdomain. *Macromolecules* **1998**, *31*(*12*), 3815-3823.

43. Nishiyama, S.; Ouchi, Y.; Takezoe, H.; Fukuda, A. Giant Electroclinic Effect in Chiral Smectic-a Phase of Ferroelectric Liquid-Crystals. *Jpn. J. Appl. Phys.* **1987**, *26*(*11*), L1787-L1789.

44. The work described in this Chapter has been published in *Polymer Chemistry* as an article. Bohannon, C. A.;† Kwok, M.-H.;†, Li, R. P.; Zhu, L.; Zhao, B. Effects of Tacticity and Chiral Center-to-Dipole Distance on Mesogen-Free Liquid Crystalline Self-Assembly of Sulfonyl-Containing Comb-like Polymers. *Polymer Chemistry* **2020**, *11*, 3018-3031. † These authors contributed equally to this work. https://pubs.rsc.org/en/content/articlelanding/2020/py/d0py00199f#!divAbstract.

Appendix A

for

Chapter 2: Effects of Tacticity and Chiral Center-to-Dipole Distance on Mesogen-Free Liquid Crystalline Self-Assembly of Sulfonyl-Containing Comb-Like Polymers

A.I. Syntheses of Starting Materials

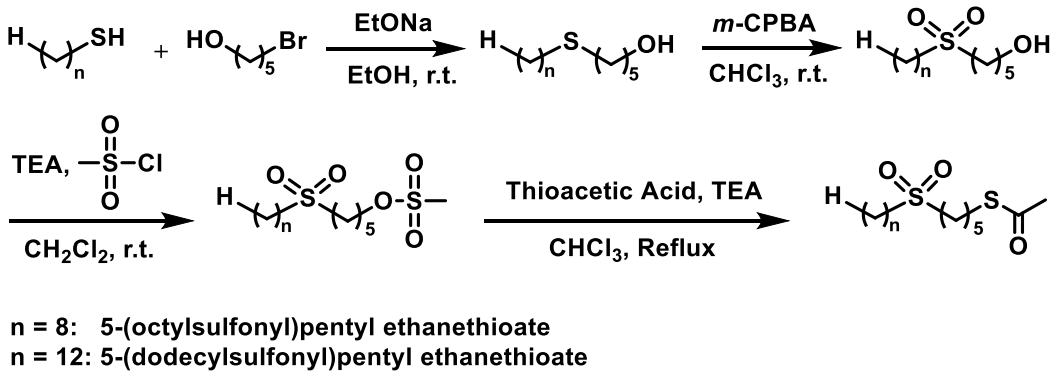

Scheme A.1. Synthesis of 5-(Octylsulfonyl)pentyl Ethanethioate and 5-(Dodecylsulfonyl)pentyl Ethanethioate.

Synthesis of 5-(*n*-Alkylthio)pentanol. *n*-Octanethiol (5.892 g, 40.3 mmol) and sodium ethoxide (5.523 g, 81.2 mmol, delivered from a stock solution of sodium ethoxide in ethanol with a concentration of 11.3 wt%) were weighed into a 250-mL two-necked round bottom flask equipped with an addition funnel and a magnetic stir bar. The flask was placed under an N_2 environment, and the mixture was stirred for 2 h at room temperature. 5-Bromopentanol (6.727 g 40.3 mmol) was added dropwise into the flask through the addition funnel, and the reaction mixture was stirred at room temperature overnight. The solvent was removed by rotary evaporation under reduced pressure, and the concentrated mixture was dissolved in dichloromethane (15 mL). The mixture was then transferred to a 250 mL separatory funnel and washed with 3 M HCl (100 mL × 2). The organic phase was dried with anhydrous sodium sulfate. After filtering off the solid and removing the solvent using a rotavapor and under vacuum, a pale-yellow liquid was obtained. The product was further purified by silica gel chromatography using a mixture of ethyl acetate and hexane (1:3, v/v) initially and then a mixture of dichloromethane and methanol (1:1, v/v) to elute the product out from the column. The solvents were evaporated and the product was dried under high vacuum, yielding a clear viscous liquid (8.001 g, 85.0% yield). ^{1}H NMR ($CDCl_3$, 500 MHz),

δ (ppm) = 3.69 – 3.62 (m, -C*H*$_2$OH, 2H), 2.54 – 2.48 (m, -*CH*$_2$SC*H*$_2$- 4H), 1.65 – 1.54 (m, -C*H*$_2$CH$_2$SCH$_2$C*H*$_2$CH$_2$C*H*$_2$CH$_2$OH 6H), 1.51 – 1.43 (m, -C*H*$_2$(CH$_2$)$_2$OH, 2H), 1.40 – 1.20 (m, CH$_3$(C*H*$_2$)$_5$CH$_2$-, 10H), 0.87 (t, C*H*$_3$CH$_2$-, 3H). ^{13}C NMR (CDCl$_3$, 126 MHz), δ (ppm) = 62.54, 32.21, 32.10, 31.97, 31.72, 29.61, 29.35, 29.12, 29.09, 28.85, 24.97, 22.54, 13.98.

5-(*n*-Dodecylthio)pentanol was synthesized using the same procedure as for 5-(*n*-octylthio) pentanol. Instead of column chromatography for 5-(octylthio)pentanol, 5-(*n*-dodecylthio)pentanol was purified by recrystallization in hexanes and obtained as a white solid after drying under high vacuum (94.4%). ^{1}H NMR (CDCl$_3$, 600 MHz), δ (ppm) = 3.64 (t, -C*H*$_2$OH, 2H), 2.54 – 2.46 (m, -*CH*$_2$SC*H*$_2$-, 4H), 1.65 – 1.52 (m, -C*H*$_2$CH$_2$SCH$_2$C*H*$_2$CH$_2$C*H*$_2$ CH$_2$OH, 6H), 1.50 – 1.44 (m, -C*H*$_2$(CH$_2$)$_2$OH, 2H), 1.40 – 1.20 (m, CH$_3$(C*H*$_2$)$_9$CH$_2$-, 18H), 0.87 (t, C*H*$_3$CH$_2$-, 3H). ^{13}C NMR (CDCl$_3$, 151 MHz), δ (ppm) = 62.77, 32.32, 32.19, 32.05, 31.89, 29.70, 29.63, 29.61, 29.58, 29.52, 29.43, 29.32, 29.24, 28.94, 25.03, 22.66, 14.09.

Synthesis of 5-(*n*-Alkylsulfonyl)pentanol. 5-(*n*-Octylthio)pentanol (8.001 g, 34.4 mmol) was weighed into a 250 mL two-necked round bottom flask fitted with a magnetic stir bar and an addition funnel. *meta*-Chloroperoxybenzoic acid (*m*-CPBA, 24.441 g, 99.1 mmol) was added into a separate 150 mL Erlenmeyer flask and dissolved with chloroform (50 mL). The *m*-CPBA solution was added dropwise into the flask in a period of 15 min, and the mixture was stirred at room temperature for 3 h. The reaction mixture was transferred into a separatory funnel and washed with 1 M NaOH (100 mL × 2). The organic layer was collected in an Erlenmeyer flask and dried with anhydrous sodium sulfate. After the solid was filtered off and the solvent was evaporated, a white crystalline powder was obtained as the pure product (7.436 g, 81.7% yield). ^{1}H NMR (CDCl$_3$, 300 MHz), δ (ppm) = 3.67 (t, -C*H*$_2$OH, 2H), 3.05 – 2.83 (m, -*CH*$_2$SO$_2$C*H*$_2$-, 4H), 2.02 – 1.72 (m, -C*H*$_2$CH$_2$SO$_2$CH$_2$C*H*$_2$-, 4H), 1.65 – 1.19 (m, -(C*H*$_2$)$_2$CH$_2$OH,

$CH_3(CH_2)_5CH_2$-, 14H), 0.88 (t, CH_3CH_2-, 3H). ^{13}C NMR ($CDCl_3$, 126 MHz), δ (ppm) = 61.90, 52.68, 52.41, 31.81, 31.54, 28.88, 28.77, 28.35, 24.69, 22.43, 21.78, 21.56, 13.91.

5-(*n*-Dodecylsulfonyl)pentanol was prepared and purified in the same manner as for 5-(*n*-octylsulfonyl)pentanol. Yield: 69.0%. ^{1}H NMR ($CDCl_3$, 600 MHz), δ (ppm) = 3.65 (t, -CH_2OH, 2H), 2.98 – 2.90 (m, -$CH_2SO_2CH_2$- 4H), 1.91 – 1.78 (m, -$CH_2CH_2SO_2CH_2CH_2$-, 4H), 1.63 – 1.20 (m, -$(CH_2)_2CH_2OH$, $CH_3(CH_2)_9CH_2$-, 22H), 0.87 (t, CH_3CH_2-, 3H). ^{13}C NMR (151 MHz, $CDCl_3$), δ (ppm) = 62.82, 52.83, 52.52, 31.94, 31.85, 29.54, 29.53, 29.45, 29.27, 29.22, 29.02, 28.47, 24.81, 22.63, 21.91, 21.68, 14.06.

Synthesis of 5-(*n*-Alkylsulfonyl)pentyl Methanesulfonate. 5-(*n*-Octylsulfonyl)pentanol (7.436 g, 32.0 mmol) and triethylamine (4.321 g, 42.7 mmol) were added into a 150 mL two-necked round bottom flask equipped with a magnetic stir bar and an addition funnel and dissolved in dichloromethane (20 mL). A solution of methanesulfonyl chloride (4.225 g, 36.9 mmol) in dichloromethane (20 mL) was transferred to the addition funnel and added dropwise for 15 min. The reaction mixture was stirred overnight at room temperature and then decanted into a separatory funnel. After washing with 3 M HCl (30 mL × 3) and a saturated sodium bicarbonate solution (30 mL × 3), the organic phase was dried with anhydrous sodium sulfate. The solid was filtered off, and the volatiles were removed first by rotary evaporation and then under high vacuum. The product was obtained as a pale-yellow liquid (9.356 g, 97.1% yield). ^{1}H NMR ($CDCl_3$, 300 MHz), δ (ppm) = 4.23 (t, -$CH_2OSO_2CH_3$, 2H), 3.00 (s, -OSO_2CH_3, 3H), 2.98 – 2.90 (m, -$CH_2SO_2CH_2$-, 4H), 1.94 – 1.74 (m, -$CH_2CH_2SO_2CH_2CH_2CH_2CH_2$ $CH_2OSO_2CH_3$, 6H), 1.64 – 1.53 (m, -$CH_2(CH_2)_2OSO_2CH_3$, 2H), 1.48 – 1.21 (m, $CH_3(CH_2)_5CH_2$-, 10H), 0.86 (t, -CH_2CH_3, 3H). ^{13}C NMR (75 MHz, $CDCl_3$), δ (ppm) = 69.22, 52.91, 52.11, 37.31, 31.58, 28.91, 28.81, 28.59, 28.39, 24.46, 22.48, 21.86, 21.23, 13.96.

5-(*n*-Dodecylsulfonyl)pentyl methanesulfonate was prepared and purified in the same manner as for 5-(*n*-octylsulfonyl)pentyl methanesulfonate. Yield: 87.4%. ^{1}H NMR ($CDCl_3$, 600 MHz), δ (ppm) = 4.24 (t, -C*H*$_2$OSO$_2$CH$_3$, 2H), 3.01 (s, -OSO$_2$C*H*$_3$, 3H), 2.98 – 2.91 (m, -*CH*$_2$SO$_2$C*H*$_2$-, 4H), 1.93 – 1.78 (m, C*H*$_2$CH$_2$SO$_2$CH$_2$C*H*$_2$CH$_2$C*H*$_2$CH$_2$OSO$_2$CH$_3$, 6H), 1.64 – 1.58 (m, -C*H*$_2$(CH$_2$)$_2$OSO$_2$CH$_3$, 2H), 1.46 – 1.21 (m, CH$_3$(C*H*$_2$)$_9$CH$_2$-, 18H), 0.87 (t, -CH$_2$C*H*$_3$, 3H). ^{13}C NMR (151 MHz, $CDCl_3$), δ (ppm) = 69.18, 53.04, 52.19, 37.42, 31.87, 29.56, 29.55, 29.46, 29.29, 29.23, 29.03, 28.68, 28.48, 24.56, 22.65, 21.95, 21.29, 14.08.

Synthesis of 5-(*n*-Alkylsulfonyl)pentyl Ethanethioate. 5-(*n*-Octylsulfonyl)pentyl methanesulfonate (9.356 g, 27.3 mmol) and triethyl amine (5.044 g, 49.8 mmol) were added along with chloroform (15 mL) into a 100 mL single-necked round bottom flask with a magnetic stir bar. The flask was then fitted with an addition funnel. After thioacetic acid (0.847 g, 55.8 mmol) in chloroform (10 mL) was added dropwise to the flask, the addition funnel was replaced with a reflux condenser and a gas flow control adaptor. The mixture was then heated in an oil bath to 70 ℃ and refluxed for 36 h. The reaction mixture was transferred into a separatory funnel; the organic phase was washed with 1 M HCl (30 mL × 3) and a saturated sodium bicarbonate solution (30 mL × 3). The organic phase was then dried with anhydrous sodium sulfate. After the removal of the solid and the volatiles, a deep red solid was obtained. Recrystallization of the product was performed by adding the crude product and *n*-hexane (60 mL) into a 250 mL Erlenmeyer flask, heating the mixture at 65 ℃ to fully dissolve the solid, and allowing it to cool naturally to room temperature. The flask was then placed in a freezer with a temperature of -14 ℃ overnight. The precipitated crystals were collected using vacuum filtration and washing with cold hexanes (30 mL × 2). The recrystallization was repeated one more time; the product was subsequently dried under high vacuum to yield a light pink crystal (5.000 g, 57% yield). ^{1}H NMR

(300 MHz, chloroform-*d*), δ (ppm) = 2.97 – 2.83 (m, -$CH_2SO_2CH_2$-, -$CH_2SC(O)CH_3$, 6H), 2.31 (s, -$CH_2SC(O)CH_3$, 3H), 1.91 – 1.75 (m, -$CH_2CH_2SO_2CH_2CH_2$ -, 4H), 1.68 – 1.17 (m, -$(CH_2)_2CH_2SC(O)CH_3$, $CH_3(CH_2)_5CH_2$-, 14H), 0.87 (t, CH_3CH_2-, 3H). ^{13}C NMR (126 MHz, $CDCl_3$), δ (ppm) = 195.88, 52.98, 52.52, 31.81, 30.76, 29.22, 29.14, 29.04, 28.67, 28.63, 27.64, 22.70, 22.08, 21.60, 14.18. MS: m/z calc $C_{15}H_{30}O_3S_2$ $[M+H]^+$: 323.1636; found: 323.1669; mass error: 3.3 ppm.

5-(*n*-Dodecylsulfonyl)pentyl ethanethioate was prepared and purified in the same manner as for 5-(*n*-octylsulfonyl)pentyl)ethanethioate. Yield: 58.9%. ^{1}H NMR (500 MHz, chloroform-*d*), δ (ppm) = 2.95 – 2.90 (m, -$CH_2SO_2CH_2$-, 4H), 2.86 (t, ,-$CH_2SC(O)CH_3$, 2H), 2.31 (s, -$CH_2SC(O)CH_3$, 3H), 1.89 – 1.77 (m, -$CH_2CH_2SO_2CH_2CH_2$-, 4H), 1.65 – 1.58 (m, -$CH_2CH_2SC(O)CH_3$, 2H), 1.55 – 1.48 (m, -$CH_2(CH_2)_2SC(O)CH_3$, 2H), 1.45 – 1.39 (m, -$CH_2(CH_2)_2SO_2CH_2$-, 2H), 1.34 – 1.19 (m, $CH_3(CH_2)_8CH_2$-, 16H), 0.87 (t, CH_3CH_2-, 3H). ^{13}C NMR (126 MHz, $CDCl_3$), δ (ppm) = 195.86, 52.96, 52.49, 32.00, 30.74, 29.69, 29.68, 29.60, 29.42, 29.36, 29.20, 29.17, 28.65, 28.62, 27.62, 22.78, 22.06, 21.58, 14.22. MS: m/z calc $C_{19}H_{38}O_3S_2$ $[M+H]^+$: 379.2341; found: 379.2343; mass error: 0.5 ppm.

Synthesis of Isotactic Poly[(*R*)-(-)-epichlorohydrin] (iPECH) by Ring Opening Polymerization. The ring opening polymerization of (*R*)-(-)-epichlorohydrin was performed in a nitrogen-filled glovebox with flame dried glassware. A representative polymerization is shown in the following as an example. (*R*)-(-)-Epichlorohydrin (1.50 mL, 19.2 mmol) and modified methylaluminoxane (MMAO-12, 1.2 mL of the solution in toluene with an aluminum concentration of 7 wt %, corresponding to approximately 73 mg aluminum) were added via micropipette into a 10 mL Schlenk tube that contained dry diethyl ether (5 mL). The polymerization mixture was stirred with a magnetic stir bar at room temperature in the glove box.

Shortly after the addition of MMAO-12, a precipitate started to appear and gradually increased in quantity as the reaction proceeded. After 24 h, the Schlenk tube was removed from the glovebox, and 2,4-pentadione (2 mL) and methanol (3 mL) were added while stirring to extract the aluminoxane species from the precipitated polymer. After stirring at room temperature for an additional 2 h, the mixture was poured into methanol (30 mL), and the solid polymer was collected by vacuum filtration using a Büchner funnel. The polymer was soaked with methanol (20 mL) and filtered again. This process was repeated once more to purify the polymer. Finally, the washed polymer was dried under vacuum, yielding a white solid (0.287 g, 19.1% yield). ^{1}H NMR (300 MHz, chloroform-*d*), δ (ppm) = 3.80 – 3.50 (m, -C*H*$_2$C*H*(C*H*$_2$Cl)O-, 5H).

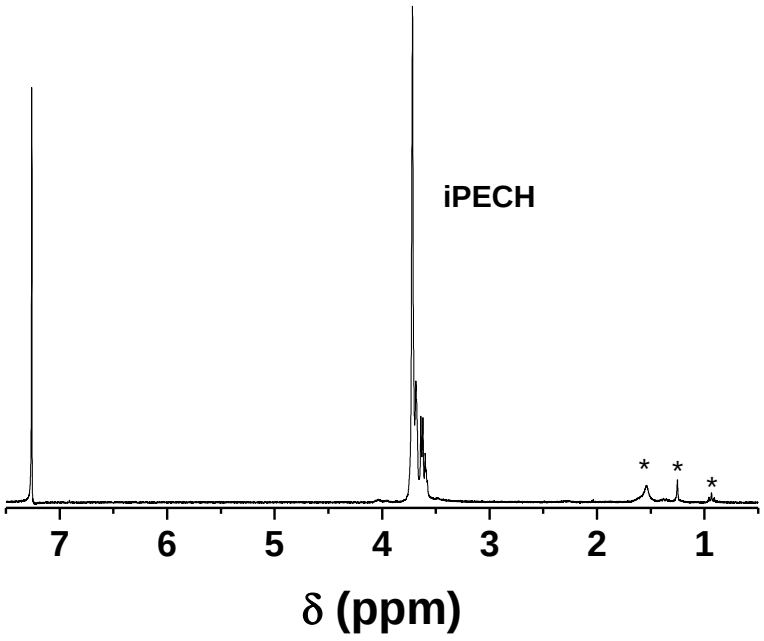

Figure A.1. ^{1}H NMR spectrum of iPECH in $CDCl_3$. Peaks labeled with * are from impurities.

II. ^{1}H and ^{13}C NMR, SEC, and TGA Characterization Data for Mono- and Di-sulfonylated Polyethers

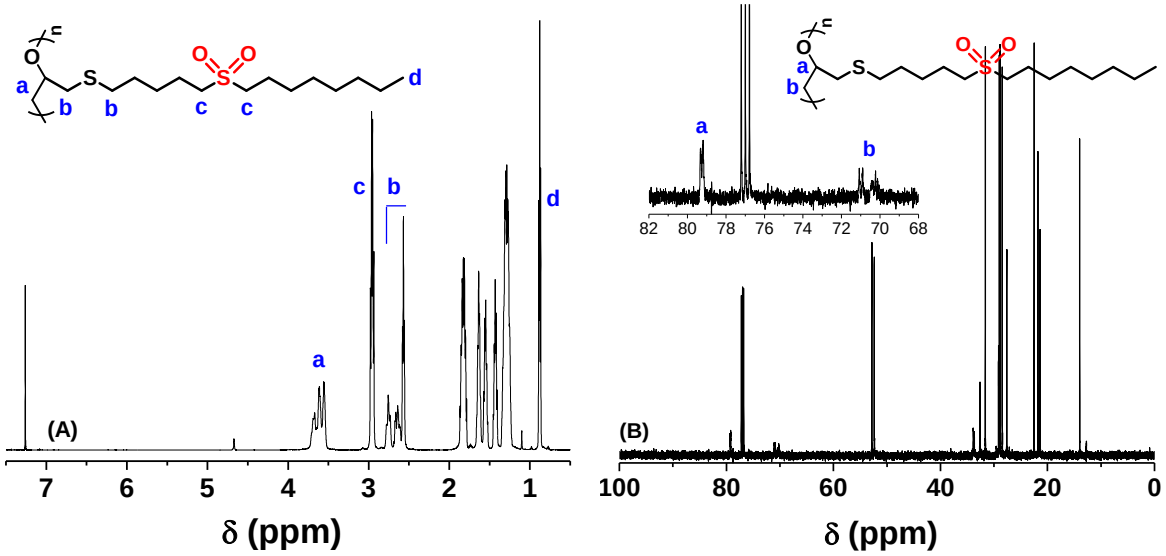

Figure A.2. (A) ^{1}H and (B) ^{13}C NMR spectra of aPOP-$SC_5SO_2C_8$ in $CDCl_3$.

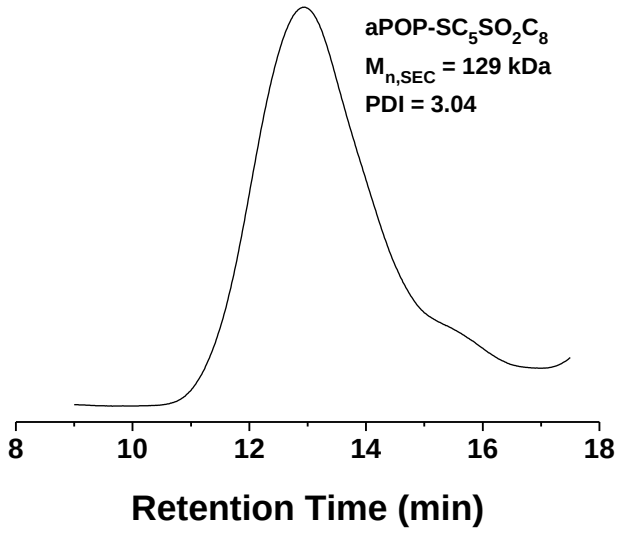

Figure A.3. Size exclusion chromatography curve of aPOP-$SC_5SO_2C_8$ using $CHCl_3$ as eluent.

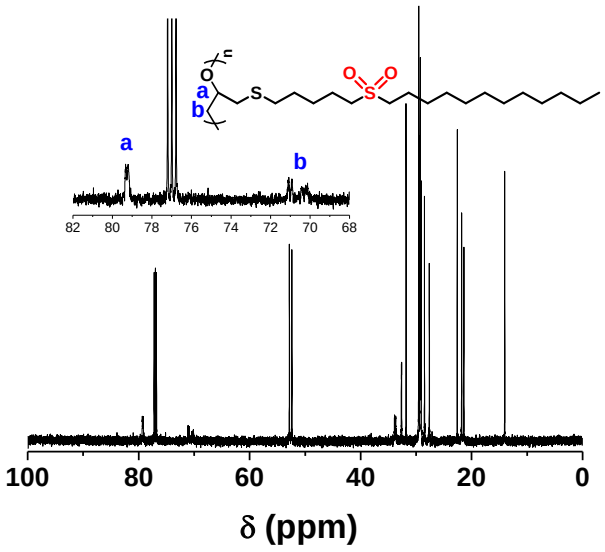

Figure A.4. ^{13}C NMR spectrum of aPOP-$SC_5SO_2C_{12}$ in $CDCl_3$.

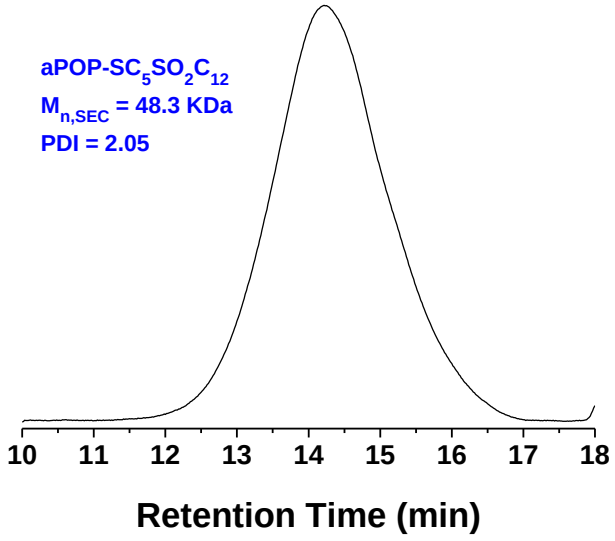

Figure A.5. Size exclusion chromatography curve of aPOP-$SC_5SO_2C_{12}$ using $CHCl_3$ as eluent.

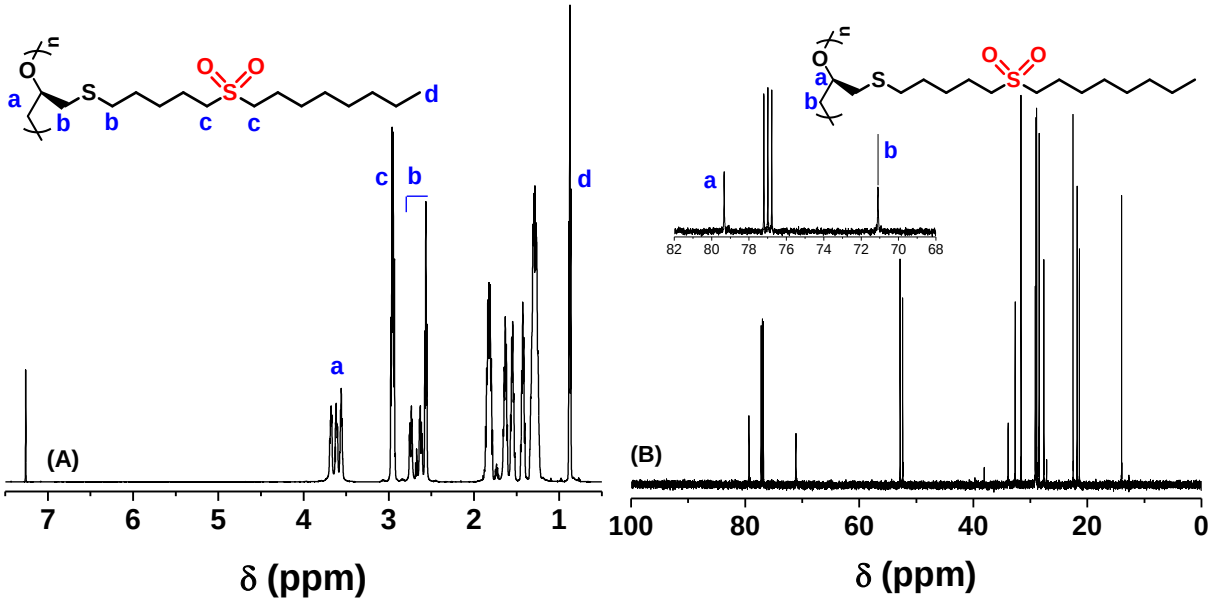

Figure A.6. (A) ^{1}H and (B) ^{13}C NMR spectra of iPOP-$SC_5SO_2C_8$ in $CDCl_3$.

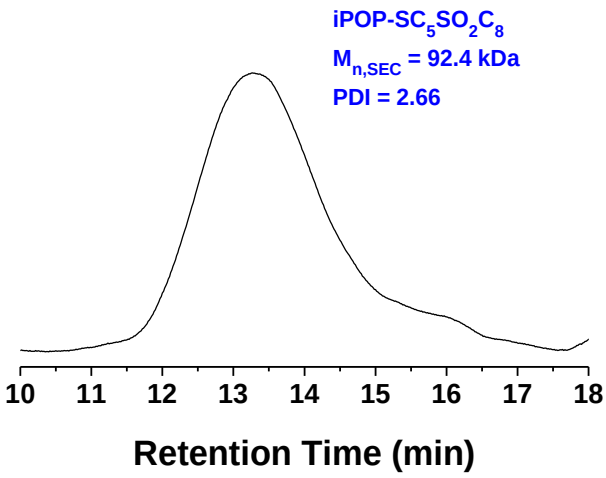

Figure A.7. Size exclusion chromatography curve of iPOP-$SC_5SO_2C_8$ using $CHCl_3$ as eluent.

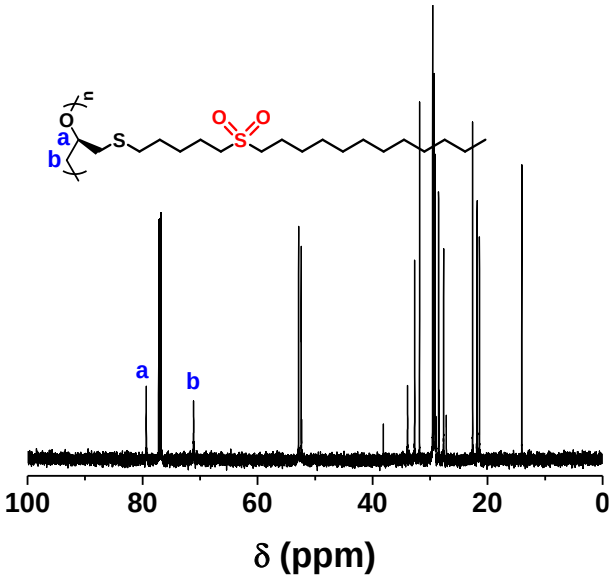

Figure A.8. ^{13}C NMR spectrum of iPOP-$SC_5SO_2C_{12}$ in $CDCl_3$.

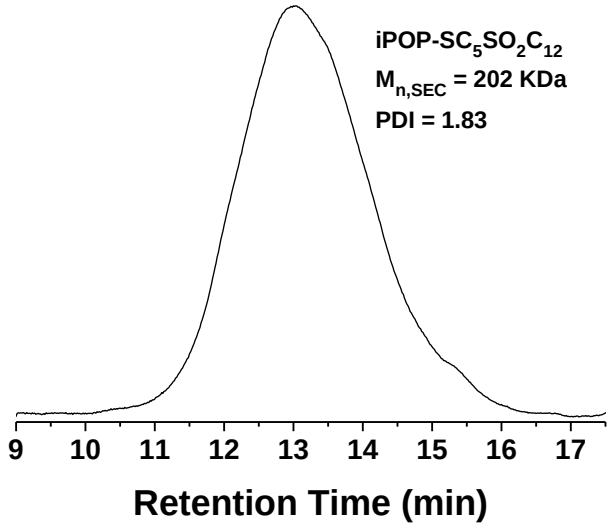

Figure A.9. Size exclusion chromatography curve of iPOP-$SC_5SO_2C_{12}$ using $CHCl_3$ as eluent.

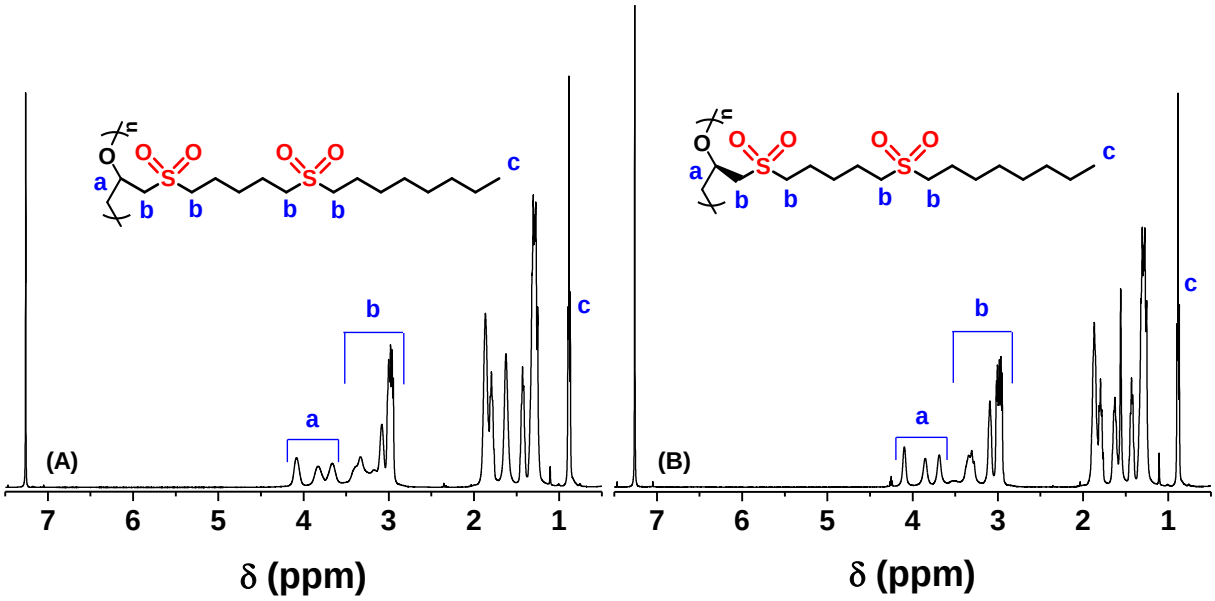

Figure A.10. ^{1}H NMR spectra of (A) aPOP-$SO_2C_5SO_2C_8$ and (B) iPOP-$SO_2C_5SO_2C_8$ in $CDCl_3$.

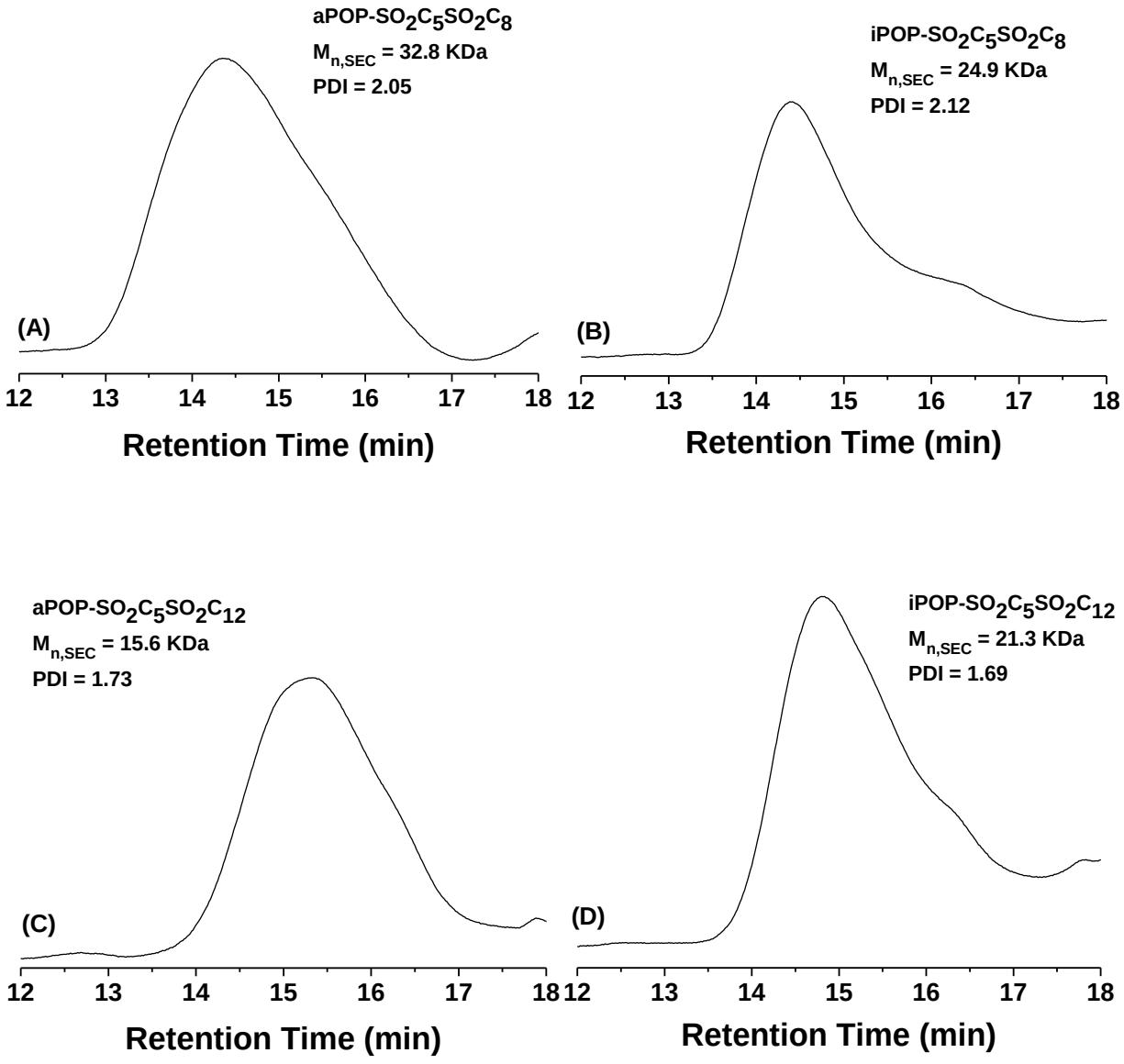

Figure A.11. Size exclusion chromatography curves of (a) aPOP-$SO_2C_5SO_2C_8$, (b) iPOP-$SO_2C_5SO_2C_8$, (C) aPOP-$SO_2C_5SO_2C_{12}$, and (D) iPOP-$SO_2C_5SO_2C_{12}$ using $CHCl_3$ as eluent.

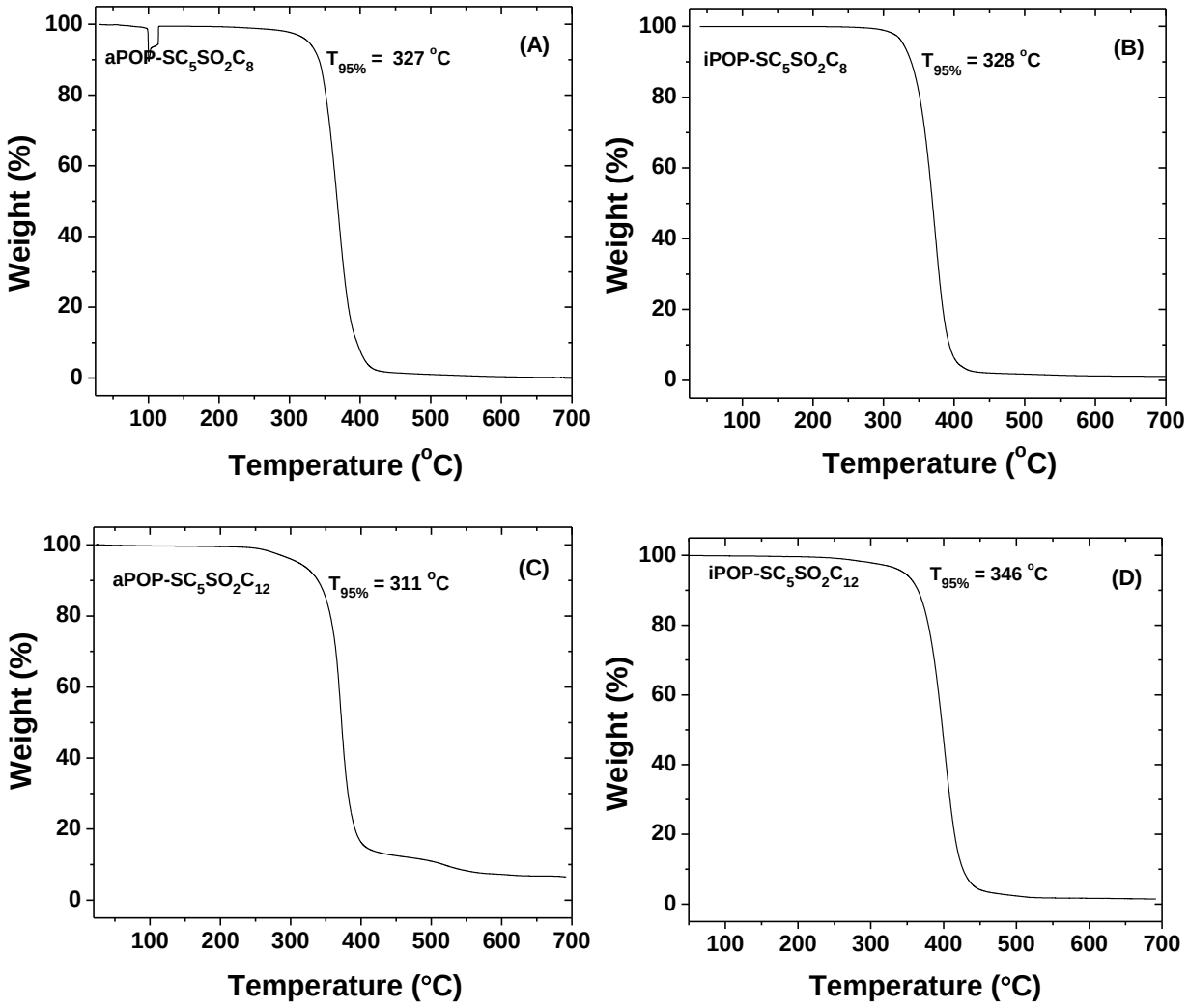

Figure A.12. Thermogravimetric analysis (TGA) curves of (A) aPOP-$SC_5SO_2C_8$, (B) iPOP-$SC_5SO_2C_8$, (C) aPOP-$SC_5SO_2C_{12}$, and (D) iPOP-$SC_5SO_2C_{12}$. TGA was performed in a dry N_2 atmosphere at a heating rate of 20 °C/min.

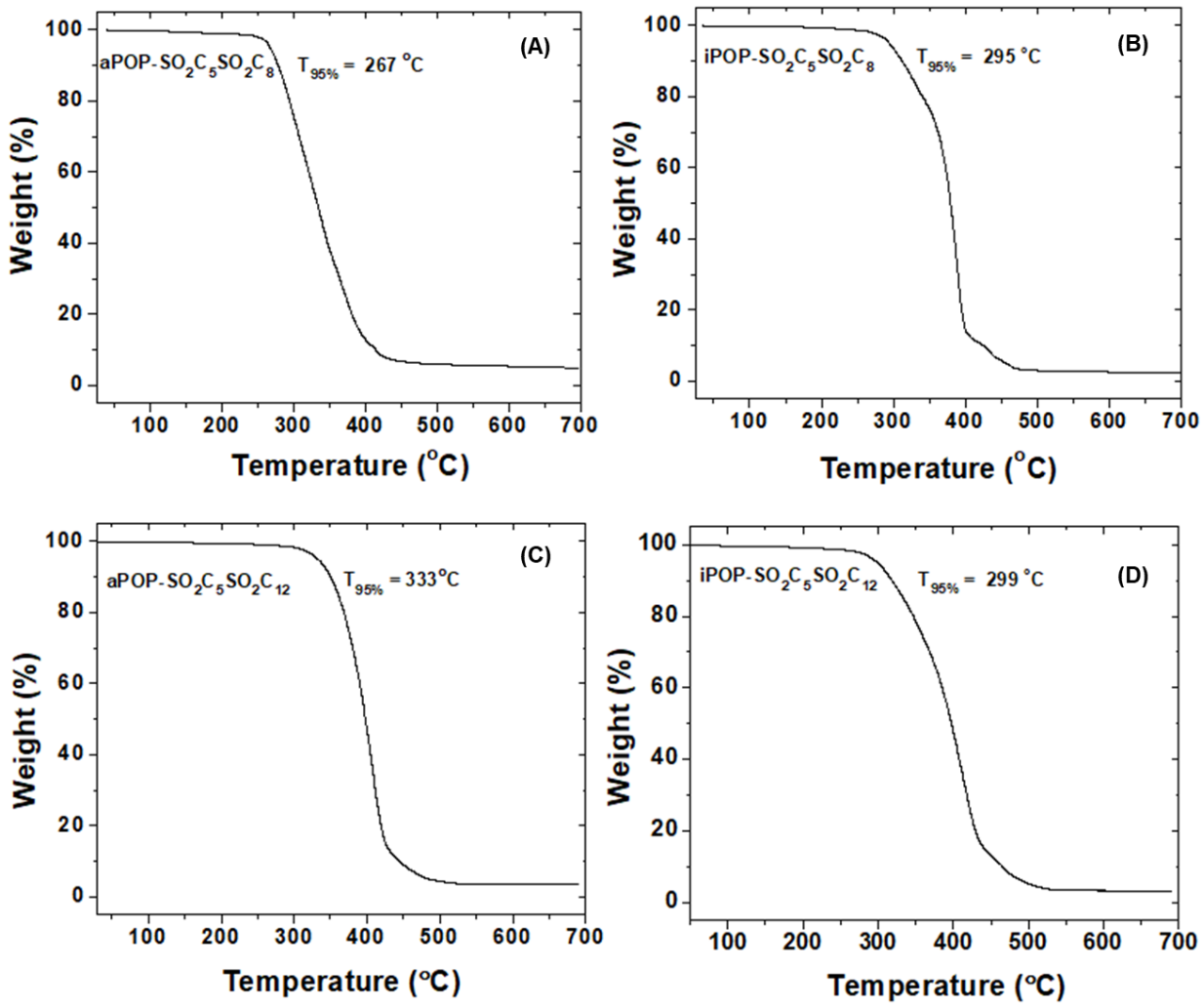

Figure A.13. Thermogravimetric analysis (TGA) curves of (A) aPOP-$SO_2C_5SO_2C_8$, (B) iPOP-$SO_2C_5SO_2C_8$, (C) aPOP-$SO_2C_5SO_2C_{12}$, and (D) iPOP-$SC_5SO_2C_{12}$. TGA was performed in a dry N_2 atmosphere at a heating rate of 20 °C/min.

III. PLM and XRD of Atactic and Isotactic POP-$SC_5SO_2C_8$ and POP-$SO_2C_5SO_2C_8$

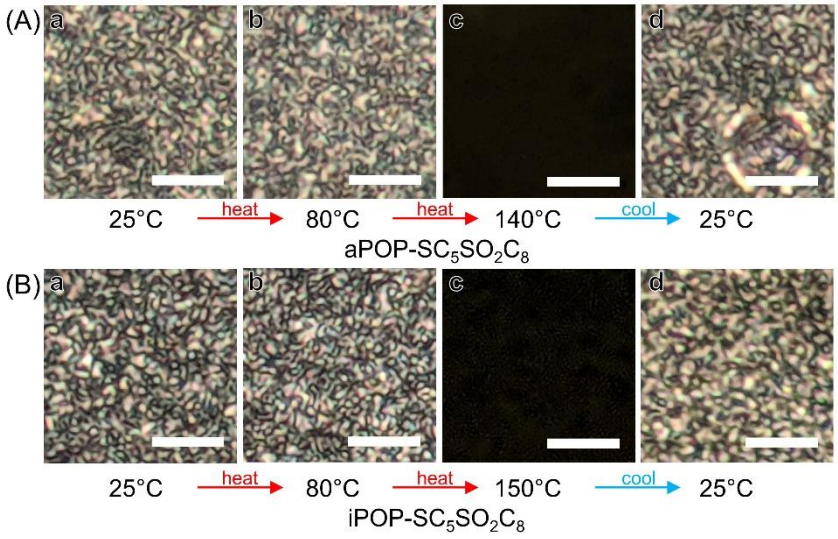

Figure A.14. PLM micrographs of (A) aPOP-$SC_5SO_2C_8$ and (B) iPOP-$SC_5SO_2C_8$ at different temperatures during the first heating and cooling cycle. The scale bar is 10 μm.

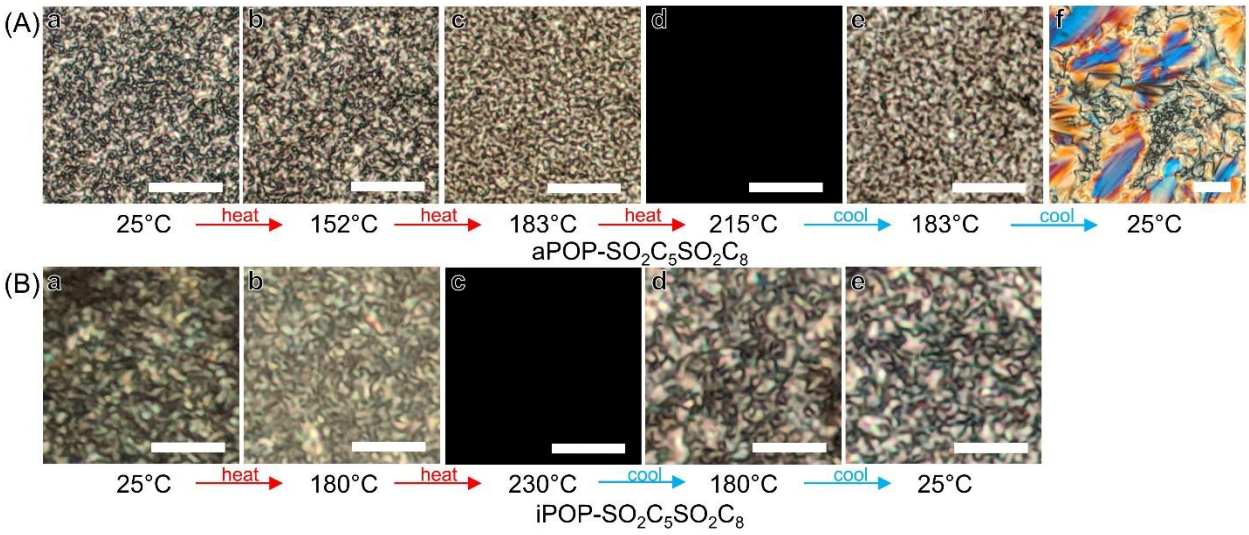

Figure A.15. PLM micrographs of (A) aPOP-$SO_2C_5SO_2C_8$ and iPOP-$SO_2C_5SO_2C_8$ at different temperatures during the first heating and cooling cycle. The scale bars is 20 μm in (A) and 10 μm in (B).

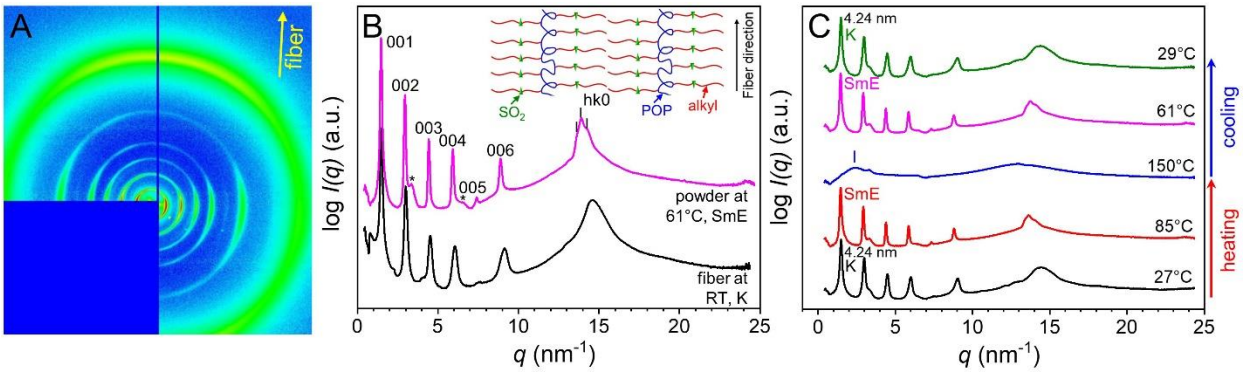

Figure A.16. (A) 2D XRD pattern for the aPOP-$SC_5SO_2C_8$ fiber at room temperature. (B) 1D XRD profiles for the fiber at room temperature and the powder at 61 °C. The inset shows the schematic double layer structure. The * symbols indicate reflections from the Kapton window. (C) 1D XRD profiles of the aPOP-$SC_5SO_2C_8$ powder sample during heating and cooling processes.

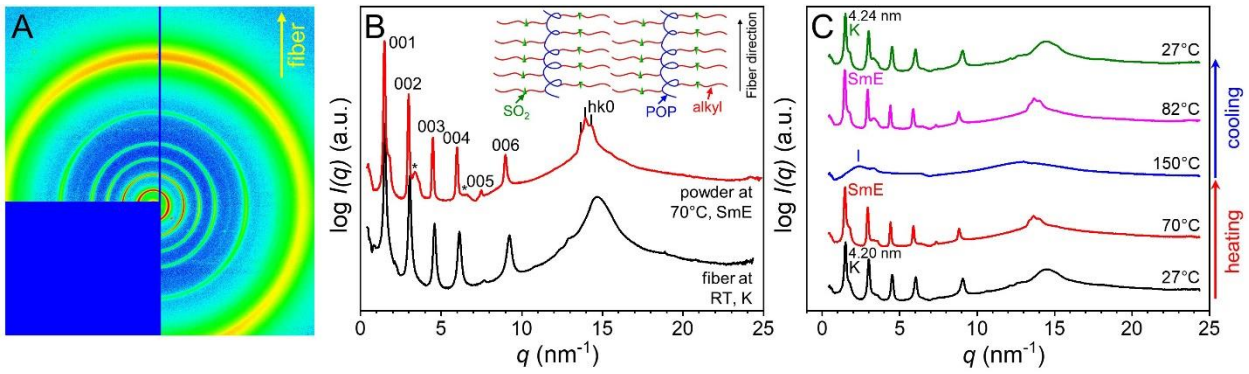

Figure A.17. (A) 2D XRD pattern for the iPOP-$SC_5SO_2C_8$ fiber at room temperature. (B) 1D XRD profiles for the fiber at room temperature and the powder at 70 °C. The inset shows the schematic double layer structure. The * symbols indicate reflections from the Kapton window. (C) 1D XRD profiles of the iPOP-$SC_5SO_2C_8$ powder sample during heating and cooling processes.

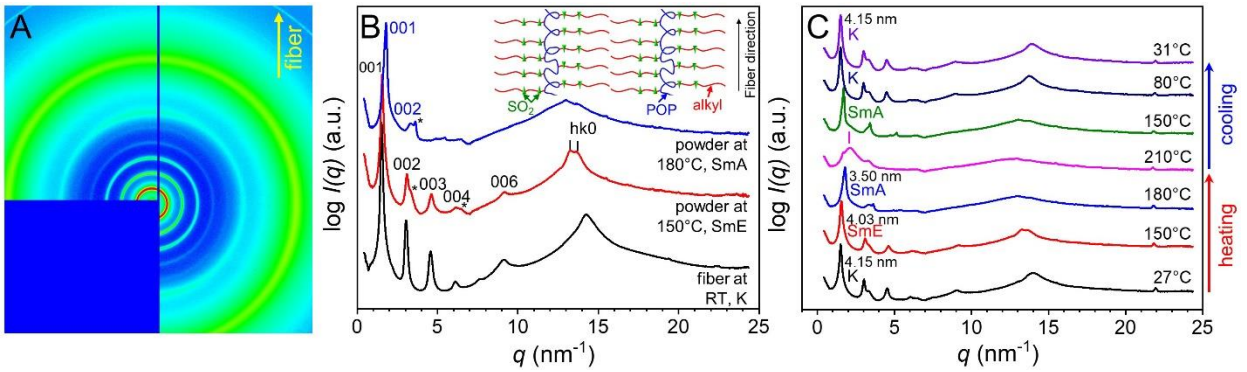

Figure A.18. (A) 2D XRD pattern for the aPOP-$SO_2C_5SO_2C_8$ fiber at room temperature. (B) 1D XRD profiles for the fiber at room temperature and the powder at 150 and 180 °C. The inset shows the schematic double layer structure. The * symbols indicate reflections from the Kapton window. (C) 1D XRD profiles of the aPOP-$SO_2C_5SO_2C_8$ powder sample during heating and cooling cycles.

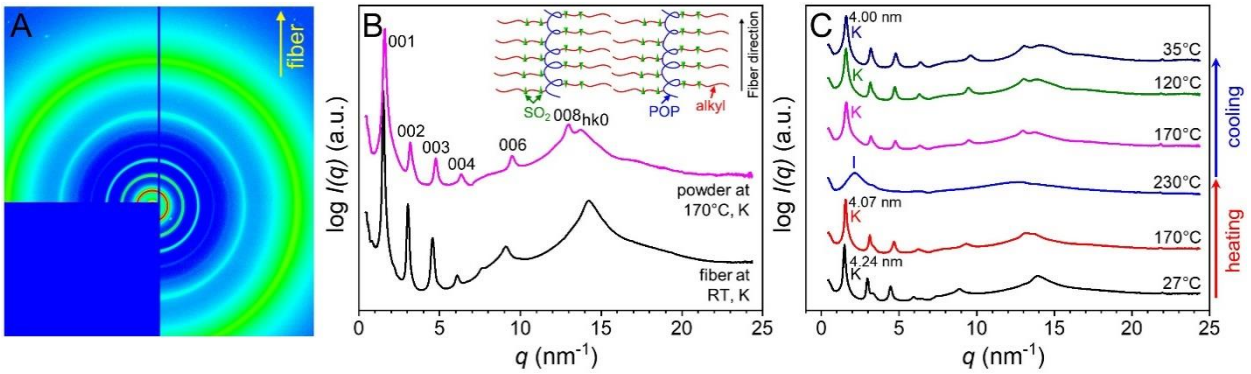

Figure A.19. (A) 2D XRD pattern for the iPOP-$SO_2C_5SO_2C_8$ fiber at room temperature. (B) 1D XRD profiles for the fiber at room temperature and the powder at 170 °C. The inset shows the schematic double layer structure. (C) 1D XRD profiles of the iPOP-$SO_2C_5SO_2C_8$ powder sample during heating and cooling cycles.

Chapter 3: Synthesis of Isotactic Polyethers with Various Degrees of *n*-Dodecylsulfonyl Substitution and Polyethers with Short Sulfonylated Methyl-Branched Side Chains

The work presented in this chapter has been published in *Giant (***2020**, *1,* 100003 *and* **2021**, *8,* 100079). I synthesized all the polymers, characterized the molecular structures, measured molecular weights using SEC, measured their optical activities in chloroform by polarimetry, and conducted preliminary differential scanning calorimetry (DSC) analysis at the University of Tennessee Knoxville. Mr. Jordan L. Crooks, a REU undergraduate student from Clemson University, participated in the synthesis under my supervision. This Chapter only presents the work that we did in the aforementioned two publications at the University of Tennessee Knoxville.

Abstract

Two strategies were attempted to achieve chiral smectic C (SmC*) phases in mesogen-free liquid crystalline polyethers with sulfonylated side chains. In the first one, the grafting density of *n*-dodecylsulfonyl side chains on isotactic poly(oxypropylene) (iPOP) polyethers was systematically reduced in hopes of inducing side chain tilting. A family of iPOPs with *n*-dodecylsulfonyl side chains of various grafting densities, ranging from 100% to 50%, were prepared by varying the molar ratio of the pendant chloromethyl group of isotactic poly[(*R*)-(-)-epichlorohydrin] to *n*-dodecylthiol in the substitution reaction and subsequently oxidizing the thioether linkages to sulfonyl groups. Structural characterizations showed a SmA phase at grafting densities of 80–100% and a hexagonal columnar self-assembled structure at the grafting densities of 60–80%. In the second strategy, a methyl branch, chiral or racemic, was introduced into the short sulfonylated side chains of atactic and isotactic poly(oxypropylene)s. It was found that the polymers with single chirality in the backbone or side chains were largely amorphous. Intriguingly, the fibers of the polyether with double chirality drawn from the melt exhibited a crystalline structure with tilted side chains.

3.1. Introduction

In the work presented in Chapter 2, we synthesized a set of mesogen-free comb-like isotactic poly(oxypropylene)s (iPOPs) bearing mono- or di-sulfonyl groups, i.e., iPOPs with *n*-alkylsulfonylpentylthioether side chains (iPOP-$SC_5SO_2C_n$, where *n* was either 12 or 8) and *n*-alkylsulfonylpentylsulfonyl side chains (iPOP-$SO_2C_5SO_2C_n$, where *n* was either 12 or 8). Although layered smectic A liquid crystalline mesophases were observed from studies by differential scanning calorimetry (DSC), polarized light microscopy (PLM), and small-angle and wide-angle X-ray scattering (SAXS and WAXS), no chiral smectic C (SmC*) phase was found.[1] In this Chapter, two new strategies were attempted to seek the SmC* phase. In the first one, the grafting density of *n*-dodecylsulfonyl side chains grafted on the isotactic polyether backbone was systematically reduced; the obtained polymers were denoted as iCOP-SO_2C_{12}-x, where x represents the degree of substitution of *n*-dodecylsulfonyl side chains (Scheme 3.1A).[2] We postulated that an appropriately reduced grafting density of sulfonylated side chains in iPOPs might be able to induce the side chain tilting due to the strong dipole-dipole interactions of sulfonyl groups among neighboring side chains and the need to maintain a constant density, which may lead to a SmC* phase. In the second strategy, we introduced a methyl branch into the short sulfonylated alkyl side chains with a total of five carbon atoms (iPOP-SO_2bC_{5s}, aPOP-SO_2bC_{5s}, and iPOP-SO_2bC_5 in Scheme 3.1B).[3] It was hypothesized that the methyl branch could cause the tilting of sulfonylated side chains. Because the thermal analysis and the structural characterizations of the polyethers made in this Chapter were principally performed by our collaborators at Case Western Reserve University, I will mainly present the synthesis work that we conducted at our University and briefly discuss the results from characterizations by DSC, PLM, and X-ray diffraction (XRD) experiments.

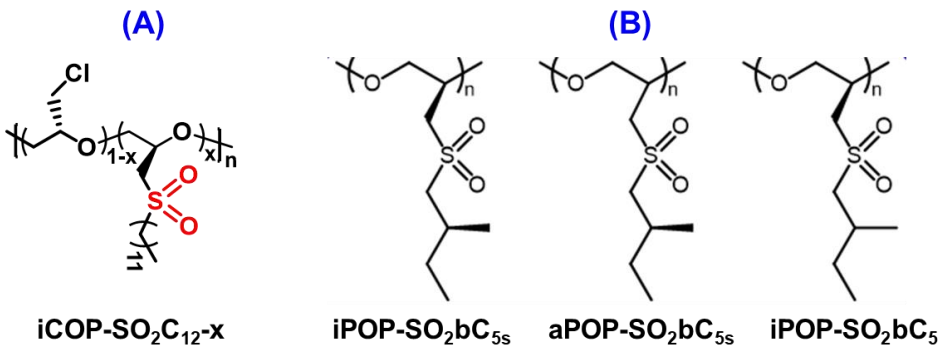

Scheme 3.1. Polyethers with Sulfonylated Alkyl Side Chains Synthesized in Chapter 3.

3.2. Experimental section

3.2.1. Materials

1-Dodecanethiol (99%, Acros), (*S*)-(+)-1-bromo-2-methylbutane (98%, AK Scientific), 2-methyl-1-butanethiol (95%, TCI America), thioacetic acid (97% Acros Organics), sodium hydride (60% dispersion in paraffin liquid, TCI America), tetrahydrofuran (THF, anhydrous, TCI America), *N*,*N*-dimethylacetamide (DMAc, 99.5%, extra dry, Acros Organics), *N*,*N*-dimethylformamide (DMF, 99.8% extra dry, Arcos Organics), and 3-chloroperoxybenzoic acid (*m*-CPBA, 70-75% balance 3-chlorobenzoic acid and water, Acros Organics) were used as received. Diethyl ether (99.8%, Fisher Scientific) and (*R*)-(-)-epichlorohydrin [(*R*)-(-)-ECH, 98%, Combi-blocks, Inc.] were stirred with calcium hydride (93%, Acros Organics) and distilled prior to use. The distilled (*R*)-(-)-ECH was stored in a nitrogen gas-filled glovebox. Modified methylaluminoxane (MMAO-12, 7 wt.% aluminum in toluene, Sigma-Aldrich) was stored in the freezer inside a nitrogen glovebox. THF was dried by refluxing over sodium/benzophenone until a deep purple color appeared and used immediately. Isotactic poly[(*R*)-(-)-ECH] (iPECH) was prepared in a Schlenk tube in a nitrogen gas-filled glove box by ring-opening polymerization of (*R*)-(-)-ECH in dry diethyl ether at room temperature using MMAO-12 as catalyst, as reported previously.[4] Solutions of $NaOCH_2CH_3$ in ethanol with concentrations of 15% and 10% were prepared by adding a certain amount of sodium metal into absolute ethanol under a nitrogen environment and stirring the mixture until the metal disappeared. All other chemicals and solvents were obtained from either Sigma-Aldrich or Fisher Scientific and used without further purification.

3.2.2. General Characterization

^{1}H and ^{13}C NMR spectra were recorded on either a Varian Mercury 300 NMR, a Varian VNMRS 500 NMR, or a Varian VNMRS 600 spectrometer using $CDCl_3$ as solvent with the

residual solvent proton signal as the internal standard. Size exclusion chromatography (SEC) of isotactic polyethers with *n*-dodecylsulfonyl pendant groups at various degrees of substitution was performed on a PL-GPC 20 system (an integrated SEC system from Polymer Laboratories, Inc.) consisting of a Knauer K-2301 refractive index detector, one PL gel 5 μm guard column (50 × 7.5 mm), and two PLgel 5 μm mixed-C columns (each 300 × 7.5 mm, linear molecular weight range of 200-2,000,000 Da). Filtered HPLC grade THF was used as the mobile phase at a flow rate of 1.0 mL/min during the analysis. The SEC system was calibrated with narrow dispersity polystyrene (PS) standards from Scientific Polymer Products, Inc., and the data was processed using the Cirrus SEC software from Polymer Laboratories, Inc.

The optical rotations of chiral polyethers with alkylthioether or alkylsulfonyl pendant groups were measured at ambient conditions (~ 20 °C) using a PerkinElmer 241 polarimeter with a Na lamp (wavelength: 589 nm) and an integration time of 5 s. The samples were prepared by dissolving the chiral polymers in $CHCl_3$ at a concentration of ~ 10 mg/mL. For each sample, three measurements were conducted, and the average value was taken as the optical rotation. The specific optical rotations of the isotactic polyethers with various degrees of *n*-dodecylthioether substitution were obtained by using equation $[\alpha]_{\lambda}^{T} = \alpha/(cl)$, where [α] is the specific rotation at a specified temperature (T) and wavelength (λ), α is the optical rotation in degrees from the optical rotation measurements, *c* is the concentration (units: g/mL), and *l* is the path length (dm). The units of specific rotation is deg·mL/(g·dm), commonly abbreviated to degrees (°).

3.2.3. Synthesis of Isotactic Polyethers with Various Degrees of *n*-Dodecylsulfonyl Substitution

iPOPs with various degrees of *n*-dodecylsulfonyl substitution were prepared by reacting iPECH and *n*-dodecanethiol at various molar ratios, followed by oxidation of thioether pendant

groups in the obtained polymers with *m*-CPBA (see Scheme 3.2). Due to the nature of random substitution, random copolymers were obtained. The intermediate isotactic poly(ECH-*co*-oxypropylene-SC_{12})-*x* is denoted as iCoP-SC_{12}-*x*, where *x* is the degree of substitution or grafting density. The sulfonylated isotactic poly(ECH-*co*-oxypropylene-SO_2C_{12})-*x* is denoted as iCoP-SO_2C_{12}-*x*. The following shows the detailed synthesis and characterization for iCoP-SO_2C_{12}-88% as an example. Other polymers were prepared using the same procedure except the different molar ratios of *n*-dodecanthiol to the monomer units of iPECH. Sodium hydride (from 60% in mineral oil, 0.071 g NaH, 3.0 mmol), *n*-dodecanthiol (0.338 g, 1.67 mmol), and dry THF (10 mL) were added into a 50 mL two-necked round bottom flask and stirred under a nitrogen atmosphere for 15 min, followed by the addition of a solution of iPECH (0.103 g, 1.11 mmol of monomer units) in dry THF (15 mL). The flask, fitted with a reflux condenser, was placed in a 70 °C oil bath, and the reaction mixture was stirred and refluxed under a nitrogen atmosphere overnight. The mixture was poured into DI water, and the polymer was re-dissolved in THF and precipitated twice in cold methanol to remove impurities. The polymer was collected and dried in a vacuum oven overnight at 80 °C. Yield: 0.220 g. ^{1}H NMR spectroscopy analysis showed that the polymer product was free of impurities. The degree of substitution was found to be 88% from ^{1}H NMR analysis, and the specific rotation of the obtained polymer [α] was -11.3° from polarimetry measurements at room temperature.

The obtained isotactic polyether with partially substituted thioether pendant groups (iCoP-SC_{12}-88%, 0.220 g) and *m*-CPBA (0.482 g, 2.79 mmol) were dissolved in chloroform (15 mL) in a 50 mL flask. After the mixture was stirred with a magnetic stir bar at ambient temperature for 3 h, it was concentrated to ~ 5 mL and precipitated dropwise in methanol (50 mL) using a pipet. The polymer was re-dissolved in $ChCl_3$ and precipitated in methanol for additional two times.

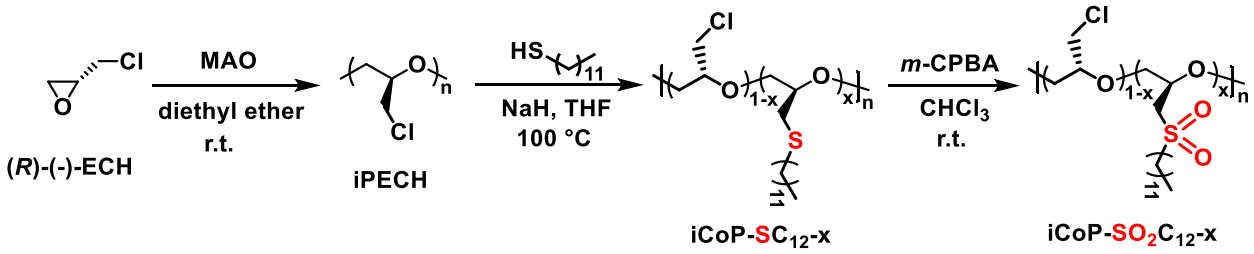

Scheme 3.2. Synthesis of Isotactic Polyethers with Various Degrees (x = 50-100%) of *n*-Dodecylsulfonyl Substitution. Note That When x = 100%, the Polymer is iPOP-SO_2C_{12}.

The purified polymer was collected, dried in a vacuum oven at 100 ℃ overnight, and obtained as an opaque, brittle solid (0.223 g, 91% yield). SEC analysis results: number-average molecular weight $M_{n,SEC}$ = 68.2 kDa, and dispersity $Đ$ = 3.35 (relative to PS standards).

3.2.4. Synthesis of (*S*)-S-(2-Methylbutyl) Ethanethioate

(*S*)-S-(2-Methylbutyl) ethanethioate was synthesized according to Scheme 3.3. (*S*)-1-Bromo-2-methylbutane (5.002, 33.1 mmol), triethyl amine (3.711 g, 36.7 mmol), thioacetic acid (2.600 g, 34.2 mmol), and dimethoxyethane (15 mL) were added into a 100 mL, two-necked flask with a stir bar. The flask was fitted with a reflux condenser and placed in a 100 °C oil batch. The reaction mixture was refluxed under stirring conditions for 2 h; the color of the mixture change from light yellow to deep red. The precipitate was filtered off using a Büchner funnel and the solution was poured into a separatory funnel, followed by the addition of diethyl ether to dilute the mixture. The organic phase was washed sequentially with deionized water (50 mL × 3), 1 M HCl (50 mL × 1), and a saturated $NaHCO_3$ solution (50 mL × 1). The organic layer was separated, transferred into an Erlenmeyer flask, and dried with anhydrous Na_2SO_4. After the removal of the solid, the solution was concentrated by rotary evaporation. Vacuum distillation was performed, yielding a pale-yellow liquid. The collected product was further purified by silica gel column chromatography, first using pure hexanes to remove impurities and then a mixture of hexanes and ethyl acetate with a volume ratio of 5:1 ratio to elute the product from the column. The product was collected and the solvent was evaporated using a stream of air flow, yielding a clear liquid as product (2.314 g, 47.8%). [α] ($CHCl_3$) = +13.8 °; ^{1}H NMR (600 MHz, $CDCl_3$), δ = 2.92 (dd, -SC*H*HCH-, 1H), 2.75 (dd, -SCH*H*CH-, 1H), 2.32 (t, -*CH*$_3$C(O)CH$_2$-, 3H), 1.60 – 1.52 (m, -CH$_2$C*H*CH$_2$-, 1H), 1.47 – 1.37 (m, CH$_3$C*H*HCH-, 1H), 1.25 -1.15 (m, CH$_3$CH*H*CH-, 1H), 0.95 -0.86 (m, C*H*$_3$CH$_2$(CH)C*H*$_3$,

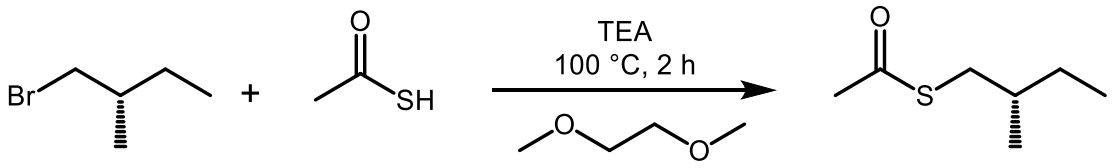

Scheme 3.3. Synthesis of (*S*)-S-(2-Methylbutyl) Ethanethioate.

6H). ^{13}C NMR (151 MHz, $CDCl_3$), δ (ppm) = 196.04, 35.77, 35.03, 30.77, 28.76, 18.81, 11.44.

3.2.5. Synthesis of iPOP-SO_2bC_{5s}, aPOP-SO_2bC_{5s}, and iPOP-SO_2bC_5

iPOP-SbC_{5s} and aPOP-SbC_{5s} were synthesized by reacting (*S*)-S-(2-methylbutyl) ethanethioate with iPECH and aPECH, respectively (Scheme 3.4). Shown below is the synthesis of iPOP-SbC_{5s}, and a similar procedure was used to prepare the atactic analogue, aPOP-SbC_{5s}. Sodium ethoxide (0.183 g, 2.69 mmol) and (*S*)-S-(2-methylbutyl) ethanethioate (0.288 g, 1.97 mmol) were added into a 50 mL two-necked round bottom flask equipped with a magnetic stir bar and a gas flow control adaptor. The mixture was stirred at room temperature for 30 min. iPECH (0.124 g, 1.34 mmol of -CH_2Cl) and *N*,*N*-dimethylacetamide (DMAc, 9.0 g) were weighed into a 20 mL scintillation vial, capped, and shaken overnight on a platform shaker. The flask that contained the solution of sodium ethoxide and (*S*)-S-(2-methylbutyl)ethanethioate in ethanol was placed in an oil bath with a preset temperature of 100 ℃. The iPECH dissolved in DMAc was heated to reduce the viscosity and added into the reaction flask under the stirring conditions. The reaction was allowed to proceed at 100 °C under a nitrogen atmosphere for 24 h, and the mixture remained clear throughout the reaction. The reaction mixture was then precipitated in water and the solid was collected using vacuum filtration. The obtained crude polymer product was subsequently dissolved in chloroform (~5 mL) and precipitated in methanol for 3 times. The polymer was collected and dried in a vacuum oven, yielding a tacky, clear solid (0.173 g, 80.5% yield). [α] ($CHCl_3$) = -2.4°. ^{1}H NMR (600 MHz, $CDCl_3$), δ (ppm) = 3.74 – 3.68 (m, -OC*H*CH_2-, 1H), 3.66 – 3.60 (m, -OCHCH*H*-, 1H), 3.60 – 3.54 (m, -OCHC*H*H-, 1H), 2.68 (dd, -OCHC*H*$_2$--S-, 2H), 2.48 (dd, -SC*H*$_2$CH(CH_3), 2H), 1.62 – 1.56 (m, -CH-$_2$C*H*(CH_3), 1H), 1.53 – 1.43 (m, CH_3C*H*H-, 1H), 1.27 – 1.15 (m, CH_3CH*H*-, 1H),

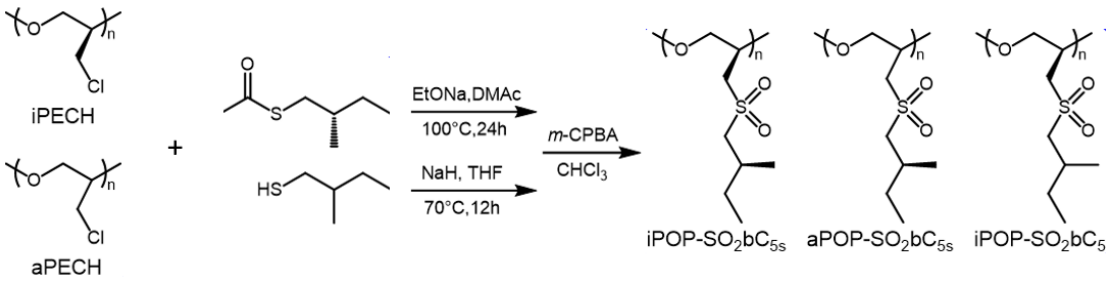

Scheme 3.4. Synthesis of iPOP-SO_2bC_{5s}, aPOP-SO_2bC_{5s}, and iPOP-SO_2bC_5.

0.97 (d, -CH(C*H*$_3$), 3H), 0.89 (t, -CH$_2$C*H*$_3$, 3H). ^{13}C NMR (151 MHz, CDCl$_3$), δ (ppm) = 79.65, 71.41, 40.73, 35.12, 34.74, 28.90, 19.07, 11.52. aPOP-SbC$_{5s}$ was prepared in a similar fashion with a yield of 81.0%. [α] (CHCl$_3$) = +16.5°. ^{1}H NMR (600 MHz, CDCl$_3$), δ (ppm) = 3.72 – 3.54 (m, -OC*H*CH$_2$-, 3H), 2.79 – 2.70 (m, -OCHCH*H*-S-, 1H), 2.68 – 2.59 (m, -OCHC*H*HS-, 1H), 2.59 – 2.52 (m, -SCH*H*CH(CH$_3$), 1H), 2.43 – 2.36 (m, -SC*H*HCH(CH$_3$), 1H), 1.62 – 1.56 (m, -CH-$_2$C*H*(CH$_3$), 1H), 1.52 – 1.44 (m, CH$_3$CH*H*-, 1H), 1.27 – 1.15 (m, CH$_3$C*H*H-, 1H), 0.97 (d, -CH(C*H*$_3$), 3H), 0.89 (t, -CH$_2$C*H*$_3$, 3H).

iPOP-SbC$_5$ was synthesized by reacting iPECH with 2-methyl-1-butanethiol (Scheme 3.4). iPECH (0.100 g, 1.08 mmol) and dry THF (10 mL) were added to a 20 mL scintillation vial and placed in an oil bath, heated to 70 ℃, and stirred overnight. 2-Methyl-1-butanethiol (0.172 g, 1.65 mmol) and sodium hydride (from 60% in paraffin liquid, 0.086 g, 3.58 mmol) were added to a 50 mL two-necked round bottom flask equipped with a stir bar and a gas flow adaptor. After the mixture was stirred under nitrogen at room temperature for 30 min, the flask was placed in an oil bath with a preset temperature of 70 ℃, followed by the addition of the solution of iPECH in THF. The flask was then fitted with a reflux condenser and the mixture was stirred at 70 ℃ overnight. The reaction mixture was cooled to room temperature and the volatiles were removed using rotary evaporation. The obtained solid was washed with water, dissolved in chloroform (~5 mL), and precipitated in methanol for 3 times. After drying under high vacuum, a highly viscous, clear polymer was obtained (0.165 g, 95.4%). [α](CHCl$_3$) = -20.0°. ^{1}H NMR (500 MHz, CDCl$_3$), δ (ppm) = 3.74 – 3.67 (m, -OC*H*CH$_2$-, 1H), 3.66 – 3.61 (m, -OCHC*H*H-, 1H), 3.61 – 3.54 (m, -OCHCH*H*-, 1H), 2.68 (dd, -OCHC*H*$_2$S-, 2H), 2.47 (dd, -SC*H*$_2$CH(CH$_3$), 2H), 1.62 – 1.53 (m, -SCH-$_2$C*H*(CH$_3$), 1H), 1.53 – 1.44 (m, CH$_3$CH*H*-, 1H), 1.25 – 1.15 (m, CH$_3$C*H*H-, 1H), 0.97 (d, -

CH(C*H*$_3$), 3H), 0.89 (t, -CH$_2$C*H*$_3$, 3H). ^{13}C NMR (126 MHz, $CDCl_3$), δ (ppm) = 79.47, 71.28, 40.60, 34.99, 34.66, 28.76, 18.94, 11.39.

iPOP-SbC$_{5s}$, aPOP-SbC$_{5s}$, and iPOP-SbC$_5$ were oxidized using the same procedure (Scheme 3.4). The following example shows the synthesis of iPOP-SO$_2$bC$_{5s}$ from iPOP-SbC$_{5s}$. iPOP-SbC$_{5s}$ (0.152 g, 0.790 mmol of thioether groups) and *m*-CPBA (0.568 g, 2.31 mmol) were dissolved in chloroform (20 mL) in a two-necked 50 mL flask and stirred with a magnetic stir bar at room temperature for 3 h. The solvent was evaporated using a rotary evaporator and the solid was washed with 1 M NaOH (20 mL). The remaining solid was dissolved with THF, and the obtained solution was condensed to ~5 mL using a rotary evaporator. The concentrated solution was precipitated in methanol three times; the precipitate was collected and dried in a vacuum oven at 60 °C overnight. The dried product was a tacky clear polymer (0.097 g, 46.0% yield). SEC results with THF as eluent: $M_{n,SEC}$ = 175 kDa and $Đ$ = 2.64, relative to PS standards. [α] ($CHCl_3$) = -33.8°. ^{1}H NMR (500 MHz, $CDCl_3$), δ (ppm) = 4.22 – 3.97 (m, -OC*H*CH$_2$-, 1H), 3.92 – 3.73 (m, -OCHC*H*H-, 1H), 3.73 – 3.51 (m, -OCHCH*H*-, 1H), 3.51 – 3.17 (m, -OCHC*H*$_2$SO$_2$-, 2H), 3.17 – 2.70 (m, -SO$_2$C*H*$_2$CH(CH$_3$), 2H), 2.25 – 2.02 (m, -CH-$_2$C*H*(CH$_3$), 1H), 1.68 – 1.21 (m, CH$_3$C*H*$_2$-, 2H), 1.12 (d, -CH(C*H*$_3$), 3H), 0.92 (t, -CH$_2$C*H*$_3$, 3H). ^{13}C NMR (151 MHz, $CDCl_3$) δ (ppm) = 73.76, 70.50, 60.65, 56.08, 29.44, 29.32, 19.49, 10.82.

The yield for the synthesis of aPOP-SO$_2$bC$_{5s}$ was 69%. SEC results with THF as eluent: $M_{n,SEC}$ = 232 kDa and $Đ$ = 2.95, relative to PS standards. [α] ($CHCl_3$) = +16°. ^{1}H NMR (300 MHz, $CDCl_3$), δ (ppm) = 4.21 – 3.99 (m, -OC*H*CH$_2$-, 1H), 3.91 – 3.73 (m, -OCHC*H*H-, 1H), 3.73 – 3.56 (m, -OCHCH*H*-, 1H), 3.51 – 3.16 (m, -OCHC*H*$_2$SO$_2$-, 2H), 3.16 – 2.70 (m, -SO$_2$C*H*$_2$CH(CH$_3$), 2H), 2.26 – 2.00 (m, -CH-$_2$C*H*(CH$_3$), 1H), 1.68 – 1.21 (m, CH$_3$C*H*$_2$-,

2H), 1.12 (d, -CH(C*H*$_3$), 3H), 0.92 (t, -CH$_2$C*H*$_3$, 3H). ^{13}C NMR (151 MHz, CDCl$_3$) δ (ppm) = 73.74, 68.5 - 71.0 (multiple peaks), 60.85, 56.25, 29.42, 29.31, 19.37, 10.79.

The yield for the synthesis of iPOP-SO$_2$bC$_5$ was 42%. SEC results with THF as eluent: $M_{n,SEC}$ = 19.7 kDa and $Đ$ = 1.56, relative to PS standards (. [α] (CHCl$_3$) = -34.5°. ^{1}H NMR (500 MHz, CDCl$_3$), δ (ppm) = 4.20 – 4.07 (m, -OC*H*CH$_2$-, 1H), 3.89 – 3.78 (m, - OCHC*H*H-, 1H), 3.74 – 3.60 (m, - OCHCH*H*-, 1H), 3.40 – 3.22 (m, -OCHC*H*$_2$--SO$_2$-, 2H), 3.09 – 3.00 (m, -SO$_2$C*H*HCH(CH$_3$), 1H), 2.92 – 2.83 (m, -SO$_2$CH*H*CH(CH$_3$), 1H), 2.19 – 2.10 (m, -CH-$_2$C*H*(CH$_3$), 1H), 1.65 – 1.47 (m, CH$_3$C*H*$_2$-, 1H), 1.41 – 1.30 (m, CH$_3$C*H*$_2$-, 1H), 1.12 (d, -CH(CH$_3$), 3H), 0.92 (t, -CH$_2$CH$_3$, 3H). ^{13}C NMR (151 MHz, CDCl$_3$), δ: 73.77, 70.50, 60.66, 56.09, 29.45, 29.33, 19.50, 10.83.

3.3. Results and Discussion

3.3.1. Synthesis of Isotactic Poly(oxypropylene) Polyethers with Various Degrees of *n*-Dodecylsulfonyl Substitution

To investigate the effect of the degree of *n*-dodecylsulfonyl substitution (or grafting density) on liquid crystalline self-assembly of mesogen-free isotactic polyethers, a set of eight samples with the degrees of substitution from 50% to 100% was prepared from iPECH by post-polymerization modifications (Scheme 3.2). iPECH was synthesized by MMAO-initiated ring-opening polymerization of (*R*)-(-)-ECH in a glovebox at room temperature. In a previous report from our group and our collaborators,[4] the isotacticity of the obtained polymer was confirmed by ^{13}C NMR spectroscopy analysis. The degree of substitution of pendant Cl groups in iPECH by *n*-dodecanethiol was varied by changing the molar ratio of the monomer units of iPECH to the thiol compound. Because of the random nature of the substitution reaction, the obtained polymers were

random copolymers and are denoted as poly(ECH-*co*-oxypropylene-SC_{12})-*x* (in short, iCoP-SC_{12}-*x*, where *x* is the degree of substitution). The fully substituted polyether is denoted as iPOP-SC_{12}. As an example, Figure 3.1A shows the ^{1}H NMR spectrum of iCoP-SC_{12}-88%. The degree of substitution was calculated from the integrals of the peaks in the range of 3.54-3.76 ppm [-C*H*$_2$C*H*(C*H*$_2$Cl)O- and -C*H*$_2$C*H*(CH_2SCH_2-)O-, labeled with a, b, c, a', and b'] and the peaks in the range of 2.59-2.78 ppm [-CH_2CH(C*H*$_2$SC*H*$_2$-)O-, labeled with c' and d']. The specific optical rotation, [α], of this polymer after purification was -11.3°, similar to the values previously reported for isotactic polyethers with *n*-alkylsulfonated pendant groups.[4]

The obtained polymer with thioether pendant groups was then oxidized using *m*-chloroperoxybenzoic acid (*m*-CPBA) in chloroform at room temperature to yield the sulfonylated isotactic polyether. The sulfonylated isotactic poly(ECH-*co*-oxypropylene-SO_2C_{12})-*x* is denoted as iCoP-SO_2C_{12}-*x*, and the fully substituted sulfonylated iPOP with *n*-dodecylsulonyl side chains is denoted as iPOP-SO_2C_{12}. ^{1}H NMR spectroscopy analysis showed that the peaks of c' and d' completely shifted to 3.29 and 3.01 ppm, respectively, with no residual peaks observed in the range of 2.59-2.78 ppm, indicating that the oxidation of thioether side chains was complete (Figure 3.1B). Size exclusion chromatography (SEC) showed that the $M_{n,SEC}$ = 68.2 kDa, and dispersity (*Đ*) = 3.35 (Figure 3.2), based on PS standards. The ^{1}H NMR and SEC data for other polymers are included in Figures B.1-B.14 in Appendix B and are summarized in Table 3.1. The relative molecular weights of these polymers were in the range of 30.6 to 121 kDa, and the *Đ* values were 1.82-3.35. As discussed in the literature,[1,4] the oxidation by *m*-CPBA could also cleave the isotactic polyether backbone, which lowered the molecular weight and somewhat decreased the dispersity. The specific optical rotation values ([α] values) for all eight polyether samples were similar,

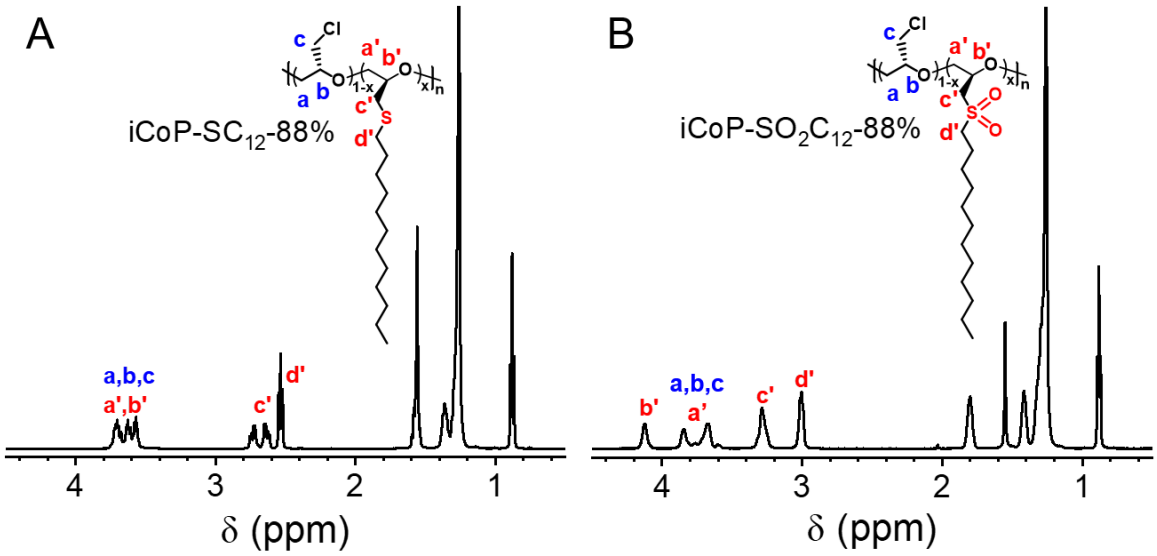

Figure 3.1. ^{1}H NMR spectra of iCoP-SC$_{12}$-88% and iCoP-SO$_2$C$_{12}$-88% in CDCl$_3$.

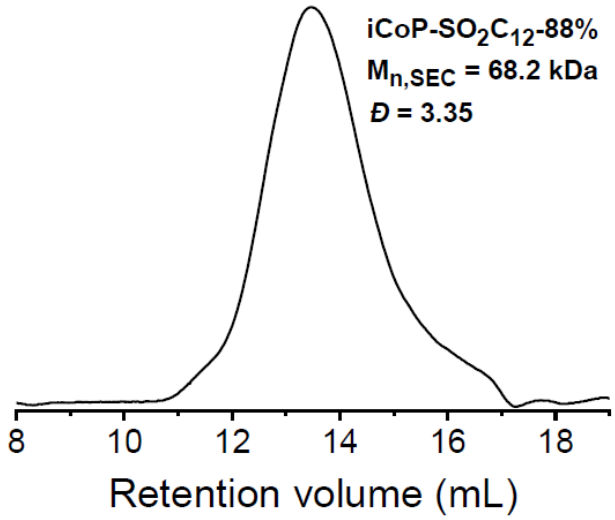

Figure 3.2. Size exclusion chromatography (SEC) curve of iCoP-SO_2C_{12}-88% using THF as the mobile phase.

Table 3.1. Summary of Characterization Data for iCoP-SO_2C_{12}-*x* and iPOP-SO_2C_{12} as well as Corresponding iPOP with Thioether Pendant Groups

Samples	*x* by ^{1}H NMR	$M_{n,SEC}$ (kDa)	*Đ*	[α] [a]
iCoP-SO_2C_{12}-50%	50.0 %	62.6	2.96	- 11.7°
iCoP-SO_2C_{12}-60%	60.0 %	65.6	3.15	- 10.6°
iCoP-SO_2C_{12}-71%	71.0 %	121	1.82	- 10.6°
iCoP-SO_2C_{12}-73%	73.4 %	30.6	2.44	- 11.4°
iCoP-SO_2C_{12}-79%	78.9 %	52.1	2.62	- 12.1°
iCoP-SO_2C_{12}-88%	87.7 %	68.2	3.35	- 11.3°
iCoP-SO_2C_{12}-92%	92.4 %	33.6	2.30	- 12.2°
iPOP-SO_2C_{12}	100 %	37.1	2.70	- 9.83°

[a] Specific optical rotations were measured for the corresponding iCoP-SC_{12}-*x*.

in the range of -9.83° to -12.2°, despite the fact that the degree of substitution varied from 50% to 100%.

3.3.2. Mesophase Self-Assembly Behavior of Isotactic Polyethers with Various Degrees of *n*-Dodecylsulfonyl Substitution

The mesophase self-assembly behavior of isotactic polyethers with various degrees of *n*-dodecylsulfonyl substitution was studied using DSC, PLM, and XRD, and the results are summarized in Figure 3.3.[2] At a grafting density higher than 80%, the majority of the backbone repeat units have strongly interacted sulfonyl side chains, and thus there exist strong dipole-dipole interactions among the side chains. Consequently, a double-layer SmA mesophase is formed upon self-assembly, similar to the fully substituted iPOP-SO_2C_{12}. In the intermediate grafting density regime between 60% and 80%, a hexagonal columnar mesophase is observed.[2] At the grafting density of 60%, the chemical structure becomes so irregular that poorly ordered mesophase is observed with a very low isotropization temperature (T_i), only less than 20 °C above the T_g. In addition, due to the isotactic backbone, these random copolymers can still slowly crystallize, and the crystallizability gradually increases upon increasing the grafting density.

3.3.3. Synthesis and Self-Assembly of Isotactic and Atactic Polyethers with Chiral or Racemic Methyl-Branched Sulfonylated C5 Side Chains

In an attempt to induce a self-assembled mesophase with tilted side chain, a methyl branch was introduced into the sulfonylated short alkyl side chains with a total of five carbon atoms in poly(oxypropylene) polyethers (Scheme 3.1B). The overall synthesis is shown in Scheme 3.3. Either chiral or racemic methyl-branched C5 side chains were grafted onto iPECH and aPECH, followed by the oxidation of thioether linkages into sulfonyl groups. These polymers are denoted

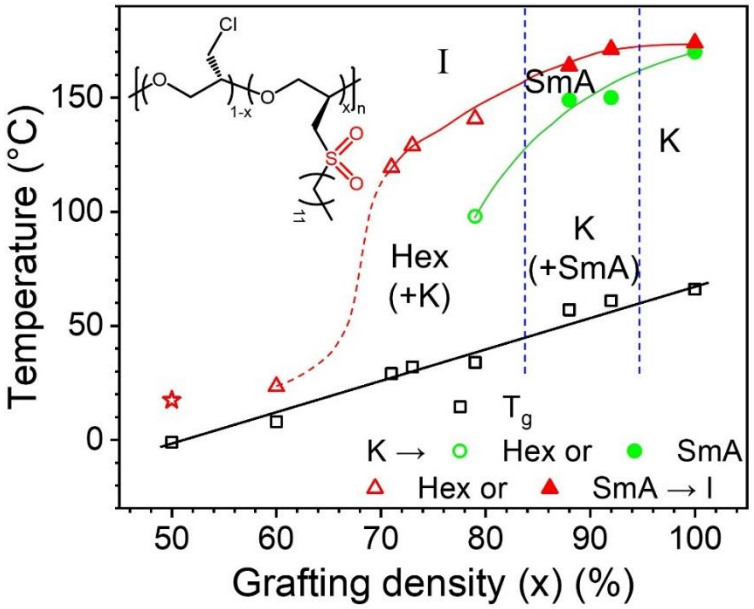

Figure 3.3. Summary of various phase transitions in iCoP-SO_2C_{12}-*x* as a function of the grafting density.

as iPOP-SO_2bC_{5s}, aPOP-SO_2bC_{5s}, and iPOP-SO_2bC_5, and their thioether precursor polymers are denoted as iPOP-SbC_{5s}, aPOP-SbC_{5s}, and iPOP-SbC_5, respectively. (*S*)-S-(2-Methylbutyl) ethanethioate used in the preparation of iPOP-SbC_{5s} and aPOP-SbC_{5s} was synthesized from (*S*)-1-bromo-2-methylbutane and thioacetic acid and purified by vacuum distillation and silica gel column chromatography. The molecular structure of this thioacetate compound was confirmed by ^1H and ^{13}C NMR spectroscopy analysis (Figure B.15. in Appendix B). iPOP-SbC_{5s} and aPOP-SbC_{5s} were then prepared by reacting iPECH and aPECH, respectively, with (*S*)-S-(2-methylbutyl) ethanethioate in *N*,*N*-dimethylacetamide (DMAc) at 100 °C. Sodium ethoxide was added to generate the corresponding thiolate from the thioacetate compound in situ for the substitution reaction. After 24 h, the polymers were collected and purified by repeated precipitation. iPOP-SbC_5 was prepared directly from the reaction between iPECH and 2-methyl-1-butanethiol in the presence of NaH at 70 °C. ^1H NMR spectroscopy analysis of the three purified polymers showed that the integrals of the peaks matched the molecular structures of the polyethers with thioether side chains (Figure B.16 in Appendix B), suggesting that the substitution reactions were essentially complete.

The thioether linkages in iPOP-SbC_{5s}, aPOP-SbC_{5s}, and iPOP-SbC_5 were then oxidized into the sulfonyl groups using *m*-CPBA in chloroform at room temperature for 3 h. ^1H NMR spectroscopy analysis showed that the peaks of the polymers with thioether side chains in the range of 2.3 – 2.8 ppm disappeared after the oxidation (Figure 3.4), indicating that the oxidation was complete. A closer look at the ^1H NMR spectra of the sulfonylated iPOPs and aPOPs in Figure 3.4 reveals that the peaks from isotactic polymers are sharper and better resolved than those from the corresponding atactic polymers, which could be attributed to the same configuration for all repeat units in the sulfonylated iPOPs. However, for aPOPs multiple diad & triad microstructures make

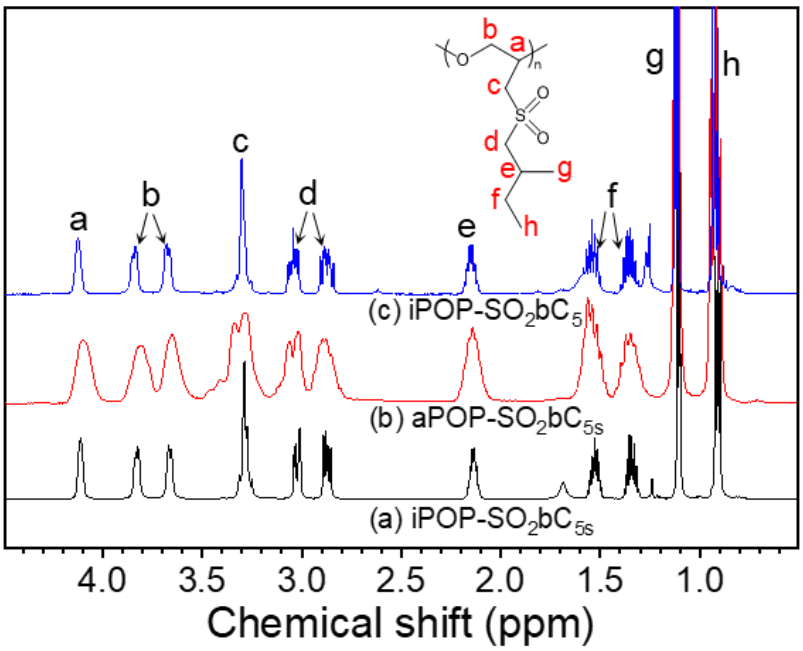

Figure 3.4. ^{1}H NMR spectra of (a) iPOP-SO_2bC_{5s}, (b) aPOP-SO_2bC_{5s}, and (c) iPOP-SO_2bC_5 in $CDCl_3$.

the peaks broader. The isotacticity of iPOP-SO_2bC_{5s} and iPOP-SO_2bC_5 was confirmed by ^{13}C NMR analysis (Figure B.17 in Appendix B); a single peak at ~ 70.5 ppm was observed for both iPOP-SO_2bC_{5s} and iPOP-SO_2bC_5, in contrast to multiple peaks at ~ 70 ppm for aPOP-SO_2bC_{5s}.

The molecular weights and dispersities of iPOP-SO_2bC_{5s}, aPOP-SO_2bC_{5s}, and iPOP-SO_2bC_5 were determined by SEC relative to polystyrene standards. The $M_{n,SEC}$ and $Đ$ values were 175 kDa and 2.64 for iPOP-SO_2bC_{5s}, 232 kDa and 2.95 for aPOP-SO_2bC_{5s}, and 19.7 kDa and 1.56 for iPOP-SO_2bC_5, respectively (Figure B.18 in Appendix B). As expected, polarimetry measurements showed that all three polyethers with sulfonated methyl-branched side chains exhibited an optical activity. The specific optical rotations of iPOP-SO_2bC_{5s}, aPOP-SO_2bC_{5s}, and iPOP-SO_2bC_5 were -2.4°, +16.5°, and -20.0°, respectively. Note that the specific optical rotations of (*R*)-(-)-epichlorohydrin and (*S*)-S-(2-Methylbutyl) ethanethioate are -35.4° and +13.8° ($CHCl_3$), respectively, which explain the observed [α] values of the three polymers.

The self-assembly behavior of the three polyether polymers with sulfonylated methyl-branched C5 side chains was investigated by DSC, PLM, and XRD.[3] aPOP-SO_2bC_{5s}, and iPOP-SO_2bC_5 were largely amorphous, even in the form of fibers drawn from the melts, and showed no ability to crystallization upon cooling from the melt. Interestingly, when fibers were drawn at ~ 140 °C from the melt, iPOP-SO_2bC_{5s} with double chirality in both main chain and side chains could crystallize, exhibiting a broad cold crystallization temperature of 86 °C and a T_m of 132 °C. However, no liquid crystalline phase was observed above the T_m. Upon cooling from the melt state, the polymer did not crystallize and only showed a glass transition temperature (T_g) around 30 °C.

3.4. Conclusions

In summary, two new strategies in the molecular design were adopted to attempt to achieve the SmC* phase in mesogen-free liquid crystalline polymers with sulfone-containing side chains: decreasing the grafting density of iPOPs with *n*-dodecylsulfonyl side chains and introducing a methyl branch into short sulfonylated side chains. A series of iPOPs with grafting densities of *n*-dodecylsulfonyl side chains from 50% to 100% were synthesized. When the grafting density of *n*-dodecylsulfonyl side chains was in the range of 80 – 100%, a SmA phase was observed. Further decreasing the grafting density to 60 – 80% resulted in a hexagonal columnar liquid crystalline phase. Introducing a methyl group into sulfonylated C5 side chains induced a crystalline structure with tilted side chains when double chirality existed in both the main chain and the side chains. It is encouraging to see the tilting of side chains in the crystalline structure through the introduction of a methyl branch in the sulfonylated side chains. To induce the formation of liquid crystalline phases, we speculate that it is necessary to increase the alkyl length in the side chains.

References

1. Bohannon, C. A.; Kwok, M.-H.; Li, R. P.; Zhu, L.; Zhao, B. Effects of Tacticity and Chiral Center-to-Dipole Distance on Mesogen-Free Liquid Crystalline Self-Assembly of Sulfonyl-Containing Comb-like Polymers. *Polymer Chemistry* **2020**, *11*, 3018-3031.
2. Kwok, M.-H.; Bohannon, C. A.; Crooks, J. L.; Li, R. P.; Zhao, B.; Zhu, L. Grafting Density-Induced Smectic A to Hexagonal Columnar Transition in Mesogen-Free Isotactic Liquid Crystalline Polyethers with n-Dodecylsulfonyl Side Groups. *Giant* **2020**, *1*, 100003.
3. Kwok, M.-H.; Bohannon, C. A.; Li, R. P., Zhao, B.; Zhu, L. Ordered Hexagonal Columnar Liquid Crystalline Self-assembly of Mesogen-free Sulfonylated Side-chain Chiral Polyethers and Their High Dielectric Property. *Giant* **2021**, *8*, 100079.
4. Kwok, M.-H.; Seymour, B. T.; Li, R.; Litt, M. H.; Zhao, B.; Zhu, L. Tacticity Effect on Mesogen-free Liquid Crystalline Self-assembly Induced by Strong Dipole-Dipole Interactions. *Macromolecules* **2019**, *52(10)*, 3601-3611.

Appendix B

for

Chapter 3: Synthesis of Isotactic Polyethers with Various Degrees of *n*-Dodecylsulfonyl Substitution and Polyethers with Short Sulfonylated Methyl-Branched Side Chains

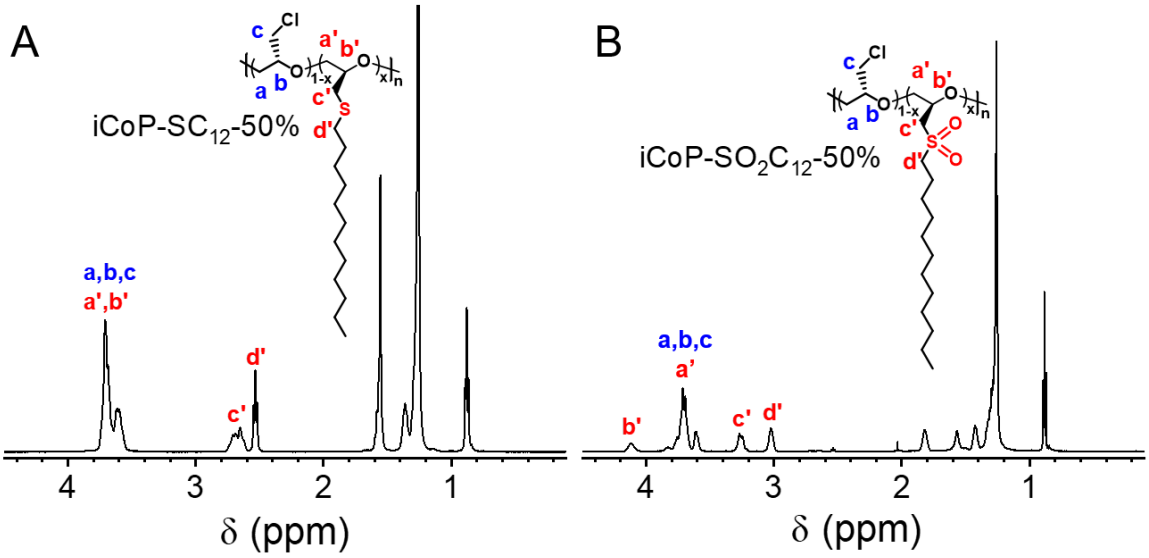

Figure B.1. ^{1}H NMR spectra of (A) iCoP-SC_{12}-50% and (B) iCoP-SO_2C_{12}-50% in $CDCl_3$.

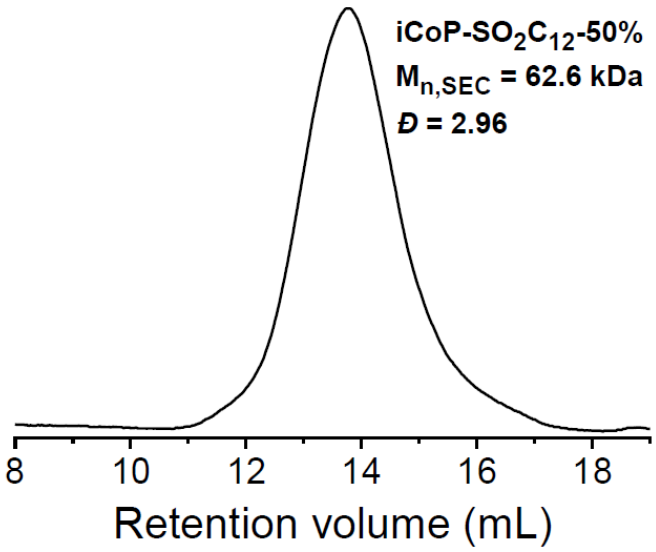

Figure B.2. Size exclusion chromatography (SEC) curve of iCoP-SO_2C_{12}-50% using THF as the mobile phase.

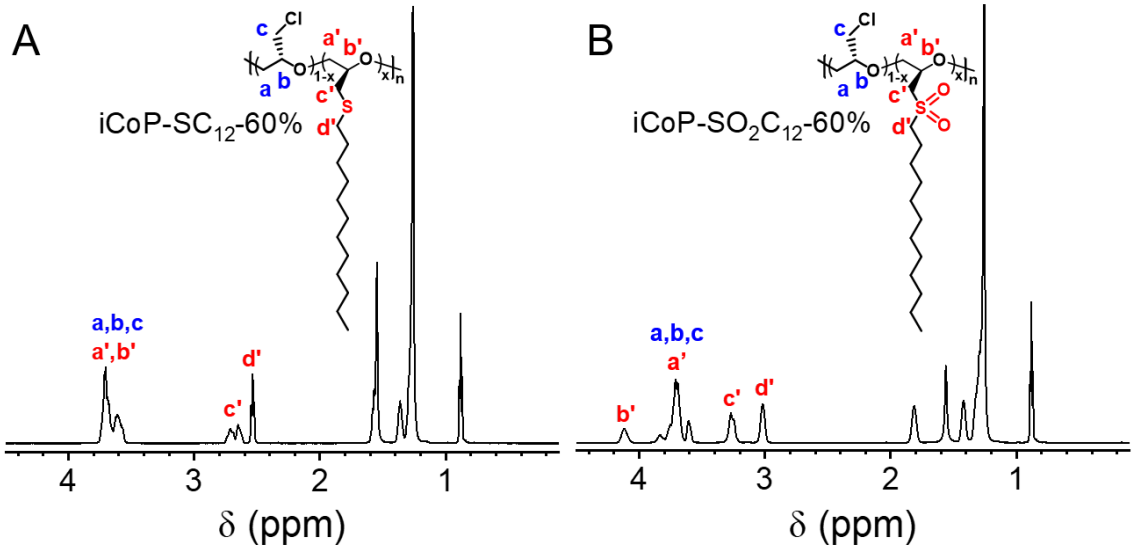

Figure B.3. ^{1}H NMR spectra of (A) iCoP-SC$_{12}$-60% and (B) iCoP-SO$_2$C$_{12}$-60% in CDCl$_3$.

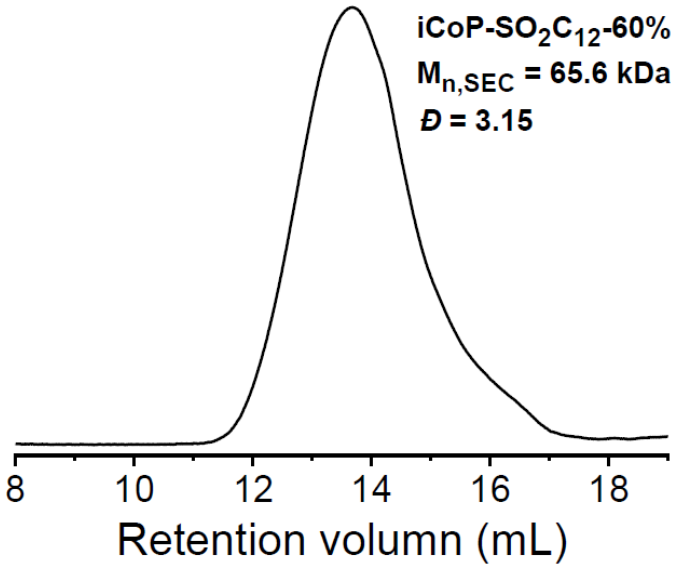

Figure B.4. Size exclusion chromatography (SEC) curve of iCoP-SO_2C_{12}-60% using THF as the mobile phase.

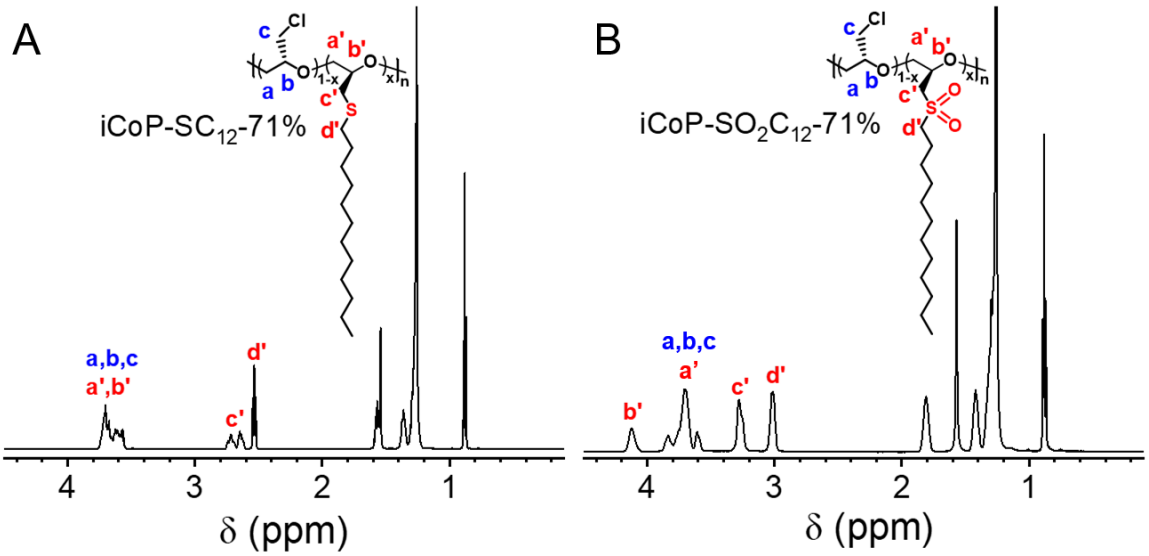

Figure B.5. ^{1}H NMR spectra of (A) iCoP-SC_{12}-71% and (B) iCoP-SO_2C_{12}-71% in $CDCl_3$.

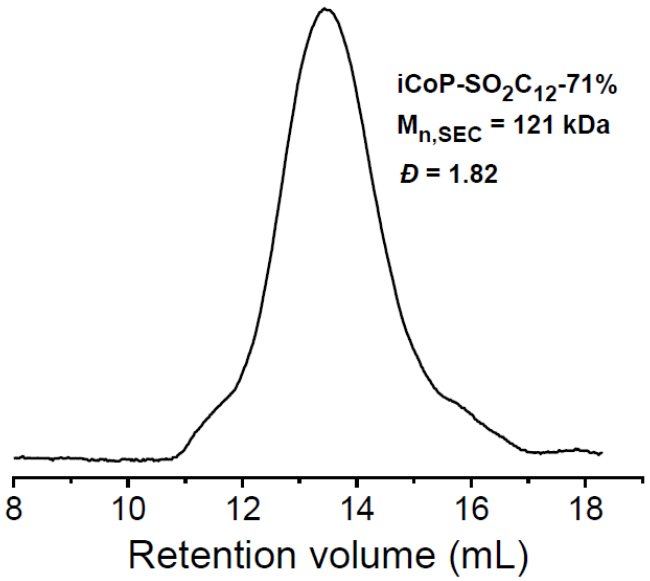

Figure B.6. Size exclusion chromatography (SEC) curve of iCoP-SO_2C_{12}-71% using THF as the mobile phase.

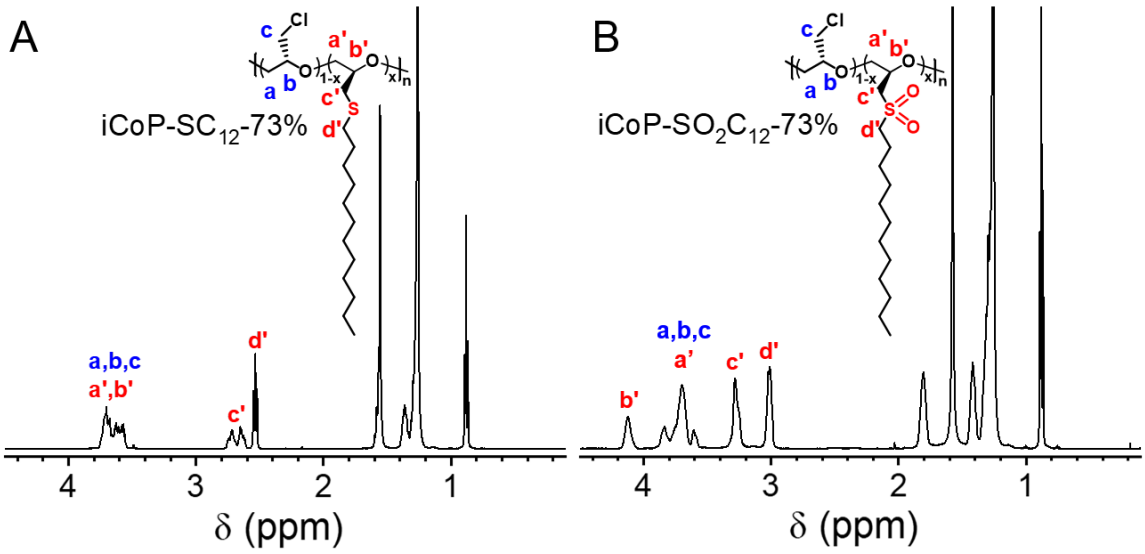

Figure B.7. ^{1}H NMR spectra of (A) iPOP-SC$_{12}$-73% and (B) iPOP-SO$_2$C$_{12}$-73% in CDCl$_3$.

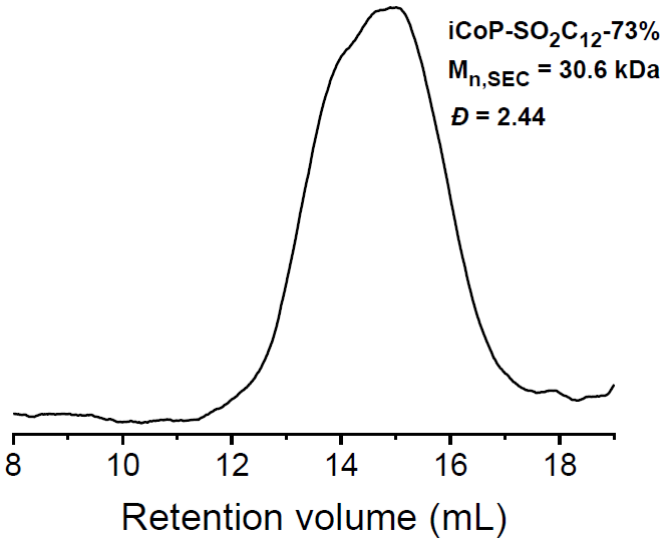

Figure B.8. Size exclusion chromatography (SEC) curve of iCoP-SO_2C_{12}-73% using THF as the mobile phase.

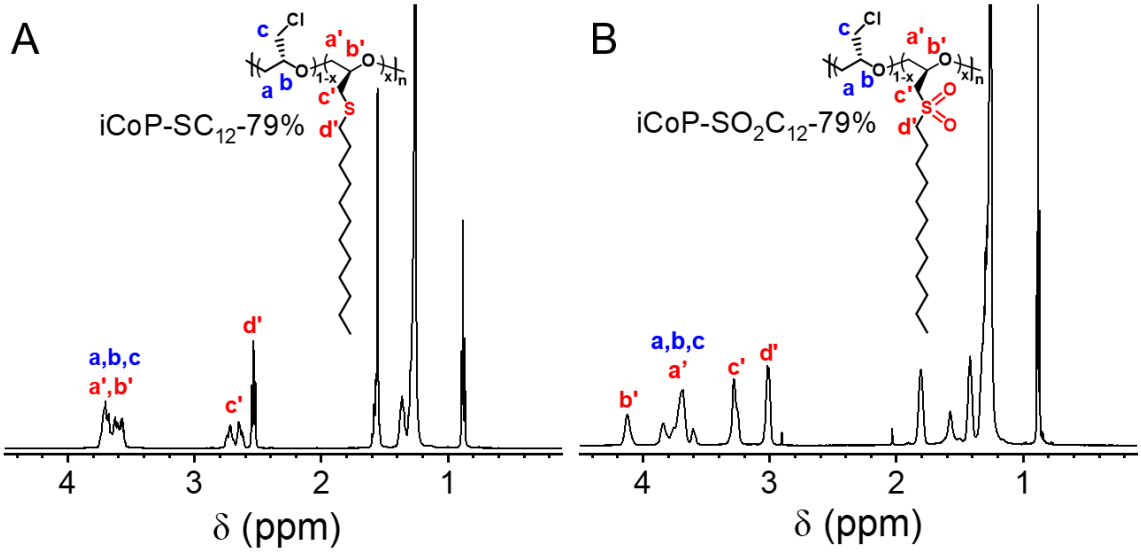

Figure B.9. ^{1}H NMR spectra of (A) iCoP-SC_{12}-79% and (B) iCoP-SO_2C_{12}-79% in $CDCl_3$.

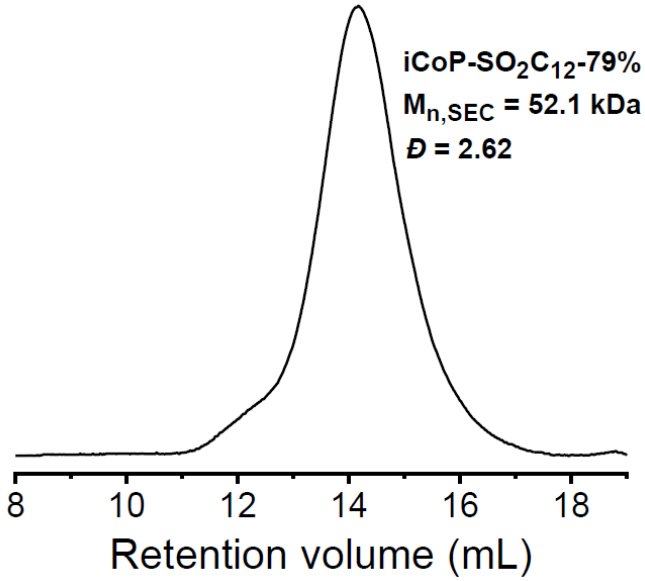

Figure B.10. Size exclusion chromatography (SEC) curve of iCoP-SO_2C_{12}-79% using THF as the mobile phase.

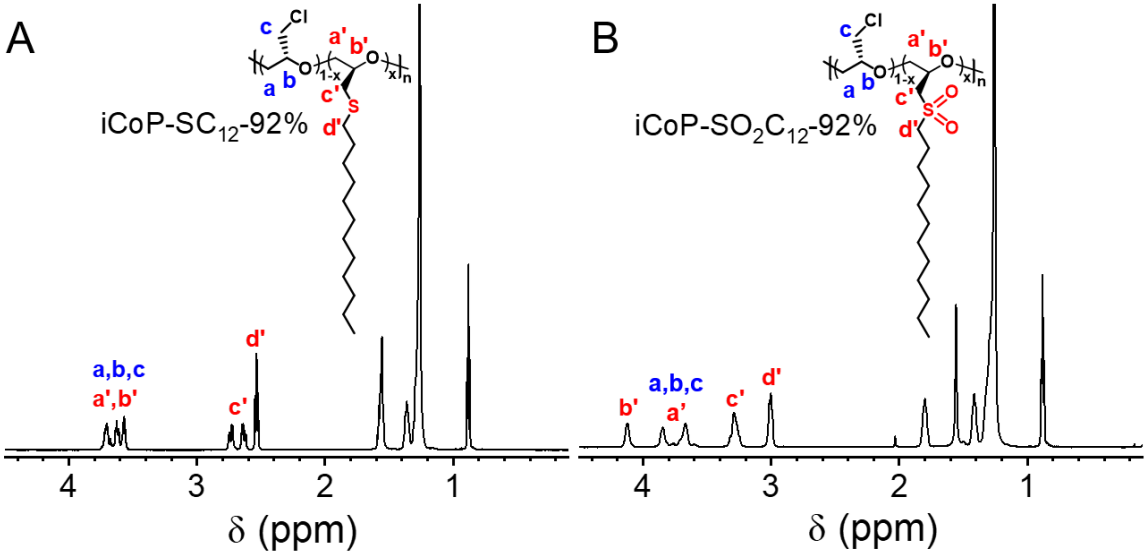

Figure B.11. ^{1}H NMR spectra of (A) iCoP-SC_{12}-92% and (B) iCoP-SO_2C_{12}-92% in $CDCl_3$.

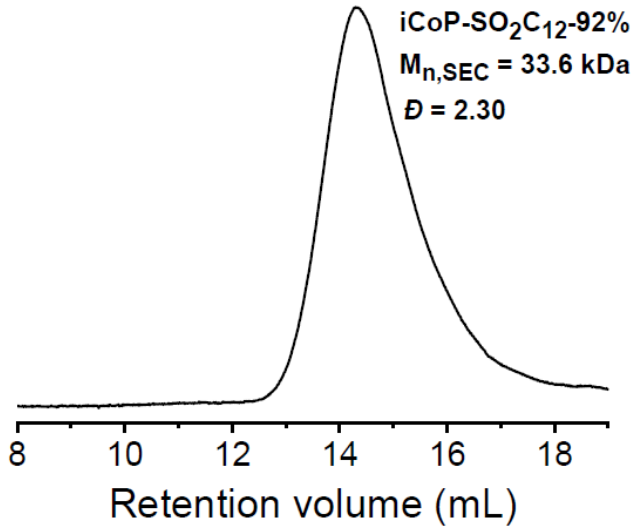

Figure B.12. Size exclusion chromatography (SEC) curve of iCoP-SO_2C_{12}-92% using THF as the mobile phase.

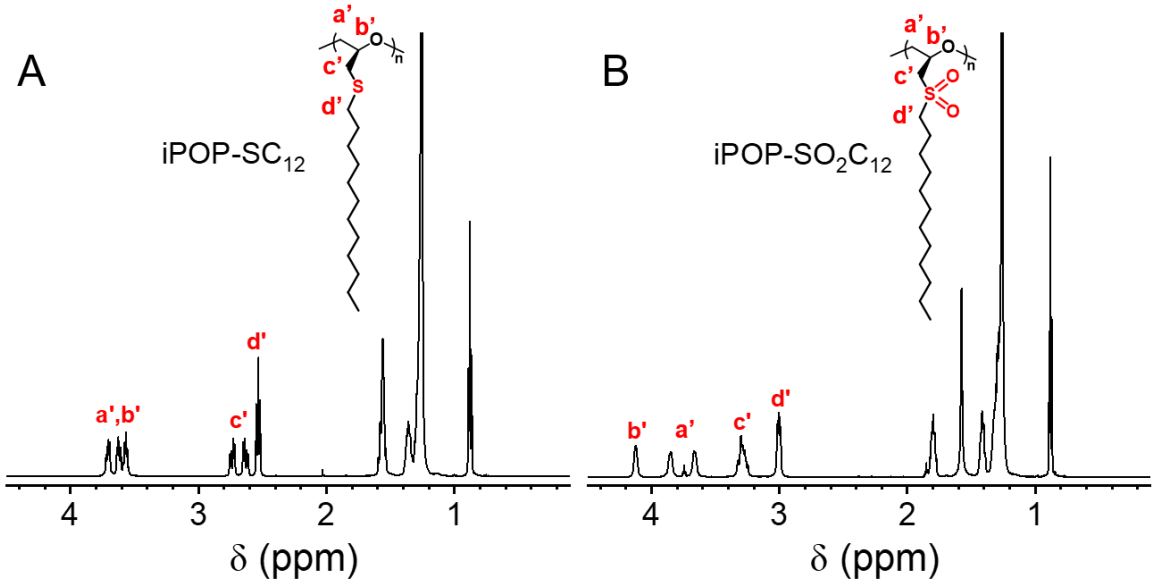

Figure B.13. ^{1}H NMR spectra of (A) iPoP-SC_{12} and (B) iPoP-SO_2C_{12} in $CDCl_3$.

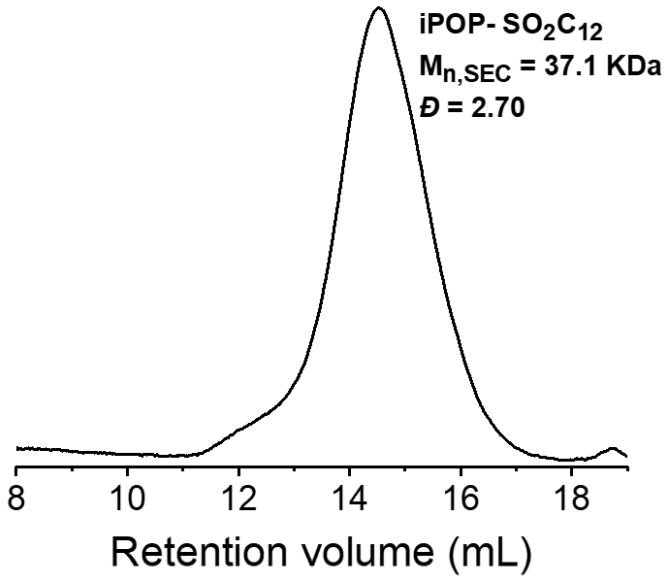

Figure B.14. Size exclusion chromatography (SEC) curve of iPoP-SO_2C_{12} using THF as the mobile phase.

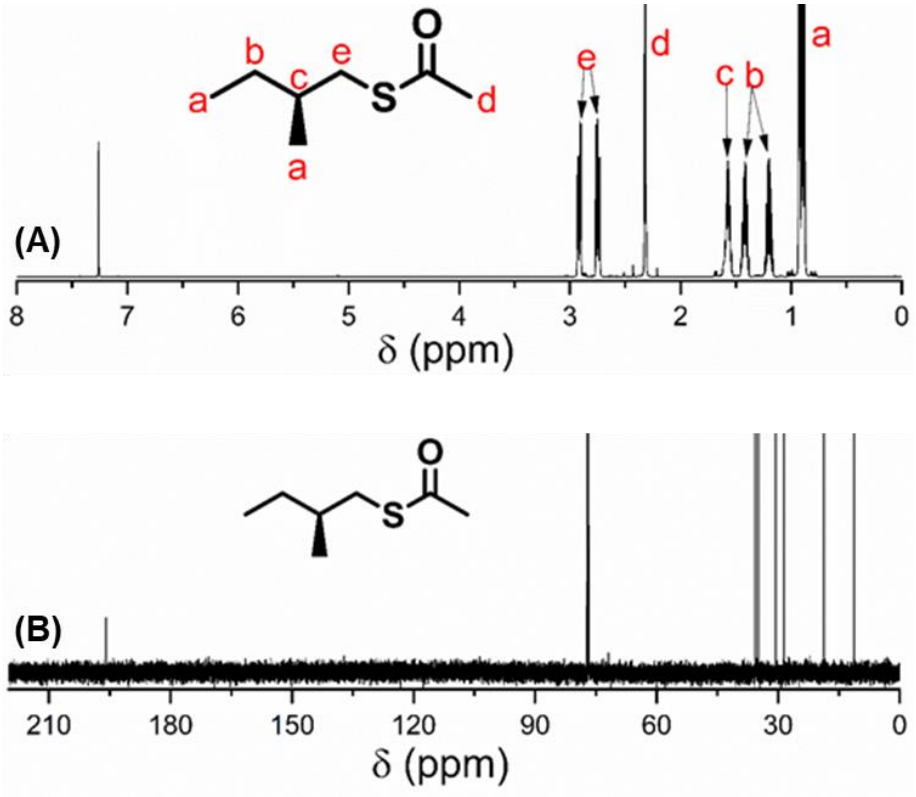

Figure B.15. (A) ^{1}H and (B) ^{13}C NMR spectra of (*S*)-S-(2-methylbutyl) ethanethioate in $CDCl_3$.

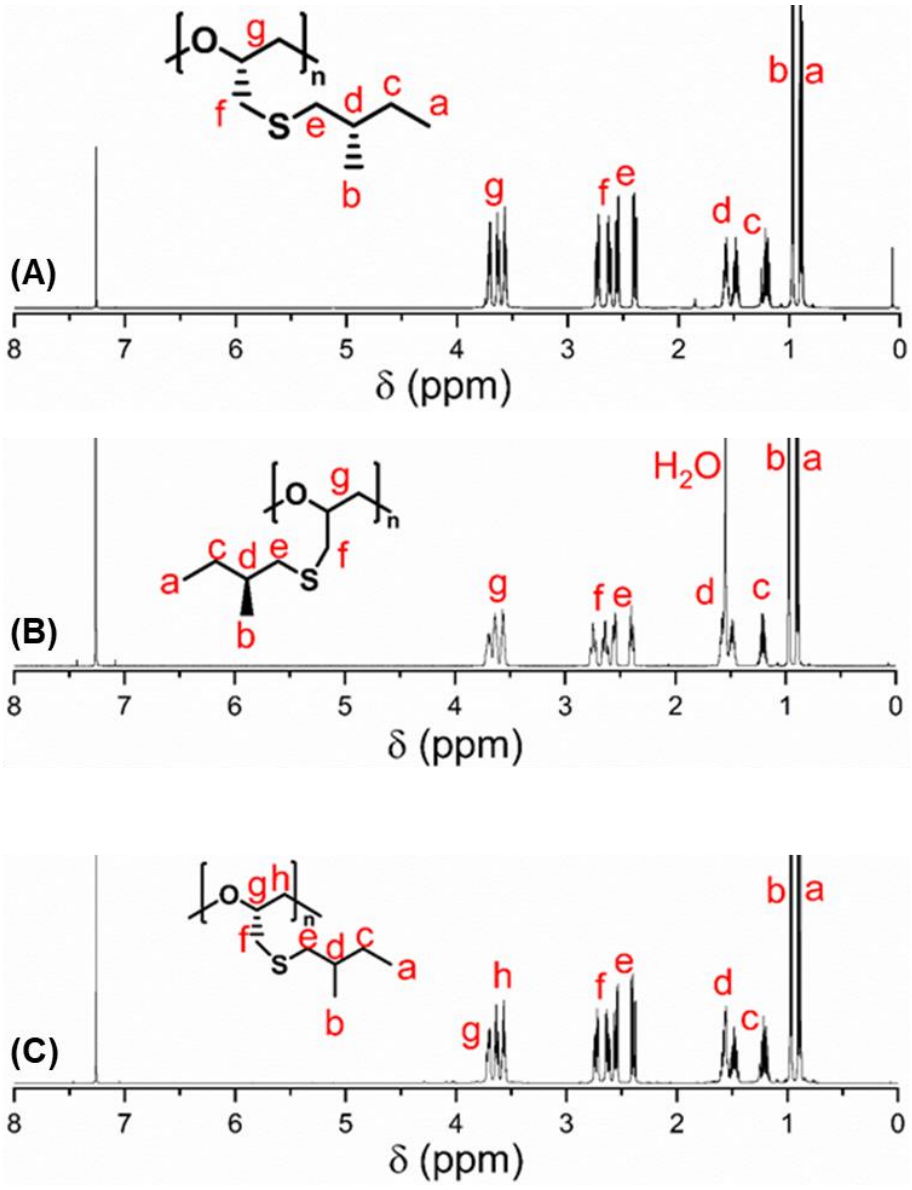

Figure B.16. ^{1}H NMR spectra of (A) iPOP-SbC$_{5s}$, (B) aPOP-SbC$_{5s}$, (C) iPOP-SbC$_{5}$ in CDCl$_{3}$.

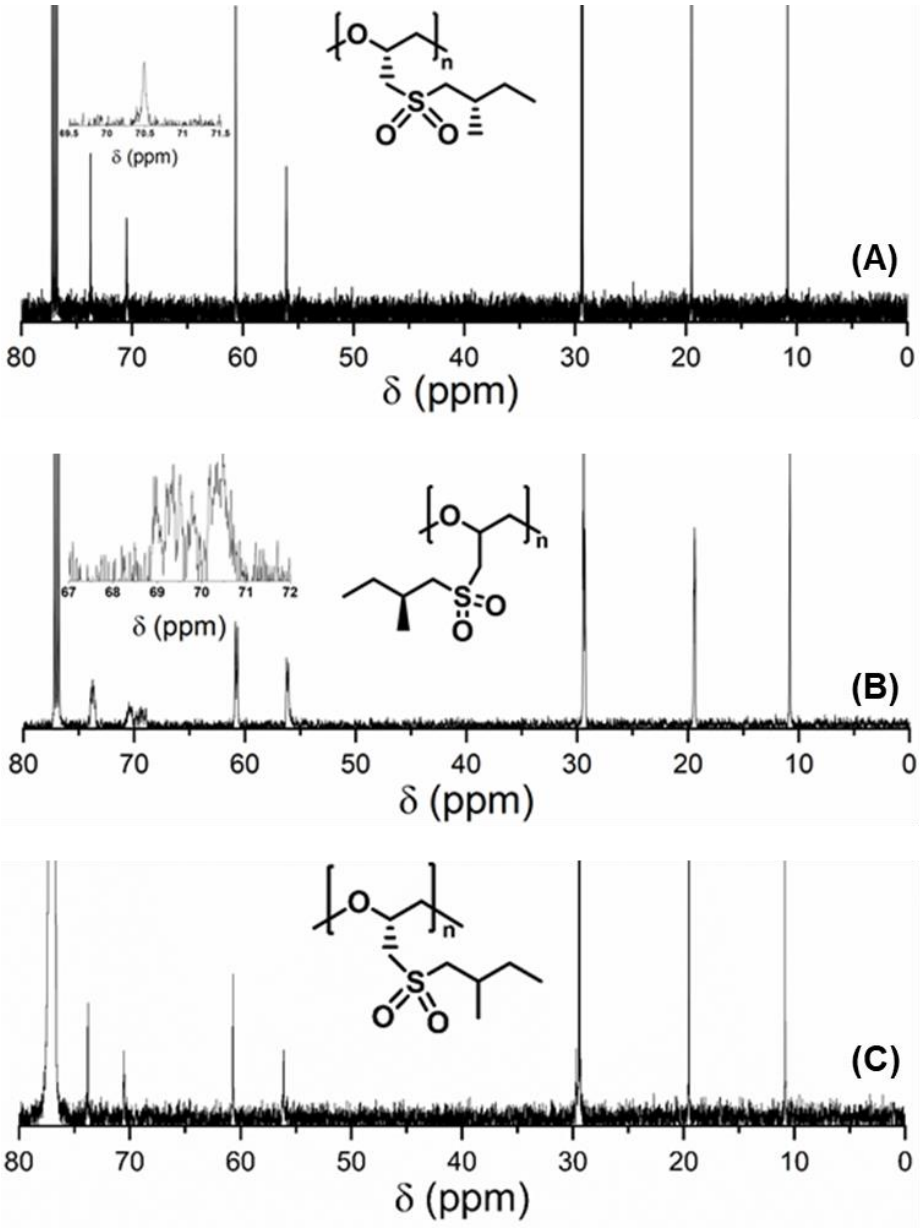

Figure B.17. ^{13}C NMR spectra of (A) iPOP-SO_2bC_{5s}, (B) aPOP-SO_2bC_{5s}, (C) iPOP-SO_2bC_5 in $CDCl_3$.

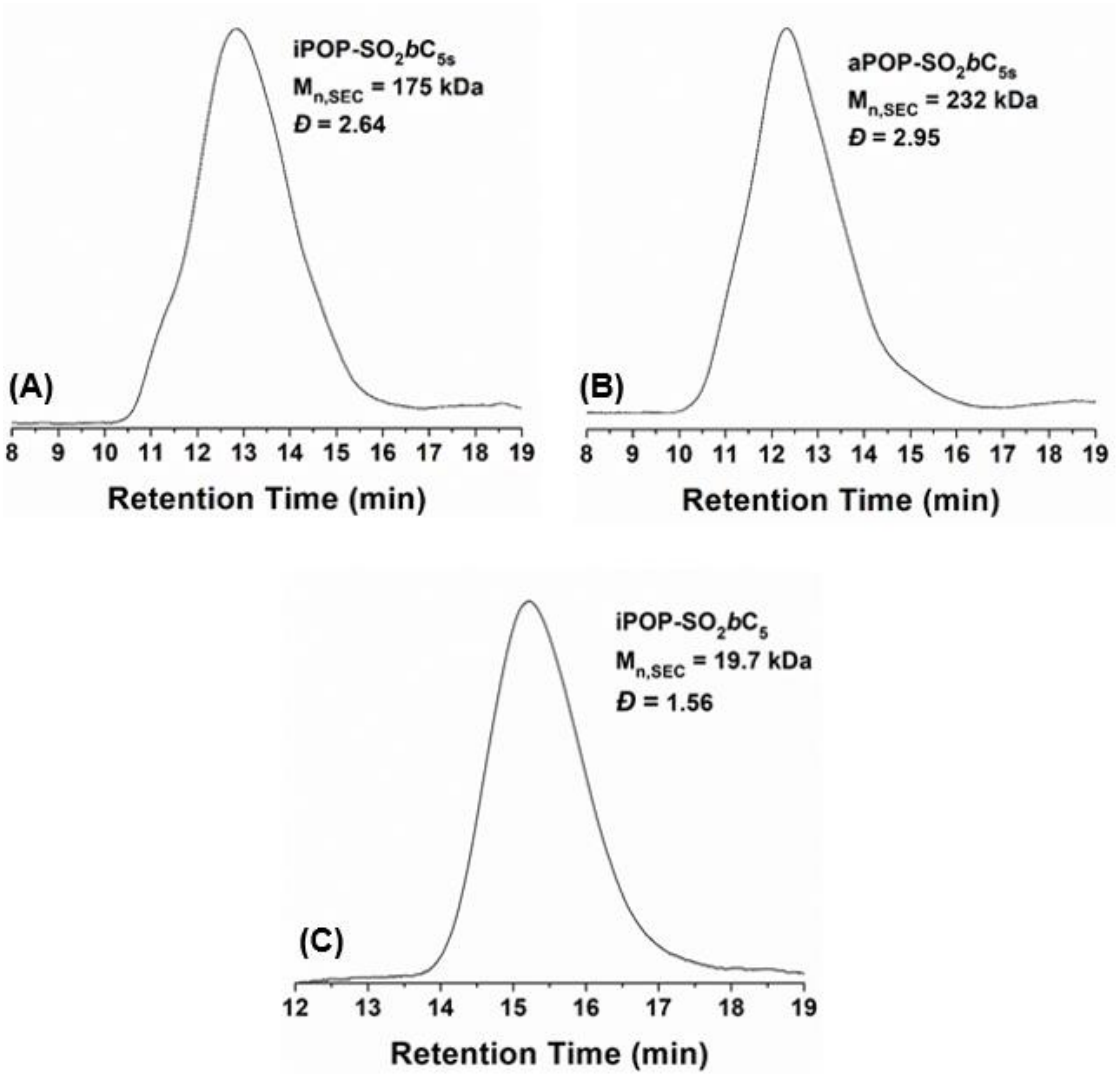

Figure B.18. Size exclusion chromatography curves of (A) iPOP-SO_2bC_{5s}, (B) aPOP-SO_2bC_{5s}, (C) iPOP-SO_2bC_5 obtained from PL-GPC-20 using THF as the mobile phase.

Chapter 4: SmC*-like Self-Assembly in Mesogen-Free Liquid Crystalline Polyethers with Sulfonylated Branched Alkyl Side Chains

For the work presented in this chapter, I synthesized and characterized all the polymers, measured the optical activities and conducted preliminary differential scanning calorimetry (DSC) analysis of all the polymers, X-ray diffraction (XRD) studies of some of the polymers at the University of Tennessee Knoxville, and participated in the discussion of DSC and XRD data and the identification of structures. Dr. Man-Hin Kwok performed in-depth DSC and polarized light microscopy experiments and prepared the samples for XRD in Brookhaven National Laboratory by Dr. Ruipeng Li. Dr. Kwok also conducted the electric displacement-electric field measurement.

Abstract

This Chapter describes our continued effort to seek the chiral smectic C (SmC*) liquid crystalline phase in mesogen-free sulfonylated liquid crystalline polyethers via a new molecular design. Chiral poly(oxypropylene) polyethers containing sulfonylated methyl-branched alkyl side chains with a -$(CH_2)_3O$- spacer between the sulfonyl and the branched alkyl group were designed and synthesized. In contrast to the linear *n*-alkyl side chains, the methyl-branched alkyl side chains induced chain tilting (ca. 60-70° from the fiber axis) in the smectic layers. When double chirality existed in both the main chain and the side chains, a crystalline structure was observed after mechanical stretching. Intriguingly, when single chirality existed in either the backbone or the side chains, a liquid crystalline smectic C*-like phase was obtained. The electric displacement-electric field study, however, did not show typical ferroelectric switching, although the dielectric constants were relatively high for these liquid crystalline polymers. This is likely because the dipole-dipole interactions among neighboring sulfonyl groups along the main chain were so strong that the ferroelectric switching was hindered. For the future work, it is desired to weaken the dipole-dipole interaction to achieve ferroelectricity in these mesogen-free liquid crystalline polymers.

4.1. Introduction

Ferroelectric liquid crystalline polymers have potential for various electronic and optical applications driven by relatively low electric fields (e.g., <10 MV/m) because of their higher molecular motion in the liquid crystalline state.[1-10] However, conventional chiral smectic C (SmC*) liquid crystalline polymers exhibit rather small spontaneous polarizations (P_s), often < 0.01 C/m^2,[8,9] which have hindered the further development. The low Ps values of conventional liquid crystalline polymers are commonly attributed to the use of bulky aromatic mesogens and polar functional groups with small dipole moments. On the other hand, although ferroelectric crystalline polymers, such as poly(vinylidene fluoride) (PVDF) and its random copolymers, can achieve P_s values of 0.05-0.14 C/m^2,[10-12] very high electric fields (E > 200 MVm^{-1}) are required to achieve saturation polarization due to the crystalline structures.

Aromatic mesogen-free liquid crystalline polymers are promising for achieving large Ps values when highly dipolar sulfonyl groups with a large dipole moment (4.5 Debye or D) are incorporated into the polymer chains.[13-21] However, it has been difficult to induce ferroelectric domains in these polymers. For example, smectic A (SmA) self-assembly is often reported because of the C_{2h} symmetry. To break the C_{2h} symmetry, chirality should be introduced into either the main chain or the side chains of mesogen-free liquid crystalline polymers, and tilted-chain smectic[9,22] or columnar[23,24] liquid crystalline phases should be achieved.

In a series of studies,[25-28] our research group and our collaborators have design and synthesized various isotactic polyoxypropylene (iPOP) with alkylsulfonyl side chains. When the alkyl side chains are *n*-alkyl, the iPOP main chains adopt a 2_1 helical conformation with perpendicular side chains in the crystalline structure.[25] Chapter 2 described an effort to weaken the dipole-dipole interactions by moving the sulfonyl groups away from the main chain,[26] and in Chapter 3, we

systematically reduced the grafting density of alkylsulfonyl side chains.[27] However, both strategies failed to induce any chain-tilting in the smectic layers. Interestingly, when a chiral methyl branch is introduced into the short sulfonylated side chains of iPOPs, i.e., iPOP-SO_2bC_{5S}, the fibers of this polyether drawn from the melt exhibited a crystalline structure with tilted side chains,[28] as mentioned in Chapter 3. Nevertheless, no ferroelectric SmC* phase was observed.

In this Chapter, we introduce chirality into either the backbone or the side chains or both of polyoxypropylenes (POPs) and a -$(CH_2)_3O$- spacer between the sulfonyl group and the methyl-branched alkyl side chain (Scheme 4.1). Intriguingly, the side chains tilt at about 60-70° from the 2_1 helical main chain. When both the main and side chains contain a chiral center (i.e., double chirality), crystalline structures are observed. However, when single chirality exists in either the backbone or side chains, a SmC*-like phase is achieved.

4.2 Experimental Section

4.2.1. Materials

2-Octanol (Fisher Chemical), 1-octanol (Fisher Chemical), thioacetic acid (97%, Acros Organics), *(R)*-2-octanol (99%, Acros Organics), (*R*)-2-decanol (97%, MilliporeSigma), 2-decanol (98%, Alfa Aesar), allyl bromide (99%, Acros Organics), sodium hydride (60% dispersion in paraffin oil, TCI America), 2,2-dimethoxy-2-phenylacetophenone (99% Acros Organics), 3-chloroperoxybenzoic acid (*m*-CPBA, 70-75% balance 3-chlorobenzoic acid and water, Acros Organics), 2,2-dimethoxy-2-phenylacetophenone (99%, ACROS Organics), and *N*,*N*-dimethylacetamide (99.5%, extra dry, Acros Organics) were used as received. Diethyl ether (99.8%, certified ACS, Fisher Chemical) and (*R*)-(-)-epichlorohydrin [(*R*)-(-)-ECH, 98%, TCI America] were each stirred with calcium hydride (93%, Acros Organics) and distilled prior to use.

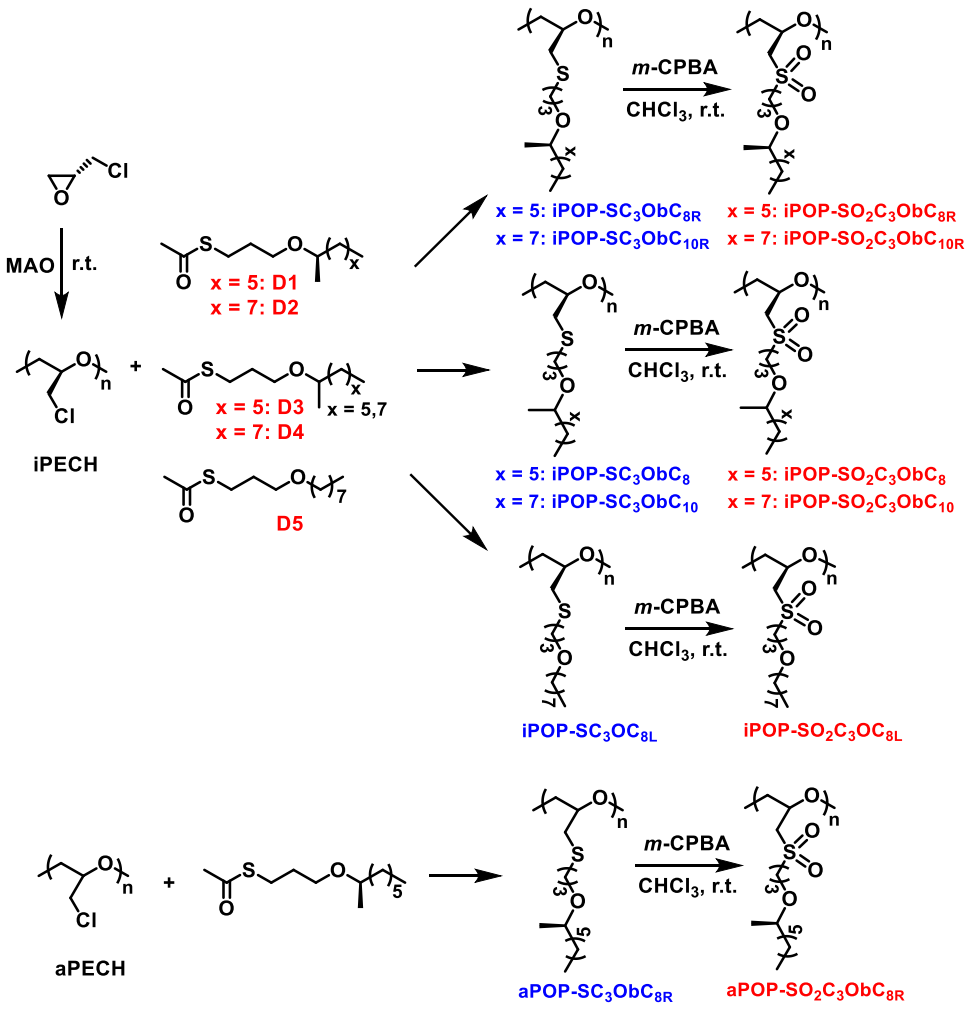

Scheme 4.1. Synthesis of Isotactic and Atactic Polyethers with Chiral and Racemic Branched Sulfonylated Pendant Groups and an Isotactic Polyether with Linear Alkylsulfonylated Pendant Groups.

Atactic polyepichlorohydrin (aPECH) with a weight-average molecular weight (M_w) of ~700,000 Da (from Millipore Sigma) was used as received. Modified methylaluminoxane (MMAO-12, 7 wt.% aluminum in toluene) was purchased from Millipore Sigma, stored in the freezer inside a nitrogen glovebox, and used directly. iPECH was prepared by MMAO-12-catalyzed ring-opening polymerization of (*R*)-(-)-ECH in a glove box at room temperature as described previously.[25] The solution of 15.0% $NaOCH_2CH_3$ in CH_3CH_2OH was made by adding sodium metal into absolute ethanol under N_2 and stirring the mixture until the metal completely disappeared. Tetrahydrofuran (THF, Fisher Scientific) was dried with sodium/benzophenone and used immediately. All other chemicals and solvents were obtained from either Fisher Scientific or Millipore Sigma and used as received.

4.2.2. Synthesis of Isotactic and Atactic Polyethers with Branched and Linear Thioether Pendant Groups.

Isotactic and atactic polyethers with chiral and racemic branched thioether pendant groups and an iPOP with linear thioether pendant groups were synthesized according to Scheme 4.1 by reacting isotactic and atactic PECHs, respectively, with corresponding branched or linear thiolates, formed from D1-D5 under the basic conditions. The synthesis and characterization of D1-D5 are described in Section C.1 of Appendix C (Figures. C.1 – C.10).

Synthesis of iPOP-SC_3ObC_{8R}. Shown below is the synthesis procedure for iPOP-SC_3ObC_{8R}, using iPECH and (*R*)-*S*-(3-(octan-2-yloxy)propyl) ethanethioate (D1). All other polyethers with thioether pendant groups were synthesized via the same procedure. iPECH (0.103 g, 1.11 mmol of -CH_2Cl) was weighed into a 20 mL scintillation vial, followed by the addition of *N*,*N*-dimethylacetamide (DMAc) (10 mL). The vial was capped tightly and shaken on a platform shaker overnight. Sodium ethoxide (0.113 g, 1.81 mmol, from a solution of 15.0% sodium ethoxide in

ethanol) and D1 (0.476 g, 1.92 mmol) were added into a 50 mL two-necked round bottom flask equipped with a magnetic stir bar and a gas flow control adaptor. After the mixture of the sodium ethoxide solution and D1 was stirred at room temperature for 30 min, the reaction flask was placed in an oil bath with a preset temperature of 100 ℃. The mixture of iPECH and DMAc was shaken and heated to form a clear solution with a reduced viscosity and added into the reaction flask. Shortly, the reaction mixture became opaque. After the reaction proceeded at 100 ℃ under the stirring condition for 24 h, the mixture was precipitated in water, and the precipitate was collected by vacuum filtration. The obtained polymer was then dissolved in THF (3 mL) and precipitated in methanol 3 times. The purified polymer was collected and dried in a vacuum oven at 60 ℃ overnight, yielding a clear, highly viscous liquid (0.199 g, 69.2% yield). Proton nuclear magnetic resonance (^{1}H NMR) (500 MHz, $CDCl_3$) δ (ppm) = 3.71 – 3.50 (m, -OC*H*$_2$C*H*(CH_2S-)- and -OC*H*(CH_3)CH_2-, 4H), 3.45 – 3.30 (m, -CH_2C*H*$_2$OCH(CH_3)CH_2-, 2H), 2.82 – 2.54 (m, -CHC*H*$_2$SC*H*$_2$$CH_2$-, 4H), 1.88 – 1.75 (m, -SCH_2C*H*$_2$$CH_2$O-, 2H), 1.57 – 1.45 and 1.40 – 1.21 (m, -OCH(CH_3)(C*H*$_2$)$_5$$CH_3$, 10H), 1.11 (d, -OCH(C*H*$_3$)CH_2-, 3H), 0.88 (t, -CH_2C*H*$_3$, 3H) (Figure 1A). Carbon-13 NMR (^{13}C NMR) (126 MHz, $CDCl_3$) δ (ppm) = 79.38, 75.53, 71.22, 66.68, 36.71, 33.93, 31.88, 30.26, 29.93, 29.44, 25.58, 22.65, 19.74, 14.12. Size-exclusion chromatography (SEC) results with THF as eluent: number-average molecular weight $M_{n,SEC}$ = 58.8 kDa and dispersity (*Đ*) = 1.78, relative to PS standards. Specific optical rotation [α] = -23.7° (chloroform).

Synthesis of iPOP-SC$_3$ObC$_{10R}$. Yield: 49.7%. ^{1}H NMR (600 MHz, $CDCl_3$) δ (ppm) = 3.70 – 3.51 (m, -OC*H*$_2$C*H*(CH_2S-)- and -OC*H*(CH_3)$CH_2$$CH_2$-, 4H), 3.45 – 3.32 (m, -$SCH_2$$CH_2$C*H*$_2$O-, 2H), 2.78 – 2.58 (m, -CHC*H*$_2$SC*H*$_2$$CH_2$-, 4H), 1.85 – 1.78 (m, -SCH_2C*H*$_2$$CH_2$O-, 2H), 1.56 – 1.20 (m, -OCH(CH_3)(C*H*$_2$)$_7$$CH_3$, 14H), 1.11 (d, -OCH(C*H*$_3$)CH_2-, 3H), 0.88 (t, -$CH_2$$CH_2$C*H*$_3$, 3H).

SEC results with THF as eluent: $M_{n,SEC}$ = 26.0 kDa and $Đ$ = 1.97, relative to PS standards. Specific optical rotation [α] = -16.5° (chloroform).

Synthesis of iPOP-SC₃ObC₈. Yield: 43.8%. ^{1}H NMR (600 MHz, $CDCl_3$) δ (ppm) = 3.71 – 3.51 (m, -OC*H*$_2$C*H*(CH$_2$S-)- and -OC*H*(CH$_3$)CH$_2$CH$_2$-, 4H), 3.44 – 3.31 (m, -CHC*H*$_2$OCH(CH$_3$)CH$_2$-, 2H), 2.78 – 2.59 (m, -CHC*H*$_2$SC*H*$_2$CH$_2$-, 4H), 1.85 – 1.78 (m, -SCH$_2$C*H*$_2$CH$_2$O-, 2H), 1.56 – 1.25 (m, -OCH(CH$_3$)(C*H*$_2$)$_5$CH$_3$, 10H), 1.11 (d, -OCH(C*H*$_3$)CH$_2$-, 3H), 0.88 (t, -CH$_2$C*H*$_3$, 3H). SEC results with THF as eluent: $M_{n,SEC}$ = 63.8 kDa and $Đ$ = 2.18, relative to PS standards. Specific optical rotation [α] = -14.8° (chloroform).

Synthesis of iPOP-SC₃ObC₁₀. Yield: 63.3%. ^{1}H NMR (500 MHz, $CDCl_3$) δ (ppm) = 3.70 – 3.53 (m, -OC*H*$_2$C*H*(CH$_2$S-)- and -OC*H*(CH$_3$)CH$_2$CH$_2$-, 4H), 3.46 – 3.30 (m, -SCH$_2$CH$_2$C*H*$_2$O-, 2H), 2.80 – 2.57 (m, -CHC*H*$_2$SC*H*$_2$CH$_2$-, 4H), 1.86 – 1.77 (m, -SCH$_2$C*H*$_2$CH$_2$O-, 2H), 1.54 – 1.22 (m, -OCH(CH$_3$)(C*H*$_2$)$_7$CH$_3$, 14H), 1.11 (d, -OCH(C*H*$_3$)CH$_2$-, 3H), 0.88 (t, -CH$_2$C*H*$_3$, 3H). SEC results with THF as eluent: $M_{n,SEC}$ = 153 kDa and $Đ$ = 5.97, relative to PS standards. Specific optical rotation [α] = -11.3° (chloroform).

Synthesis of iPOP-SC₃OC₈L. Yield: 59.7%. ^{1}H NMR (500 MHz, $CDCl_3$) δ (ppm) = 3.77 – 3.54 (m, -OC*H*$_2$C*H*(CH$_2$S-)- 3H), 3.50 – 3.36 (m, -SCH$_2$CH$_2$C*H*$_2$OC*H*$_2$CH$_2$-, 4H), 2.79 – 2.57 (m, -CHC*H*$_2$SC*H*$_2$CH$_2$-, 4H), 1.88 – 1.79 (m, -SCH$_2$C*H*$_2$CH$_2$O-, 2H), 1.60 – 1.21 (m, -OCH$_2$(C*H*$_2$)$_6$CH$_3$, 12H), 0.88 (t, -CH$_2$CH$_2$C*H*$_3$, 3H). SEC results with THF as eluent: $M_{n,SEC}$ = 52.5 kDa and $Đ$ = 7.25, relative to PS standards. Specific optical rotation [α] = -13.3° (chloroform).

Synthesis of aPOP-SC₃ObC₈R. Yield: 50.5%. ^{1}H NMR (500 MHz, $CDCl_3$) δ (ppm) = 3.68 – 3.52 (m, -OC*H*$_2$C*H*(CH$_2$S-)- and -OC*H*(CH$_3$)CH$_2$-, 4H), 3.46 – 3.30 (m, -CHC*H*$_2$OCH(CH$_3$)CH$_2$-, 2H), 2.70 – 2.59 (m, -CHC*H*$_2$SC*H*$_2$CH$_2$-, 4H), 1.86 – 1.77 (m, -SCH$_2$C*H*$_2$CH$_2$O-, 2H), 1.54 – 1.23 (m, -OCH(CH$_3$)(C*H*$_2$)$_5$CH$_3$, 10H), 1.11 (d, -OCH(C*H*$_3$)CH$_2$-, 3H), 0.88 (t, -CH$_2$C*H*$_3$, 3H) (Figure

1B). ^{13}C NMR (126 MHz, $CDCl_3$) δ (ppm) = 79.25, 75.53, 70.60, 66.67, 36.69, 33.75, 31.87, 30.25, 29.91, 29.42, 25.57, 22.63, 19.73, 14.11. SEC results with THF as eluent: $M_{n,SEC}$ = 74.8 kDa and $Đ$ = 3.06, relative to PS standards. Specific optical rotation [α] = -7.2° (chloroform).

4.2.3. Synthesis of Atactic and Isotactic Polyethers with Branched and Linear Sulfonylated Pendant Groups

Synthesis of iPOP-$SO_2C_3ObC_{8R}$. All atactic and isotactic polyethers with branched and linear thioether pendant groups were oxidized using the same procedure. The following shows the synthesis of iPOP-$SO_2C_3ObC_{8R}$ as an example. 3-Chloroperoxybenzoic acid (*m*-CPBA) (0.297 g, 1.72 mmol) and iPOP-SC_3ObC_{8R} (0.187 g, 0.71mmol) were dissolved in chloroform (15 mL) in a 50 mL two-necked flask fitted with a gas flow control adaptor. After the mixture was stirred with a magnetic stir bar at room temperature for 3 h, the solvent was evaporated using a rotary evaporator. The solid was washed with 1 M NaOH (20 mL), and the liquid was decanted. The remaining solid was dissolved with THF, and the solution was concentrated by rotary evaporation to ~5 mL. The concentrated polymer solution was precipitated in methanol three times. The final precipitate was collected and dried in a vacuum oven at 60 ℃ overnight, yielding a viscous, clear polymer (0.182 g, 86.6%). ^1H NMR (600 MHz, $CDCl_3$) δ (ppm) = 4.18 – 3.63 (m, -OC*H*$_2$C*H*(CH_2SO_2-)-, 3H), 3.61 – 3.43 (m, -$SO_2CH_2CH_2CH_2$O-, 2H), 3.40 – 3.22 (m, -C*H*$_2SO_2(CH_2)_3OCH(CH_3)CH_2$-, 3H), 3.17 – 3.07 (m, -$CH_2SO_2CH_2CH_2CH_2$O-, 2H), 2.11 – 1.98 (m, -$SO_2CH_2CH_2CH_2$O-, 2H), 1.56 – 1.23 (m,-$OCH_2(CH_2)_5CH_3$, 10H), 1.10 (d, -OCH(C*H*$_3$)CH_2-, 3H), 0.88 (t, -CH_2CH_3, 3H). SEC results with THF as eluent: $M_{n,SEC}$ = 51.6 kDa and $Đ$ = 2.28, relative to PS standards. Specific optical rotation [α] = -41.0° (chloroform).

Synthesis of iPOP-$SO_2C_3ObC_{10R}$. Yield: 80.6%. ^1H NMR (600 MHz, $CDCl_3$) δ (ppm) = 4.17 – 3.63 (m, -OC*H*$_2$C*H*(CH_2SO_2-)-, 3H), 3.59 – 3.44 (m, -$SO_2CH_2CH_2CH_2$O-, 2H), 3.40 – 3.22 (m,

-C*H*$_2$SO$_2$(CH$_2$)$_3$OC*H*(CH$_3$)CH$_2$-, 3H), 3.17 – 3.04 (m, -CH$_2$SO$_2$C*H*$_2$CH$_2$CH$_2$O-, 2H), 2.12 – 1.97 (m, -SO$_2$CH$_2$C*H*$_2$CH$_2$-, 2H), 1.57 – 1.25 (m, -OCH$_2$(C*H*$_2$)$_7$CH$_3$, 14H), 1.11 (d, -OCH(C*H*$_3$)CH$_2$-, 3H), 0.88 (t, -CH$_2$C*H*$_3$, 3H). SEC results with THF as eluent: $M_{n,SEC}$ = 24.6 kDa and *Đ* = 2.00, relative to PS standards. Specific optical rotation [α] = -33.1° (chloroform).

*Synthesis of iPOP-SO$_2$C$_3$ObC$_8$***.** Yield: 32.2%. ^{1}H NMR (600 MHz, CDCl$_3$) δ (ppm) = 4.15 – 3.64 (m, -OC*H*$_2$C*H*(CH$_2$SO$_2$-)-, 3H), 3.59 – 3.43 (m, -SO$_2$CH$_2$CH$_2$C*H*$_2$O-, 2H), 3.40 – 3.22 (m, -C*H*$_2$SO$_2$(CH$_2$)$_3$OC*H*(CH$_3$)CH$_2$-, 3H), 3.15 – 3.07 (m, -CH$_2$SO$_2$C*H*$_2$CH$_2$CH$_2$O-, 2H), 2.10 – 2.00 (m, -SO$_2$CH$_2$C*H*$_2$CH$_2$O-, 2H), 1.57 – 1.21 (m, -OCH(CH$_3$)(C*H*$_2$)$_5$CH$_3$, 10H), 1.10 (d, -OCH(C*H*$_3$)CH$_2$-, 3H), 0.88 (t, -CH$_2$C*H*$_3$, 3H). SEC results with THF as eluent: $M_{n,SEC}$ = 27.4 kDa and *Đ* = 2.81, relative to PS standards. Specific optical rotation [α] = -26.9° (chloroform).

Synthesis of iPOP-SO$_2$C$_3$ObC$_{10}$. Yield: 36.1%. ^{1}H NMR (500 MHz, CDCl$_3$) δ (ppm) = 4.18 – 3.67 (m, -OC*H*$_2$C*H*(CH$_2$SO$_2$-), 3H), 3.60 – 3.44 (m, -SO$_2$CH$_2$CH$_2$C*H*$_2$O-, 2H), 3.40 – 3.21 (m, -C*H*$_2$SO$_2$(CH$_2$)$_3$OC*H*(CH$_3$)CH$_2$-, 3H), 3.18 – 3.06 (m, -CH$_2$SO$_2$C*H*$_2$CH$_2$CH$_2$O-, 2H), 2.11 – 1.98 (m, -SO$_2$CH$_2$C*H*$_2$CH$_2$O-, 2H), 1.55 – 1.23 (m, -OCH(CH$_3$)(C*H*$_2$)$_7$CH$_3$, 14H), 1.11 (d, -OCH(C*H*$_3$)CH$_2$-, 3H), 0.88 (t, -CH$_2$C*H*$_3$, 3H). SEC results with THF as eluent: $M_{n,SEC}$ = 16.2 kDa and *Đ* = 4.75, relative to PS standards. Specific optical rotation [α] = -23.0° (chloroform).

Synthesis of iPOP-SO$_2$C$_3$OC$_{8L}$. Yield: 46.1%. ^{1}H NMR (500 MHz, CDCl$_3$) δ (ppm) = 4.17 – 3.63 (m, -OC*H*$_2$C*H*(CH$_2$SO$_2$-)-, 3H), 3.55 – 3.37 (m, -C*H*$_2$OC*H*$_2$-, 4H), 3.34 – 3.05 (m, -C*H*$_2$SO$_2$C*H*$_2$-, 4H), 2.09 – 2.02 (m, -SO$_2$CH$_2$C*H*$_2$CH$_2$O-, 2H), 1.58 – 1.25 (m, -OCH$_2$(C*H*$_2$)$_6$CH$_3$, 12H), 0.88 (t, -CH$_2$C*H*$_3$, 3H) SEC results with THF as eluent: $M_{n,SEC}$ = 17.9 kDa and *Đ* = 3.27, relative to PS standards. Specific optical rotation [α] = -24.4° (chloroform).

Synthesis of aPOP-SO$_2$C$_3$ObC$_{8R}$. Yield: 21.2%. ^{1}H NMR (500 MHz, CDCl$_3$) δ (ppm) = 4.09 – 3.65 (m, -OC*H*$_2$C*H*(CH$_2$SO$_2$-)-, 3H), 3.60 – 3.41 (m, -SO$_2$CH$_2$CH$_2$C*H*$_2$O-, 2H), 3.37 – 3.08 (m, -

C*H*$_2$SO$_2$C*H*$_2$CH$_2$CH$_2$OC*H*(CH$_3$)CH$_2$-, 5H), 2.08 – 1.98 (m, -SO$_2$CH$_2$C*H*$_2$CH$_2$O-, 2H), 1.54 – 1.22 (m, -OCH(CH$_3$)(C*H*$_2$)$_5$CH$_3$, 10H), 1.10 (d, -OCH(C*H*$_3$)CH$_2$-, 3H), 0.88 (t, -CH$_2$C*H*$_3$, 3H). SEC results with THF as eluent: $M_{n,SEC}$ = 18.5 kDa and $Đ$ = 2.29, relative to PS standards. Specific optical rotation [α] = -9.7° (chloroform).

4.2.4. Fiber-Drawing Process

Fibers were drawn using tweezers from either the molten or liquid crystalline state on an Instec HCS402 hot stage (Instec, Inc., Boulder, CO). Specifically, the fiber-drawing temperatures were the following. iPOP-SO2C3ObC8R: ~120 °C, iPOP-SO2C3ObC8: ~100 °C, iPOP-SO2C3ObC10R: ~120 °C, iPOP-SO2C3ObC10: room temperature, aPOP-SO2C3ObC8R: room temperature, and iPOP-SO2C3ObC8L: ~90 °C.

4.2.5. Instrumentation and Characterization

^{1}H and ^{13}C NMR spectra were obtained using either a Varian VNMRS 500 NMR or a Varian VNMRS 600. SEC of all the poly(oxypropylene) polyethers synthesized in this work was performed on a PL-GPC 20 system (Polymer Laboratories, Inc.) comprising a refractive index detector, one PLgel 5 μm guard column (50 × 7.5 mm), and two PLgel 5 μm mixed-C columns (each 300 × 7.5 mm, linear molecular weight range of 200-2,000,000 Da). Filtered HPLC-grade tetrahydrofuran (THF) was used as the solvent, and during the analysis the flow rate was set at 1.0 mL/min. A set of narrow dispersity polystyrene (PS) standards (Scientific Polymer Products, Inc.) was used to calibrate the SEC system. Cirrus SEC software (Polymer Laboratories, Inc.) was used to analyze the data to obtain $M_{n,SEC}$ and $Đ$.

A PerkinElmer 241 polarimeter equipped with a sodium lamp with a wavelength of 589 nm was used to measure the optical activities of chiral poly(oxypropylene) polyethers with thioether and sulfonyl pendant groups in chloroform at ambient temperature (~20 °C). The integration time

for the measurements was 5 s. The polyethers were dissolved in $CHCl_3$ to obtain a concentration of ~ 10 mg/mL for the optical activity measurements. Three measurements were performed for each solution, and the average value was calculated and taken as the optical rotation. The specific optical rotations were obtained by using equation $[\alpha]_{\lambda}^{T}=\alpha/(cl)$, where [α] is the specific optical rotation at a specified wavelength (λ) and temperature (T), α is the optical rotation in degrees from the optical rotation measurements, c is the polymer concentration in $CHCl_3$ (units: g/mL), and *l* is the path length in dm (1 dm for the polarimeter used here). The unit of specific rotation is deg·mL/(g·dm), often abbreviated to degrees (°). The optical activity of a thin film of iPOP-SC_3ObC_{8R} on quartz was measured using the same polarimeter with an integration time of 5 s. The film was made by drop casting of a solution of iPOP-SC_3ObC_{8R} (16.2 mg) in chloroform (3.222 g) on a 1″ circular quartz (thickness: 1/16″), and the optical rotations were measured at 9 different positions. The average value was -0.024°, which is used directly here.

A TA Discovery DSC250 or a TA Q2000 instrument (TA Instruments, New Castle, DE) was used to perform differential scanning calorimetry (DSC) experiments. For each polymer sample, approximately 3 mg was used, and the scanning rate was either 10 °C/min or 5 °C/min. Polarized light microscopy (PLM) was performed on an Olympus BX60 (Olympus America, Inc., Center Valley, PA), equipped with an Instec HCS402 hot stage. Digital images were taken by a 16-megapixel AmScope digital camera.

Synchrotron X-ray diffraction (XRD) experiments were conducted at the 11-BM Complex Materials Scattering beamline of National Synchrotron Light Source II (NSLS-II), Brookhaven National Laboratory. The monochromatized X-ray wavelength was 0.0918 nm or 0.07293 nm. The diffraction data were collected using an in-vacuum Pilatus 800K detector (Dectris, Baden-Dättwil, Switzerland). The sample-to-detector distance was 259 mm, which was calibrated using silver

behenate with the first-order reflection at a scattering vector q = 1.076 nm^{-1}. The data acquisition time was 30 s or 10 s. Additional XRD experiments were performed using a Rigaku (Rigaku Americas Corporation, The Woodlands, TX) WAXD instrument (MacroMax 002^{+}) equipped with a Confocal Max-Flux® optic and a microfocus X-ray tube source operating at 45 kV and 0.88 mA. The X-ray wavelength was 0.1542 nm (Cu Kα). The XRD patterns were collected using a Fujifilm image plate scanned by a Cytiva Amersham Typhoon scanner at a resolution of 50 μm/pixel (Cytiva Company, Marlborough, MA). A Linkam THMS 600 hot stage equipped with a liquid nitrogen cooling accessory was used for temperature control (Linkam Scientific Instruments Ltd., Tadworth, UK). One-dimensional (1D) XRD curves were obtained by integration of the corresponding two-dimensional (2D) patterns using the xPolar software (Stonybrook Technology and Applied Research, Inc.). Additional XRD experiments were also carried out using a Xenocs Xeuss 3.0 SAXS Instrument as described in Section 2.2.2 of Chapter 2.

4.3. Results and Discussion

4.3.1. Synthesis of Isotactic and Atactic Polyethers with Branched and Linear Sulfonylated Pendant Groups

Isotactic and atactic polyethers with chiral or racemic methyl-branched sulfonylated side chains were prepared by the substitution of Cl atoms in the pendant groups of iPECH and aPECH with 3-(branched alkoxy)propanethiolates, formed in-situ from the corresponding thioacetates, and the subsequent oxidation of thioether linkages (Scheme 4.1). These polyethers are denoted as iPOP-$SO_2C_3ObC_{8R}$, iPOP-$SO_2C_3ObC_{10R}$, iPOP-$SO_2C_3ObC_8$, iPOP-$SO_2C_3ObC_{10}$, and aPOP-$SO_2C_3ObC_{8R}$, where R in the subscript means a *R* configuration for the chiral center in the pendant group, while no specification in the subscript just means racemic. Among them, iPOP-

$SO_2C_3ObC_{8R}$ and iPOP-$SO_2C_3ObC_{10R}$ contained two chiral centers in each repeat unit, whereas iPOP-$SO_2C_3ObC_8$, iPOP-$SO_2C_3ObC_{10}$, and aPOP-$SO_2C_3ObC_{8R}$ had only one, either in the main chain or side chain. For comparison, we also made iPOP-$SO_2C_3OC_{8L}$ with each repeat unit containing a chiral center in the backbone and a linear pendant group. iPECH was prepared by MMAO-12-catalyzed ring-opening polymerization of (*R*)-(-)-epichlorohydrin,[25] while aPECH was purchased from MilliporeSigma and had a weight-average molecular weight (M_w) of ~700,000 Da (from the vendor). The isotacticity of isotactic poly[(*R*)-(-)-epichlorohydrin] (iPECH) was previously confirmed by ^{13}C NMR spectroscopy, which showed a single peak at 69.86 ppm for the backbone methylene carbon, while for aPECH two peaks with nearly equal intensities were observed at 69.67 and 69.39 ppm.[25]

The small molecule precursors for the pendant groups of the polyethers with thioether side chains, 3-(branched or linear alkoxy)propyl ethanethioates (D1 to D5 in Scheme 4.1), were prepared through two-step procedures (Scheme C.1 in Appendix C). The first step was the reaction of allyl bromide with a branched alcohol, either chiral or racemic, or 1-octanol, followed by a UV light-induced thiol-ene reaction with thioacetic acid using 2,2-dimethoxy-2-phenylacetophenone as the photoinitiator. The products were thoroughly purified by silica gel column chromatography and characterized by ^1H and ^{13}C NMR spectroscopy analysis. The [α] values of the two chiral products, D1 and D2, were measured in chloroform at room temperature by polarimetry. Since the reactions for the synthesis of D1 and D2 did not involve bond breaking and formation at the chiral center, the chirality was preserved, and the products exhibited optical activities, [α] = -5.1° and -3.9°, respectively.

The substitution reactions of iPECH and aPECH with 3-(branched or linear alkoxy)propanethiolates, which were generated in-situ in the reaction mixtures from the hydrolysis

of D1-D5 catalyzed by sodium ethoxide, were performed at 100 °C in DMAc for 24 h. Shortly after the mixing of the solution of iPECH or aPECH in DMAc with the solution of a 3-(alkoxy)propanethiolate, the mixture turned opaque, indicating that the reaction occurred. After 24 h, the reaction was stopped, and the substituted polymer was precipitated in water. The polymer was then purified by three cycles of dissolution in THF and precipitation in methanol. Figure 1A,B shows the ^{1}H NMR spectra of iPOP-SC_3ObC_{8R} and aPOP-SC_3ObC_{8R} in $CDCl_3$. The ^{1}H NMR spectra of iPOP-SC_3ObC_{10R}, iPOP-SC_3ObC_8, iPOP-SC_3ObC_{10}, and iPOP-SC_3OC_{8L} can be found in Section C.2 of Appendix C. The substitution reactions were found to be essentially complete for all the polymers, as evidenced by the integrals of the peaks in the range of 3.7-3.5 ppm (-OC*H*$_2$C*H*(CH$_2$S-)- and -OC*H*(CH$_3$)CH$_2$CH$_2$-, 4H) and 3.5-3.3 ppm (-CH$_2$C*H*$_2$OC*H*(CH$_3$)CH$_2$-, 2H) for the polyethers with branched side chains, or 3.7-3.5 ppm (-OC*H*$_2$C*H*(CH$_2$S-)- from the backbone, 3H) and 3.5-3.3 ppm (-CHC*H*$_2$OC*H*$_2$CH$_2$-, 4H) for the polyether with linear side chains (i.e., iPOP-SC_3OC_{8L}).

The obtained polyethers with thioether pendant groups showed good solubility in common organic solvents, such as chloroform and THF, allowing for characterization of their optical activities by polarimetry, tacticity through ^{13}C NMR spectroscopy, and molecular weights and dispersities via SEC. The polarimetry and SEC data are summarized in Table 4.1. Polarimetry measurements showed that all the polyethers exhibited optical activities in chloroform, consistent with the expectation because their repeat units contained at least one chiral center. iPOP-SC_3ObC_{8R} and iPOP-SC_3ObC_{10R} with two chiral centers in each repeat unit exhibited the highest optical activities ([α] = -23.7° and -16.5°, respectively), which can be attributed to the additive effect of the backbone and side chain chiral centers as the [α] values of (*R*)-(-)-ECH, D1, and D2 were all

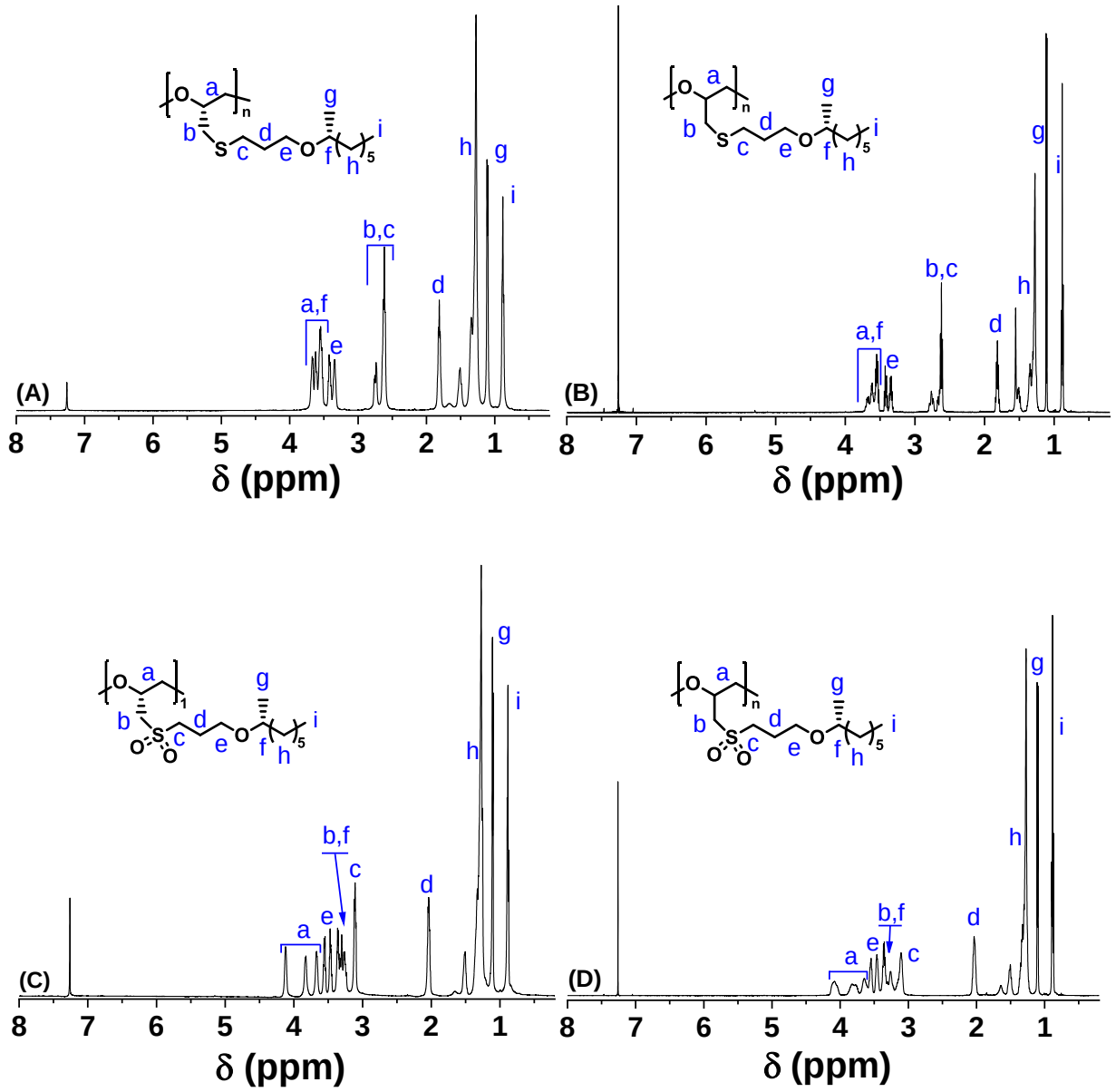

Figure 4.1. ^{1}H NMR spectra of (a) iPOP-SC$_3$ObC$_{8R}$, (b) aPOP-SC$_3$ObC$_{8R}$, (c) iPOP-SO$_2$C$_3$ObC$_{8R}$, and (d) aPOP-SO$_2$C$_3$ObC$_{8R}$ in CDCl$_3$.

Table 4.1. SEC and Polarimetry Data for Isotactic and Atactic Polyethers with Branched and Linear Pendant Groups

Polyether sample	$M_{n,SEC}$ (kDa) [a]	$Đ$ [a]	$[\alpha]_D^{20}$ [b]
iPOP-SC_3ObC_{8R}	58.8	1.78	–23.7°
iPOP-$SO_2C_3ObC_{8R}$	51.6	2.28	–41.0°
iPOP-SC_3ObC_{10R}	26.0	1.97	–16.5°
iPOP-$SO_2C_3ObC_{10R}$	24.6	2.00	–33.1°
iPOP-SC_3ObC_8	63.8	2.18	–14.8°
iPOP-$SO_2C_3ObC_8$	27.4	2.81	–26.9°
iPOP-SC_3ObC_{10}	153	5.97	–11.3°
iPOP-$SO_2C_3ObC_{10}$	16.2	4.75	–23.0°
aPOP-SC_3ObC_{8R}	74.8	3.06	–7.2°
aPOP-$SO_2C_3ObC_{8R}$	18.5	2.29	–9.7°
iPOP-SC_3OC_{8L}	52.5	7.25	–13.3°
iPOP-$SO_2C_3OC_{8L}$	17.9	3.27	–24.4°

[a] $M_{n,SEC}$ and dispersity Đ were determined using SEC with THF as the mobile phase and polystyrene standards for calibration.

[b] Optical activities were measured using ~10 mg/mL solutions of the polymers in chloroform at room temperature (~20 °C).

negative. The difference in [α] of iPOP-SC_3ObC_{8R} and iPOP-SC_3ObC_8 was 8.9°, which was similar to the [α] of D1 (-5.1°), while the difference in the optical activities of iPOP-SC_3ObC_{10R} and iPOP-SC_3ObC_{10} was 5.2°, which was even closer to the [α] of D2 (-3.9°). Among all the polyethers with thioether pendant groups, the lowest [α], –7.2°, was observed for aPOP-SC_3ObC_{8R}, whose optical activity was derived only from the chiral center located in the pendant group and much lower than those of the iPOPs. This is presumably because the [α] of D1 (-5.1°) is much lower than that of (*R*)-(-)-ECH (-35.4°). As an example, we also measured the optical rotation of a thin film of iPOP-SC_3ObC_{8R} on quartz prepared by drop-casting using the same polarimeter. The average of 9 measurements in different locations of the film was -0.024°, consistent with the observation of a negative rotation value from the polymer solution. This optical activity is believed to originate from the chiral centers in the polymer rather than from the secondary structures formed in the neat polymer film. Note that the specific optical rotation of a chiral compound in a solution is 100 times the average reading from the instrument when the concentration is 10 mg/mL (see the formula in the Experimental Section). Figure 4.2 shows the ^{13}C NMR spectra of iPOP-SC_3ObC_{8R} and aPOP-SC_3ObC_8. While the backbone methine (-C*H*-) of the atactic polymer manifested as multiple peaks over the range of 78.6-79.7 ppm, there was only a single peak at 79.4 ppm for its isotactic analogue, indicating a single chemical environment for the isotactic methine carbon and confirming the isotactic configuration. The observation for the backbone methylene (-CH_2-) was similar (a single peak at 71.2 ppm for iPOP-SC_3ObC_{8R} versus multiple peaks in the range of 70.1 to 71.6 ppm for aPOP-SC_3ObC_{8R}). These are consistent with the reports in the literature.[25] SEC analysis of the polyethers with thioether pendant groups showed that the $M_{n,SEC}$ ranged from 16.2 to 153 kDa and the $Đ$ values were 1.8-7.3, relative to the PS standards (Section C.2 of Appendix C).

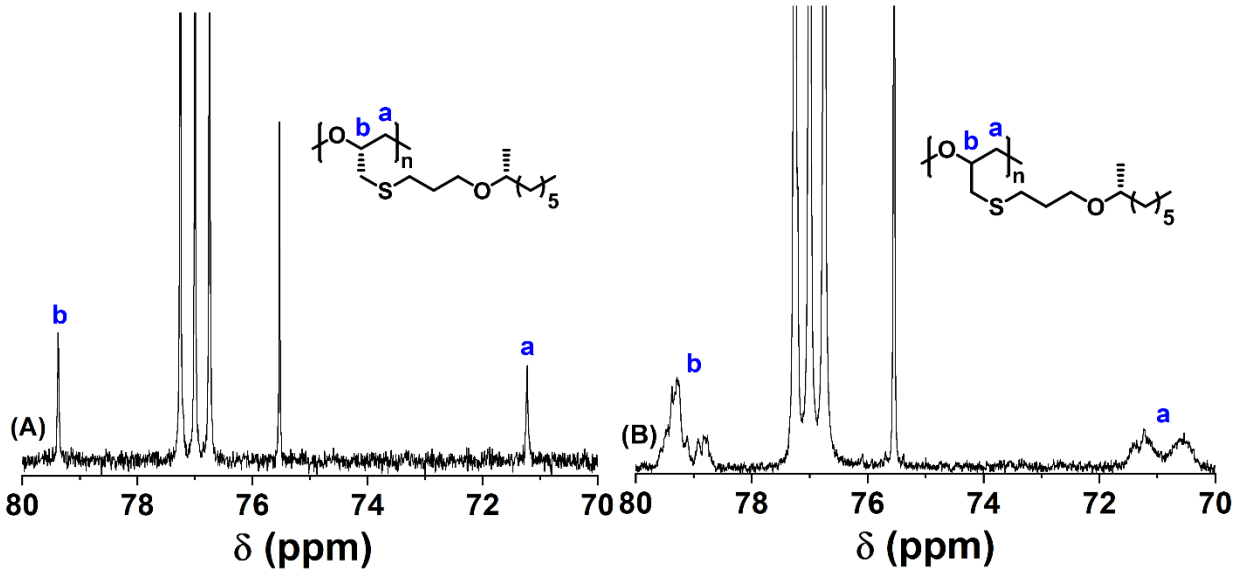

Figure 4.2. ^{13}C NMR spectra in the range of 80–70 ppm of (A) iPOP-SC_3ObC_{8R} and (B) aPOP-SC_3ObC_{8R} in $CDCl_3$.

The thioether linkages in the side chains of isotactic and atactic polyethers were oxidized to sulfonyl groups by *m*-CPBA in chloroform at room temperature for 3 h. The purified polyethers with the sulfonylated pendant groups were characterized by NMR, polarimetry, and SEC as for the precursor polymers. Figure 1C,D shows the ^{1}H NMR spectra of iPOP-$SO_2C_3ObC_{8R}$ and aPOP-$SO_2C_3ObC_{8R}$ in $CDCl_3$, and the NMR spectra of other oxidized polyethers are included in Section C.2 in Appendix C. For all the polymers, the peaks in the range of 2.5 – 2.8 ppm (-C*H*$_2$SC*H*$_2$- in the side chains) completely disappeared, indicating the complete oxidation of the thioether linkages. Polarimetry measurements showed that for every isotactic polyether [α] increased considerably, by ~100%, after the oxidation of the thioether to the sulfonyl groups (Table 4.1). This is presumably caused by a dramatic change in the chemical environment of the backbone chiral centers after the conversion of -CH_2SCH_2- to -$CH_2SO_2CH_2$-. For the atactic polyether, [α] showed a much smaller change, from -7.2° to -9.7°, likely because the sulfonyl group was much farther away from the chiral center in the pendant group (4 atoms) than from the backbone chiral center in the iPOPs. SEC analysis showed that the molecular weight decreased after the oxidation (see Table 4.1 and Section C.2 in Appendix C), suggesting that *m*-CPBA also cleaved the polyether backbone.

4.3.2. Thermal Behavior of Various Sulfonylated Polyethers

All the polyethers with thioether pendant groups, whether isotactic or atactic, were transparent viscous liquids at room temperature with the glass transition temperatures (T_g) well below 0 °C. Example DSC analysis results of iPOP-SC_3ObC_{8R} and aPOP-SC_3ObC_{8R} are shown in Figure C.23A. Except for two T_ms at -45 and -36 °C for iPOP-SC_3ObC_{8R} due to the isotacticity of the backbone, no T_g could be identified between -70 and 50 °C for both samples. As shown in Figure

C.23B, aPOP-SC_n for n > 4 exhibited T_g below -70 °C.[25] Based on the comparison of these two systems, it is likely that the T_gs of iPOP-SC_3ObC_{8R} and aPOP-SC_3ObC_{8R} are below -70 °C.

After oxidation, the polyethers with sulfonyl pendant groups developed ordered crystalline or liquid crystalline structures. The phase behavior of these polyethers was first studied by DSC. Fibers were drawn from either the melt or the liquid crystalline phases to achieve oriented structures. The first heating (fiber samples) and subsequent first cooling/second heating (non-fiber samples because they had been heated to above T_m or T_i during the first heating process) DSC curves are shown in Figure 4.3. After the oxidation of the thioether groups into the sulfonyl groups, the T_g of the corresponding samples increased to ≥ -1 °C (see the second heating curves in Figure 4.3C) due to the stronger dipole-dipole interactions among the sulfonyl groups. Similar results were also seen for the aPOP-SO_2C_n system (Figure C.23C).[25] Combined with the structural characterization using XRD, different phases were identified for these samples (see later discussion for details). For iPOP-$SO_2C_3ObC_{8R}$, iPOP-$SO_2C_3ObC_8$, and iPOP-$SO_2C_3bC_{10R}$ fibers, crystalline structures (K) were obtained (Figure 4.3A). Upon heating, they directly melt into the isotropic phase (I). Upon cooling, only iPOP-$SO_2C_3ObC_{8R}$ crystallized at 84 °C into the crystalline structure, and its crystallization and melting transitions are thermally reversible with a large hysteresis (Figure 4.3B,C). In contrast, iPOP-$SO_2C_3ObC_8$ and iPOP-$SO_2C_3ObC_{10R}$ did not crystallize but entered a liquid crystalline phase (i.e., SmC*-like) upon cooling with a small heat of transition (ΔH_f) at 18 (0.78 J/g) and 47 °C (1.2 J/g), respectively. Upon the second heating, both iPOP-$SO_2C_3ObC_8$ and iPOP-$SO_2C_3ObC_{10R}$ exhibited reversible isotropization at 33 and 57 °C, respectively. iPOP-$SO_2C_3ObC_{10R}$ underwent a cold-crystallization at 81 °C and finally melted at 115 °C (Figure 4.3B,C).

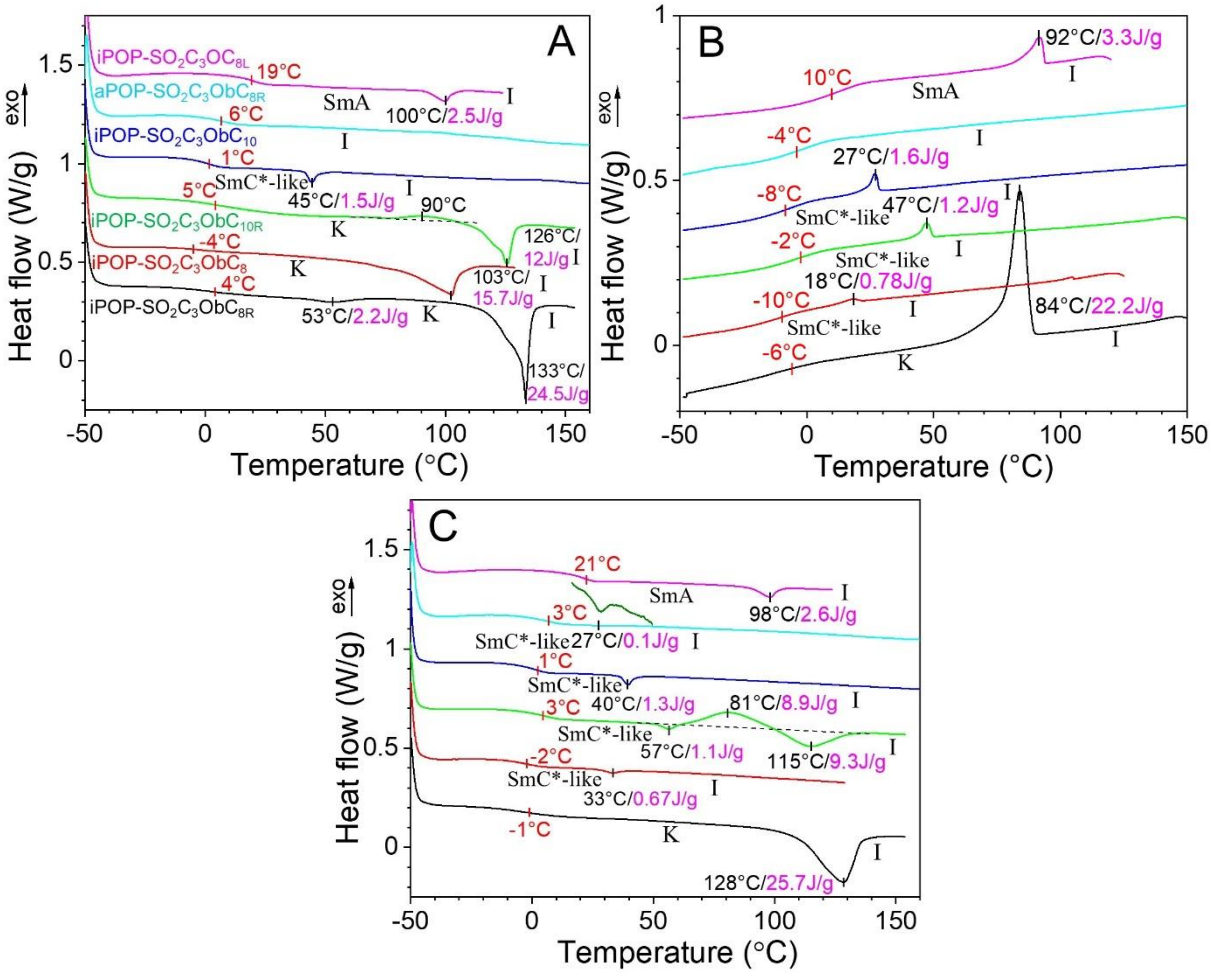

Figure 4.3. (A) First heating, (B) first cooling, and (C) second heating DSC curves of various sulfonylated side-chain polyether fibers. The heating and cooling rates were 10 °C/min.

Different from the above samples, iPOP-$SO_2C_3bC_{10}$ exhibited reversible liquid crystalline phase transitions between the SmC*-like and the I phase, regardless of fiber-drawing or not. If the chirality was kept only in the side chains, aPOP-$SO_2C_3ObC_{8R}$ remained largely amorphous with a very weak T_i at 27 °C (ΔH_f is only 0.1 J/g; see the magnified cyan curve in Figure 4.3C). For comparison, iPOP-$SO_2C_3OC_{8L}$ with linear C8 side chains exhibited reversible SmA-to-I phase transitions.

From this DSC study, it seems that double chirality in both main chain and side chains is important for the crystallization of these chiral polyethers. If single chirality exists, either in the main chain or the side chains, it is likely to self-assemble into the SmC*-like phase. However, chirality in the main chain seems more important than in the side chains. Meanwhile, the side chain length also plays a role: the longer the side chains, the higher the possibility to form liquid crystalline phases without crystallization.

4.3.3. Self-assembly of Various Sulfonylated Polyethers Studied by XRD and PLM

The self-assembly structures of these chiral polyethers were studied by 2D XRD. Figure 4.4A,C,E shows the 2D fiber patterns for melt-drawn iPOP-$SO_2C_3ObC_{8R}$, iPOP-$SO_2C_3ObC_{10R}$, and iPOP-$SO_2C_3ObC_8$ fibers, respectively. For these fiber patterns, a similar orthorhombic crystalline structure could be determined. Lamellar reflections were seen on the equator, and the a-axis could be determined. The (002) reflection was seen on the meridian, and the c-axis was determined to be 0.550 nm. From this c-axis and two-layer fiber patterns, it was considered that the main chains must adopt a 2_1 helical conformation, which is similar to that reported for iPOP-SO_2C_n with linear side chains.[25] Finally, the b-axis (0.475 nm) could be assigned using the (010) reflection at high angles on the equator. In the quadrant, (h01) and (h02) reflections could be identified, suggesting tilting of the branched side chains from the layer normal direction. The tilt

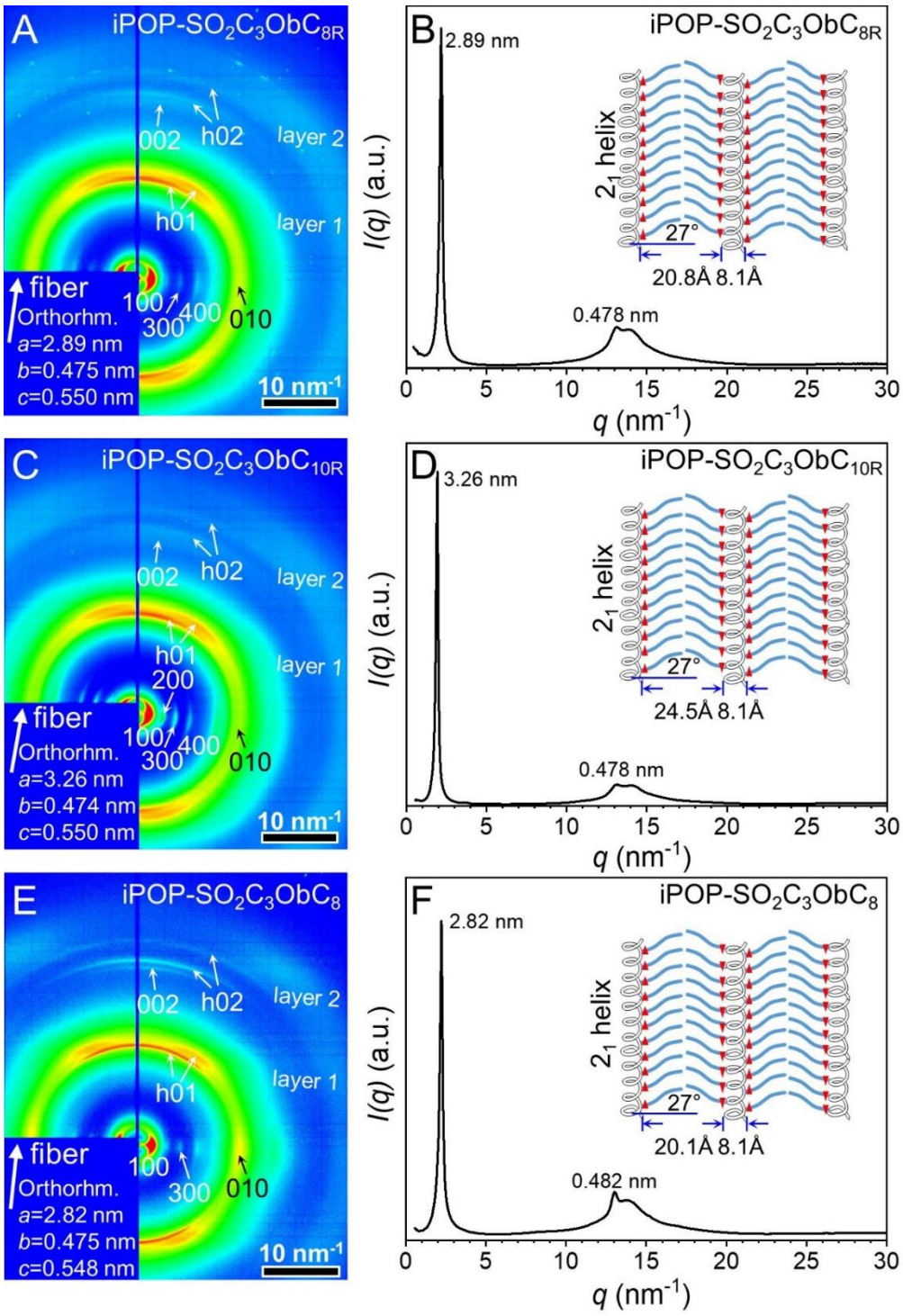

Figure 4.4. Room temperature (A,C,E) 2D and (B,D,F) 1D XRD results for (A,B) iPOP-$SO_2C_3ObC_{8R}$, (C,D) iPOP-$SO_2C_3ObC_{10R}$, and (E,F) iPOP-$SO_2C_3ObC_8$, respectively. The intensity in 2D XRD patterns is in the logarithmic scale. The insets in (B,D,F) show the double-layer crystalline structures with tilted side chains.

angle was estimated to be 27° (i.e., 63° from the chain axis). Assuming all trans conformation in the -C_3ObC_8 side chains and the core thickness of the main-chain 2_1 helix of 0.807 nm,25 the interdigitated layer and double layer thicknesses are calculated to be 2.05 and 3.30 nm. From the lamellar spacing around 2.85 nm for iPOP-$SO_2C_3ObC_{8R}$ and iPOP-$SO_2C_3ObC_8$, the tilted side chains should contain certain twists and then pack into double layers, rather than the interdigitated (even partially) layers. Similarly, the -C_3ObC_{10r} side chains should also be tilted in the lamellar structure. The schematic crystalline structures are shown in the insets of Figure 4.4B,D,F. Upon heating, the lamellar crystalline structures in these fibers directly melted into the isotropic state, as evidenced by replacing the sharp lamellar reflections at low angles with a broad halo centered around 2.6 nm^{-1} for iPOP-$SO_2C_3ObC_{8R}$/iPOP-$SO_2C_3ObC_8$ and 2.4 nm^{-1} for iPOP-$SO_2C_3ObC_{10R}$ (see Figure C.24).

The PLM images for the iPOP-$SO_2C_3ObC_{8R}$, iPOP-$SO_2C_3ObC_{10R}$, and iPOP-$SO_2C_3ObC_8$ fibers are shown in Figure 4.5 a-f, g-l, and m-r, respectively. Obvious birefringence was observed for all fiber samples at room temperature. Upon heating above the T_m, birefringence disappeared. Upon cooling, no observable birefringence was observed for iPOP-$SO_2C_3ObC_{8R}$ and iPOP-$SO_2C_3ObC_{10R}$, even though the temperature was already below the crystallization or liquid crystal formation temperatures (see DSC results in Figure 4.3B). Only for iPOP-$SO_2C_3ObC_8$, weak birefringence was observed at 25 °C for the SmC*-like phase. The lack of (or faint) birefringence is explained by the fact that crystalline or liquid crystalline grains were significantly smaller than ~200 nm (i.e., half of the wavelength of the incident light), as reported before.[28] On the contrary, XRD detects ordered structures on the sub-nanometer to tens of nanometer length scales. Therefore, XRD and PLM do not need to match each other for samples with small crystalline and liquid crystalline grains.

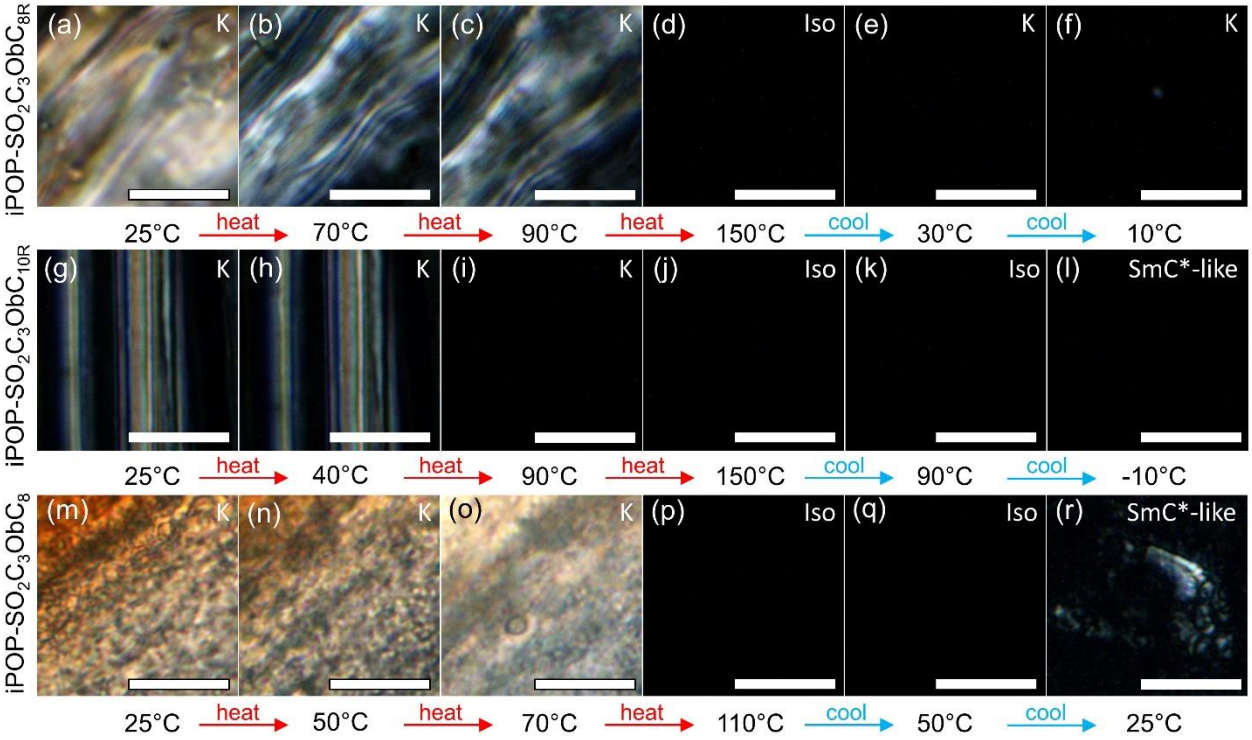

Figure 4.5. PLM images of (a-f) iPOP-$SO_2C_3ObC_{8R}$, (g-l) iPOP-$SO_2C_3ObC_{10R}$, and (m-r) iPOP-$SO_2C_3ObC_8$ stretched fibers during the first heating and the subsequent cooling processes. Different phases are assigned based on both DSC and XRD results. K: crystal, SmC*-like: smectic C*-like, and Iso: isotropic. The scale bars are 20 μm.

If only single chirality existed in the polyethers, liquid crystalline self-assembly was obtained. The fiber patterns for aPOP-$SO_2C_3ObC_{8R}$ and iPOP-$SO_2C_3ObC_{10}$ at -10 °C are shown in Figure 4.6A,D, respectively. Lamellar reflections were seen on the equator with spacings being 2.64 nm for aPOP-$SO_2C_3ObC_{8R}$ and 2.90 nm for iPOP-$SO_2C_3ObC_{10}$ (Figure 4.6B,E). In the wide-angle range, a broad halo was found around the meridian. However, the azimuthal scan results showed two peaks around 180° for this scattering halo, indicating a chain-tilting angle around 20°. Based on the calculation, again the double layers could be determined for these liquid crystalline phases with tilted side chains. The schematic representations are shown in the insets of Figure 4.6B,E. Because of existence of chiral centers in these polyethers, we could assign this liquid crystalline phase as SmC*-like. At this moment, it is not clear whether there is any helical arrangement in the tilted side chains, as observed in other systems.[29,30] In this sense, this SmC*-like phase is different from the conventional SmC* phase of ferroelectric liquid crystals, where aromatic mesogens are often aligned along the stretching direction and smectic layers are tilted.[9,22] Meanwhile, the molecular dipoles arrange in a helical configuration in consecutive smectic layers. These fibers exhibited clear birefringence in the PLM images, Figures 4.7a-d for aPOP-$SO_2C_3ObC_{8R}$ and 4.7e-i for iPOP-$SO_2C_3ObC_{10}$. Upon heating, birefringence disappeared above the T_i. Upon cooling, relatively weak birefringence reappeared after cooling below room temperature. This is consistent with the fact that liquid crystalline SmC*-like phase was developed in both samples.

After replacing the methyl-branched side chains with linear side chains, iPOP-$SO_2C_3OC_{8L}$ exhibited a typical double-layer SmA structure, as shown in Figure 4.6G-I. Essentially the same results were obtained for the fibers of iPOP-$SO_2C_3OC_{8L}$ at room temperature using a Xenocs Xeuss 3.0 SAXS Instrument in the Polymer Characterization Laboratory at the University of Tennessee Knoxville (Figure 4.8). Note, this sample was different from iPOP-SO_2C_{12L} reported previously,[25]

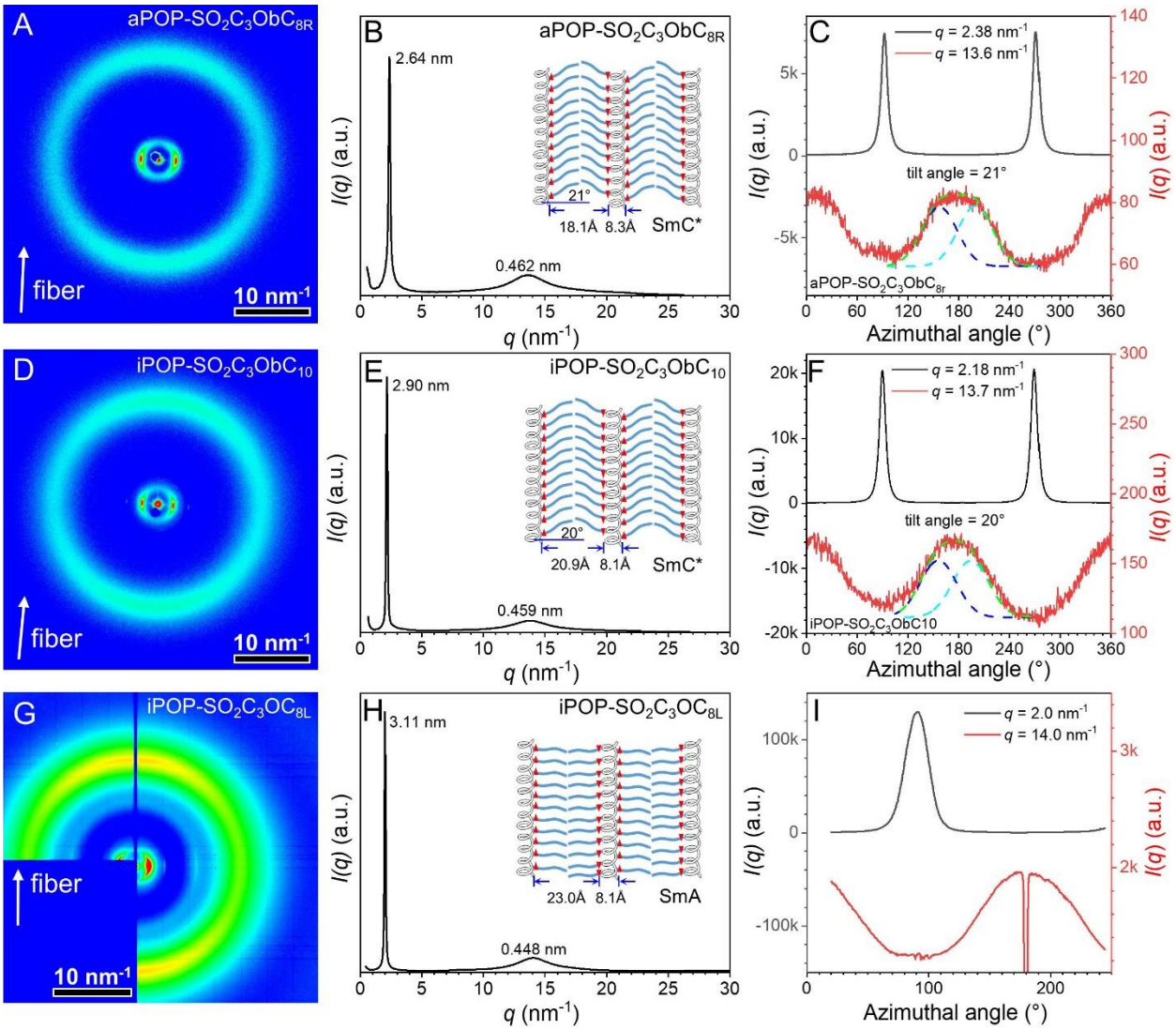

Figure 4.6. (A,D,G) 2D and (B,E,H) 1D XRD results, and (C,F,I) the corresponding azimuthal scan curves for (A-C) aPOP-$SO_2C_3ObC_{8R}$ (-10 °C), (D-F) iPOP-$SO_2C_3ObC_{10}$ (-10 °C), and (G-I) iPOP-$SO_2C_3OC_{8L}$ (25 °C) fibers, respectively. The intensity in 2D XRD patterns is in the logarithmic scale. The insets in (B,E,H) show the double-layer SmC*-like/SmA structures of the melt-drawn fibers.

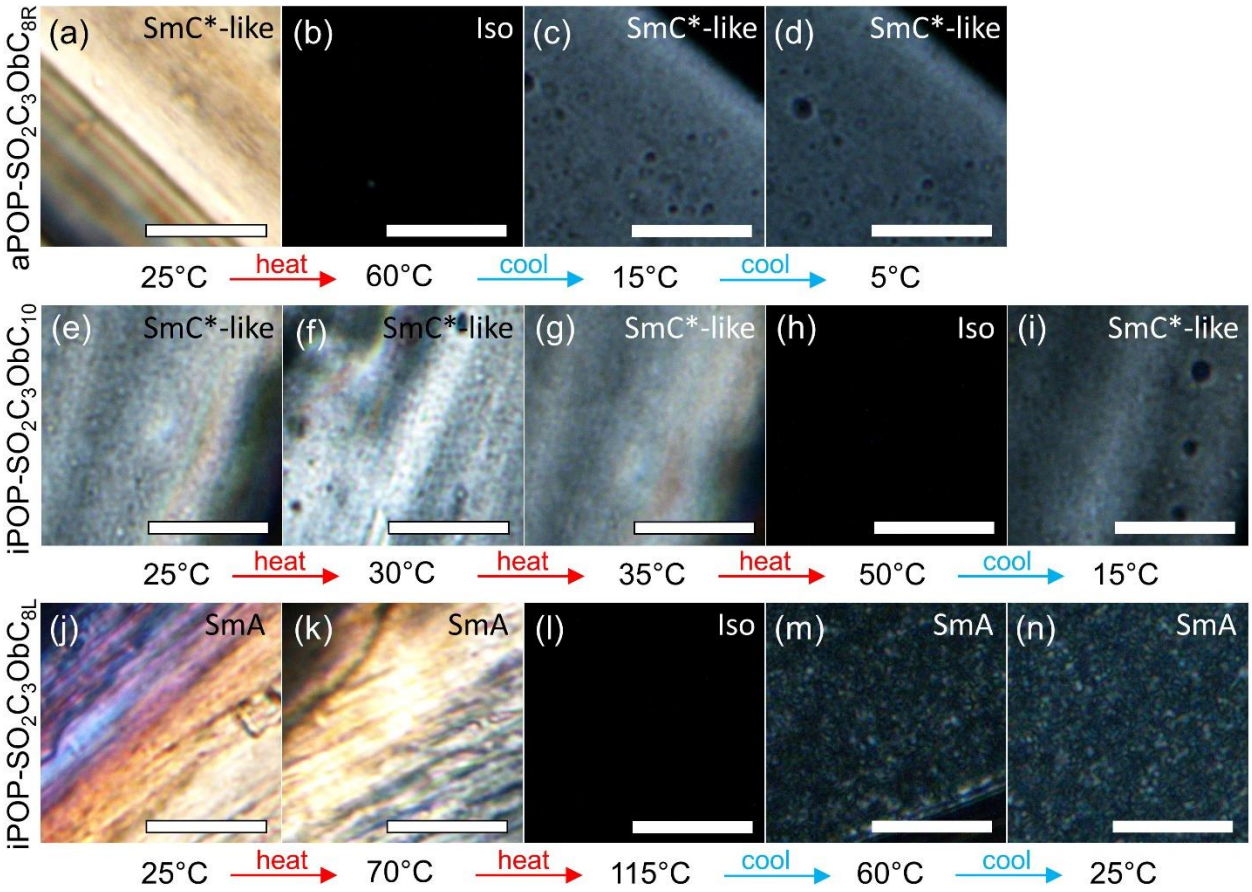

Figure 4.7. PLM images of (a-d) aPOP-$SO_2C_3ObC_{8R}$, (e-i) iPOP-$SO_2C_3ObC_{10}$, and (j-n) iPOP-$SO_2C_3OC_{8L}$ fibers during the heating and the subsequent cooling processes. Different phases are assigned based on both DSC and XRD results. K: crystal, SmC*-like: smectic C*-like, and Iso: isotropic. The scale bars are 20 μm.

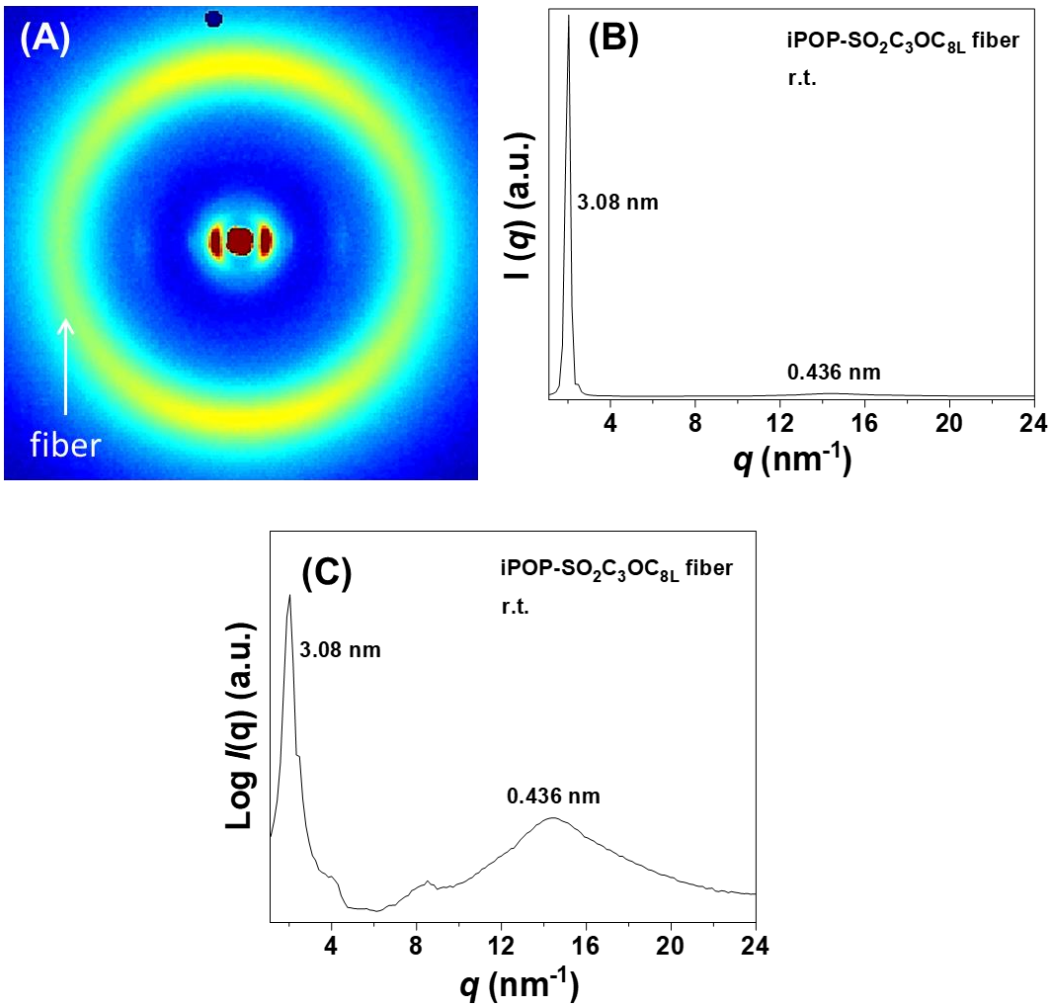

Figure 4.8. 2D (A) and 1D XRD (B and C; B: linear scale and C: logarithmic scale for Y-axis) results for the iPOP-$SO_2C_3OC_{8L}$ fiber at room temperature.

because iPOP-SO_2C_{12L} formed a high T_m crystal. Therefore, the oxygen linker in the linear side chain provided more flexibility for the liquid crystalline self-assembly. When studied with PLM (Figure 4.7j-n), the iPOP-$SO_2C_3OC_{8L}$ fiber exhibited strong birefringence at room temperature. Upon heating, it entered the isotropic melt at 115 °C. Upon cooling below 60 °C, the SmA phase appeared with small grains. Comparing the polyethers with branched and linear side chains, it is clear that the methyl branches are important in achieving tilting of side chains and thus the SmC*-like phase.

4.3.4. Dielectric Property Study

Given the large dipole moment of sulfonyl groups (4.5 D), it would be interesting to explore if the above polyethers could exhibit any ferroelectric property. To this end, D-E loops were measured for the hot-pressed films (~20 μm) at room temperature. After subtraction of the AC electronic conduction (see Figure C.25), the results are shown in Figure 4.9. When the poling electric field was below 50 MV/m, linear D-E loops were seen for these samples. High dielectric constants were obtained from the linear slopes: 7.9 for iPOP-$SO_2C_3ObC_8$, 11.6 for aPOP-$SO_2C_3ObC_{8R}$, and 11.7 for iPOP-$SO_2C_3ObC_{10}$, respectively. The high dielectric constants for aPOP-$SO_2C_3ObC_{8R}$ and iPOP-$SO_2C_3ObC_{10}$ could be attributed to the liquid crystalline SmC*-like phases. Upon increasing the poling electric field up to 200 MV/m, the D-E loops progressively broadened (Figure C.25), representing enhanced dielectric losses. The first dielectric loss originated from the AC electronic conduction during bipolar poling (see the horizontal dashed line loops in each plot of Figure C.25), as reported recently.[11,31] Even after the subtraction of the AC electronic conduction, the D-E loops in Figure 4.9 were still relatively broad. The broadening of D-E loops could be attributed primarily to the conduction of impurity ions in the sample. As such, these D-E loops did not appear to be typical ferroelectric switching of the SmC* phases. We

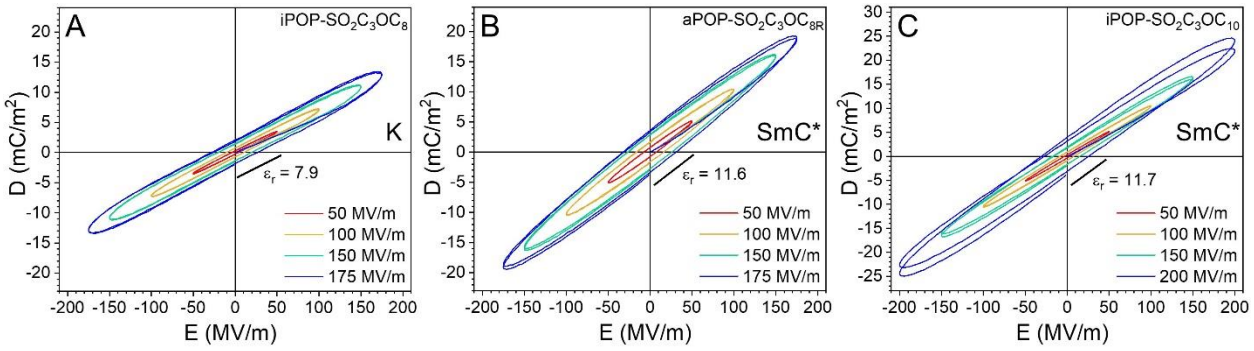

Figure 4.9. Bipolar D-E loops for (A) iPOP-$SO_2C_3ObC_8$, (B) aPOP-$SO_2C_3ObC_{8R}$, and (C) iPOP-$SO_2C_3ObC_{10}$ at room temperature. The poling frequency was 100 Hz with a sinusoidal waveform. The AC electronic conduction is subtracted from these D-E loops (see Figure C.25).

consider that neighboring sulfonyl dipoles, which connect tightly to the main chain, strongly interact with each other and “lock” together to form the liquid crystalline SmC*-like phase (see the schematics in the insets of Figure 4.6B,E). As a result, large ferroelectric switching could hardly be induced by the poling electric field.

4.4. Conclusions

To achieve the SmC* phase in mesogen-free liquid crystalline polymers, a series of chiral polyethers with branched sulfonylated side chains were designed and prepared. Through structural analysis, double chirality in both the main chain and the side chains favored the formation of crystalline structures in the stretched fibers. When single chirality existed in these polyethers, whether in the main chain or in the side chains, liquid crystalline self-assembly was achieved. 2D fiber XRD analysis suggested a SmC*-like phase, where the main chains were aligned along the fiber axis and the branched alkyl side chains tilted about 70° from the fiber axis. As demonstrated in the bipolar D-E hysteresis loops, no typical ferroelectric switching was observed, although relatively high dielectric constants (7.9-11.7) were obtained. We consider that this SmC*-like phase should be different from the conventional ferroelectric SmC* phase, which contains a helical arrangement of the dipole moment in consecutive smectic layers.

References

1. Zentel, R.; Brehmer, M. Ferroelectric Liquid-Crystalline Elastomers. *Adv. Mater.* **1994,** *6*, 598-599.
2. Brehmer, M.; Zentel, R.; Wagenblast, G.; Siemensmeyer, K. Ferroelectric Liquid-Crystalline Elastomers. *Macromol. Chem. Phys.* **1994,** *195*, 1891-1904.
3. Shilov, S.; Gebhard, E.; Skupin, H.; Zentel, R.; Kremer, F. Electric-Field-Induced Segmental Reorientation in Ferroelectric Liquid Crystalline Polymers and Elastomers. *Macromolecules* **1999,** *32*, 1570-1575.
4. Kremer, F.; Lehmann, W.; Skupin, H.; Tolksdorf, C.; Gebhard, E.; Zentel, R.; Kruger, P.; Losche, M. Giant Lateral Electrostriction in Ferroelectric Liquid-Crystalline Elastomers. *Nature* **2001,** *410*, 447-450.
5. Yu, Y.; Maeda, T.; Mamiya, J.; Ikeda, T. Photomechanical Effects of Ferroelectric Liquid-Crystalline Elastomers Containing Azobenzene Chromophores. *Angew. Chem. Int. Ed.* **2007,** *46*, 881-883.
6. Ohm, C.; Brehmer, M.; Zentel, R. Liquid Crystalline Elastomers as Actuators and Sensors. *Adv. Mater.* **2010,** *22*, 3366-3387.
7. Wang, L.; Urbas, A. M.; Li, Q. Nature-Inspired Emerging Chiral Liquid Crystal Nanostructures: From Molecular Self-Assembly to DNA Mesophase and Nanocolloids. *Adv. Mater.* **2020,** *32*, 1801335.
8. Pirkl, S.; Glogarova, M., Ferroelectric Liquid Crystals with High Spontaneous Polarization. In *Ferroelectrics - Physical Effects*; Lallart, M., Eds.; InTech: 2011; Chapter 17, pp 407-428.

9. Scherowsky, G., Ferroelectric Liquid Crystal (FLC) Polymers. In *Ferroelectric Polymers: Chemistry, Physics, and Applications*; Nalwa, H. S., Eds.; Marcel Dekker, Inc.: New York, 1995; Chapter 6, pp 435-537.

10. Tashiro, K., Crystal Structure and Phase Transition of PVDF and Related Copolymers. In *Ferroelectric Polymers: Chemistry, Physics, and Applications*; Nalwa, H. S., Eds.; Marcel Dekker: New York, 1995; Chapter 2, pp 63-182.

11. Huang, Y.; Rui, G.; Li, Q.; Allahyarov, E.; Li, R.; Fukuto, M.; Zhong, G.-J.; Xu, J.-Z.; Li, Z.-M.; Taylor, P. L.; Zhu, L. Enhanced Piezoelectricity from Highly Polarizable Oriented Amorphous Fractions in Biaxially Oriented Poly(vinylidene fluoride) with Pure β Crystals. *Nat. Commun.* **2021,** *12*, 675.

12. Rui, G.; Huang, Y.; Chen, X.; Li, R.; Wang, D.; Miyoshi, T.; Zhu, L. Giant Spontaneous Polarization for Enhanced Ferroelectric Properties of Biaxially Oriented Poly(vinylidene fluoride) by Mobile Oriented Amorphous Fractions. *J. Mater. Chem. C* **2021,** *9*, 894-907.

13. Lee, J. C.; Litt, M. H. Crystallization Behavior of Poly(oxyethylene)s with (Alkylsulfonyl)methyl Side Groups. *J. Ind. Eng. Chem.* **1999,** *5*, 155-159.

14. Lee, J. C.; Litt, M. H.; Rogers, C. E. Synthesis and Properties of (Alkylthio)methyl-Substituted Poly(oxyalkylene)s and (Alkylsulfonyl)methyl-Substituted Poly(oxyalkylene)s. *Macromolecules* **1997,** *30*, 3766-3774.

15. Lee, J. C.; Litt, M. H.; Rogers, C. E. Synthesis and Properties of Liquid Crystalline Polymers Containing an Oxyethylene Backbone and *n*-Octylsulfonylmethyl Side Groups. *Macromolecules* **1998,** *31*, 2440-2446.

16. Lee, J. C.; Oh, K.; Lee, H. B.; Kim, Y. G.; Jho, J. Y.; Kwak, S. Y.; Park, S. Y.; Farmer, B. L. Synthesis and Mesomorphic Properties of Poly(oxyethylene) with [(6-

Heptylsulfonyl)hexylthio]methyl Side Groups. *Macromol. Rapid Commun.* **2001,** *22*, 815-819.

17. Park, S. Y.; Farmer, B. L.; Lee, J. C. The Structures of Poly(oxyethylene)s Having Sulfone Groups in the Side Chains. *Polymer* **2002,** *43*, 177-183.
18. Lee, J. C.; Han, S. H.; Cha, S. H.; Park, S. Y.; Farmer, B. L. Synthesis and Dipole-Dipole Interaction-Induced Mesomorphic Behavior of Poly(oxyethylene)s Containing (*n*-Octylsulfonyl)alkylthiomethyl or (*n*-Octylsulfonyl)alkylsulfonylmethyl Side Groups. *Polymer* **2003,** *44*, 7413-7425.
19. Kim, J. U.; Lee, J. C. Synthesis and Liquid Crystalline Properties of Poly(ethylene oxide) Brushes with Amphiphilic Side Groups. *Macromol. Chem. Phys.* **2005,** *206*, 951-960.
20. Kim, B. G.; Moon, J. K.; Sohn, E. H.; Lee, J. C.; Yeo, J. K. Polysiloxanes Containing Alkyl Side Groups: Synthesis and Mesomorphic Behavior. *Macromol. Res.* **2008,** *16*, 36-44.
21. Kim, B. G.; Chung, J. S.; Sohn, E. H.; Kwak, S. Y.; Lee, J. C. Comb-Like Fluorinated Polystyrenes Having Different Side Chain Interconnecting Groups. *Macromolecules* **2009,** *42*, 3333-3339.
22. Lagerwall, S. T. *Ferroelectric and Antiferroelectric Liquid Crystals*; Wiley-VCH: Weinheim, 1999.
23. Miyajima, D.; Araoka, F.; Takezoe, H.; Kim, J.; Kato, K.; Takata, M.; Aida, T. Ferroelectric Columnar Liquid Crystal Featuring Confined Polar Groups Within Core-Shell Architecture. *Science* **2012,** *336*, 209-213.
24. Furukawa, S.; Wu, J. Y.; Koyama, M.; Hayashi, K.; Hoshino, N.; Takeda, T.; Suzuki, Y.; Kawamata, J.; Saito, M.; Akutagawa, T. Ferroelectric Columnar Assemblies from the Bowl-to-Bowl Inversion of Aromatic Cores. *Nat. Commun.* **2021,** *12*, 768.

25. Kwok, M.; Seymour, B.; Li, R.; Litt, M.; Zhao, B.; Zhu, L. Tacticity Effect on Mesogen-Free Liquid Crystalline Self-assembly Induced by Strong Dipole-Dipole Interactions. *Macromolecules* **2019,** *52*, 3601-3611.

26. Bohannon, C.; Kwok, M.; Li, R.; Zhu, L.; Zhao, B. Effects of Tacticity and Chiral Center-to-Dipole Distance on Mesogen-Free Liquid Crystalline Self-Assembly of Sulfonyl-Containing Comb-Like Polymers. *Polym. Chem.* **2020,** *11*, 3018-3031.

27. Kwok, M. H.; Bohannon, C. A.; Crooks, J. L.; Li, R.; Zhao, B.; Zhu, L. Grafting Density-Induced Smectic A to Hexagonal Columnar Transition in Mesogen-Free Isotactic Liquid Crystalline Polyethers with *n*-Dodecylsulfonyl Side Groups. *Giant* **2020,** *1*, 100003.

28. Kwok, M. H.; Bohannon, C. A.; Li, R.; Zhao, B.; Zhu, L. Ordered Hexagonal Columnar Liquid Crystalline Self-Assembly of Mesogen-Free Sulfonylated Side-Chain Chiral Polyethers and Their High Dielectric Property. *Giant* **2021,** *8*, 100079.

29. Huang, S.; Yu, H.; Li, Q. Supramolecular Chirality Transfer toward Chiral Aggregation: Asymmetric Hierarchical Self-Assembly. *Adv. Sci.* **2021**, *8*, 2002132.

30. Huang, S.; Chen, Y.; Ma, S.; Yu, H. Hierarchical Self-Assembly in Liquid-Crystalline Block Copolymers Enabled by Chirality Transfer. *Angew. Chem. Int. Ed.* **2018**, *57*, 12524-12528.

31. Yang, L.; Allahyarov, E.; Guan, F.; Zhu, L. Crystal Orientation and Temperature Effects on Double Hysteresis Loop Behavior in a Poly(vinylidene fluoride-*co*-trifluoroethylene-*co*-chlorotrifluoroethylene)-*graft*-Polystyrene Graft Copolymer. *Macromolecules* **2013,** *46*, 9698-9711.

Appendix C

for

Chapter 4: SmC*-like Self-Assembly in Mesogen-Free Liquid Crystalline Polyethers with Sulfonylated Branched Alkyl Side Chains

Section C.1. Synthesis of Thioacetate Side Chain Precursors

Chiral and racemic allyl ethers, C1 – C5, and thioacetate compounds, D1 – D5 were synthesized according to Scheme C.1.

Synthesis of (R)-(2-Allyloxy)octane (C1). (*R*)-2-Octanol (2.00 g, 15.4 mmol), sodium hydride (0.987 g of 60% dispersion in paraffin oil, 24.7 mmol), and dry THF (5 mL) were added into a 25 mL two-necked round bottom flask equipped with a magnetic stir bar and a gas flow control adaptor. After the mixture was stirred in an oil bath at room temperature under a nitrogen gas atmosphere for 1 h, allyl bromide (10.0 g, 82.7 mmol) was added into the mixture through an addition funnel. The reaction flask was fitted with a reflux condenser, and the reaction proceeded at 75 ℃ overnight under stirring conditions. After the crude mixture was concentrated under a reduced pressure by rotary evaporation, chloroform was added into the flask, and the mixture was poured into a separatory funnel and washed with water (30 mL × 3). The organic phase was collected and dried with anhydrous sodium sulfate. The solvents were removed by rotary evaporation; the product was further dried under high vacuum and obtained as a lightly yellow liquid (C1) (2.433 g, 93.0% yield). The product was pure enough for the next-step reaction. ^{1}H NMR (600 MHz, $CDCl_3$) δ (ppm) = 6.00 – 5.87 (m, CH_2=C*H*CH_2-, 1H), 5.26 (d, C*H*H=CH-, 1H), 5.13 (d, CH*H*=CH-, 1H), 4.02 (dd, CH_2=CHC*H*HO-, 1H), 3.92 (dd, CH_2=CHCH*H*O-, 1H), 3.46 – 3.38 (m, -OC*H*(CH_3)CH_2-, 1H), 1.59 – 1.49 and 1.43 – 1.23 (m, -OCH(CH_3)(C*H*$_2$)$_5$$CH_3$, 10H), 1.13 (d, -OCH(C*H*$_3$)CH_2-, 3H), 0.88 (t, -CH_2CH_2C*H*$_3$, 3H) (Figure C.1A). ^{13}C NMR (151 MHz, $CDCl_3$) δ (ppm) = 135.63, 116.21, 74.92, 69.31, 36.64, 31.84, 29.40, 25.49, 22.61, 19.61, 14.06 (Figure C.1B).

C2, C3, C4, and C5 were synthesized by using the same procedure as for C1. The yields and characterization data are listed below along with ^{1}H and ^{13}C NMR spectra.

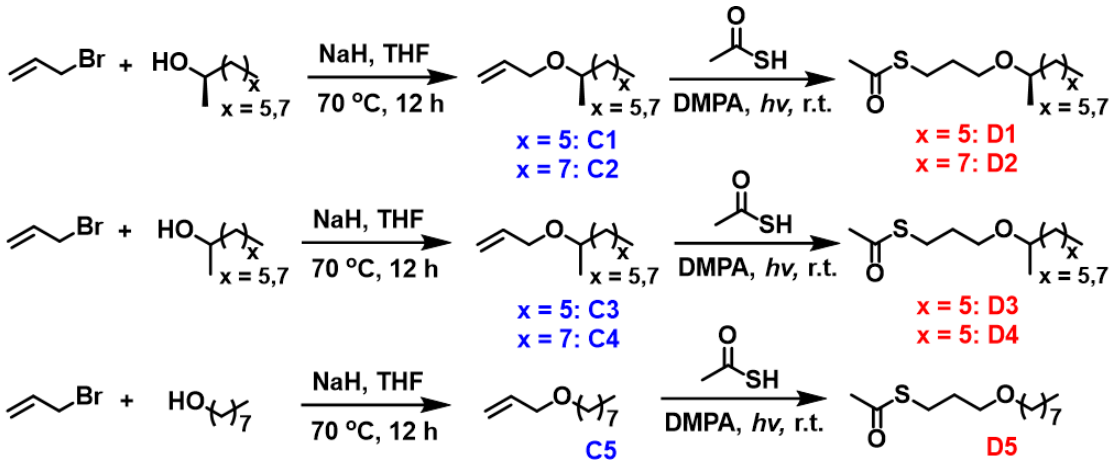

Scheme C.1. Synthesis of Chiral and Racemic Branched Thioacetate Side Chain Precursors and a Linear Side Chain Precursor.

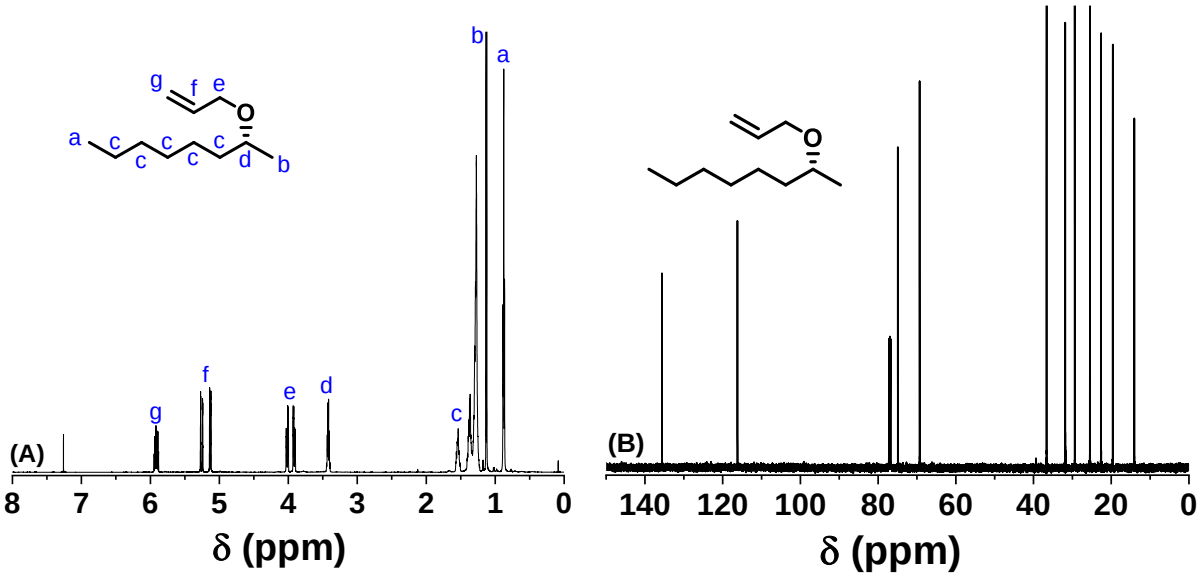

Figure C.1. (A) ^{1}H and (B) ^{13}C spectra of (*R*)-(2-allyloxy)octane (C1) in $CDCl_3$.

Synthesis of (R)-2-(Allyloxy)decane (C2). Yield: 57.0%. ^{1}H NMR (600 MHz, $CDCl_3$) δ (ppm) = 5.97 – 5.87 (m, CH_2=C*H*CH_2-, 1H), 5.26 (d, C*H*H=CH-, 1H), 5.13 (d, CH*H*=CH-, 1H), 4.01 (dd, CH_2=CHC*H*HO-, 1H), 3.91 (dd, CH_2=CHCH*H*O-, 1H), 3.46 – 3.39 (m, -OC*H*(CH_3)CH_2-, 1H), 1.59 – 1.50 and 1.45 – 1.21 (m, -OCH(CH_3)(C*H*$_2$)$_7$$CH_3$ 14H), 1.13 (d, -OCH(C*H*$_3$)CH_2-, 3H), 0.88 (t, -CH_2CH_2C*H*$_3$, 3H) (Figure C.2A). ^{13}C NMR (151 MHz, $CDCl_3$) δ (ppm) = 135.65, 116.26, 74.95, 69.33, 36.65, 31.88, 29.75, 29.59, 29.28, 25.55, 22.65, 19.64, 14.10 (Figure C.2B).

Synthesis of 2-(Allyloxy)octane (C3). Yield: 65.4%. ^{1}H NMR (600 MHz, $CDCl_3$) δ (ppm) = 5.97 – 5.86 (m, CH_2=C*H*CH_2-, 1H), 5.25 (d, C*H*H=CHCH_2-, 1H), 5.13 (d, CH*H*=CHCH_2-, 1H), 4.01 (dd, CH_2=CHC*H*HO-, 1H), 3.91 (dd, CH_2=CHCH*H*O-, 1H), 3.46 – 3.38 (m, -OC*H*(CH_3)CH_2-, 1H), 1.58 – 1.49 and 1.42 – 1.21 (m, -OCH(CH_3)(C*H*$_2$)$_5$$CH_3$, 10H), 1.13 (d, -OCH(C*H*$_3$)CH_2-, 3H), 0.87 (t, -CH_2CH_2C*H*$_3$, 3H) (Figure C.3A). ^{13}C NMR (151 MHz,$CDCl_3$) δ (ppm) = 135.62, 116.20, 74.92, 69.31, 36.64, 31.84, 29.39, 25.49, 22.60, 19.60, 14.04 (Figure C.3B).

Synthesis of 2-(Allyloxy)decane (C4). Yield: 71.0%. ^{1}H NMR (500 MHz, $CDCl_3$) δ (ppm) = 5.98 – 5.86 (m, CH_2=C*H*CH_2-, 1H), 5.26 (d, C*H*H=CH-, 1H), 5.14 (d, CH*H*=CH-, 1H), 4.02 (dd, CH_2=CHC*H*HO-, 1H), 3.92 (dd, CH_2=CHCH*H*O-, 1H), 3.47 – 3.38 (m, -OC*H*(CH_3)CH_2-, 1H), 1.60 – 1.49 and 1.41 – 1.23 (m, -OCH(CH_3)(C*H*$_2$)$_7$$CH_3$, 14H), 1.13 (d, -OCH(C*H*$_3$)CH_2-, 3H), 0.88 (t, -CH_2CH_2C*H*$_3$, 3H) (Figure C.4A). ^{13}C NMR (126 MHz, $CDCl_3$) δ (ppm) = 135.65, 116.23, 74.94, 69.32, 36.65, 31.88, 29.74, 29.59, 29.28, 25.54, 22.66, 19.63, 14.09 (Figure C.4B).

Synthesis of 1-(Allyloxy)octane (C5). Yield: 61.8%. ^{1}H NMR (500 MHz, $CDCl_3$) δ (ppm) = 5.97 – 5.86 (m, CH_2=C*H*CH_2-, 1H), 5.26 (d, C*H*H=CH-, 2H), 5.16 (d, CH*H*=CH-, 2H), 3.99 – 3.93 (m, CH_2=CHC*H*$_2$O-, 2H), 3.42 (t,-OC*H*$_2$$CH_2CH_2$-, 2H), 1.63 – 1.53 (m, -OCH_2C*H*$_2$$CH_2$-, 2H), 1.39 – 1.21 (m, -OCH_2CH_2(C*H*$_2$)$_5$$CH_3$, 10H), 0.87 (t, -$CH_2$C*H*$_3$, 3H) (Figure C.5A). ^{13}C NMR

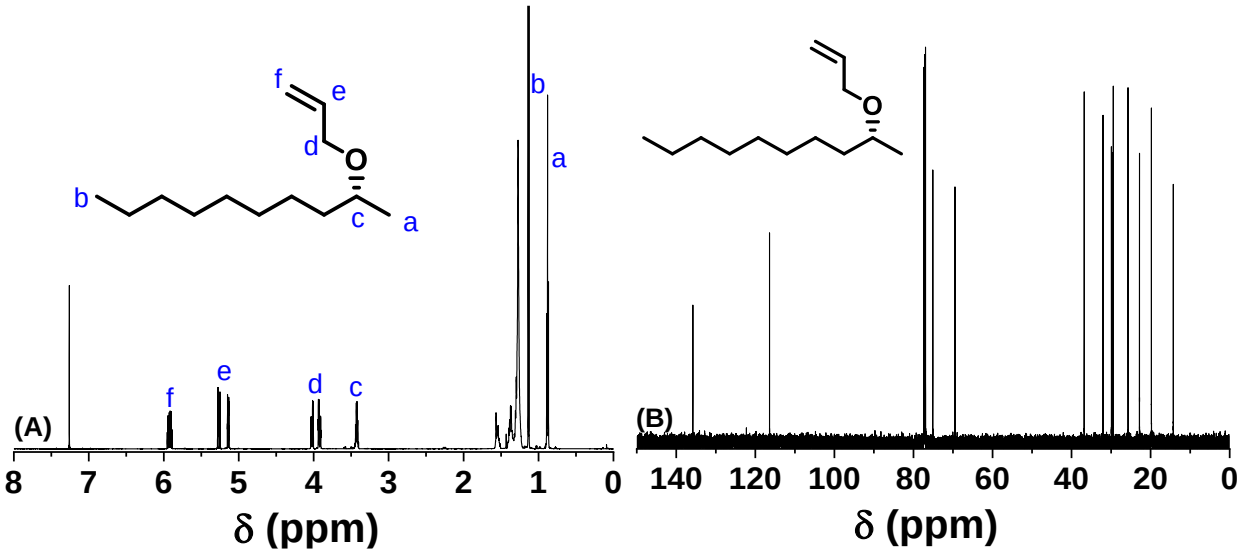

Figure C.2. (A) ^{1}H and (B) ^{13}C NMR spectra of (*R*)-2-(allyloxy)decane (C2) in $CDCl_3$.

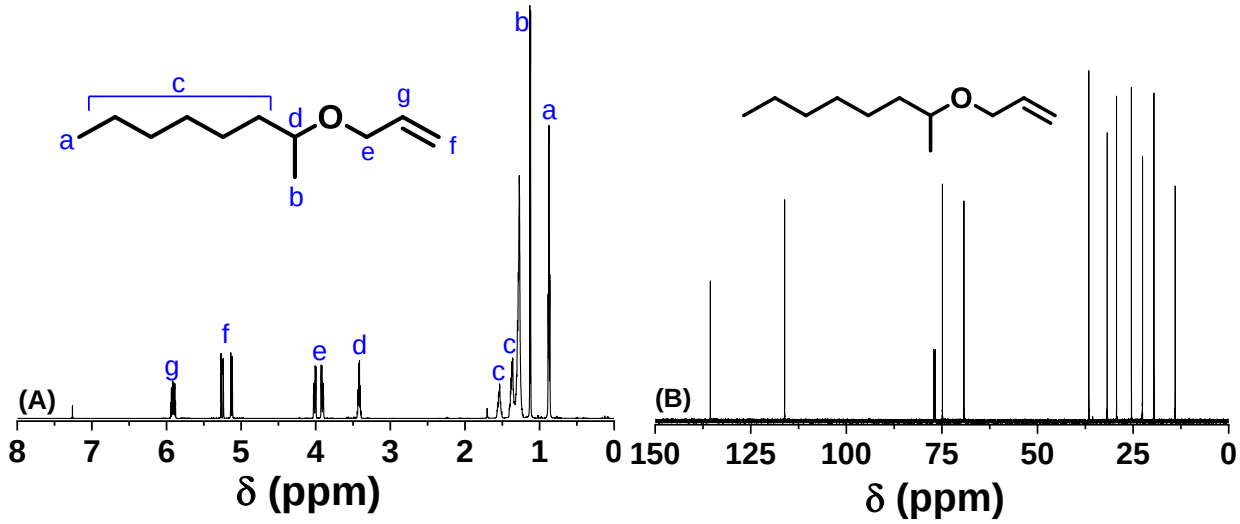

Figure C.3. (A) ^{1}H and (B) ^{13}C spectra of 2-(allyloxy)octane (C3) in $CDCl_3$.

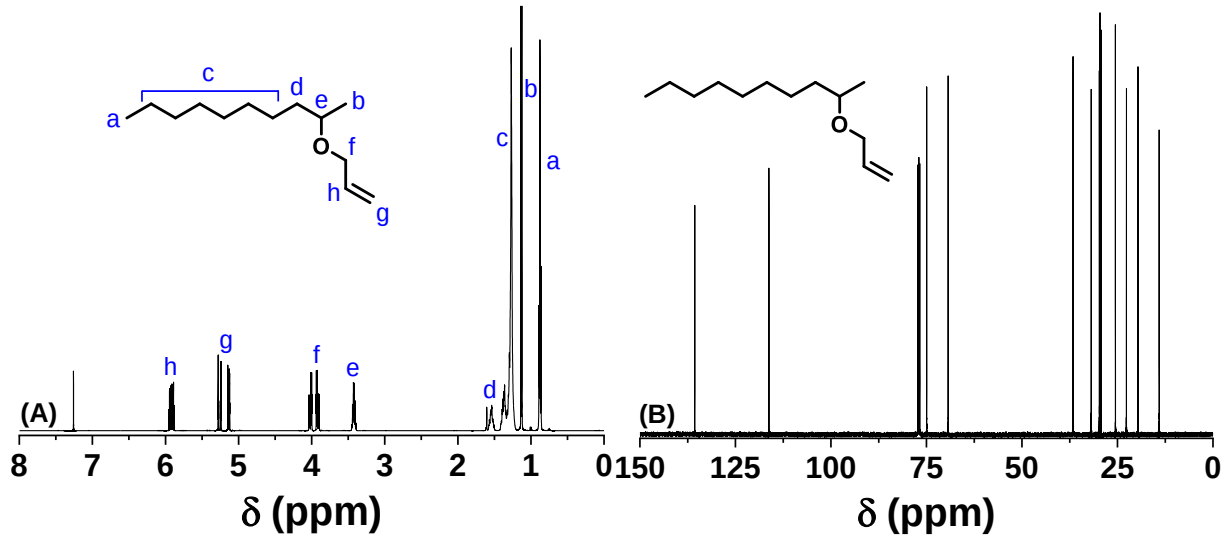

Figure C.4. (A) ^{1}H and (B) ^{13}C NMR spectra of 2-(allyloxy)decane (C4) in $CDCl_3$.

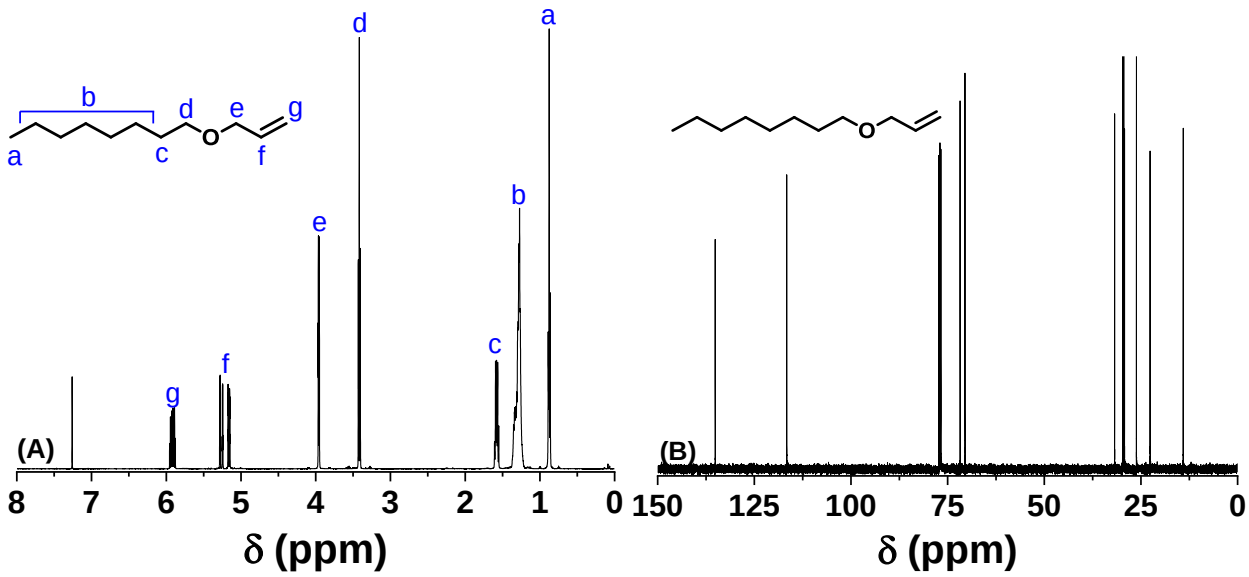

Figure C.5. (A) ^{1}H and (B) ^{13}C spectra of 1-(allyloxy)octane (C5) in $CDCl_3$.

(126 MHz, $CDCl_3$) δ (ppm) = 135.12, 116.62, 71.78, 70.51, 31.82, 29.76, 29.46, 29.25, 26.18, 22.64, 14.07 (Figure C.5B).

Synthesis of (R)-S-(3-(Octan-2-yloxy)propyl) Ethanethioate (D1). Thioacetates D1-D5 were synthesized using photo-initiated thiol-ene click reaction. The following shows the detailed procedure for D1. (*R*)-(2-Allyloxy)octane (C1) (2.00 g, 11.7 mmol), thioacetic acid (4.503 g, 59.2 mmol), and 2,2-dimethoxy-2-phenylacetophenone (3.00 g, 11.7 mmol) were added into a 25 mL two-necked round bottom flask with a stir bar. After the mixture was bubbled with nitrogen gas for 30 min, the flask was exposed to UV light (λ = 360 nm) from a handheld TLC detector (Spectroline Model ENF-240C, 4 W) for 10 min. Full disappearance of the vinyl peaks in the range of 5.00 to 6.00 ppm was observed via ^{1}H NMR spectroscopy analysis. The reaction mixture was diluted with diethyl ether (10 mL), poured into a 250 mL separatory funnel, and washed with a saturated sodium bicarbonate solution (30 mL × 4). The organic phase was retrieved and dried with anhydrous sodium sulfate in an Erlenmeyer flask. The solvent was removed using rotary evaporation to give a crude yellow mixture. Silica gel column chromatography was performed using a mixture of ethyl acetate and hexanes (1:10, v/v) as the eluent to remove the impurities and isolate the pure compound. The product was obtained as a clear liquid after the removal of the solvents by rotary evaporation and drying under high vacuum (1.106 g, 38.2% yield). ^{1}H NMR (500 MHz, $CDCl_3$) δ (ppm) = 3.53 – 3.48 and 3.39 – 3.29 (m,-$CH_2CH_2OCH(CH_3)CH_2$-, 3H), 2.94 (t, -SCH_2CH_2-, 2H), 2.30 (s, CH_3COSCH_2-, 3H), 1.84-1.77 (m, -$SCH_2CH_2CH_2$-, 2H), 1.54 – 1.44 and 1.39 – 1.19 (m, -$OCH(CH_3)(CH_2)_5CH_3$, 10H), 1.09 (d, -$OCH(CH_3)CH_2$-, 3H), 0.86 (t, -CH_2CH_3, 3H) (Figure C.6A). ^{13}C NMR (126 MHz, $CDCl_3$) δ (ppm) = 195.83, 75.53, 66.47, 36.62, 31.81, 30.55, 30.00, 29.35, 26.14, 25.49, 22.58, 19.60, 14.04 (Figure C.6B). Specific optical rotation [α] = -5.1° (chloroform).

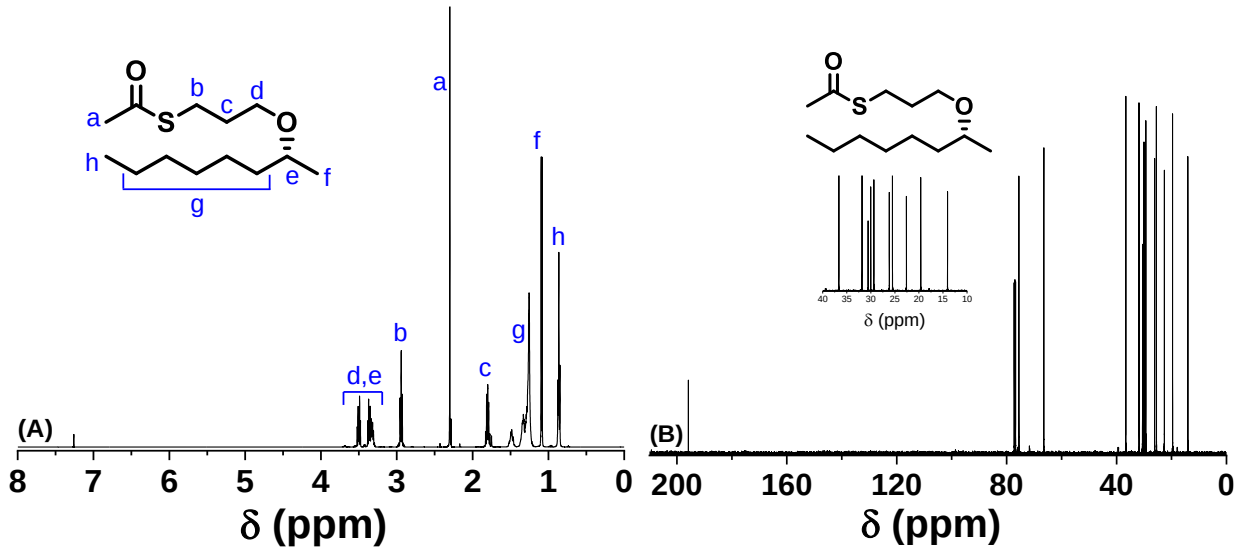

Figure C.6. (A) ^{1}H and (B) ^{13}C spectra of (*R*)-*S*-(3-(octan-2-yloxy)propyl) ethanethioate (D1) in $CDCl_3$.

D2, D3, D4, and D5 (see Scheme S1) were synthesized by using the same procedure and purification method as for (*R*)-*S*-(3-(octan-2-yloxy)propyl) ethanethioate (D1). The following are the characterization data for these compounds.

Synthesis of (R)-S-(3-(Decan-2-yloxy)propyl) Ethanethioate (D2). Yield: 74.3%. ^{1}H NMR (600 MHz, $CDCl_3$) δ (ppm) = 3.54 – 3.49 and 3.41 – 3.30 (m, -CHC*H*$_2$OC*H*(CH_3)CH_2-, 3H), 2.94 (t, -SC*H*$_2$$CH_2$$CH_2$-, 2H), 2.32 (s, C*H*$_3COSCH_2$-, 3H), 1.82 (p, -S$CH_2$C*H*$_2$$CH_2$-, 2H), 1.55 – 1.46 and 1.37 – 1.23 (m, -O$CH_2$$CH_2$(C*H*$_2$)$_7$$CH_3$, 14H), 1.11 (d, -OCH(C*H*$_3$)CH_2-, 3H), 0.88 (t, -CH_2C*H*$_3$, 3H) (Figure C.7A). ^{13}C NMR (151 MHz, $CDCl_3$) δ 195.94, 75.58, 66.51, 36.65, 31.88, 30.60, 30.03, 29.73, 29.59, 29.28, 26.18, 25.57, 22.67, 19.64, 14.09 (Figure C.7B). Specific optical rotation [α] = -3.90° (chloroform).

Synthesis of S-(3-(Octan-2-yloxy)propyl) Ethanethioate (D3). Yield: 57.3%. ^{1}H NMR (500 MHz, $CDCl_3$) δ (ppm) = 3.56 – 3.48 and 3.42 – 3.29 (m, -CHC*H*$_2$OC*H*(CH_3)CH_2-, 3H), 2.95 (t, -SC*H*$_2$$CH_2$$CH_2$-, 2H), 2.32 (s, C*H*$_3COSCH_2$-, 3H), 1.81 (p, -S$CH_2$C*H*$_2$$CH_2$-, 2H), 1.56 – 1.45 and 1.40 – 1.22 (m, -OCH(CH_3)(C*H*$_2$)$_5$$CH_3$, 10H), 1.11 (d, -OCH(C*H*$_3$)CH_2-, 3H), 0.88 (t, -CH_2C*H*$_3$, 3H) (Figure C.8A). ^{13}C NMR (126 MHz, $CDCl_3$) δ (ppm) = 195.93, 75.58, 66.51, 36.65, 31.85, 30.60, 30.02, 29.38, 26.18, 25.53, 22.62, 19.64, 14.08 (Figure C.8B).

Synthesis of S-(3-(Decan-2-yloxy)propyl) Ethanethioate (D4). Yield: 77.7%. ^{1}H NMR (500 MHz, $CDCl_3$) δ (ppm) = 3.53 – 3.45 and 3.39 – 3.26 (m, -CHC*H*$_2$OC*H*(CH_3)CH_2-, 3H), 2.93 (t, -SC*H*$_2$$CH_2$$CH_2$-, 2H), 2.29 (s, C*H*$_3COSCH_2$-, 3H), 1.81 (p, -S$CH_2$C*H*$_2$$CH_2$-, 2H), 1.52 – 1.42 and 1.37 – 1.19 (m, -O$CH_2$$CH_2$(C*H*$_2$)$_7$$CH_3$, 14H), 1.08 (d, -OCH(C*H*$_3$)CH_2-, 3H), 0.85 (t, -CH_2C*H*$_3$, 3H) (Figure C.9A). ^{13}C NMR (126 MHz, $CDCl_3$) δ (ppm) = 195.70, 75.49, 66.43, 36.60, 31.82, 30.49, 29.98, 29.67, 29.53, 29.22, 26.11, 25.50, 22.59, 19.57, 14.02 (Figure C.9B).

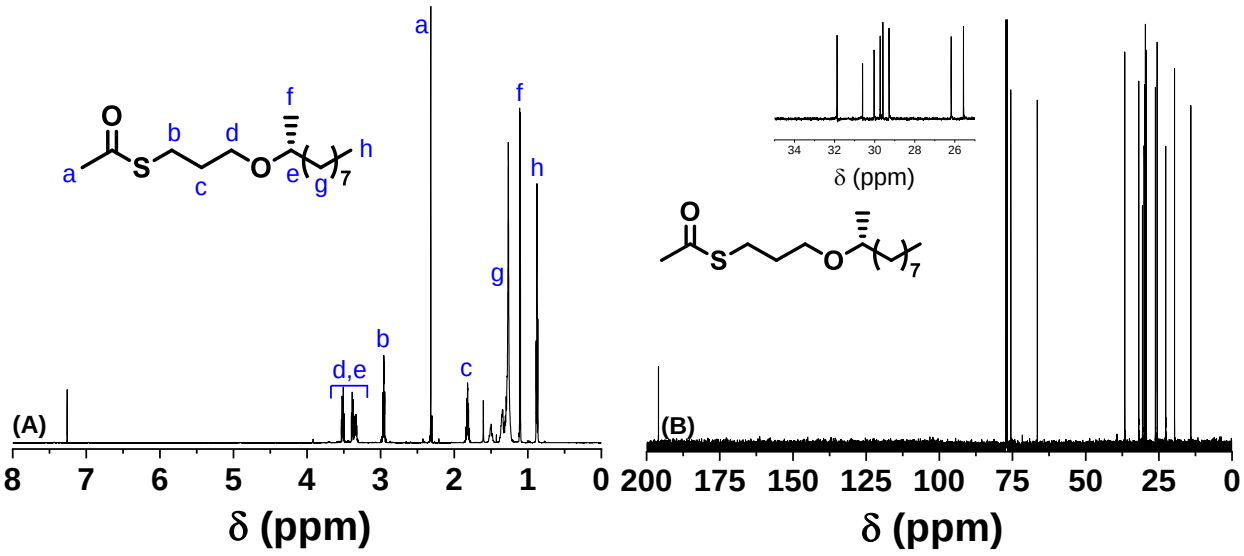

Figure C.7. (A) ^{1}H and (B) ^{13}C spectra of (*R*)-*S*-(3-(decan-2-yloxy)propyl) ethanethioate (D2) in $CDCl_3$.

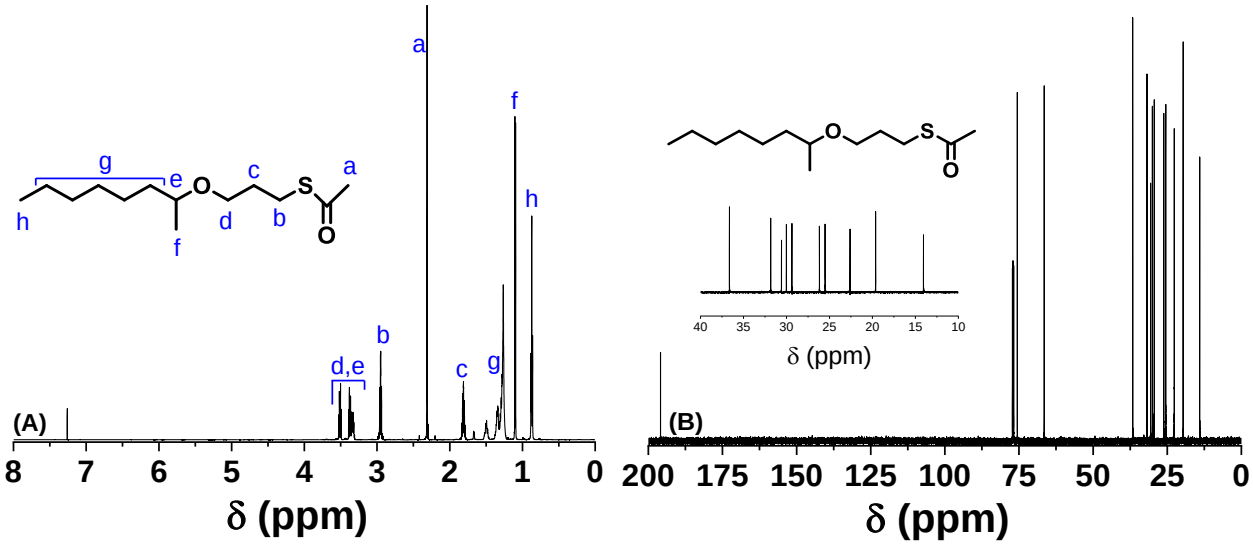

Figure C.8. (A) ^{1}H and (B) ^{13}C spectra of *S*-(3-(octan-2-yloxy)propyl) ethanethioate (D3) in $CDCl_3$.

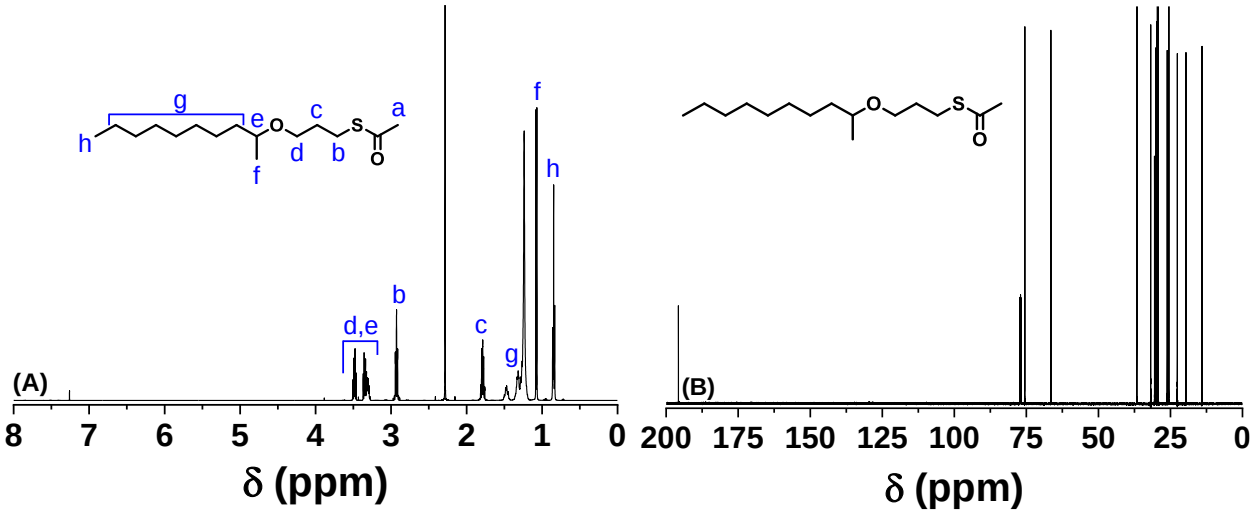

Figure C.9. (A) ^{1}H and (B) ^{13}C spectra of *S*-(3-(decan-2-yloxy)propyl) ethanethioate (D4) in $CDCl_3$.

Synthesis of *S*-(3-(Octyloxy)propyl) Ethanethioate (D5). Yield: 61.8%. ^{1}H NMR (500 MHz, $CDCl_3$) δ (ppm) = 3.44 (t, -S$(CH_2)_2$C*H*$_2$O-, 2H), 3.39 (t, - S$(CH_2)_2CH_2OC$*H*$_2CH_2$-, 2H), 2.95 (t,-SC*H*$_2CH_2$-, 2H), 2.32 (s, C*H*$_3$COS-, 3H), 1.84 (p, -SCH_2C*H*$_2CH_2$O-, 2H), 1.59 – 1.51 (m, -S$CH_2CH_2CH_2OCH_2$C*H*$_2$-, 2H), 1.35 – 1.22 (m, -OCH_2CH_2(C*H*$_2)_5CH_3$, 10H), 0.87 (t, -CH_2C*H*$_3$, 3H) (Figure C.10A). ^{13}C NMR (151 MHz, $CDCl_3$) δ (ppm) = 195.91, 71.08, 69.01, 31.81, 30.59, 29.68, 29.66, 29.43, 29.24, 26.15, 26.10, 22.64, 14.08 (Figure C.10B).

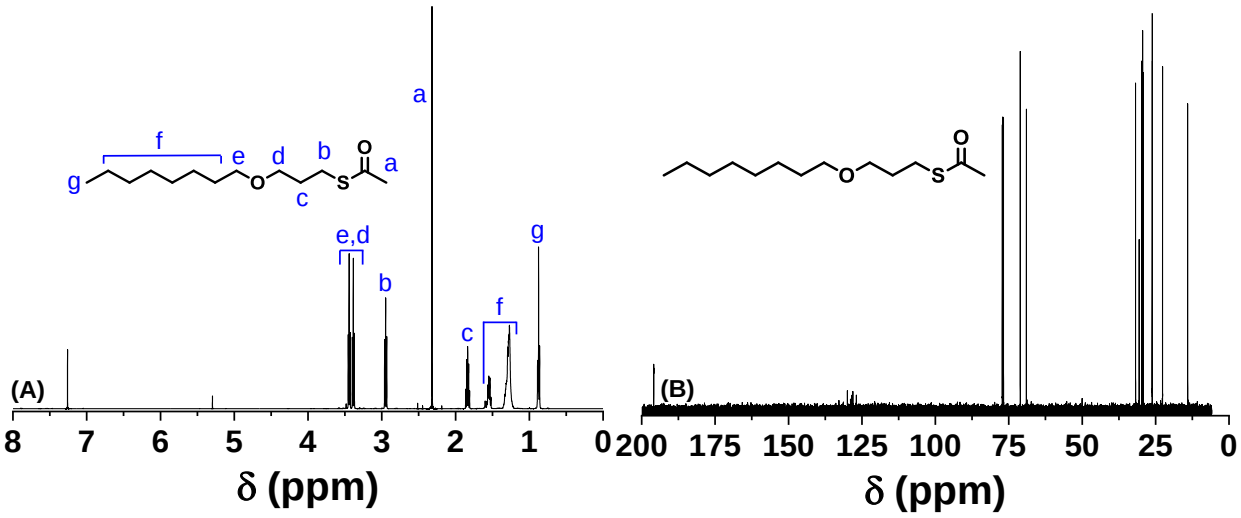

Figure C.10. (A) ^{1}H and (B) ^{13}C spectra of *S*-(3-(octyloxy)propyl) ethanethioate (D5) in $CDCl_3$.

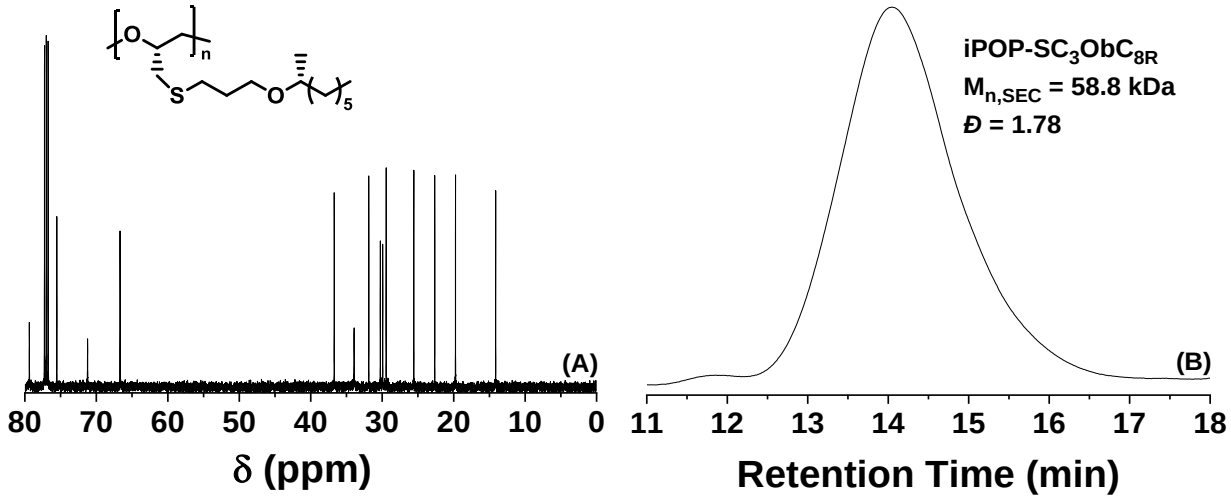

Figure C.11. (A) ^{13}C NMR spectrum of iPOP-SC_3ObC_{8R} in $CDCl_3$ and (B) size exclusion chromatography trace of iPOP-SC_3ObC_{8R} using THF as solvent.

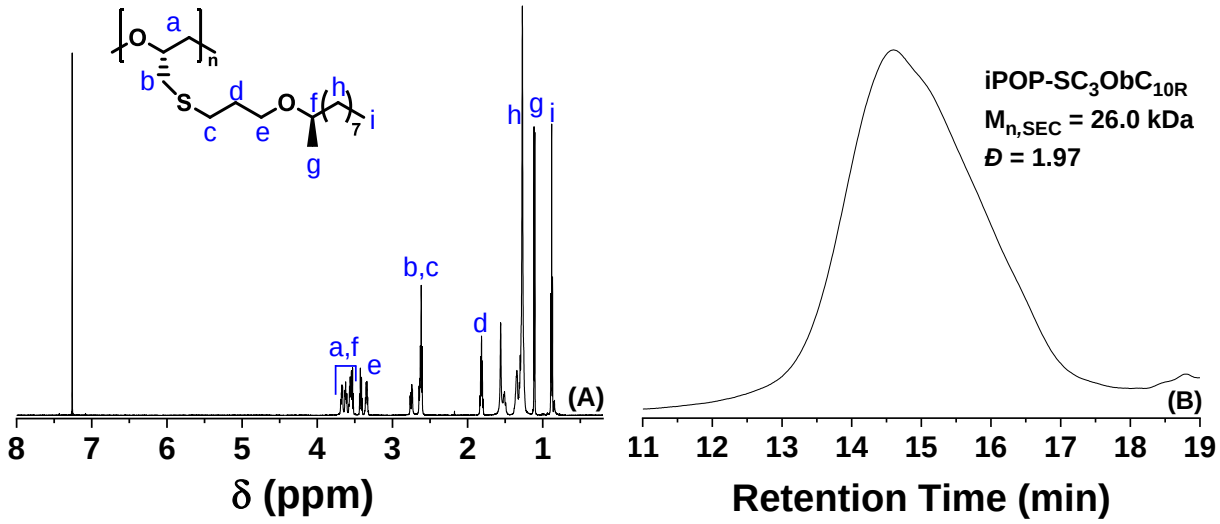

Figure C.12. (A) ^{1}H NMR spectrum of iPOP-SC$_3$ObC$_{10R}$ in CDCl$_3$ and Size exclusion chromatography trace of iPOP-SC$_3$ObC$_{10R}$ using THF as solvent.

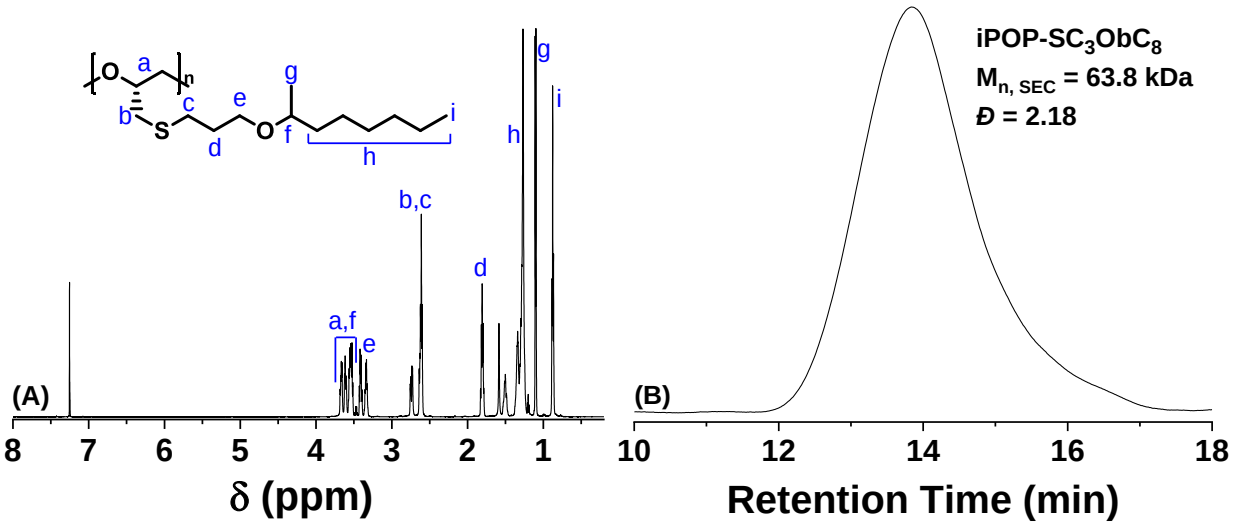

Figure C.13. (A) ^{1}H NMR spectrum of iPOP-SC$_3$ObC$_8$ in CDCl$_3$ and (B) size exclusion chromatography of iPOP-SC$_3$ObC$_8$ with THF as the mobile phase.

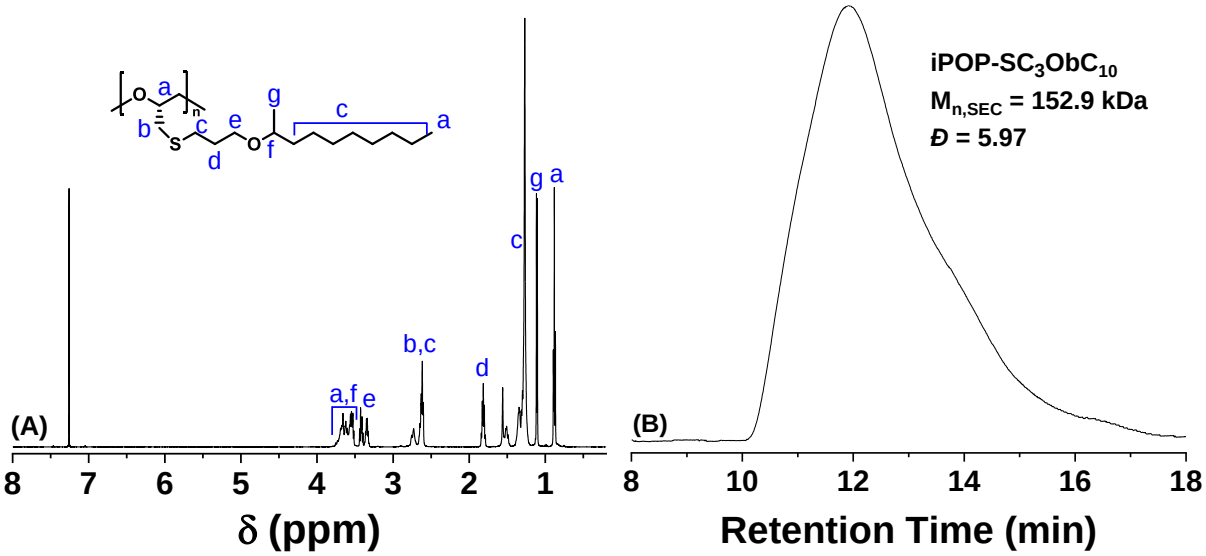

Figure C.14. (A) ^{1}H NMR spectrum of iPOP-SC$_3$ObC$_{10}$ in CDCl$_3$ and size exclusion chromatography of iPOP-SC$_3$ObC$_{10}$ with THF as the mobile phase.

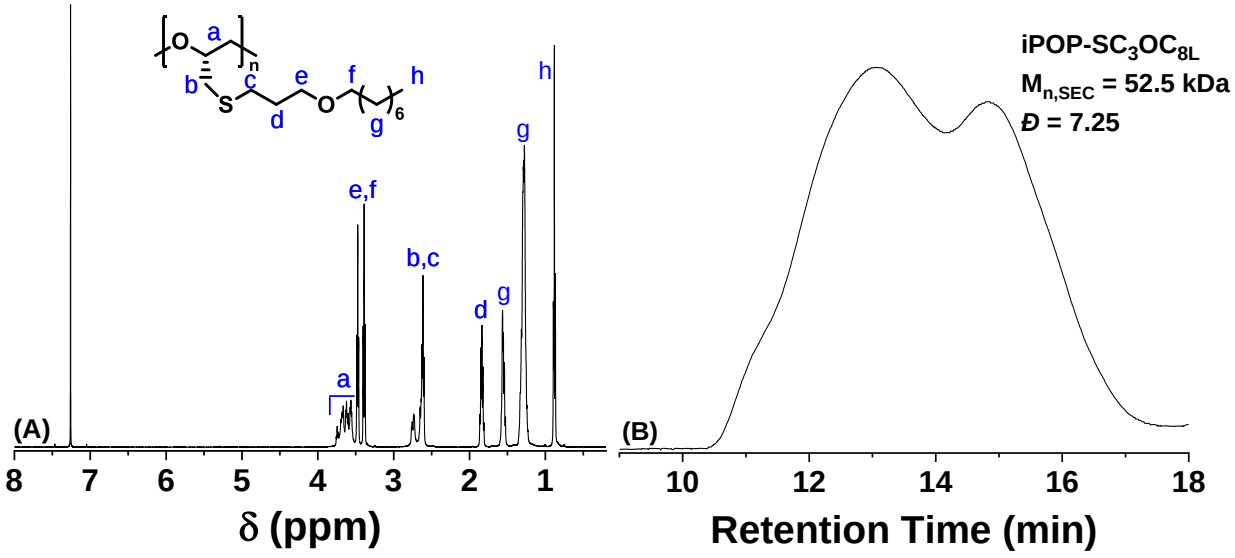

Figure C.15. (A) ^{1}H NMR spectrum of iPOP-SC_3OC_{8L} in $CDCl_3$ and (B) size exclusion chromatography of iPOP-SC_3OC_{8L} with THF as the mobile phase.

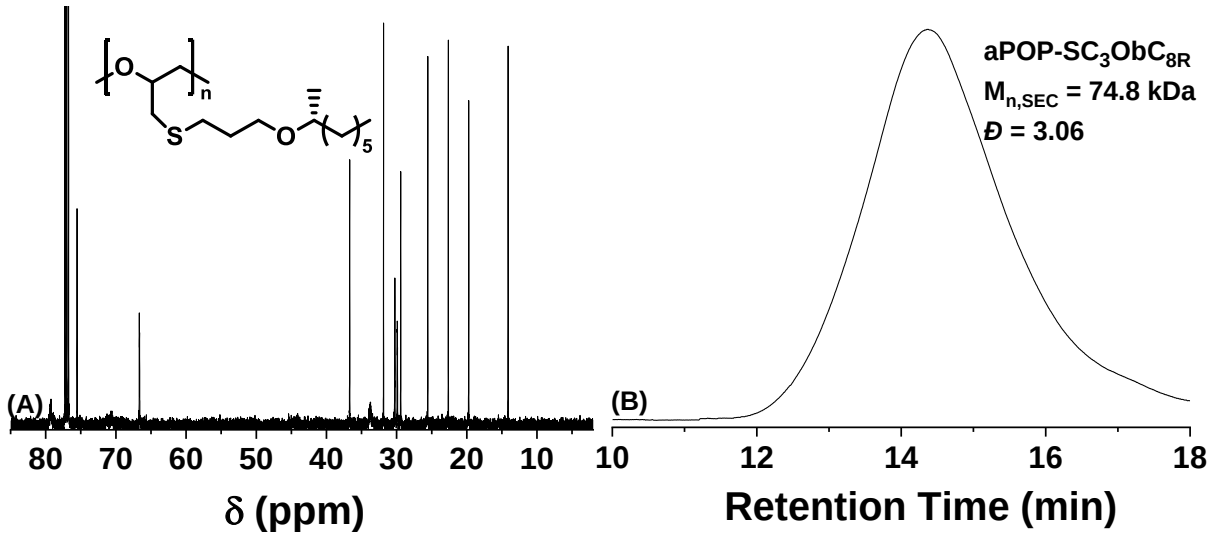

Figure C.16. (A) ^{13}C NMR spectrum of aPOP-SC_3ObC_{8R} in $CDCl_3$ and (B) size exclusion chromatography of aPOP-SC_3ObC_{8R} with THF as the mobile phase.

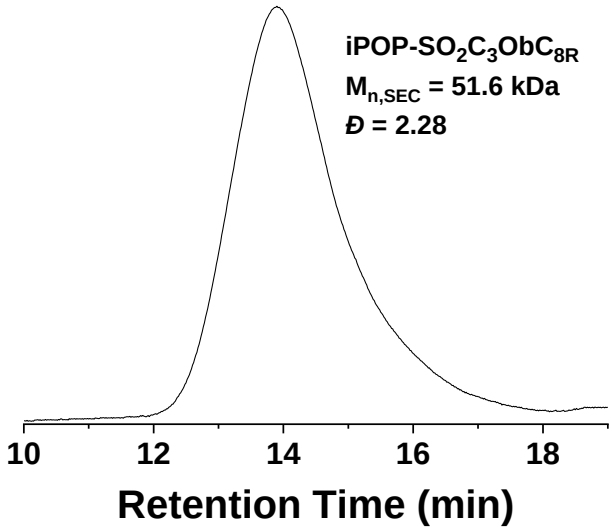

Figure C.17. Size exclusion chromatography trace of iPOP-$SO_2C_3ObC_{8R}$ using THF as the mobile phase.

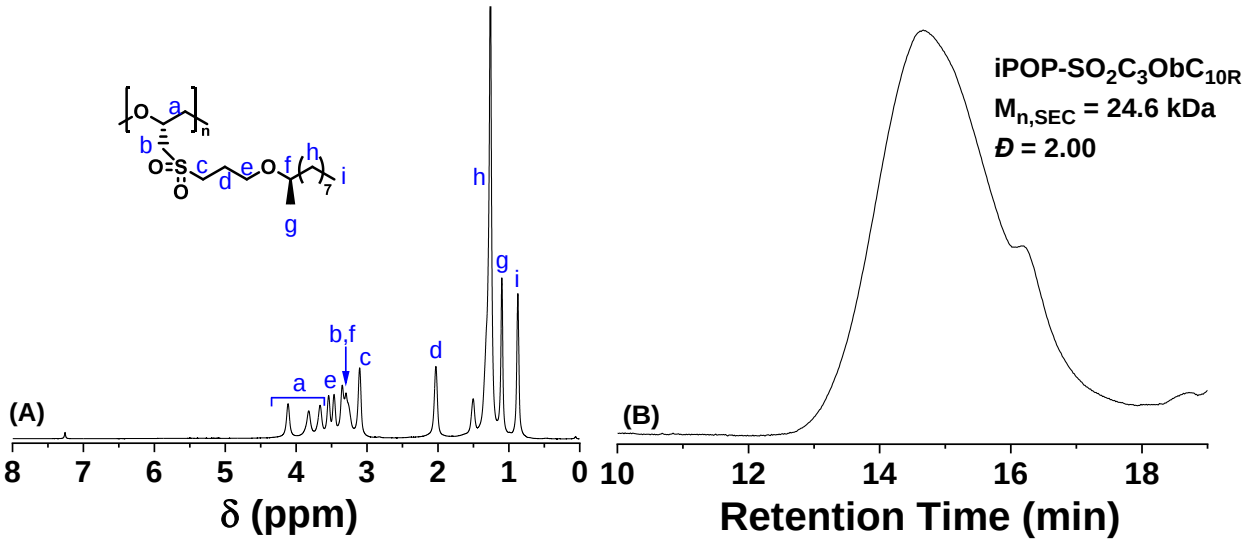

Figure C.18. (A) ^{1}H NMR spectrum of iPOP-$SO_2C_3ObC_{10R}$ in $CDCl_3$ and (B) size exclusion chromatography trace of iPOP-$SO_2C_3ObC_{10R}$ using THF as the mobile phase.

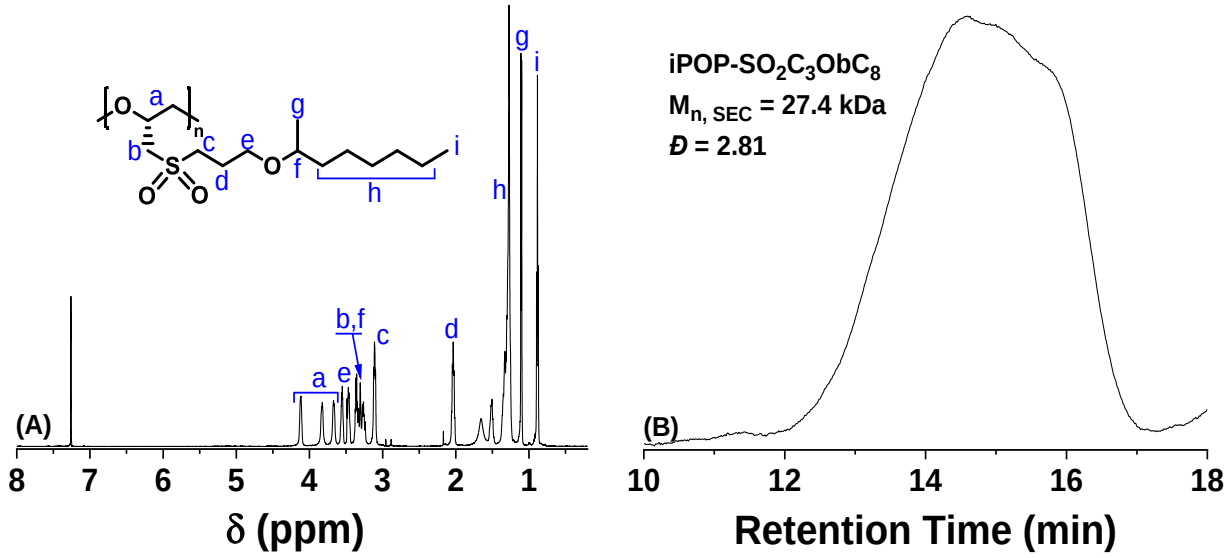

Figure C.19. (A) ^{1}H NMR spectrum of iPOP-$SO_2C_3ObC_8$ in $CDCl_3$ and (B) size exclusion chromatography trace of iPOP-$SO_2C_3ObC_8$ in $CDCl_3$.

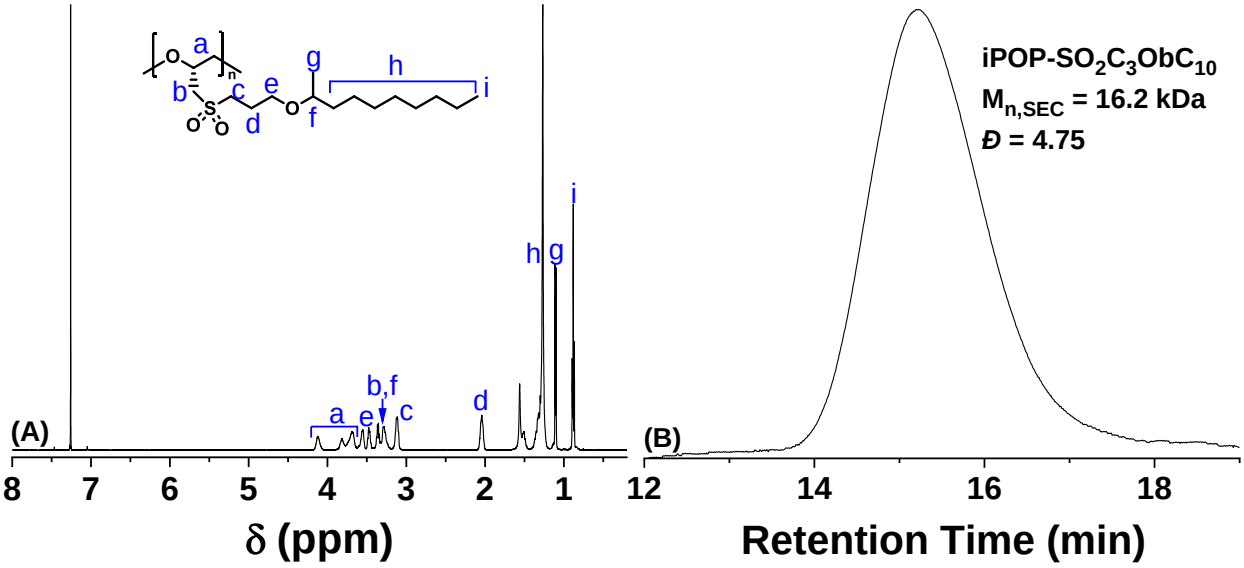

Figure C.20. (A) ^{1}H NMR spectrum of iPOP-$SO_2C_3ObC_{10}$ in $CDCl_3$ and (B) size exclusion chromatography trace of iPOP-$SO_2C_3ObC_{10}$ in $CDCl_3$.

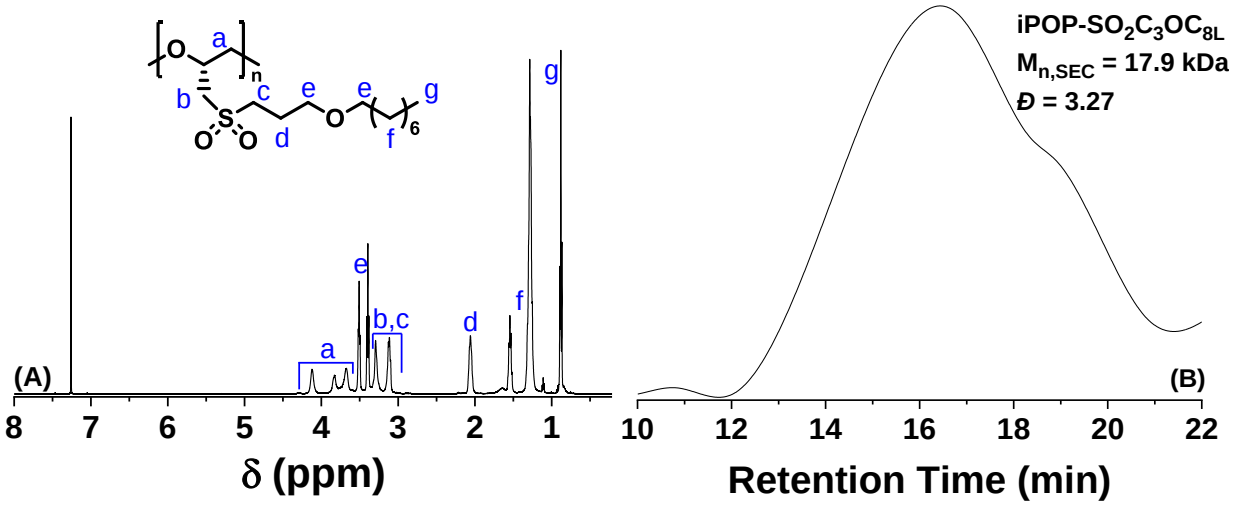

Figure C.21. (A) ^{1}H NMR spectrum of iPOP-$SO_2C_3OC_{8L}$ in $CDCl_3$ and (B) size exclusion chromatography trace of iPOP-$SO_2C_3OC_{8L}$ using THF as the mobile phase.

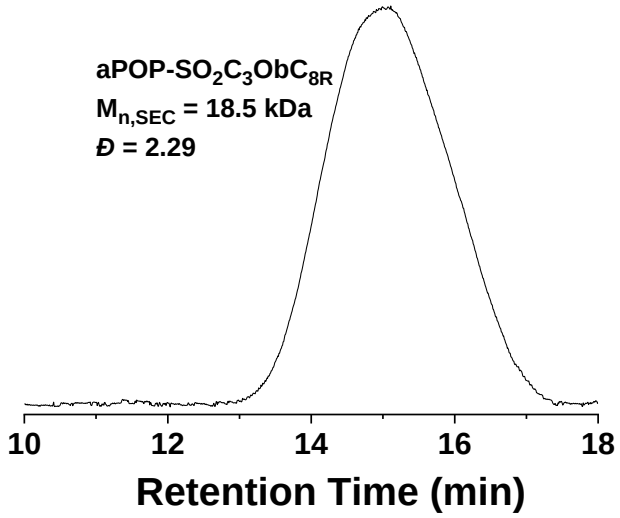

Figure C.22. Size exclusion chromatography trace of aPOP-$SO_2C_3ObC_{8R}$ using THF as the eluent.

Section C.3. DSC Analysis of iPOP-SC_3ObC_{8R} and aPOP-SC_3ObC_{8R}

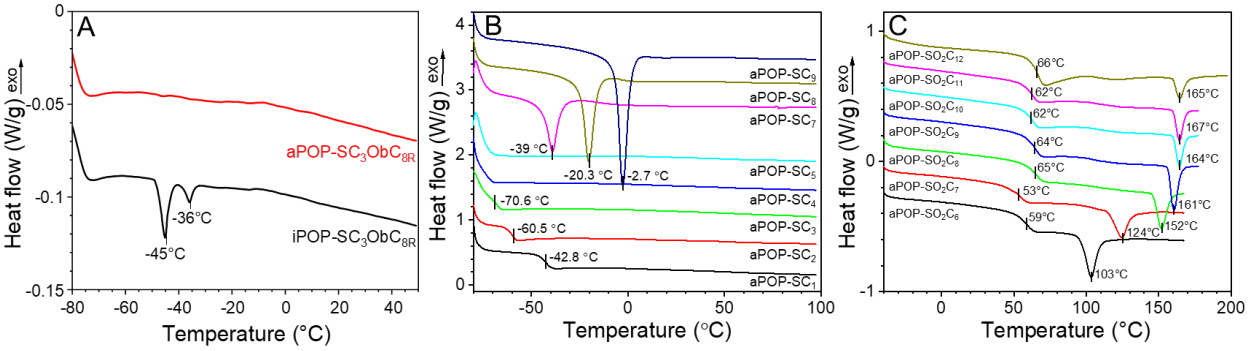

Figure C.23. (A) DSC second heating curves for iPOP-SC_3ObC_{8R} and aPOP-SC_3ObC_{8R}. The heating rate was 5 °C/min for both polymers. DSC second heating curves for (B) aPOP-SC_n and (C) aPOP-SO_2C_n from ref. 40 in the main text (copyright American Chemical Society 2019).

Section C.4. Heating XRD for Various Chiral Polyether Fibers

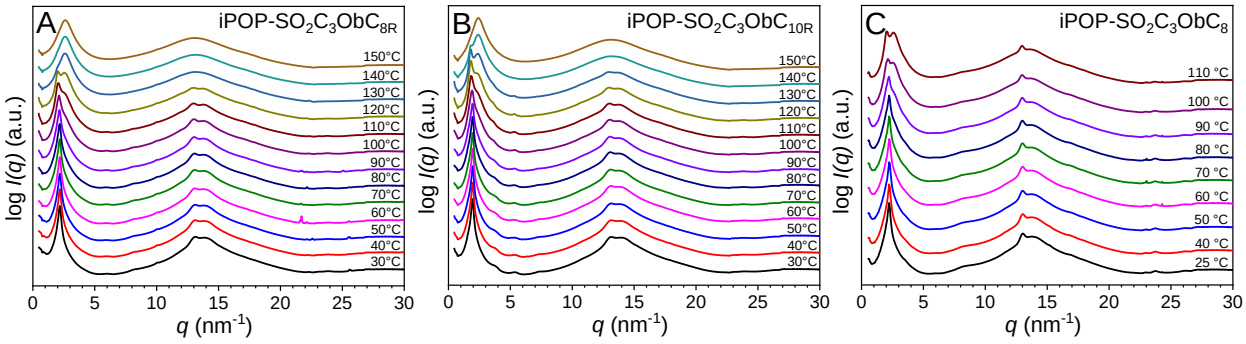

Figure C.24. 1D XRD profiles of (A) iPOP-$SO_2C_3ObC_{8R}$, (B) iPOP-$SO_2C_3ObC_{10R}$, and (C) iPOP-$SO_2C_3ObC_8$ fibers during the heating process.

Section C.5. Raw Data D-E Loops

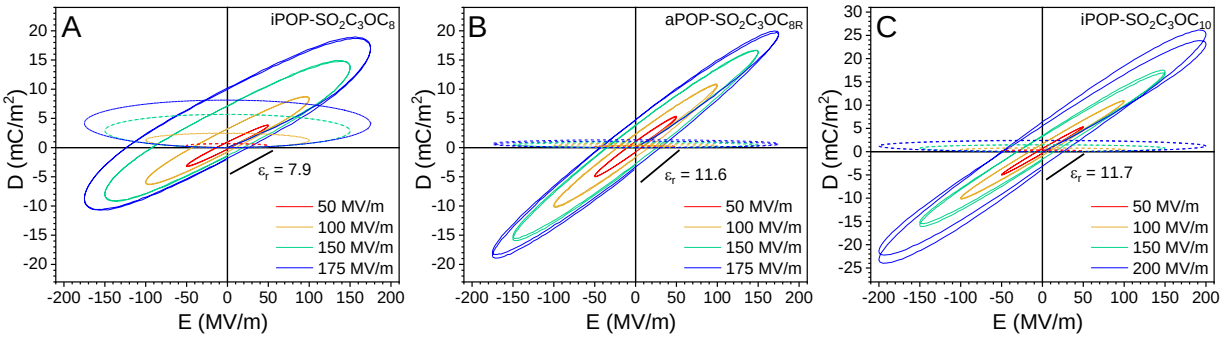

Figure C.25. Raw data bipolar D-E loops for (A) iPOP-$SO_2C_3ObC_8$, (B) aPOP-$SO_2C_3ObC_{8R}$, and (C) iPOP-$SO_2C_3ObC_{10}$ at room temperature. The poling frequency was 100 Hz with a sinusoidal waveform. The dashed line horizontal loops are AC electronic conduction loops. After subtraction of the AC electronic conduction, the treated loops are presented in Figure 4.9 in the main text.

Chapter 5: Adaptable Multivalent Hairy Inorganic Nanoparticles

The work presented in this chapter has been published as a communication in *J. Am. Chem. Soc.* **2021**, *143(41)*, 16919–16924. I did all the transmission electron microscopy work and the image analysis. Binary mixed poly(*tert*-butyl acrylate)/polystyrene brush-grafted silica nanoparticles were synthesized by Andrew J. Chancellor. Michael T. Kelly and Tram T. Le contributed to the synthesis of the initiator.

Abstract

A polymer brush-based approach is described for fabricating multivalent patchy nanoparticles (NPs) with the number of nanodomains (valency) from 6 to 10, potentially from 1 to 10, by exploiting the lateral microphase separation of binary mixed homopolymer brushes grafted on NPs with a radius comparable to the polymer sizes. Well-defined mixed brushes were grown on 20.4 nm silica NPs by two-step surface-initiated reversible deactivation radical polymerizations and microphase separated laterally upon casting from a good solvent, producing multivalent NPs on 2D surfaces. A linear relationship between valency and average core size for the corresponding valency was observed. The mixed brush NPs exhibited abilities to form "bonds" through the overlap of nanodomains and to change the valency when interacting with adjacent NPs. This method could open up a new avenue for studying patchy NPs.

5.1. Introduction

Patchy particles are a class of unconventional particles where the surface is patterned with a small number of discrete, distinct domains.[1-5] These particles, including the simplest version – Janus particles with contrasting properties on the opposite sides of the particles,[6-9] hold promise for many applications.[1-9] They are used as effective Pickering emulsion stabilizers,[8] for constructing meta-materials with complex structures that cannot be achieved with particles of uniform surface characteristics,[1,2] and for building colloidal assemblies that mimic organic compounds (colloidal molecules).[3] Polymer brushes have emerged as a versatile bottom-up means for fabricating patchy NPs owing to their ability to undergo self-reorganization in response to environmental changes.[4,10-14] Most notably, surface patterning of homopolymer-grafted NPs with relatively low grafting densities was attained upon lowering solvent quality to collapse the uniform brushes into surface-pinned micelles, producing patchy NPs with a small number of domains or helicoidal patterns.[4,10,11] Multicomponent brushes provide greater flexibility toward patchy NPs and assemblies.[12-20] Programmed surface patterning and assembly of diblock copolymer-grafted gold NPs were realized by first formation of patchy NPs through the collapse of the inner block and then self-assembly into small, well-defined clusters.[14] Soft patchy NPs with a polymeric core were made from ABC triblock copolymer micelles by collapsing one of the two outer blocks in the corona and self-assembled into complex well-ordered structures.[5] Despite the progress, it remains a challenge to prepare patchy NPs with a valency from 1 to 10 using polymer brush-grafted NPs (hairy NPs).

Herein a method is described for fabricating patchy NPs with the number of nanodomains (valency) from 6 to 10 (i.e., multivalent NPs[21]), potentially from 1 to 10, without resorting to poor solvents by using binary mixed homopolymer brush-grafted small NPs. These NPs can form

"bonds" through the overlap of their nanodomains and change their valency according to the environment. Mixed brushes, composed of two distinct homopolymers randomly or alternately end-tethered on a surface, exhibit intriguing behaviors.[21-32] Simulations have shown that for mixed brushes on spherical NPs with a radius comparable to the polymers' unperturbed root-mean-square end-to-end distances (R_{rms}), various islanded structures are formed from lateral microphase separation of the two grafted polymers, yielding multivalent NPs with 2 to 12 (except 11) nanodomains,.[21,31,32] The valency is governed by core size, grafting density (σ), chain length, etc., among which core size plays a significant role.[31] Moreover, upon assembly, polymer microphase separation competes with NP close packing; both commensurate and incommensurate structures could occur, rendering this type of multivalent particles intrinsically adaptable.

5.2. Experimental Section

5.2.1. Synthesis of Mixed Poly(*tert*-butyl acrylate) (P*t*BA)/polystyrene (PS) Brush-Grafted 20.4 nm Silica NPs

All the mixed P*t*BA/PS brush-grafted 20.4 nm silica NP samples were synthesized by Mr. Andrew J. Chancellor; the details can be found in his M.S. thesis.[33]

5.2.2. Transmission Electron Microscopy (TEM) Study of Polymer Brush-Grafted Silica NPs

TEM was performed using a JEOL JEM-1400 microscope with an accelerating voltage of 120 kV. The bright field images were taken with a bottom mounted Gatan UltraScan US4000XP Model 1095 CCD camera. To prepare TEM samples, hairy NPs were dispersed in chloroform at a concentration of 0.25 mg/mL, drop cast onto carbon-coated, copper TEM grids using a glass pipette, solvent annealed with chloroform vapor in a closed container for at least 3 h, allowed to

dry at ambient conditions, and then stained with RuO_4 vapor for 7 min (for general visualization) or 2 min (for study of the relationship between core size and valency).

5.3. Results and Discussion

Mixed P*t*BA/PS brushes were grown on 20.4 nm silica NPs by a two-step surface-initiated reversible deactivation radical polymerization process (Scheme 5.1), which was performed by Mr. Andrew J. Chancellor. The synthesis details can be found in Mr. Chancellor's M.S. thesis. Briefly, a monochlorosilane-terminated asymmetric difunctional initiator (Y-I-Silane), containing one atom transfer radical polymerization (ATRP[34]) initiating group and one nitroxide-mediated radical polymerization (NMRP[35]) initiating moiety, was immobilized onto 20.4 nm silica NPs. The initiator-functionalized NPs were used for growing brushes by sequential surface-initiated ATRP of *tert*-butyl acrylate at 75 °C and surface-initiated NMRP of styrene at 120 °C, each with the addition of a free initiator.[36,37] The polymer brush-grafted silica NPs were isolated from the polymerization mixture and purified by multiple cycles of dispersion in tetrahydrofuran and ultracentrifugation separation. The hairy NPs were characterized by thermogravimetric analysis for the polymer content. The molecular weights and dispersities of the free polymers formed from the free initiators were analyzed by size exclusion chromatography. A total of nine mixed brush NP samples with a fixed P*t*BA M_n of 19.6 kDa and various PS M_ns (from 6.1 to 31.5 kDa) were prepared. The calculated PS grafting densities were in the range of 0.27–0.49 chains/nm^2,[38] similar to σ_{PtBA} (0.37 chains/nm^2). The P*t*BA's R_{rms} was estimated to be 8.3 nm, while the PS R_{rms} values ranged from 5.2 to 11.7 nm,[37,39] comparable to the radius of silica NPs. With increasing PS M_n, the volume fraction of PS (f_{PS}) increased and became > 0.50 at PS M_n = 20.0 kDa. The characterization data and calculated values are summarized in Table 5.1.

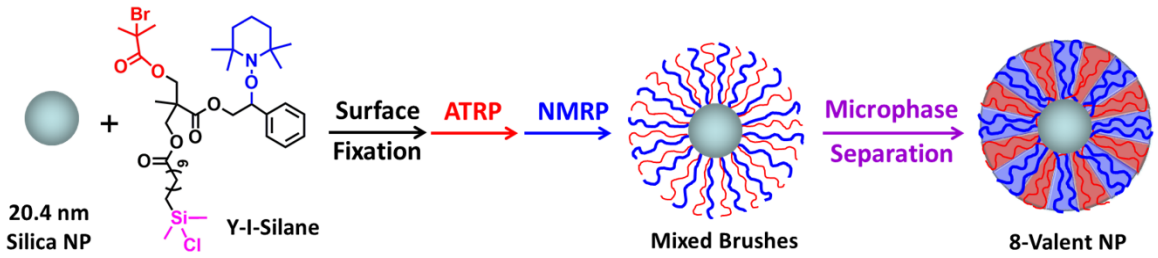

Scheme 5.1. Synthesis of Binary Mixed Homopolymer Brushes on 20.4 nm Silica NPs and Formation of Multivalent NPs with an 8-Valent NP as Example.

Table 5.1. Characterization of Mixed P*t*BA/PS Brush-Grafted Silica NPs

Hairy NPs	PS M_n (kDa), Đ [a]	σ_{PS} (chains/nm^2) [b]	PS R_{rms} (nm) [c]	f_{PS} [d]
BNP-6.1k	6.1, 1.27	0.45	5.2	0.27
BNP-9.7k	9.7, 1.26	0.37	6.5	0.32
BNP-10.9k	10.9, 1.18	0.33	6.9	0.32
BNP-12.9k	12.9, 1.28	0.32	7.5	0.35
BNP-15.2k	15.2, 1.17	0.27	8.1	0.35
BNP-20.0k	20.0, 1.18	0.39	9.3	0.51
BNP-23.0k	23.0, 1.17	0.37	10.0	0.53
BNP-27.6k	27.6, 1.19	0.40	10.9	0.59
BNP-31.5k	31.5, 1.25	0.40	11.7	0.62

[a] The number-average molecular weight (M_n) and dispersity (Đ) were determined by size exclusion chromatography (SEC) using PS standards. The M_n and Đ of P*t*BA were 19.6 kDa and 1.20, respectively. It was previously found that the P*t*BA M_n from SEC was similar to the M_n determined from the monomer conversion.[37] [b] σ_{PtBA}: 0.37 chains/nm^2. [c] The R_{rms} values of P*t*BA and PS were calculated using $R_{rms} = (C_\infty n l^2)^{1/2}$, where C_∞ is the characteristic ratio, n is the backbone C-C bond number, and l is the C-C bond length (1.54 Å).[39] The C_∞ for P*t*BA was unavailable, and we used PS C_∞ (9.5) for estimating P*t*BA's R_{rms}, giving 8.3 nm. [d] The densities of P*t*BA (1.008 g/cm^3) and PS (1.052 g/cm^3) were used in calculating f_{PS}.

To visualize the NPs' morphologies, TEM was performed. The brush NPs were drop-cast on carbon-coated TEM grids from $CHCl_3$ at 0.25 mg/mL, annealed with chloroform vapor for > 3 h, and stained with RuO_4 for 7 min. RuO_4 selectively stains PS, making it dark under TEM.[37] Figure 5.1a-j shows TEM micrographs of one P*t*BA NP without staining and single NPs of nine mixed brush samples. All mixed brushes were microphase separated, yielding spoke-like multivalent NPs with a small number of nanodomains extending outward from the core. The most common valency was 8 except for BNP-6.1k whose nanodomains were difficult to discern due to the short nanodomains (Figure 5.1b). The clearest multivalent NPs were found for the samples with PS M_n from 10.9 to 23.0 kDa (Figure 5.1d-h). The size of brush NPs and the length of dark nanodomains increased with increasing PS M_n. The PS domains were somewhat uniform in width when the PS M_n was ≤ 15.2 kDa (~ 7 nm for BNP-12.9k) but became truncated wedge-like at PS M_n = 20.0 kDa.[40] Upon further increasing PS M_n, the dark domains gradually enclosed the bright nanodomains and for BNP-27.6k and -31.5k the bright domains were fully covered by PS chains. Note that the degrees of polymerization (DPs) of PS for BNP-27.6k (265) and -31.5k (302) were significantly larger than the P*t*BA's DP. This is consistent with the simulation result that for asymmetric mixed brushes with a large chain length asymmetry the laterally phase-separated layer is covered with the longer species.[30]

The observed multivalent NPs under TEM are 2D projections; therefore, the valency $V \sim \frac{r}{w}$, where *r* is the NP radius and *w* is the nanodomain width. Compared with other patchy brush NPs, the valency here arises from the intrinsic lateral microphase separation of mixed brushes and therefore can be tuned by varying parameters such as M_n, *f*, Flory-Huggins parameter, and σ. Moreover, *r* plays a significant role as shown above and by simulations.[31,32] The silica NPs used here exhibited a certain dispersity. To elucidate how the core size affected the valency, BNP-15.2k

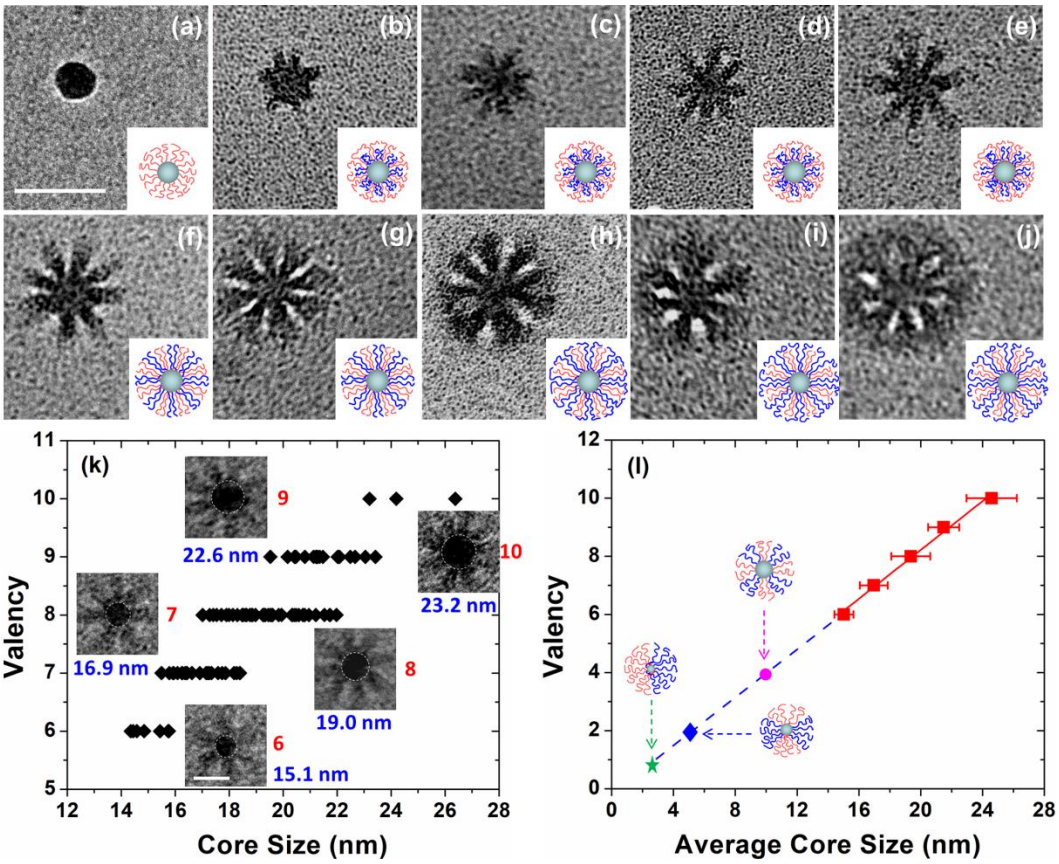

Figure 5.1. TEM micrographs of one P*t*BA-grafted silica NP (a), BNP-6.1k (b), -9.7k (c), -10.9k (d), -12.9k (e), -15.2k (f), -20.0k (g), -23.0k (h), -27.6k (i), and -31.5k (j). Scale bar: 50 nm. The mixed brush NPs were stained with RuO_4 for 7 min. (k) Plot of valency vs. core size for BNP-15.2k after stained with RuO_4 for 2 min. Scale bar: 25 nm. (l) Plot of valency versus average core diameter for the corresponding valency with the standard deviation. The star, diamond, and circle indicate mono-, di-, and tetra-valent NPs from extrapolation.

was stained for 2 min, which made both core NP and PS nanodomains visible under TEM (Figure 5.1k). For a guided view of nanodomains in Figure 5.1k, see Figure 5.2. We analyzed 102 NPs for core size and valency, and the results are plotted in Figure 5.1k. A trend was seen that the valency decreased with decreasing core dimension, and each valency corresponded to a size range, which qualitatively agreed with the simulation results.[32] A linear relationship between valency and average core size for each valency was observed (Figure 5.1l), with a slope of 0.42. Extrapolation showed that monovalent (i.e., Janus NPs), divalent, and tetravalent NPs would be obtained from mixed brush NPs with a core diameter of 2.8, 5.2, and 10 nm. Kim et al. studied mixed brush-grafted, ~ 3 nm gold NPs in toluene by neutron scattering and found that with increasing molecular weights, the brush NPs phase separated into Janus NPs.[41] Note that di- and tetravalent NPs could self-assemble into uncommon square lattices.[42]

These multivalent NPs can interact with each other and form "bonds". Figure 5.3 shows TEM images of BNP-15.2k, from individual NPs to various-sized clusters and NP lattice. Bonds were formed between NPs via the overlap of nanodomains, much like the σ-bond formation through head-to-head overlap of electron orbitals. The bonded domains were slightly darker and similar in length to those unbonded nanodomains (i.e., dangling bonds). In Figure 5.3c, the formation of two bonds, indicated by arrows, appeared to be in the process. As mentioned earlier, eight was the most frequent valency of individual NPs, and analysis of 304 hairy NPs showed an average valency of 7.86 ± 0.95. For the lattice (Figure 5.3l), the most common valency appeared to be six. Analysis of different-sized assemblies found that the average valency per NP decreased gradually from 7.86 ± 0.95 for individual NPs to 7.12 ± 1.05 for dimers (212 NPs analyzed), 6.55 ± 0.91 for trimers (123 NPs), 6.40 ± 0.91 for tetramers (156 NPs), 6.35 ± 1.00 for 5-mers (115 NPs), 6.24 ± 0.70 for 6-mers (84 NPs), 6.07 ± 0.79 for 7-mers (126 NPs), 6.09 ± 0.65 for 8-to-10-mers (150 NPs), and

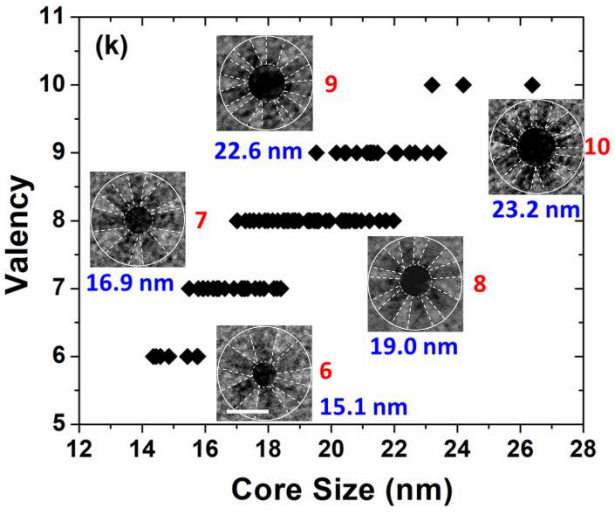

Figure 5.2. Plot of valency vs. core size for BNP-15.2k after stained with RuO_4 for 2 min. Scale bar: 25 nm. This figure is the same as Figure 5.1k except that for each multivalent NP, dashed lines with a larger circle are drawn to guide the view of nanodomains.

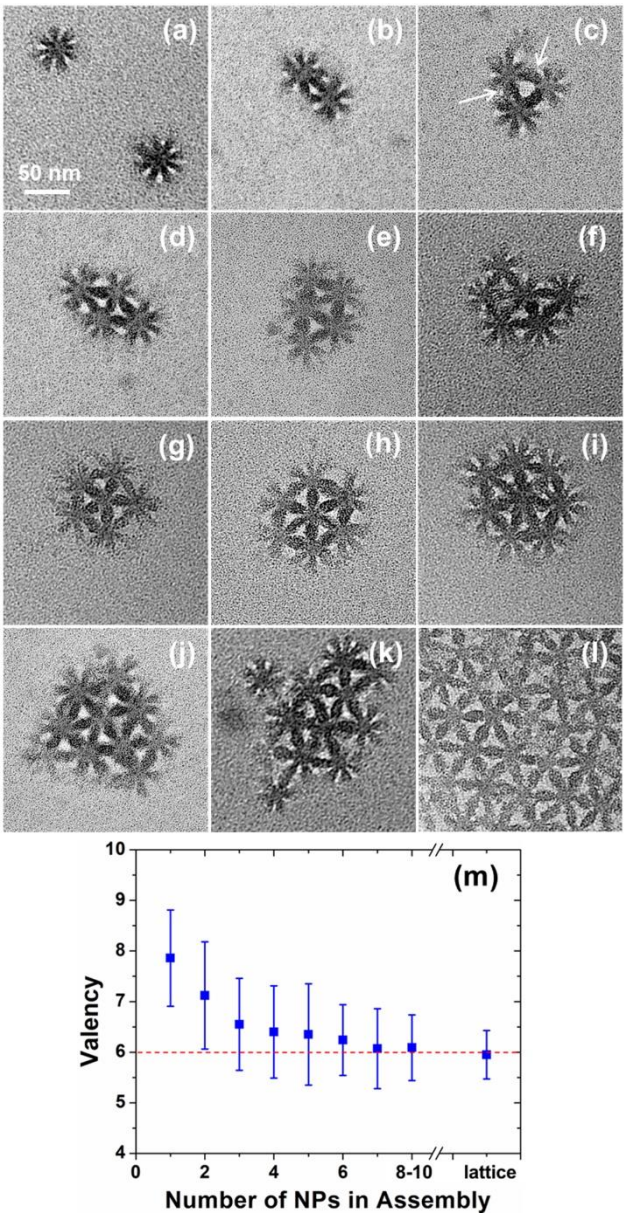

Figure 5.3. TEM micrographs of individual NPs, different-sized assemblies, and NP lattice for BNP-15.2k (a-l). (m) Plot of average NP valency versus NP number in the assembly.

5.95 ± 0.48 for the lattice (212 NPs) (Figure 5.3m), indicating that these multivalent NPs were environmentally adaptable. This intriguing observation can be attributed to the competition of two separate self-assembly processes: brush microphase separation, which leads to a finite, NP size-dependent valency for individual NPs, and NP close packing on 2D surfaces, which prefers a hexagonal symmetry. The NP's valency is preserved when it is commensurate with the lattice site's coordination number 6. However, when they are incommensurate, the NP packing dominates the assembly process and the brushes appear to be able to reconfigure their nanodomain sizes to adapt to the lattice, indicating that the lattice's packing requirement could overwrite the core size's effect. It is also possible that the brushes could dictate the packing of smaller NPs. Computer simulations have shown that when the ratio of the spherical core radius (r) to the polymer size (R_{rms} in the unperturbed state) in the symmetric mixed brush-grafted NPs is < 1, the most stable NP packing is simple cubic crystal lattices in 3D and square arrays in 2D (i.e., brushes dominate).[32] At the ratios of r to R_{rms} > 1, the most stable NP arrangement is body-centered cubic lattices in 3D and hexagonal arrays in 2D (i.e., core NPs dominate).

Figures 5.4 and 5.5 shows the TEM micrographs of small and large NP assemblies for nine mixed brush samples, respectively. While the bonds between NPs for BNP-6.1k to -15.2k were formed by dark nanodomains, they changed to bright domains for BNP-20.0k, -23.0k and -27.6k. This bond inversion was caused by the changes of relative molecular weights and f_{PS}. When the PS M_n was ≥ 20.0 kDa (f_{PS} > 0.50), P*t*BA became the minority component, forming the bonds between NPs. For BNP-6.1k, the bonds were rather weak due to the short PS chains. On the other hand, for BNP-31.5k, PS was significantly longer than P*t*BA, making it difficult for P*t*BA nanodomains to form bonds, as evidenced by the dark gaps between mutually-pointing bright nanodomains. Interestingly, the PS bonds in Figure 5.4e bulged out in the center, while they were

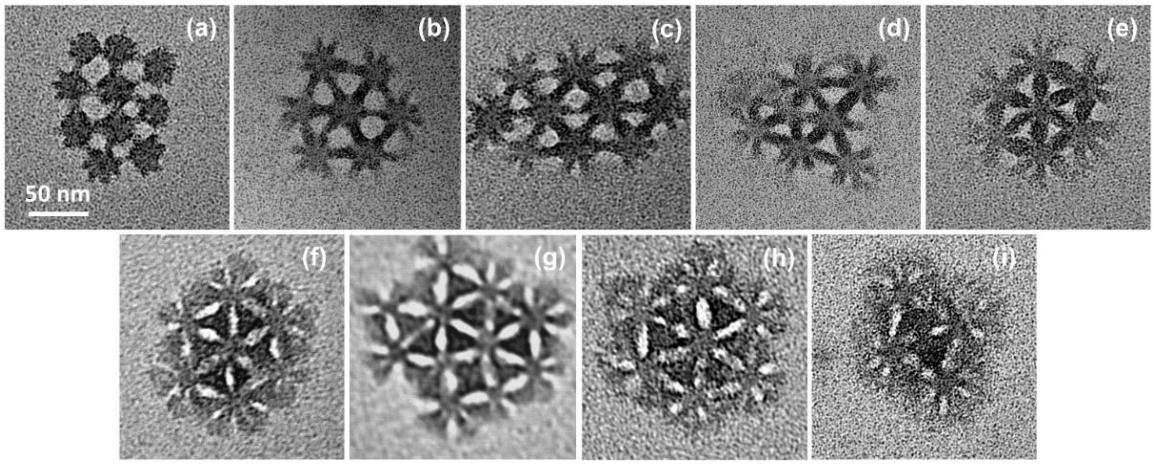

Figure 5.4. TEM micrographs of small NP assemblies of BNP-6.1k (a), -9.7k (b), -10.9k (c), -12.9k (d), -15.2k (e), -20.0k (f), -23.0k (g), -27.6k (h), and -31.5k (i).

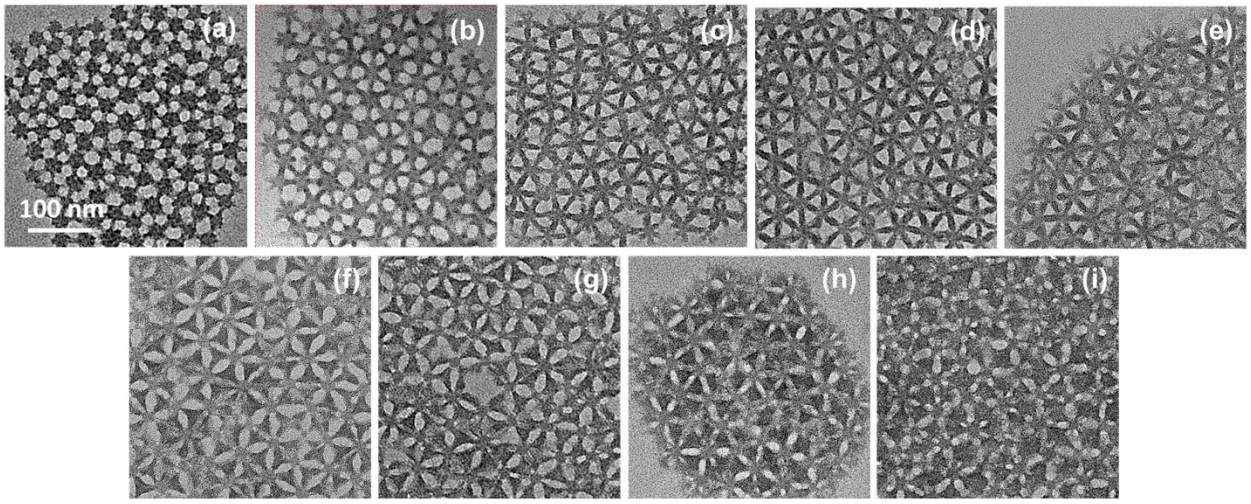

Figure 5.5. TEM micrographs of NP assemblies of BNP-6.1k (a), -9.7k (b), -10.9k (c), -12.9k (d), -15.2k (e), -20.0k (f), -23.0k (g), -27.6k (h), and -31.5k (i). The hairy NPs were drop cast onto carbon-coated TEM grids, annealed with $CHCl_3$ vapor for ≥ 3 h, and stained with RuO_4 for 7 min.

straighter in Figure 5.4b-c, indicating that the PS in BNP-15.2k was more relaxed. Similarly, the P*t*BA bonds were more flower-like in BNP-20.0k and -23.0k but more uniform in width in BNP-27.6k (Figure 5.5).

5.4. Conclusions

In summary, we demonstrated the fabrication of multivalent NPs with a valency of 6 to 10 utilizing the spontaneous microphase separation of binary mixed brushes grafted on NPs with a radius similar to the polymer sizes.[45] A linear relationship was observed between valency and average core size. These NPs can form bonds through the overlap of nanodomains, and the valency decreased with increasing NP number in the assembly, showing the NPs' adaptability. Moreover, we observed the bond inversion from one polymer to another with the change of relative molecular weights of the two polymers. The multivalent NPs presented here were on 2D surfaces (i.e., 2D multivalent NPs). Fox et al. previously observed by cryo-electron tomography that mixed poly(acrylic acid)/polystyrene brushes grafted on 50-90 nm silica NPs phase separated laterally in *N*,*N*-dimethylformamide.[43] On the other hand, simulation studies showed that mixed brushes in nonselective solvents phase separated laterally over a wide range of solvent conditions when the two polymers were sufficiently immiscible.[21,31,44] Thus, it is feasible to make 3D multivalent NPs from mixed brush-grafted small NPs in solvents. We plan to explore 3D multivalent NPs by using cryo-TEM, selective crosslinking of nanodomains, freeze-drying, etc. By tuning the core size and brush parameters, multivalent NPs with a valency from 1 to 10 are likely achievable, and thus this bottom-up approach could open up new opportunities for studying patchy NPs, not only in the fabrication but also in the self-assembly behavior in 3D, e.g., by changing the solvent quality, and in 2D, e.g., at the air-water interface by the Langmuir-Blodgett technique.

References

1. Zhang, Z. L.; Glotzer, S. C. Self-Assembly of Patchy Particles. *Nano Lett.* **2004**, *4*, 1407-1413.
2. Chen, Q.; Bae, S. C.; Granick, S. Directed Self-Assembly of a Colloidal Kagome Lattice. *Nature* **2011**, *469*, 381-384.
3. Wang, Y. F.; Wang, Y.; Breed, D. R.; Manoharan, V. N.; Feng, L.; Hollingsworth, A. D.; Weck, M.; Pine, D. J. Colloids with Valence and Specific Directional Bonding. *Nature* **2012**, *491*, 51-55.
4. Choueiri, R. M.; Galati, E.; Thérien-Aubin, H.; Klinkova, A.; Larin, E. M.; Querejeta-Fernández, A.; Han, L.; Xin, H. L.; Gang, O.; Zhulina, E. B.; Rubinstein, M.; Kumacheva, E. Surface Patterning of Nanoparticles with Polymer Patches. *Nature* **2016**, *538*, 79-83.
5. Gröschel, A. H.; Walther, A.; Löbling, T. I.; Schacher, F. H.; Schmalz, H.; Müller, A. H. E. Guided Hierarchical Co-assembly of Soft Patchy Nanoparticles. *Nature* **2013**, *503*, 247-251.
6. Walther, A.; Müller, A. H. E. Janus Particles: Synthesis, Self-Assembly, Physical Properties, and Applications. *Chem. Rev.* **2013**, *113*, 5194–5261
7. Wang, B. B.; Li, B.; Zhao, B.; Li, C. Y. Amphiphilic Janus Gold Nanoparticles via Combining "Solid State Grafting to" and "Grafting-from" Methods. *J. Am. Chem. Soc.* **2008**, *130*, 11594-11595.
8. Aveyard, R. Can Janus Particles Give Thermodynamically Stable Pickering Emulsions? *Soft Matter* **2012**, *8*, 5233-5240.
9. Liu, H.; Luo, J. C.; Shan, W. P.; Guo, D.; Wang, J.; Hsu, C.-H.; Huang, M. J.; Zhang, W.; Lotz, B.; Zhang, W.-B.; Liu, T. B.; Yue, K.; Cheng, S. Z. D. Manipulation of Self-Assembled Nanostructure Dimensions in Molecular Janus Particles. *ACS Nano* **2016**, *10*, 6585–6596.

10. Kim, J.; Song, X.; Kim, A.; Luo, B.; Smith, J. W.; Ou, Z.; Wu, Z.; Chen, Q. Reconfigurable Polymer Shells on Shape-Anisotropic Gold Nanoparticle Cores. *Macromol. Rapid Commun.* **2018**, *39*, 1800101.

11. Galati, E.; Tao, H. C.; Tebbe, M.; Ansari, R.; Rubinstein, M.; Zhulina, E. B.; Kumacheva, E. Helicoidal Patterning of Nanorods with Polymer Ligands. *Angew. Chem. Int. Ed.* **2019**, *58*, 3123-3127.

12. Yu, L.; Shi, R.; Qian, H-J.; Lu, Z.-Y. Versatile Fabrication of Patchy Nanoparticles via Patterning of Grafted Diblock Copolymers on NP Surface. *Phys. Chem. Chem. Phys.* **2019**, *21*, 1417-1427.

13. Zhou, Y. R.; Ma, X. D.; Zhang, L. S.; Lin, J. P. Directed Assembly of Functionalized Nanoparticles with Amphiphilic Diblock Copolymers. *Phys. Chem. Chem. Phys.* **2017**, *19*, 18757-18766.

14. Rossner, C.; Zhulina, E. B.; Kumacheva, E. Staged Surface Patterning and Self-Assembly of Nanoparticles Functionalized with End-Grafted Block Copolymer Ligands. *Angew. Chem. Int. Ed.* **2019**, *58*, 9269-9274.

15. Yang, Y. Q.; Yi, C. L.; Duan, X. Z.; Wu, Q.; Zhang, Y.; Tao, J.; Dong, W. H.; Nie, Z. H. Block-Random Copolymer-Micellization-Mediated Formation of Polymeric Patches on Gold Nanoparticles. *J. Am. Chem. Soc.* **2021**, *143*, 5060−5070.

16. Yi, C. L.; Yang, Y. Q.; Nie, Z. H. Alternating Copolymerization of Inorganic Nanoparticles. *J. Am. Chem. Soc.* **2019**, *141*, 7917-7925.

17. Yi, C. L.; Liu, H.; Zhang, S. Y.; Yang, Y. Q.; Zhang, Y.; Lu, Z. Y.; Kumacheva, E.; Nie, Z. H. Self-Limiting Directional Nanoparticle Bonding Governed by Reaction Stoichiometry. *Science* **2020**, *369*, 1369-1374.

18. Rossner, C.; Tang, Q.; Müller, M.; Kothleitner, G. Phase Separation in Mixed Polymer Brushes on Nanoparticle Surfaces Enables the Generation of Anisotropic Nanoarchitectures. *Soft Matter* **2018**, *14*, 4551-4557.

19. Tao, H. C.; Chen, L. Y.; Galati, E.; Manion, J. G.; Seferos, D. S.; Zhulina, E. B.; Kumacheva, E. Helicoidal Patterning of Gold Nanorods by Phase Separation in Mixed Polymer Brushes. *Langmuir* **2019**, *35*, *48*, 15872–15879.

20. Zhang, N.; Yu, L.; Li, Y.-C.; Liu, H.; Lu, Z.-Y. Novel Nano-Patterned Structures of Mixed Hairy Nanoparticles in Single Layer. *Polymer* **2020,** *192*, 122295.

21. Roan, J.-R. Soft Nanopolyhedra as a Route to Multivalent Nanoparticles. *Phys. Rev. Lett.* **2006,** *96*, 248301.

22. Marko, J. F.; Witten, T. A. Phase Separation in a Grafted Polymer Layer. *Phys. Rev. Lett.* **1991**, *66*, 1541-1544.

23. Zhulina, E.; Balazs, A. C. Designing Patterned Surfaces by Grafting Y-Shaped Copolymers. *Macromolecules* **1996,** *29*, 2667-2673.

24. Sidorenko, A.; Minko, S.; Schenk-Meuser, K.; Duschner, H.; Stamm, M. Switching of Polymer Brushes. *Langmuir* **1999,** *15*, 8349-8355.

25. Minko, S.; Müller, M.; Usov, D.; Scholl, A.; Froeck, C. Stamm, M., Lateral versus Perpendicular Segregation in Mixed Polymer Brushes. *Phys. Rev. Lett.* **2002,** *88*, 035502.

26. Zubarev, E. R.; Xu, J.; Sayyad, A.; Gibson, J. D. Amphiphilicity-Driven Organization of Nanoparticles into Discrete Assemblies. *J. Am. Chem. Soc.* **2006**, *128*, 15098-15099.

27. Zhao, B.; Zhu, L. Mixed Polymer Brush-Grafted Particles: A New Class of Environmentally Responsive Nanostructured Materials. *Macromolecules* **2009**, *42*, 9369-9383.

28. Song, J. B.; Cheng, L.; Liu, A. P.; Yin, J.; Kuang, M.; Duan, H. W. Plasmonic Vesicles of Amphiphilic Gold Nanocrystals: Self-Assembly and External-Stimuli-Triggered Destruction. *J. Am. Chem. Soc.* **2011**, *133*, 10760–10763.

29. Guzman-Juarez, B.; Abdelaal, A.; Kim, K.; Toader, V.; Reven, L. Fabrication of Amphiphilic Nanoparticles via Mixed Homopolymer Brushes and NMR Characterization of Surface Phase Separation. *Macromolecules* **2018**, *51*, 9951−9960.

30. Wang, J.; Müller, M. Microphase Separation of Mixed Polymer Brushes: Dependence of the Morphology on Grafting Density, Composition, Chain-Length Asymmetry, Solvent Quality, and Selectivity. *J. Phys. Chem B* **2009,** *113*, 11384-11402.

31. Wang, Y.; Yang, G.; Tang, P.; Qiu, F.; Yang, Y.; Zhu, L. Mixed Homopolymer Brushes Grafted Onto a Nanosphere. *J. Chem. Phys.* **2011,** *134*, 134903.

32. Chen, C.; Zhang, T.; Zhu, L.; Zhao, B.; Tang, P.; Qiu, F. Hierarchical Superstructures Assembled by Binary Hairy Nanoparticles. *ACS Macro Lett.* **2016,** *5*, 718-723.

33. Chancellor, A. J. Synthesis of Well-Defined Binary Mixed Brushes on 20 nm Silica Nanoparticles and Asymmetrically End-Functionalized Semicrystalline Poly(ε-caprolactone)s. M.S. Thesis, University of Tennessee Knoxville, 2020.

34. Matyjaszewski, K.; Xia, J. Atom Transfer Radical Polymerization. *Chem. Rev.* **2001**, *101*, 2921-2990.

35. Hawker, C. J.; Bosman, A. W.; Harth, E. New Polymer Synthesis by Nitroxide Mediated Living Radical Polymerizations. *Chem. Rev.* **2001**, *101*, 3661-3688.

36. Li, D. J.; Sheng, X.; Zhao B. Environmentally Responsive “Hairy” Nanoparticles: Mixed Homopolymer Brushes on Silica Nanoparticles Synthesized by Living Radical Polymerization Techniques. *J. Am. Chem. Soc.* **2005,** *127*, 6248-6256.

37. Bao, C. H.; Tang, S. D.; Wright, R. A. E.; Tang, P.; Qiu, F.; Zhu, L.; Zhao, B. Effect of Molecular Weight on Lateral Microphase Separation of Mixed Homopolymer Brushes Grafted on Silica Particles. *Macromolecules* **2014**, *47*, 6824-6835.

38. Chancellor, A. J.; Seymour, B. T.; Zhao, B. Characterizing Polymer-Grafted Nanoparticles: From Basic Defining Parameters to Behavior in Solvents and Self-Assembled Structures. *Anal. Chem.* **2019**, *91*, 6391-6402.

39. Hiemenz, P. C.; Lodge, T. P. *Polymer Chemistry*, 2nd ed.; CRC Press: Boca Raton, FL, 2007.

40. Horton, J. M.; Tang, S.; Bao, C.; Tang, P.; Qiu, F.; Zhu, L.; Zhao, B. Truncated Wedge-Shaped Nanostructures Formed from Lateral Microphase Separation of Mixed Homopolymer Brushes Grafted on 67 nm Silica Nanoparticles: Evidence of the Effect of Substrate Curvature. *ACS Macro Lett.* **2012,** *1*, 1061-1065.

41. Kim, S.; Kim, T.-H.; Huh, J.; Bang, J.; Choi, S.-H. Nanoscale Phase Behavior of Mixed Polymer Ligands on a Gold Nanoparticle Surface. *ACS Macro Lett.* **2015**, *4*, 417-421.

42. Tang, C.; Lennon, E. M.; Fredrickson, G. H.; Kramer, E. J.; Hawker, C. J. Evolution of Block Copolymer Lithography to Highly Ordered Square Arrays. *Science* **2008**, *322*, 429-432.

43. Fox, T. L.; Tang, S. D.; Horton, J. M.; Holdaway, H. A.; Zhao, B.; Zhu, L.; Stewart, P. L. In-Situ Characterization of Binary Mixed Polymer Brush-Grafted Silica Nanoparticles in Aqueous and Organic Solvents by Cryo-Electron Tomography. *Langmuir* **2015**, *31*, 8680.

44. Soga, K. G.; Zuckermann, M. J.; Guo, H. Binary Polymer Brush in a Solvent. *Macromolecules* **1996**, *29*, 1998–2005.

45. The work described in this Chapter has been published in *J. Am. Chem. Soc.* as a communication. Bohannon, C. A.;† Chancellor, A. J.;† Kelly, M. T.; Le, T. T.; Zhu, L.; Li,

C. Y.; Zhao, B. Adaptable Multivalent Hairy Inorganic Nanoparticles. *J. Am. Chem. Soc.* **2021**, *143(41)*, 16919–16924. † These authors contributed equally to this work.

https://pubs.acs.org/doi/abs/10.1021/jacs.1c08261

Chapter 6: Conclusions and Future Work

Electrocaloric materials, which undergo temperature changes upon the application and removal of an electrical field, show great promise in the area of microelectronic cooling without the need for bulky motors or refrigerant. Traditional ferroelectric ceramics and polymers as electrocaloric materials, however, suffer from limitations such as small temperature changes, high electric fields needed for switching of the polar moieties, and joule heating. This dissertation research is aimed at overcoming these hurdles through the design and synthesis of ferroelectric, aromatic mesogen-free, liquid crystalline polymers for potential use as an electrocaloric material. Mesogen-free sulfonylated liquid crystalline polymers could exhibit high spontaneous polarizations under relatively low electric fields because of the large dipole moment of the sulfonyl groups and the high mobility in the liquid crystalline state. A series of chiral poly(oxypropylene) (POP) polyethers with sulfonylated alkyl side chains were synthesized, with chirality being introduced into either the backbone or side chains or both to seek the chiral smectic C (SmC*) phase, and their liquid crystalline self-assembly behavior was investigated using a combination of differential scanning calorimetry (DSC), polarized light microscopy (PLM), and X-ray diffraction (XRD).

In Chapter 2, we first explored the strategy of introducing chirality into the POPs with sulfonylated linear alkyl chains. A series of mesogen-free comb-like isotactic POPs (iPOPs) grafted with *n*-alkylsulfonylpentylthioether side chains (iPOP-$SC_5SO_2C_n$, where C_n is the alkyl tail and *n* is either 12 or 8) were first synthesized from isotactic poly[(*R*)-(-)-epichlorohydrin] and then oxidized into iPOPs with *n*-alkylsulfonylpentylsulfonyl side chains (iPOP-$SO_2C_5SO_2C_n$).[1] For comparison, atactic POPs with the same side chains were also prepared. The key points that we learned from the structure study of these polymers by DSC, PLM, and XRD are summarized below. (i) More liquid crystalline phases were observed when the distance between the sulfonyl group and the chiral center in the backbone of iPOP-$SC_5SO_2C_n$ was increased compared with the

iPOPs containing *n*-alkylsulfonyl side chains (iPOP-SO_2C_n) due to the weakened dipole-dipole interactions. (ii) The backbone chirality of iPOP-$SC_5SO_2C_n$ played an insignificant role in inducing liquid crystalline phases as similar phase transitions were observed for both isotactic and atactic polymers. (iii) A longer linear alkyl tail helped stabilize the liquid crystalline phase as a SmA phase was observed between SmE and I for iPOP-$SC_5SO_2C_{12}$ but not iPOP-$SC_5SO_2C_8$. (iv) After the oxidation of POPs with *n*-alkylsulfonylpentylthioether side chains into POPs with *n*-alkylsulfonylpentylsulfonyl side chains, the liquid crystalline phase transition temperatures increased significantly due to the enhanced chiral center-dipole and dipole-dipole interactions among side chains as well as the higher dipole density. Although the SmC* phase was not realized but the chiral SmA phase (SmA*, with chirality in the backbone), the understanding gained from this study will help us in the future design of mesogen-free liquid crystalline polymers. Note that the SmA* phase has been reported to exhibit the electroclinic properties.[2]

In Chapter 3, we explored two strategies to attempt to induce the SmC* phase. We hypothesized that when the grafting density of sulfonylated side chains in iPOPs is reduced to a certain degree, a tilted layered liquid crystalline phase might form due to the requirement of maintaining a constant density and the strong dipole-dipole interactions among neighboring side chains.[3] We systematically decreased the grafting density of *n*-dodecylsulfonyl side chains of iPOPs from 100% to 50%. Unfortunately, we found only SmA phases at higher grafting densities (80–100%) and a hexagonal columnar structure at lower grafting densities (60–80%). In the second strategy, we introduced a methyl branch, chiral or racemic, into the short sulfonylated alkyl side chains with 4 carbon atoms of atactic and isotactic POPs.[4] The incorporation of a chiral methyl moiety paired with the chiral isotactic main chain showed the most promise for inducing tilted side chains as XRD analysis of a stretched fiber revealed titled side chains in the crystalline phase of

the polymer, similar to what is seen in a SmC* LC morphology.[4] This prompted us to further explore this approach in Chapter 4 to seek the SmC* phase.

Having learned in the study in Chapter 2 that a longer alkyl tail can stabilize the liquid crystalline phases, we increased the alkyl tail length from a total of five carbon atoms in Chapter 3 to 8 and 12 carbon atoms with a chiral or racemic methyl branch in each side chain of isotactic and atactic POPs. In addition, a -$CH_2CH_2CH_2O$- spacer was incorporated between the sulfonyl group and the methyl branch in the alkyl tail to increase the flexibility of the side chains. The polyethers were made and their structures were characterized. Similar to the observation in Chapter 3, the methyl branch in the sulfonylated side chains induced chain tilting in the smectic layers. With double chirality in both the backbone and the side chains, the polymer exhibited a crystalline structure after stretching. When single chirality existed, whether in the main chain or in the side chain, a smectic C*-like phase with tilted side chains was observed. However, no ferroelectric switching was observed in the electric displacement-electric field study, likely due to the strong dipole-dipole interactions. Nevertheless, it is exciting to see the SmC*-like phase in our chiral mesogen-free liquid crystalline polymers. Future work could consider the weakening of the dipole-dipole interactions by moving the sulfonyl groups away from the backbone. Use of an ethyl branch in place of a methyl moiety may elicit a higher tilt angle and subsequently a SmC* phase. Although the genuine ferroelectric SmC* phase has not been achieved, the above studies provide us valuable guidance towards this goal. Future research will be carried out to achieve ferroelectricity in these mesogen-free liquid crystalline polymers.

Chapter 5 presents a side project on the use of transmission electron microscopy to characterize the morphology of binary mixed poly(*tert*-butyl acrylate) (P*t*BA)/polystyrene (PS) brushes grafted on 20.4 nm silica nanoparticles (NPs) upon casting from a good solvent for both polymers.

Although computer simulations had long predicted that mixed brushes grafted on nanospheres with a radius comparable to the polymer sizes phase separated into a small and defined number of nanodomains, producing multivalent brush NPs, no experimental work was performed. A series of well-defined mixed P*t*BA/PS brush-grafted silica NPs with the same P*t*BA M_n but different PS molecular weights were synthesized by my colleague, Andrew J. Chancellor, and imaged and analyzed by me using transmission electron microscopy (TEM). The brush NPs were drop cast onto carbon-coated TEM grids, annealed in chloroform, and stained using ruthenium tetraoxide. TEM imaging revealed that the mixed brush NPs phase separated into patchy NPs with a valency ranging from 6 to 10.[5] A linear relationship was observed between the valency and the average core size and valency. Interestingly, these multivalent brush NPs can interact with each other and form bonds through the overlap of nanodomains. They were also found to change the valency by reconfigure the microphase separation of the mixed brushes upon interacting with other NPs. The work provides a new experimental approach toward multivalent NPs. Future work could consider the synthesis of well-defined binary mixed homopolymer brushes on smaller NPs, with a diameter from a few nanometers to 20 nanometers.

References

1. Bohannon, C. A.;† Kwok, M.-H.;† Li, R.; Zhu, L.; Zhao, B. Effects of Tacticity and Chiral Center-to-Dipole Distance on Mesogen-Free Liquid Crystalline Self-Assembly of Sulfonyl-Containing Comb-Like Polymers. *Polymer Chemistry* **2020,** *11* (17), 3018-3031. † Contributed equally to the work.
2. Nishiyama, S.-i.; Ouchi, Y.; Takezoe, H.; Fukuda, A. Giant Electroclinic Effect in Chiral Smectic A Phase of Ferroelectric Liquid Crystals. *Japanese Journal of Applied Physics* **1987,** *26* (Part 2, No. 11), L1787-L1789.
3. Kwok, M.-H.;† Bohannon, C. A.;† Crooks, J. L.; Li, R.; Zhao, B.; Zhu, L., Grafting Density-Induced Smectic A to Hexagonal Columnar Transition in Mesogen-Free Isotactic Liquid Crystalline Polyethers with *n*-Dodecylsulfonyl Side Groups. *Giant* **2020,** *1*, 100003. † Contributed equally to the work.
4. Kwok, M.-H.;† Bohannon, C. A.;† Li, R.; Zhao, B.; Zhu, L., Ordered Hexagonal Columnar Liquid Crystalline Self-Assembly of Mesogen-Free Sulfonylated Side-Chain Chiral Polyethers and Their High Dielectric Property. *Giant* **2021,** *8*, 100079. † Contributed equally to the work.
5. Bohannon, C. A.;† Chancellor, A. J.;† Kelly, M. T.; Le, T. T.; Zhu, L.; Li, C. Y.; Zhao, B. Adaptable Multivalent Hairy Inorganic Nanoparticles. *J. Am. Chem. Soc.* **2021**, *143(41)*, 16919–16924. † Contributed equally to the work.

Vita

Caleb Alexander Bohannon was born in Statesboro, Georgia, U.S.A in 1993. In December 2016 he received his B.S degree in chemistry from Georgia Southern University in Statesboro, Georgia. Upon completion of his undergraduate studies, he enrolled as a graduate student at the University of Tennessee, Knoxville in August 2017. Soon after entering, he joined Professor Bin Zhao's research group, where his research focused on the synthesis and characterization of chiral mesogen-free liquid crystalline polymers as well as TEM analysis of multivalent brush nanoparticles. He received a Doctor of Philosophy Degree in Chemistry from the University of Tennessee, Knoxville in May 2022.